Italian National Agency for New Technologies,
Energy and Sustainable Economic Development

High Performance Computing on CRESCO infrastructure: research activities and results 2021

December 2022

Italian National Agency for New Technologies,
Energy and Sustainable Economic Development

High Performance Computing on CRESCO Infrastructure: research activity and results 2021

December 2022

High Performance Computing on CRESCO Infrastructure:
research activity and results 2021

Contributions provided by a selection of users of the CRESCO infrastructure
Scientific Editor: Luigi Bucci, ENEA, TERIN-ICT-HPC
Cover: Amedeo Trolese, ENEA, TERIN-ICT, CR Frascati
Cover image: FUGAKU Supercomputer
ISBN: 978-88-8286-440-8

Contents

FOREWORD

During the year 2021, the CRESCO high performance computing clusters have provided 150 million hours of "core" computing time, at a high availability rate, to about 150 users, supporting ENEA research and development activities in many relevant scientific and technological domains. In the framework of joint programs with ENEA researchers and technologists, computational services have been provided also to academic and industrial communities.

This report, the thirteenth of a series started in 2008, is a collection of 33 papers illustrating the main results obtained during 2021 using the CRESCO/ENEAGRID HPC facilities. The significant number of contributions proves the importance of the HPC facilities in ENEA for the research community. The topics cover various fields of research, such as materials science, efficient combustion, climate research, nuclear technology, molecular dynamics, plasma physics, biotechnology, complex systems physics, renewable energies, environmental issues, HPC technology. The report shows the wide spectrum of applications of high performance computing, which has become an all-round enabling technology for science and engineering.

Since 2008, the main ENEA computational resources are located near Naples, in Portici Research Centre. This is a result of the CRESCO Project (Computational Centre for Research on Complex Systems), co-funded, in the framework of the 2001-2006 PON (European Regional Development Funds Program), by the Italian Ministry of Education, University and Research (MIUR).
The CRESCO Project provided the financial resources to set up the first HPC x86_64 Linux cluster in ENEA; a major computing installation for both the Italian and the International context: it ranked 126 in the HPC Top 500 June 2008 world list, with 17.1 Tflops and 2504 cpu cores. It was later decided to keep CRESCO as the name for all the Linux clusters in the ENEAGRID infrastructure, which integrates all ENEA scientific computing systems, and is currently distributed in six Italian sites.
CRESCO computing resources were later upgraded in the framework of PON 2007-2013 with the project TEDAT and the cluster CRESCO4, 100 Tflops computing power. In 2020 the ENEAGRID computational resources consist of ~25000 computing cores and a raw data storage of about 5 PB.
In 2015 ENEA and CINECA, the main HPC institution in Italy, signed a collaboration agreement to promote joint activities and projects in HPC. In this framework, CINECA and ENEA participated successfully to a selection launched by EUROfusion, the European Consortium for the Development of Fusion Energy, for the procurement of a several PFlops HPC system, beating the competition of 7 other institutions. The new system MARCONI-FUSION started operation in July 2016 at 1 Pflops computation power level which has been increased to 5 Pflops in the summer of 2017 and thanks to a new awarded tender, the HPC services of MARCONI Fusion have been extend until 2023 with a power peak of 8 PFlops of conventional processors Intel Skylake and 2 PFlops of accelerated GPU partition of CINECA Marconi 100.
The ENEA-CINECA agreement is the key basis for ENEA HPC developments. The CRESCO6 cluster has been installed in 2018 and its own 1.4 PFlops peak computing power, ranked 420th in November 2018 Top500 list. CRESCO6 has been a challenge in HPC co-design system thanks to implement a multi-fabric network able for working Infiniband and Omni-Path on a single GPFS cluster using the same storage systems of CRESCO data centre.

The success and the quality of the results produced by CRESCO stress the role that HPC facilities can play in supporting science and technology for all ENEA activities, national and international collaborations, and the ongoing renewal of the infrastructure provides the basis for an upkeep of this role in the forthcoming years.

Dipartimento Tecnologie Energetiche e Fonti Rinnovabili,
Divisione per lo Sviluppo di Sistemi per l'Informatica e l'ICT - CRESCO Team

ENEA EUROHPC PROJECT: TEXTAROSSA

F.Iannone*,M.Celino, P.Palazzari and *CRESCO team*:
L.Acampora, D.Alderuccio, F.Ambrosino, E.Andreassi, G.Baldassarre, T.Bastianelli, R.Bertini, G.Bracco, L.Bucci, F.Buonocore, M.Caiazzo, B.Calosso, G.Cannataro, M.Caporicci, G.Caretto, M.Chinnici, R.Clemente, D.De Chiara, M.De Rosa, D.Di Mattia, S.D'Onofrio, S.Ferriani, G.Ferro, G.Formisano, A.Funel, S.Giusepponi, G.Guarnieri, M.Gusso, W.Lusani, M.Marano, A.Mariano, S.Migliori, M.Mongelli, S.Pagnutti, F.Palombi, S.Pecoraro, A.Perozziello, S.Pierattini, G.Ponti, M.Puccini, N.Quercioli, C.Ronchetti, G.Santomauro, A.Scalise, F.Simoni, M.Steffè, D.Visparelli,

Energy Technologies & Renewable Sources Department - Information Communication Technologies, Lungotevere Thaon di Revel, 76, 00196 Rome Italy

* Corresponding author. E-mail: *francesco.iannone@enea.it*

ABSTRACT. The ENEA ICT division is involved in several projects activities in the deployment of HPC services for users as well as new HPC technologies. In particular ENEA is the coordinator of the TEXTAROSSA EuroHPC project to address technology gaps aiming to achieve high performance under power tight power consumption for exascale systems. The technology gaps include: energy efficiency and thermal control of hardware; high performance computing using accelerated devices and new arithmetic precision; methods and tools for seamless integration of reconfigurable accelerators (FPGA) in heterogeneous HPC multi-node platforms.

1 Introduction

Rising energy costs, and the increase in data center power consumption driven by an ever increasing demand for data services, are becoming a dominating factor for the Total Cost of Ownership over the lifetime of a computing system. Additionally, current semiconductor technology will be hitting a point where downsizing and, thus, inherent reduction of power, will no longer be possible mainly due to the increase in leakage currents. Many high profile studies show the increase of data center power demands as well as the power challenges that high performance exascale computing will provide. Global data center electricity demand in 2019 was around 200 TWh, or around 0.8% of global final electricity demand. If current trends in the efficiency of hardware and data centre infrastructure can be maintained, global data centre energy demand can remain nearly flat through 2022, despite a 60% increase in service demand. For HPC data centre the main challenge is the threshold of the power consumption to a 20 MW in the exascale systems, e.g. 20 mWatt per GFlops [Handbbok on Data Centers, S.U.Khan, 2015]. To better understand the challenge, figure 1 shows the performances in terms of mW/GFlops of the HPC systems in the first position of the top 500 list in the last 13 years.
The increasing power density in modern post-Dennard scaling Multi-Processor System on Chips (MPSoCs) raises chip temperature and on-chip thermal gradients, leading to a wear-out of silicon devices and putting at stake the lifetime reliability of chips, defined as the long-term reliability. Together, performance and lifetime reliability issues make joint power and thermal management crucial and inevitable for MPSoCs, and also pose an important challenge from the energy efficiency perspective. The next step in higher intensity, more energy efficient cooling in data centers is the move

to “on-chip” cooling, with much higher heat transfer removable rates than air cooling. A new two-phase cooling system using flow of boiling heat transfer to cool electronic devices, and compared to traditional cooling systems (liquid cooling or heat pipes), can achieve significantly.
higher heat transfer coefficients at significantly lower flow rates and pumping power able to achieve a PUE (Power Usage Effectiveness) close to 1, verified by monitoring all relevant information.
In the last decade, mainly because of the continuously increasing graphics processing demands of the video game industry, Graphics Processing Units (GPUs) have evolved into massively parallel computing engines. The current pre-exascale HPC systems in the last Top 10 list, are supercomputers GPU based. On the other hand, FPGA solutions can also offer high throughput to numerous data-intensive applications with critical time constraints

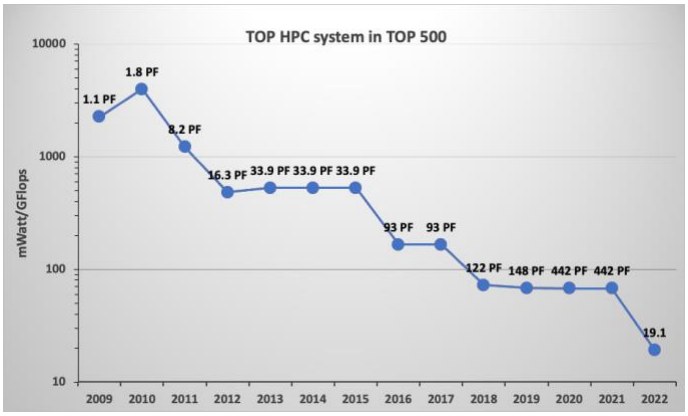

Fig.1: Electric Power consuming per GFlops of the top HPC systems in the TOP 500 lists since 2009

In particular, the FPGA accelerator boards got 2/4 QSFP network interfaces that allow to design HPC systems based on heterogenous architectures with network topologies: 1D torus or 2D mesh/torus with 2/4 node degrees and diameters as n/2 or n1/2.
The heterogenous architectures based on FPGA got a level of flexibility able to set dynamically mixed precision methods suitable to save energy when solving $Ax=b$ using Iterative Refinement (IR). The idea of the mixed precision method is to utilize a low precision for $O(N^3)$ LU solver, while attaining a solution accuracy through $O(N^2)$ refinement, where N is a matrix size. The energy efficiency can be further improved shifting thermal evaluation from the chip design phase to the run-time thermal management. In this context, accurate, fast and flexible thermal simulators help understanding the power dissipation requirements, tailoring the cooling to the chip requirements to best utilize HPC infrastructures while keeping cooling costs at a minimum and enabling run-time thermal management. It can be implemented with more flexibility on programmable accelerator boards FPGA based.
Starting from European Processor Initiative (EPI) activities are planned on the Stencil/tensor accelerator, boosting it using mixed-precision/trans-precision arithmetic and/or Posits and developing an accelerator with an hardware posit processing unit for HPC computation. Alternative to floats Posits are promising to increase bandwidth and memory efficiency and hence boosting performance and saving power either for AI services (Posit8 instead of float16/32), or for scientific computation (posit16/32 instead of float64/128). IPs will be prototyped on reconfigurable technology.
In order to optimize the usage of the available resources, runtime services have to be deployed by taking advantage of energy-saving features provided by the underlying hardware with respect to the application needs. At the runtime services level the operating system is an important part of the energy-saving possibilities. Most HPC systems use the Linux kernel which has an active community maintaining and updating it, thus providing further developments for new energy-saving features. The

Resource Management System, which handles the system resources allocation and workload management, is highly customized for its integration with thermal management tools already available at node level. For example, many available scheduling systems can be optimized via pre-defined policies. Additionally, one could implement software-based support for specific energy saving policies in the scheduling system itself or as a higher level tool on top of the scheduler. This higher-level tool could, for example, validate the workloads energy requirements in order to assure that certain energy driven policies are not violated before the workload is actually scheduled.
In order to design HPC heterogenous system running on FPGA accelerators, the availability of a High-Level Synthesis tool and the possibility to use in the flow pre-designed computation/interfacing IP is mandatory to lower the access barrier currently limiting the widespread adoption of FPGA devices.
One of the basic guidelines in energy efficient computing is the optimization and the acceleration of algorithms and software libraries that provide a reduction of the elapsed time of HPC applications and, as consequence turn, a significant cut in energy consumption.
The new power-to-solution metrics requires a rethinking of many computational kernels of HPC applications looking for a trade-off between the reduction of the total energy and the minimization of the time-to-solution, promoting scalability also for solving ever larger problems as required by high-resolution simulations and big data applications.
Within this context, new open-source high-performance algorithms and software libraries for some, among the most widely used, kernels in numerical linear algebra and graph computation, will be deployed. The library kernels will be of immediate use in a wide range of applications, ranging from simulation of phenomena driven by Partial Differential Equations to complex network analysis.
The algorithms will be designed and optimized having as target platforms clusters of hybrid nodes, with thousands of simple computing units and a memory hierarchy that is much more exposed to the developer's control with respect to the traditional multi-level cache-based systems. It is not unusual for algorithms, inefficient on traditional computing platforms, to become very much competitive on accelerators like GPU because additional computations are well tolerated and convenient when using complex memory access patterns. On the new platforms also data structures may need an in-depth revision. As for GPU, for instance, thread-locality rather than data-locality must be privileged. We are going to investigate also the chance of using, where possible, single-precision floating-point arithmetic that offers many advantages in terms of memory footprint and computational efficiency on GPUs (latest generation GPUs also offer a half-precision, 16 bit-based floating-point arithmetic). Although in general algorithms should be oblivious to the precision of the floating-point arithmetic, at the level of software implementation, any algorithm must be double checked under different conditions (size of the problem, range of the values that the variables can assume, presence of reduction operators), in order to guarantee that single precision and potentially half precision can be safely used, within several IR (Iterative Refinement) techniques for obtaining user's required accuracy.

2 TEXTAROSSA Project

TEXTAROSSA (*Towards EXtreme scale Technologies and Accelerators for euROhpc hw/Sw Supercomputing Applications for exascale*) is a three-year project co-funded by the European High Performance Computing (EuroHPC) Joint Undertaking. The project is led by ENEA (Italy) and aggregates 17 institutions and companies, including the linked third parties, located in 5 European countries: CINI, an Italian consortium grouping together three leading universities, Politecnico di Milano, Università degli studi di Torino, and Università di Pisa, Fraunhofer (Germany), INRIA (France), ATOS (France), E4 Computer Engineering (Italy), BSC (Spain), PSNC (Poland), INFN (Italy), CNR (Italy), In Quattro (Italy), Université de Bordeaux (France), CINECA (Italy) and

Universitat Politecnica de Catalunya (UPC). More information on the activities carried out during the execution of TEXTAROSSA can be found in the project website [1].
From a methodology point of view TEXTAROSSA adopts a co-design process as key strategy for Fast Forward and Exascale computing, considering the entire system stack from underlying technologies to applications. The co-design process concerns five layers covering the whole HPC stack:

1. User Application: representing a wide range of scenarios, from mathematical libraries, to miniApps and flagship codes for numerical modelling with massive parallelism in HPC/HPDA/AI applications. The performance of HPC applications is tied to their level of optimization and the capacity of the underlying tools they use. Research usually focuses on both facets separately: optimizing the applications on one side and improving hardware/middleware layers on the other side. This is not the case with our co-design approach: We aim at connecting both aspects by evaluating the impact of novel technologies on a set of target HPC applications, and, at the same time, studying which improvements at lower levels could be beneficial to these applications.

2. Runtime Services: ensuring that application requirements are dynamically satisfied and mapped onto system resources, and including execution models with workload handling, fault tolerance, and data management. These services are well established in traditional HPC data centers, and the users, mainly belonging to academic and big enterprises research, are aware enough to use the computing resources. Because there has been a growth of edge applications in the last years aimed at effectively analyzing big data in a timely manner, a cloud edge continuum enabling HPC/HPDA is becoming a business case. As the levels and fidelity of instrumentation increase and the types and volumes of available data grow, new classes of applications are being explored that seamlessly combine real-time data with complex programming models and data analytics to monitor and manage systems of interest.

3. Programming Models: underlying the applications, they define the toolchains and SW development tools able to implement applications in parallel architectures. The HPC community provided several programming models that have demonstrated their potential to develop efficient applications. However, parallelization models are used separately, and most of them target CPUs or combinations of CPUs/GPUs, but not FPGAs. However, FPGAs open new possibilities that can be highly beneficial to almost any HPC application, providing toolchains to handle heterogeneous architectures.

4. System Architecture: including the processor core's micro-architecture, the arrangement of cores within a chip, memory hierarchy, system interconnect, and storage subsystems. Future HPC platforms increasingly depend on heterogeneous node architectures to meet power and performance requirements. In the HPC landscape, two main approaches have appeared as viable solutions for a possible system architecture bridging the current gaps in terms of power and performance that are required in Exascale computing: the first approach relies on multi-core processors whose high performance is boosted by the use of GPU-based accelerators; the second approach aims at integrating FPGA-based accelerator within the host architecture. Additionally, interconnection networks featuring very low latency are going to be indispensable to support the high performance of the computation nodes.

5. Platforms: concerning the HW platform at node and rack levels, they need to be able to achieve performance requirements in terms of computing power and energy consumption. High-density computing power at node/rack level requires new technologies of direct cooling on the chip able to remove heat with high efficiency in order to reduce energy consumption. Direct cooling provides a more efficient method to transfer the heat from these hot components to the building chilled water loop and then outside with very little additional energy, compared to transferring the heat first to air and then

to the building chilled water system. In addition, in a direct cooling system, the water temperature returning after cooling the IT equipment is much higher than typically found in data centers, and provides more opportunity for heat reuse or the ability to reject this heat to the atmosphere with a dry cooler, thereby eliminating the requirement of a cooling tower or chiller plant in most climates.

The co-design approach adopted in TEXTAROSSA, addresses the five layers of the HPC stack are in each of the four main stages of the co-design process:

1. Gap Analysis: to compare the current state-of-art of the technological assets with the objectives of the project in order to identify the gap to be filled by developments or update in co-design process.
2. Requirements: to define specifications and requirements of the technological solutions for designing and developing.
3. Proof of Concept: to develop HW/SW prototype solutions able to achieve the KPIs (Key Performance Indicators) of the project objectives.
4. Benchmarking: to provide performance results of the technological solutions by means of benchmark tools.

3 Data Compression in Runtime Services

Scientific applications produce massive amounts of data as high-performance computing (HPC) systems are moving toward exascale. The ever-increasing volumes of data are posing challenges for scientists to store, share, analyse, and visualize them. Compression algorithms have become a crucial component of data management in scientific workflows. Data reduction enables simulations to produce more data without worrying about exceeding storage quotas, thus enabling the capture of more insights in the simulation. However, due to the complexity and poor performance of I/O and compression libraries as well as of parallel file systems, the overall compression and I/O performance vary significantly. Scientific simulations on HPC systems often execute on hundreds of thousands of CPU/GPU cores and generate tens of terabytes of data periodically, such as outputting time-history solutions and checkpoint files every certain number of simulation steps. While data is being transferred from the HPC compute nodes' memory to the storage system, the computation of scientific applications is forced to stall for long periods of time, due to the gap between the computational speed and the I/O bandwidth. This can contribute a significant amount to the total execution time.

Data reduction techniques, such as compression, transformations and deduplication are straightforward solutions to minimize the energy consumption of storage systems by reducing the amount of storage hardware required to store the data. However, data reduction itself can consume significant amounts of energy, potentially negating its beneficial effects on energy efficiency. Indeed, algorithms with a good compression ratio are also very CPU-intensive, thus resulting in a further increase in the processing time. This is where FPGAs come into the picture offloading a CPU from specific tasks, such as compression, encryption, and other functionalities, as FPGAs can be programmed to do specific tasks (compression, in this case) more efficiently and in less time. In this way, we can achieve high compression of data in the same or a shorter amount of time by offloading the compression task to an FPGA, thus freeing the CPU for other tasks, thereby accelerating the overall workload. Next-generation big-data systems will be data-driven heterogeneous architectures that leverage the integration of CPU/GPU/FPGA-accelerated computing.

Other than accelerating computation and offloading the CPU, FPGA accelerators may also give a significant improvement in the power consumption of the overall solution: FPGA technology is in fact

less power-hungry than conventional processors, as performance is achieved through parallelism and not through the high clock frequency [2].
By offloading compute-heavy compression tasks to the FPGA, the CPU is freed to perform other tasks, and the IT organization can take advantage of the significant savings in performance, space, power, and cooling arising from the FPGA implementation of compression.
In cascade data compression, like for instance the Deflate algorithm [3], different compression blocks can be used in combination: in the case of the Deflate algorithm, the LZ77 [4] and the Huffman coding [5] are applied in sequence. The Huffman coding is an example of bitpacking, i.e. it is a compression block implementing a bit-level operation for reducing the number of bits required to store each value; the Huffman algorithm encodes each character of the input through a number of bits inversely proportional to its frequency. Of course, it is highly desirable that data compression could come with the less additional costs possible, both in terms of execution time and required electrical power. To achieve that, a Proof of Concept (PoC) focusing on the acceleration of a bitpacking algorithm has been designed on FPGA.
The bitpacking algorithm has been implemented through the Vitis High-Level Synthesis flow from Xilinx [6]. In this PoC, the aim is to accelerate through FPGA the compression of images coming from a high-speed video camera. The need originated from nuclear fusion experiments with plasmas magnetically confined, where fast cameras with high-performance CMOS sensor technology are usually adopted for acquiring and storing images of plasma discharges. Images come from a Photron FASTCAM SA4 camera installed on the Proto-Sphera (Spherical Plasma for HElicity Relaxation Assessment) experiment [7] in ENEA Frascati (Rome) and used in several tokamak experiments [8]. The FASTCAM SA4 camera provides up to 3600 frames/s at 1024x1024 pixel resolution collected on a 12-bit depth image. 12-bit data are packed in 16-bit words, exposing an alignment that eases subsequent processing, but wastes disk space. The following picture shows a typical plasma discharge image taken with the SA4 camera.

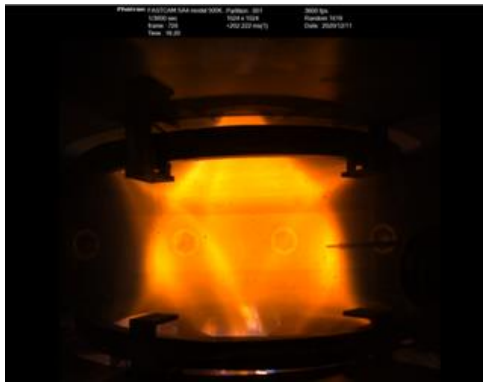

Fig.2: Plasma discharge image from the FASTCAM SA4 camera

The raw data acquired with a digital camera like SA4 is a measure of the radiant intensity which refers to the magnitude or quantity of light energy reflected from or transmitted through the object being imaged by an analog or digital device. It is the only variable that can be utilized by processing techniques in quantitative scientific experiments. The 12-bit pixel depth, associated with the huge amount of data produced by the SA4 camera, poses a problem with the storage. As the video camera can produce nearly 7GB of data per second, it is important to reduce disk space used for the storage without losing any information: this can be achieved by removing, in each 16-bit word codifying a pixel, the most significant 4 bits. In such a way information is fully preserved and 25% of disk space is saved. This simple bitpacking algorithm has been implemented on an Alveo280 Xilinx board.

The compression kernel

As we need to compress the image coming from the SA4 camera, removing the four leading bits in the pixel components, the first functionality designed is the compression function which receives through the input stream the input image and produces through the output stream the compressed image. If m and n are the numbers of bits used to store a component of a colour $N \times N$ image, the input image has dimension $3mN^2/8$ bytes and the output image $3nN^2/8$ bytes, so the compression ratio is m/n. Let's indicate with S the size, in bit, of the input and output streams of the kernel; S is constrained to be a power of 2. In the beginning, input and output images are aligned with respect to S, i.e., both the input and output streams have a pixel component starting at bit 0 of their input/output ports; to determine how many pixels must be read to be aligned again both at the input and at the output streams, we have to find the smallest $k \in \mathbb{N}^+$ satisfying the following equation (% is the modulus operator):

$$(k \cdot m) \,\%\, S = (k \cdot n) \,\%\, S \qquad (1)$$

With the constraint that, when both the input and output data are aligned again, they are aligned at the 0^{th} bit, i.e. (1) must satisfy the following constraint:

$$(k \cdot m) \,\%\, S = 0 \qquad (2)$$

From (1) and (2) it is easy to verify that the solution is:

$$k=LCM(LCM(m,S)/m,LCM(n,S)/n) \qquad (3)$$

where *LCM(a,b)* returns the *Last Common Multiplier* of *a* and *b* and *LCM(p,S)/*p is the smallest number of words with *p* bits necessary to be newly aligned at bit 0. In our case the stream size is *S=512 bits* (thus saturating the PCIe bandwidth in the reasonable hypothesis to use *fck=300 MHz*), *m=16 bits* and *n=12 bits*; the expression (3) gives *k=128*. As we read/write from/to the stream *S* bits, data are newly aligned after $k \cdot m / S=4$ reads from the input stream and $k \cdot n / S=3$ writes to the output stream. From previous computations, the structure of the compression function is shown in the Algorithm 1 and the corresponding Vitis HLS code, in the case *S=512*, *m=16*, *n=12*, is given in the Algorithm 2:

Algorithm 1: compression kernel

```
for (i=0; i<InputImageSize/S; i+= km/S){
   read km/S words from the input stream;
   while (not all the input bits have been copied) {
      copy n bits from the input word to the output word;
      skip (n-m) bits of the input word
    }
    write the kn/S words that have just been filled
}
```

Algorithm 2: HLS code

```
 for (i = 0; i < ImgSize/(S/m)-3; i+=4){
#pragma HLS pipeline
  di = inStream.read();
  for (int j=0; j<(S/m); j++)
{
#pragma HLS unroll
  do.range((j+1)*12-1,12*j) = di.range(16*(j+1)-5,16*j);
 }
 di = inStream.read();
 for (j=0; j<10; j++){
#pragma HLS unroll
do.range(384+(j+1)*12-1,12*j+384)=(di.range(16*(j+1)-
5,16*j));}
do.range(511,504)=(di.range(16*10+7,16*10));
out_stream << do;  //output of the first word
   …//repeat till 4 words have been read
  …// and 3 words have been transmitted
```

```
}
```

in the previous code, thanks to the unroll pragma, all the assignments from the S/m=32 input components to the 32 output components are executed in parallel, in the same clock cycle. As we specified the HLS pipeline pragma, the loop body will be pipelined and, every 4 clock cycles, a new execution of the loop body will start, thus resulting in a continuous reading from the input stream of 64 bytes/cycle; at the same, as the loop body has 3 write operations, every 4 clock cycles 3 words of 64 bytes are written to the output stream.

The auxiliary I/O management kernels

As Alveo U280 Board does not allow streaming from the host to the FPGA card, we designed 2 kernels to access the external memory; one, *loadInput*, reads data from the external memory and writes them to the output stream and the other, *storeOutput*, reads data from the input streams and writes them to the external memory. Both the streams and the memory ports have width *S=512*. The interface with external memory uses the AXI4 standard, but this is completely transparent to the user.
The code to implement the *loadInput* and *storeOutput* kernels is reported below; vectors *in[]* and *out[]* are both stored in two external DDR banks.

Algorithm 3: *loadInput* kernel	**Algorithm 4:** *storeOutput* kernel
for (int i = 0; i < (BitImgSize)/S; i++) *in_stream.write(in[i]);*	*for (int i = 0; i < (BitImgSize)/S; i++)* *out[i] = out_stream.read();*

As Vitis HLS recognizes that the two loops in Algorithms 3 and 4 can be pipelined, at each clock cycle S bits are read from external memory and are written to the bitpacking input stream and, at the same time, S bits are read from the bitpacking output stream and are written to the external memory.

Integration design

Once the bitPacking, loadInput and storeOutput kernels have been designed, they have been put together, originating the design shown in fig. 2.

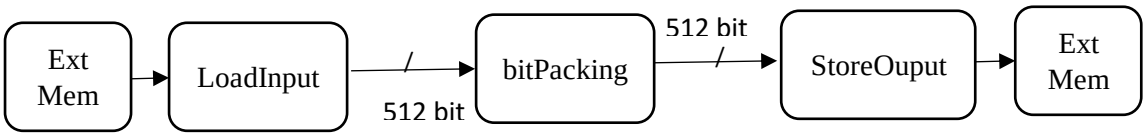

Fig.2: The kernels for the complete FPGA compressing solution

As we can see from the following picture showing the waveforms taken from the *HDL* simulation of the design, the bitpacking input stream is always reading data (512 bits each) while every 3 out of 4 clock cycles output data (512 bits each) are written into the bitpacking output stream.

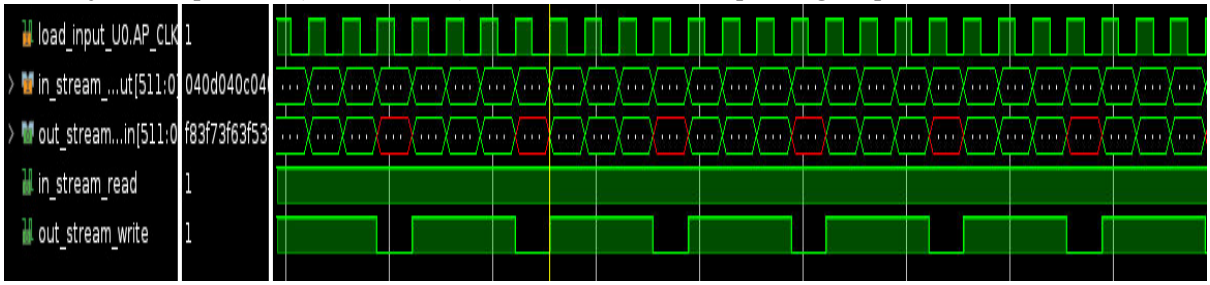

Fig.3: Waveforms from HDL simulation evidencing I/O activity of the bitpacking kernel

Synchronization scheme

To allow the overlapping of communication between host and card with the compression on the FPGA card, we adopted a double buffering scheme that uses two HBM banks *HBMreadA* and *HBMwriteA* in one phase (A) of the computation and *HBMreadB* and *HBMwriteB* in the other phase (B). The host code has three threads: producer thread (Algorithm 8) that sends images to be compressed to an input host buffer accessible to the card, consumer thread (Algorithm 9) that receives the compressed images from an output host buffer accessible to the card, and the main thread that controls the start of the kernels on the card and the data transfers between HBM memory banks on the card and the buffers on the host.

Algorithm 5: *Producer*

```
while(){
    sem_wait(&canProduceIn)
    write image to Bin
    sem_post(&canConsumeIn)
}
```

Algorithm 6: *Consumer*

```
while(){
    sem_wait(&canConsumeOut)
    read image from Bout
    sem_post(&canProduceOut)
}
```

The main thread is synchronized with the producer and consumer threads through semaphores (*canProduceIn(1)*, *canConsumeIn(0)*, *canProduceOut(0)*, *can-ConsumeOut(0)* – in brackets we indicate the initial value for the semaphore) which control the access to the input and output buffers, shared with the FPGA card. The synchronization between the main thread and the FPGA card is achieved through *readEvent*, *writeEvent*, and *RunEvent* that inform the main thread about the end of a read transfer, of a write transfer, and of a kernel execution (all data transfers and kernel executions are used as asynchronous, non-blocking functions).

Algorithm 7: Main thread

```
while(){
    sem_wait(&canConsumeIn);
    doTransferHost2Card(Bin, &H2C_event);
    H2C_event.wait();
    startKernels(krnl, &krnl_event);
    sem_post(&canProduceIn);
    krnl_event.wait();
    sem_wait(&canProduceOut);
    doTransferCard2Host(Bout, &C2H_event);
    sem_post(&canConsumeOut);
}
```

In the fragments of code reported in Algorithm 7, the basic synchronization scheme among the producer, consumer, and main threads, is sketched. For the sake of readability, we do not show the implementation of the ping pong buffer which alternates between the bank pairs HMB0/HBM1 and HBM2/HBM3: when transferring to/from HBM0/HBM1 the kernels are processing images on HBM2/HBM3 and vice-versa.

The following Fig.4 shows the graphical report produced by Vitis using the events registered during the actual run on the Xilinx U280 board. As we see, the compressing kernels (evidenced in green) are always running and, at the same time, there is always a transfer to/from the external HBM banks (either HBM0/HBM1 or HBM2/HBM3).

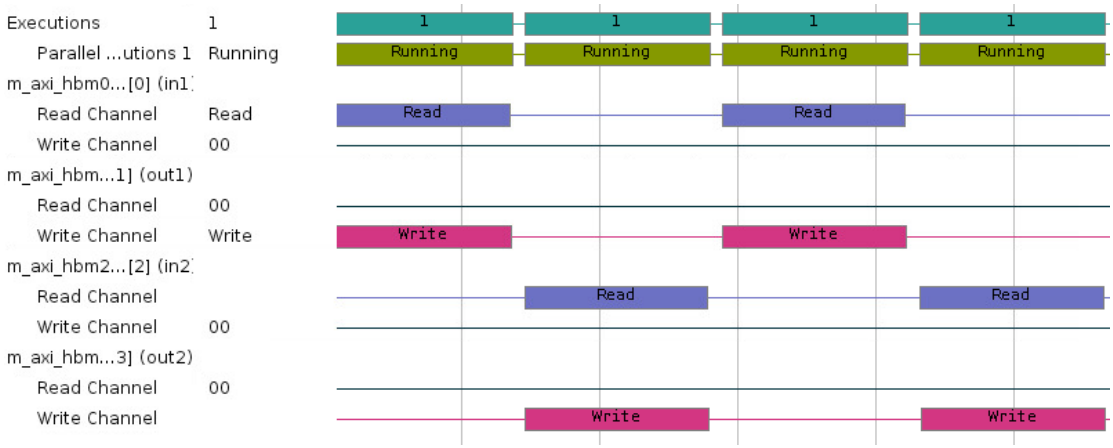

Fig.5: Overlap of the run of compressing kernels with I/O on HBM banks (ping pong scheme).

4 Power-Performance metrics

Together with HW/SW architecture of the PoC, some KPIs must be defined to check if the proposed design reaches its goals. Let's start by reviewing come of the main power performance metrics.

Usually the following four classes of metrics are used to quantify the power-performance characteristics of an HPC system [Feng,2005].

- *Power*. It is responsible for heat dissipation rate or system operating temperature. For an HPC system, power can be defined at various levels of granularity, from the highest to the lowest: HPC system (PHPC), compute node (PCN) and component (PC). Furthermore, the power consumption varies with the HPC workload. Since an application uses only a part of the power absorbed by the system, we define this part as the power application (PA), which can be divided into idle and load power. The idle power is the power consumption under zero workload (i.e., it is the system overhead) and the load power is the increased part of the power consumption when workloads execute on a node. Usually, the idle power is constant while the load power varies with time and workload.
- *Energy*. The energy consumed by a HPC system in the time interval $[t_1, t_2]$ is:
-

$$E_S = \int_{t_t}^{t_2} P_{HPC}\, dt \qquad (4)$$

The application Energy is:

$$E_A = \int_0^D P_A\, dt \qquad (5)$$

Here *D* is delay which is equivalent to $(t_2\text{-}t_1)$ in the Power system equation or TTS (Time-to-solution for the application). Similarly, application energy consumption can be broken into idle and load parts.

- *Performance*. Performance (i.e. reduced TTS) is the critical design constraint in high-performance systems. For fixed workload, speedup can be used to quantify performance comparisons between two alternatives designs or two operating points.
- *Power Performance efficiency*. Sometimes, the performance of HPC systems is improved at the cost of more energy consumption. For example, the number of nodes or operating points used by an application directly affects both energy consumption and TTS; for a fixed problem size on an increasing number of nodes, it is likely that there is an operating point where increasing the number of nodes results in largely increased energy consumption with little or no performance gain (i.e. TTS). Therefore, to quantify the power-performance trade-off of an

application on different system configurations, the energy-delay product, $E \cdot D$ and/or energy-delay-square product (ED2P) $E \cdot D^2$ is used to quantify power-performance efficiency in the context of parallel scalability.

For the power Performance efficiency, there are some specific definitions [9]. The most obvious one is to compare the TTS to the energy-to-solution (ETS) for a set of runs of both codes and benchmarks. The power performance efficiency can be estimated in terms of Energy Delay Product (EDP). The EDP proposed by Cameron, is a metric to evaluate trade-off between TTS and ETS. The EDP is defined as:

$$EDP = E \times T^w \qquad (6)$$

where E is the total energy consumed during the run, T is TTS and w is a parameter to weight performance versus power. Common values of this parameter are $w=1,2,3$. The larger is the w exponent the greater the weight we assign to its performance. Following the previous discussion, we take as KPI the clear reduction, i.e. at least a factor 2, of the EDP, defined for $w=1$, with respect to CPU and GPU technologies.

5 Experimental setup design

The PoC of the *bitpacking* data compression and decompression has been designed and developed on the ENEA FPGA LAB in the CRESCO Data Centre. The ENEA CRESCO FPGA LAB (Fig. 6) has made available to the TextaRossa Project a pool of compute nodes equipped with:

- n.6 Linux X86_64 nodes with 2 x Intel Xeon Haswell CPU, 128 GB RAM
- n.2 Xilinx U280 + n.2 Xilinx U250 FPGA boards
- Sys.Op. Linux Centos 7.4
- Development software tools: Xilinx VITIS 2021.1

Access to the FPGA Lab resources is available by getting an account in the ENEAGRID infrastructure following the access rules reported in the ENEA CRESCO portal [10]. The compute nodes equipped with FPGA boards can be accessed via ssh on the front-end node: cresco-in.portici.enea.it and forwarding on to: *cresco-xilinx0/1/2/3/4/5.portici.enea.it*

A graphical remote access to compute nodes of the FPGA Lab is available using ENEA F.A.R.O. (Fast Access Remote Objects) using a client ThinLinc on the front-end node: *cresco-in-gui.portici.enea.it*

For the TextaRossa project are available some Development Operations tools as follow:

- A gitlab for source codes and data benchmark repositories [11].
- ENEA Staging Storage Sharing system based on Owncloud using AFS (Andrew File System),
- The geographical distributed filesystem of the ENEAGRID infrastructure as backend [12]

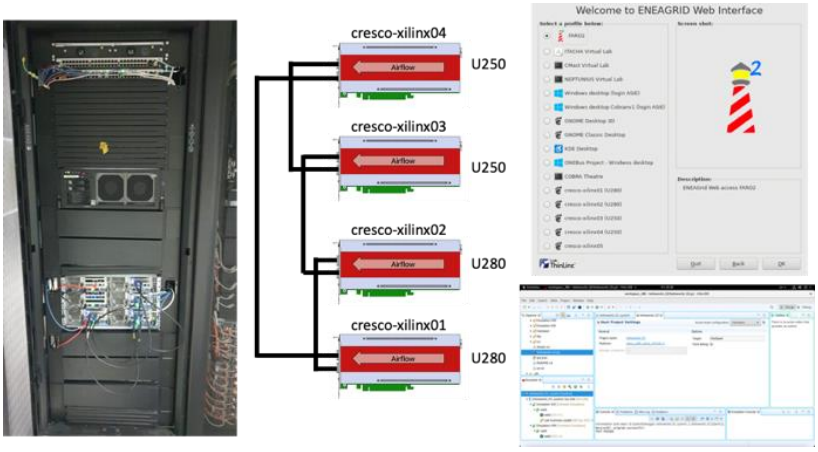

Fig.6: The ENEA FPGA Lab, with F.A.R.O as GUI to develop with VITIS.

Power analysis: tools and procedures for the measure

Power is defined as the amount of electrical energy consumed per unit of time, where the unit of power is Joule/second or commonly Watt. There are various techniques to measure and report electric power. For example, measures can be done on the instantaneous raw power, the average power, the peak power, the minimum power, the root mean square (RMS) power, or the moving average applied to the raw power data. A standard measure in computing systems is the so-called "1-second moving average", which is the power analysis thermally relevant for this kind of systems. The averaging provides a correlation to real-world measurable thermal events. For example, the measure of instantaneous power in the millisecond range, useful for other power analysis, detects spikes in power levels for short durations that will not have measurable impacts on the silicon temperature on the heat sink or on other thermal solutions. Many chipsets provide power sensors with 1-second moving average when reporting the total electric power consumed for computing.

Another common power term is the Thermal Design Power (TDP). This is the CPU power rating which is typically specified in watts. The TDP rating refers to the maximum amount of heat generated by the CPU for which the designed cooling system is required to dissipate while running common software. This does not mean that power is strictly limited to the TDP rating. The TDP rating is not the "peak power" but it is a power figure referring to the execution of typical parallel number-crunching applications. The TDP specification is also a good baseline number of the wattage power budget needed to run a processor to full performance (100% of utilization). It is possible for processors to consume more than the TDP power specification for a short period of time without it being thermally significant because heat will take some time to propagate, so a short spike in power consumption typically will not violate TDP. To ensure that many CPUs stay within the thermal specifications under such over-TDP power consumption, the CPUs have built-in power management hardware which reduces the power absorbed by the processor by reducing the voltage and/or modulating the processor clock frequency (throttling) until the thermal violation is corrected.

Accurate and timely information regarding power consumption of compute nodes in large scale HPC systems is important in establishing ways to mitigate both the energy consumed and the overall cost.

Monitoring tools enable the measurement of the energy efficiency of an HPC data center focusing on energy modelling, profiling capabilities, and calibration of models.

There are both hardware and software solutions available today to measure the power consumption of HPC systems while running parallel workloads. One the easiest and most common hardware solutions for measuring total system power is the usage of an AC power meter. This is an instrument that passes power to compute node under load and measures the power consumption in real time. Most of these instruments have ethernet/GPIB/USB interfaces allowing a power data logging. Another hardware method used to measure system power is the usage of power distribution units (PDUs). These are typically used in data center racks that house HPC systems. The PDU is a smart AC power strip that has an embedded controller that is continually monitoring the total power consumption or load of all compute nodes it supplies with power in a rack including its temperature. These smart PDUs are accessible using a simple web interface or a Simple Network Management Protocol (SNMP) to gather and log the total system power.

On the other hand software tools are able to utilise various data sources such as Baseboard Management Controllers (BMCs) that have various sensors for reporting on the physical hosts. These sensors include measurements for the energy and power consumed of a physical host and are able to report this using the Intelligent Platform Management Interface (IPMI). These sensors are however subject to error and cannot be practically substituted with more accurate Watt meters.

In order to gather sensor data there are two main sources for monitoring the infrastructures to collect data. The first is reporting data from the operating system, which can utilize special structures such as

/proc/ on Linux. The second is to use more specialized hardware such as baseboard management controllers (BMCs) and standardized interfaces.
This can include aspects such as CPU performance counters as well as standardized interfaces such as IPMI. IPMI allows sensors, that are integrated into the hardware of current-generation servers, to be accessed through a common API. The sensors that have traditionally been used to remotely manage and monitor large clusters of physical machines are starting to include power sensing capabilities. The data gathered by these sensors can then be utilized to generate a model, that can calculate the power consumed based on utilization. Errors in the values reported by the models that drive the energy modeler and Watt meter emulator can occur at two stages. The first is the calibration phase and the second is at operation time.
The calibration phase results in an inaccurate model that does not correctly represent the relationship between load and power consumption. This can occur for several different reasons:

- Unsynchronized metric update intervals for different metric types: This could occur when measuring CPU utilization and power together. For calibration to be accurate, it requires the measurements to be perfectly synchronized or the utilization to remain stable during the measurement phase, so that both measurements represent the physical host's true state.
- *Measurement arrival latency (Monitoring infrastructure over-head)*: Differing on the above case, where synchronisation issues may occur, this is caused by the inherent delays in taking a measurement, transferring the value across a network and recording it in the monitoring infrastructure. This effects the detection of the start and end of periods of induced load. This can be mitigated by performing the calibration run locally without the use of a full monitoring infrastructure, such as Zabbix, Ganglia etc. This however will only work during the calibration and will not work during normal operations. Locally monitoring load will however have the side effect of measuring a small amount of load induced by itself.
- *Averaging and time windows of measurement's values*: Measurements arrive with a given polling interval, however measurements such as CPU load also have a time window in which the measurement was taken e.g. over the last minute. This averaging causes errors in the model and requires the CPU utilisation measurement window to be made as small as possible. One alternative is for measurements used in the calibration dataset to only start to be taken after load has been induced for a time that is longer than the length of the averaging period.
- Update interval of a sensor's reported value Sensors such as power measurements taken over IPMI update slower than the interval at which the baseboard can be queried. Thus rapid polling of the interface can result in the previously reported value been reported again, without prospect of change. Hence the poll interval should not exceed this update interval. In the case of IPMI power values polling should hence restricted to every 1 seconds.

Therefore this provides the basis of several recommendations which we implement in that should be followed while calibrating an energy model:

- to use metrics that represent the physical host in its most recent state, which we call spot metrics and tend to avoid averaging and representing long periods of time. The sensors base data acquisition of the compute nodes is generally of the millisecond scale, but the firmware of chipset motherboards provides different sampling periods ranging from a minimum of 1 second up to the minutes. Usually the IPMI command interfacing the Data Center Manageability Interface (DCMI) provides electric power measurement of compute node like this:

Linux IPMI Command:
ipmitool -H nodename -U XXXXX -P XXXXX dcmi power reading
with the following output:
Instantaneous power reading: 89 Watts
Minimum during sampling period: 87 Watts
Maximum during sampling period: 89 Watts
Average power reading over sample period: 88 Watts
IPMI timestamp: Wed May 18 18:07:25 2022
Sampling period: 00000001 Seconds.
Power reading state is: activated

For example, the Lenovo compute nodes in ENEA FPGA labs provide an average power reading with a sampling period of 1 second; instead, the Supermicro compute nodes of CRESCO5F ENEA HPC clusters provide a sampling period of 1 minute. In order to gather electric power measurement of a Supermicro compute node the IPMI command is the following:

ipmitool raw -H nodename -U XXXXX -P XXXXX 0x30 0xe2 0x00

Unfortunately, a complete description of the IPMI tool in raw mode is not available by Supermicro computing node.

- The CPU/GPU/FPGA load should be induced followed by waiting a set period of time for the values to stabilize and then taking measurements. A further addition to this is to detect plateaus in the measured values and only use congruent data points as shown in Fig.7, which can be used as a mechanism to determine how long to wait before accepting measurements as being valid when a compute node is loaded by applications.

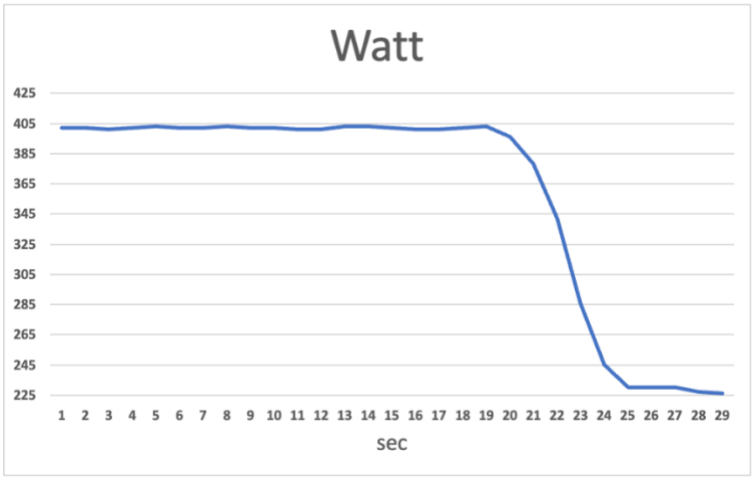

Fig.7: Power monitoring of compute node via IPMI.

An alternative technique to collect power consumption induced by applications is to embed in the source code some event probes providing start and end timestamps of the event. Each event also reports the identifier of its type (”eventType”), which allows identifying different types of events for the same application and analyzing them separately. For example, a typical json structure is the following:

Json structure for power monitoring via IPMI

```
{
        "schema version":
        {
                "schema": "JSON",
                "creation_date": "Wed Aug  3 14:37:51 2022 GMT"
        }
        "event":
        {
                 "appID": "App 1",
                 "eventType": "Event 1",
                "deviceID": "fpga 0000:0b:00.1",
                "starttime:" Wed Aug  3 14:37:51 2022 GMT",
                "endtime:" Wed Aug  3 14:37:55 2022 GMT",
        }
}
```

- to take measurements remotely avoiding intrusive monitoring overloading compute node. Network Time Protocol (NTP) has to be used to sync timestamps between remote and undertest compute nodes. The sync accuracy is of few msec. The timestamp collected within function kernels in user applications should provide a reliable measure of energy to solution.
- About the granularity, in terms of energy consumption of single hardware components, it depends on the BMC sensors list that doesn't include the energy consumption of GPU/FPGA processors installed in the node under test.
  The commands like : nvidia-smi for GPU NVIDIA as well as xbutil for FPGA Xilinx can be run only in intrusive mode consuming CPU power of the node under test. In GPU NVIDIA, the NVIDIA System Management Interface (nvidia-smi) is a command line utility, based on top of the NVIDIA Management Library (NVML), intended to aid in the management and monitoring of NVIDIA GPU devices. The command provides all runtime metric data of GPU devices installed into the compute node and it works also in virtualized environment based on ESXI and XenServer. It allows the usage for logging with timeout linux command set the queries in a time window. An example of query with 1 second steps on 5 seconds of time window for GPU id 0 is as follows:

```
timeout 5  nvidia-smi -i 0 --query-gpu= timestamp, name, pstate, pcie.link.gen.max, pcie.link.gen.current,
temperature.gpu, utilization.gpu, utilization.memory, memory.total,memory. free,memory.used, power.draw --
format=csv -l 1
timestamp, name, pstate, pcie.link.gen.max, pcie.link.gen.current, temperature.gpu, utilization.gpu [%],
utilization.memory [%], memory.total [MiB], memory.free [MiB], memory.used [MiB], power.draw [W]
2022/08/04 14:39:47.721, NVIDIA A100-PCIE-40GB, P0, 4, 4, 30, 0 %, 0 %, 40960 MiB, 40300 MiB, 53 MiB, 32.82 W
2022/08/04 14:39:48.728, NVIDIA A100-PCIE-40GB, P0, 4, 4, 30, 0 %, 0 %, 40960 MiB, 40300 MiB, 53 MiB, 32.82 W
2022/08/04 14:39:49.733, NVIDIA A100-PCIE-40GB, P0, 4, 4, 30, 0 %, 0 %, 40960 MiB, 40300 MiB, 53 MiB, 32.82 W
2022/08/04 14:39:50.738, NVIDIA A100-PCIE-40GB, P0, 4, 4, 30, 0 %, 0 %, 40960 MiB, 40300 MiB, 53 MiB, 32.92 W
2022/08/04 14:39:51.745, NVIDIA A100-PCIE-40GB, P0, 4, 4, 30, 0 %, 0 %, 40960 MiB, 40300 MiB, 53 MiB, 32.82 W
```

  The above command provides several metric data tagged with a timestamps including: temperature in Celsius degree, GPU and memory utilization as percentage, power consumption in Watt. In the FPGA Xilinx Alveo boards, the Xilinx Runtime Library (XRT) provides a standardized software interface that facilitates communication between the application code and the accelerated-kernels deployed on the

reconfigurable portion of PCIe based Alveo accelerator cards. The stack software of the XRT is shown in Fig.8:

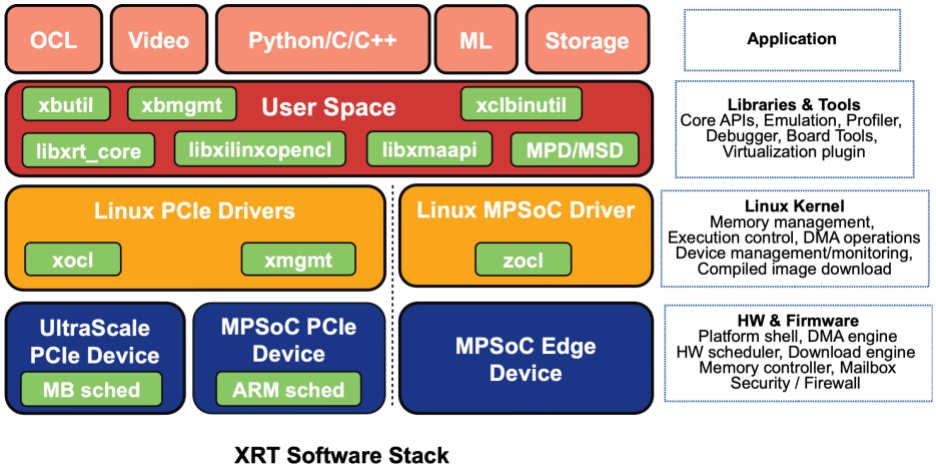

Fig.8: ALVEO XRT software stack.

The command *xbutil examine -d <fpga_device> -r all* provides all runtime data of FPGA device, including:

Electrical	***Thermals***
Max Power : 225 Watts	*PCB Top Front : 25 C*
Power : 24.823374 Watts	*PCB Top Rear : 24 C*
Power Warning : false	*FPGA : 29 C*
Power Rails : Voltage Current	*FPGA HBM : 24 C*
12 Volts Auxillary : 12.223 V, 0.857 A	
12 Volts PCI Express : 12.253 V, 1.171 A	
3.3 Volts PCI Express : 3.278 V	
3.3 Volts Auxillary : 3.379 V	
Internal FPGA Vcc : 0.850 V, 11.250 A	
DDR Vpp Bottom : 2.500 V	
DDR Vpp Top : 2.496 V	
5.5 Volts System : 5.458 V	
Vcc 1.2 Volts Top : 1.198 V	
Vcc 1.2 Volts Bottom : 1.199 V	
1.8 Volts Top : 1.795 V	
0.9 Volts Vcc : 0.897 V	
12 Volts SW : 12.166 V	
Mgt Vtt : 1.197 V	

These data can be selected also with electrical and thermals options of the *xbutil* examine command.

6 Results for bitpacking compression algorithm

The *bitpacking* algorithm, described in section 3, has been implemented, other than on the Xilinx Alveo U280 board, on the Xeon CPU (using both 1 and 32 cores, in the latter case using OpenMP for the parallelization), and on the GPU NVidia A100.

We compressed a set of images coming from the fast camera and, for each compression, we registered the compression time and the power consumed by the node, so we could compute both the energy required to compress all the images, the time needed, and the Energy-Delay-Product (EDP) through which we verify if the KPI has been met.
The following figures 9 (a,b), report, respectively, the execution time, the energy for the *bitpacking* implemented on FPGA, CPU 1-core, CPU 32-cores, A100 GPU.

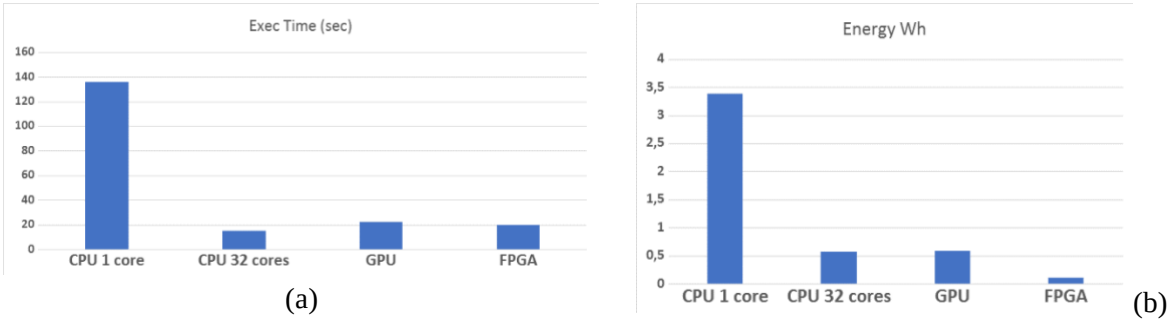

(a) (b)

Fig.9: (a) Execution time and (b) Energy consumption for *bitpacking* algorithm in CPU/GPU/FPGA.

.As shown in Fig. 10, the EDP for the FPGA implementation is more than 2 times smaller than the EDP achieved with the other implementations, so the PoC acceptance criterion is met.

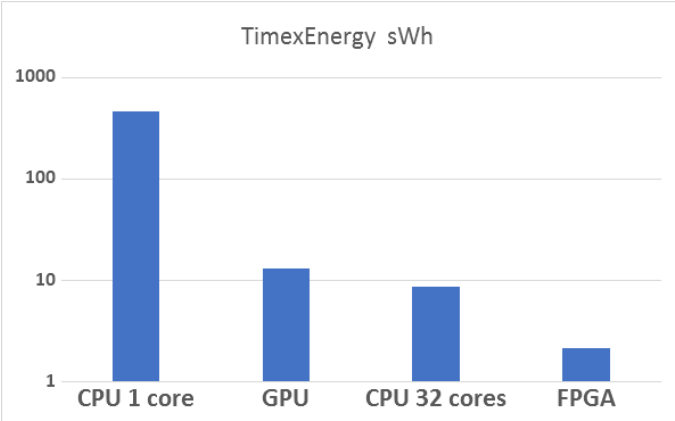

Fig.10: EDP for *bitpacking* algorithm in CPU/GPU/FPGA.

7 Conclusions

The EuroHPC TEXTAROSSA project addresses technology gaps towards pre-Exascale and Exascale scenarios, developing new IPs, algorithms, methods and software components for HPC-AI, HPC and HPDA applications on heterogeneous architectures.

Acknowledgements

The work presented here has been carried out within the following EU projects:
H2020-EU.2.1.1.2.: Extreme scale computing and data driven technologies - Grant Agreement n. 956831;

References

[1] TEXTAROSSA website: https://textarossa.eu

[2] McCool, M. et al: “Structured Parallel Programming”, chapter 2.5.3 (Power), Elsevier, 2012.

[3] “RFC 1951DEFLATE Compressed Data Format Specification” https://www.rfc-editor.org/rfc/rfc195.

[4] Ziv, J., Lempel, A. "A Universal Algorithm for Sequential Data Compression". IEEE Transactions on Information Theory. 23 (3): 337–343. May 1977.

[5] Huffman, D. "A Method for the Construction of Minimum-Redundancy Codes". Proceedings of the IRE. 40 (9): 1098–1101, 1952.

[6] “Vitis High-Level Synthesis User Guide (UG1399)”. https://docs.xilinx.com/r/en-US/ug1399-vitis-hls.

[7] “The Proto-SPHERA project”, https://www.afs.enea.it/project/protosphera/.

[8] Lampasi at al. “Progress of the Plasma Centerpost for the PROTO-SPHERA Spheri-cal Tokamak”, Energies 2016, 9, 508. https://doi.org/10.3390/en9070508.

[9] Goz, David et al. “Direct N-body application on low-power and energy-efficient parallel architectures.” PARCO (2019). https://doi.org/10.48550/arXiv.1910.14496.

FIRST-PRINCIPLES INVESTIGATION OF COPPER-BASED HOLE TRANSPORT MATERIALS FOR SOLAR CELLS.

Ana B. Muñoz García,[1*] Adriana Pecoraro,[1] Pasqualino Maddalena,[1] Michele Pavone[2]

[1]*University of Naples "Federico II", Department of Physics "Ettore Pancini", Comp. Univ. Monte Sant'Angelo Via Cintia 21, 80126, Naples, Italy*

[2]*University of Naples "Federico II", Department of Chemical Sciences, Comp. Univ. Monte Sant'Angelo Via Cintia 21, 80126, Naples, Italy*

ABSTRACT. We have performed DFT calculations to investigate the capabilities of three inorganic copper-based materials (CuI, CuSCN and Cu_2O) as hole transport layers for dye sensitized and perovskite solar cells. We have studied both the pristine and the Cu defective compounds to evaluate the effect of vacancies on the band alignment with the active material, crucial for charge transport across interfaces and a proper device working.

1 Introduction

The research carried out at the University of Naples "Federico II" has mainly targeted on the search of efficient hole transport materials for solar cells. We have focused on two 3rd generation photovoltaic technologies: p-type Dye Sensitized Solar Sells (DSCs) and Perovskite Solar Cells (PSCs). p-type DSCs are used in cascade with the traditional n-type counterpart in the so-called "tandem architecture" in which the band alignment among the different parts fulfils the scheme depicted in Figure 1a.

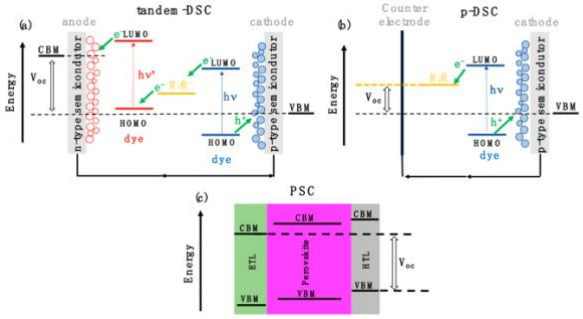

Figure 1: Band alignment required for efficiently working tandem-DSC(a), p-type DSC (b), and PSC (c).

In a p-type DSC the photo-generated hole jumps from the dye's HOMO to the valence band maximum of a p-type semiconductor whose VBM is at a higher energy than the HOMO of the dye (Figure 1b). Such a scheme allows to widen the solar spectrum portion accessible to the cell and improves the efficiency of the device. NiO is the most employed photocathode but there are some concerns about its toxicity and several drawbacks, such as low electrical conductivity, low hole mobility and high valence band edge potential with respect to the most common I^-/I^-_3 electrolyte that result in too low power conversion efficiencies.[1] For these reasons, alternative photocathodes are needed to make this technology competitive. In PSCs the active material is a perovskite, that after photoexcitation injects the charge carriers to an electron and a hole transport layers (ETL and HTL, respectively). Such a

charge transport is possible only if the energetics of the different parts of the cell fulfils the scheme in Figure 1c. Spiro-OMeTAD, together with other organic materials such as PTAA and PEDOT:PSS, still remain the materials of choice as HTL but are often responsible for the device instability. NiO has been proposed as inorganic alternative, however it is found to generate trap states and poor interface charge dynamics in PSCs.[2] We have studied from a theoretical point of view, three inorganic copper-based materials, namely CuI, CuSCN and Cu_2O to assess their capabilities as HTL for both technologies. We have performed Density Functional Theory (DFT) calculations on both pristine and Cu-defective materials focusing on the band alignment with the photoactive material (perovskite/dye) fundamental for a properly working device.[3]

2.1 Methods and Computational details

Performed calculations are based on DFT with projector-augmented wave (PAW) potentials[4,5] and a plane wave (PW) basis set as implemented within the Vienna ab Initio Simulation Package (VASP, version 5.4.4) code.[6] We have used PBE+U approach to correct the self-interaction error.[7,8] A U-J=6.0 eV value for Cu[9] has been employed. Dispersion interactions have been treated within the Grimme's D3 framework with the damping scheme proposed by Becke and Johnson (D3-BJ).[10,11] The plane wave energy cutoff has been set to 700 eV in all calculations. Γ-Centered k-point sampling grids of 4 × 4 × 4, 6 × 6 × 2 and 6 × 6 × 6 have been used for CuI, hexagonal CuSCN and Cu_2O bulk materials, respectively.

2.2 Results and Discussion

To construct the models for HTLs, we have started from the minimum energy bulk structures for the three materials from which we have cleaved the surface slab models along the most favourite planes. For CuI we have considered a 6-layer slab of the 2×1×1 bulk supercell that we have cut along the (110) plane. For CuSCN we have considered the (100) surface that has been cleaved from a 4 × 1 × 1 supercell, and the (110) for which we have considered the 1 × 2 × 1 one. Both slabs consist of 9 layers. For Cu_2O we have studied the $\sqrt{3} \times \sqrt{3}\, R(30°)$ supercell cut along the (111) direction, containing an oxygen vacancy in the topmost layer of the slab. In each slab we have mimicked the presence of a Cu defect by removing one neutral copper atom from the central inner layer. The bulk and the pristine slab models are both depicted in Figure 2.

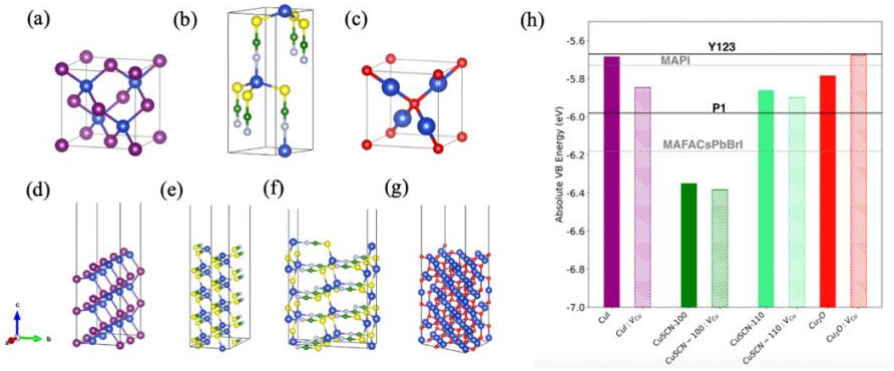

Figure 2: Bulk models for CuI (a), CuSCN (b) and Cu_2O (c). Slab models of the (110) surface of CuI (d), (100) and (110) for CuSCN, (e) and (f) respectively, and the (111) of Cu_2O (g). Absolute positions of the VB edges of pristine (fully colored rectangles) and Cu-defective (hatched rectangles) CuI, CuSCN and Cu_2O slabs, in comparison to that of MAPI and triple cation MAFACsPbBrI perovskites (dotted gray lines) and the P1 and Y123 dyes' HOMO (solid black lines).

For all the slab models, we have evaluated the absolute positions of the valence band maximum, both for the pristine and the copper defective materials. We have followed the approach proposed by Toroker et al.[12] In this framework, we have employed the band gap center positions of our slab models as predicted by DFT and the experimental measures of the bandgap for all the considered compounds CuI (3.1 eV)[13] CuSCN (3.60 eV)[14] and Cu_2O (2.17 eV).[15] The calculated VB positions are reported in Figure 2 in comparison to that of MAPI, calculated within the same theoretical framework,[16] the triple cation (MAFACsPbBrI)[17] and to the experimentally measured HOMO of the widely employed P1[18] and Y123[19] dyes.

2.3 Conclusions

Our results suggest that in CuI, the presence of a defect lowers the VBM, leading to an unfavorable band alignment with respect to the MAPI perovskite VBM, while preserving a good match with the triple cation and the P1 dye's HOMO. In the thiocyanate, the copper vacancy has no significant effects on the VBM position. Our model predicts a likely good alignment of the (110) surface with the P1 dye and the triple cation perovskite while both (100) and the (110) surfaces seem not suitable for applications in devices involving both MAPI and Y123. The presence of the vacancy in Cu_2O is crucial to allow for the charge transfer across the interface with all photoactive materials. These results have been gathered in a paper that has been recently published on Materials.[3] The computing resources and the related technical support used for this work have been provided by CRESCO/ENEAGRID High Performance Computing infrastructure and its staff; CRESCO/ ENEAGRID High Performance Computing infrastructure is funded by ENEA, the Italian National Agency for New Technologies, Energy and Sustainable Economic Development and by Italian and European research programmes. See: http://www.cresco.enea.it/english for information.[20]

References

[1] H. Tian, Sustain. Energy Fuels **3**, 888 (2019).
[2] D. Di Girolamo, F. Matteocci, F.U. Kosasih, G. Chistiakova, W. Zuo, G. Divitini, L. Korte, C. Ducati, A. Di Carlo, D. Dini, and A. Abate, Adv. Energy Mater. **9**, 1901642 (2019).
[3] A. Pecoraro, P. Maddalena, M. Pavone, and A.B. Muñoz García, Materials **15**, 5703 (2022).
[4] G. Kresse and D. Joubert, Phys. Rev. B **59**, 1758 (1999).
[5] G. Kresse and J. Hafner, J. Phys. Condens. Matter **6**, 8245 (1994).
[6] G. Kresse and J. Hafner, Phys. Rev. B **49**, 14251 (1994).
[7] S.L. Dudarev, G.A. Botton, S.Y. Savrasov, C.J. Humphreys, and A.P. Sutton, Phys. Rev. B **57**, 1505 (1998).
[8] A. Rohrbach, J. Hafner, and G. Kresse, J. Phys. Condens. Matter **15**, 979 (2003).
[9] M. D'Arienzo, L. Gamba, F. Morazzoni, U. Cosentino, C. Greco, M. Lasagni, D. Pitea, G. Moro, C. Cepek, V. Butera, E. Sicilia, N. Russo, A.B. Muñoz-García, and M. Pavone, J. Phys. Chem. C **121**, 9381 (2017).
[10] S. Grimme, J. Antony, S. Ehrlich, and H. Krieg, J. Chem. Phys. **132**, 154104 (2010).
[11] A.D. Becke, J. Chem. Phys. **98**, 1372 (1993).
[12] M.C. Toroker, D.K. Kanan, N. Alidoust, L.Y. Isseroff, P. Liao, and E.A. Carter, Phys. Chem. Chem. Phys. **13**, 16644 (2011).
[13] M. Grundmann, F.-L. Schein, M. Lorenz, T. Böntgen, J. Lenzner, and H. von Wenckstern, Phys. Status Solidi A **210**, 1671 (2013).

[14] K. Tennakone, A.H. Jayatissa, C. a. N. Fernando, S. Wickramanayake, S. Punchihewa, L.K. Weerasena, and W.D.R. Premasiri, Phys. Status Solidi A **103**, 491 (1987).
[15] L. Zhang, L. McMillon, and J. McNatt, Sol. Energy Mater. Sol. Cells **108**, 230 (2013).
[16] A. Pecoraro, A.D. Maria, P.D. Veneri, M. Pavone, and A.B. Muñoz-García, Phys. Chem. Chem. Phys. **22**, 28401 (2020).
[17] A. Agresti, A. Pazniak, S. Pescetelli, A. Di Vito, D. Rossi, A. Pecchia, M. Auf der Maur, A. Liedl, R. Larciprete, D.V. Kuznetsov, D. Saranin, and A. Di Carlo, Nat. Mater. **18**, 1228 (2019).
[18] P. Qin, H. Zhu, T. Edvinsson, G. Boschloo, A. Hagfeldt, and L. Sun, J. Am. Chem. Soc. **130**, 8570 (2008).
[19] H.N. Tsao, J. Burschka, C. Yi, F. Kessler, M.K. Nazeeruddin, and M. Grätzel, Energy Environ. Sci. **4**, 4921 (2011).
[20] G. Ponti, F. Palombi, D. Abate, F. Ambrosino, G. Aprea, T. Bastianelli, F. Beone, R. Bertini, G. Bracco, M. Caporicci, B. Calosso, M. Chinnici, A. Colavincenzo, A. Cucurullo, P. Dangelo, M. De Rosa, P. De Michele, A. Funel, G. Furini, D. Giammattei, S. Giusepponi, R. Guadagni, G. Guarnieri, A. Italiano, S. Magagnino, A. Mariano, G. Mencuccini, C. Mercuri, S. Migliori, P. Ornelli, S. Pecoraro, A. Perozziello, S. Pierattini, S. Podda, F. Poggi, A. Quintiliani, A. Rocchi, C. Scio, F. Simoni, A. Vita The role of medium size facilities in the HPC ecosystem: the case of the new CRESCO4 cluster integrated in the ENEAGRID infrastructure, *Int. Conf. on High Perform.Comp. & Simul. (HPCS)* pp 1030-1033 (2014).

DATA ANALYTICS IN HEALTH 4.0: EXTRACTING KNOWLEDGE FROM BIG DATA IN PANDEMIC TIMES

Daniela Alderuccio[1*], Rossana Cotroneo[2]

[1]*ENEA – TERIN-ICT-HPC – Rome, Italy*[1]
[2]*ENEA – ISV –DST-PM Rome, Italy*

ABSTRACT. Knowledge extraction from Big Data in Digital Health sector is relevant in the analysis both of bidirectional interactions between healthcare providers and patients, and of exchange of information among patients. Extracting re-usable knowledge activates a process of creating value, able to support prediction and prescriptive models in the healthcare sector. In this paper, we present an exploratory study on Digital Health Data in pandemic times. In Health 4.0, Knowledge is organized in: Providers' Knowledge, Patient's Knowledge, both accessing Organization knowledge (data/information available for providers and patients). Health Knowledge is used for disease prediction and prevention, personalized medicine, enhanced patient-centred care, and proactive treatment. In this on-going research we process e-Health multilingual data collection, and extract specific Knowledge and keywords, in order to adopt ad hoc strategies for crawling and analysing data from open sources (online news, websites, social media platforms, etc.). We design a pipeline of sequential steps to be performed, for processing and analysing data in digital Health domain. This pipeline could be standardized and used as a model to be applied to other domains of interest. First results show that - before crawling, extracting, processing, and analysing data using Text Mining methodologies – the adoption of a cross-linguistic semantic perspective to multilingual data is a propaedeutic step in the process and refines crawling and analysis strategies. Pandemic has created high level importance to the digital health and propelled to the ongoing developments. Data acquisition, processing, analysing, visualization, sharing, storage, lay the groundwork for a healthier society, combining ICT with medical and behavioural knowledge.
Keywords: Big Data - Social Media Analytics - Knowledge Extraction - Digital Health – Health 4.0 – Text Mining – Digital Epidemiology

1. Introduction

Big Data, Cloud Computing, and the Internet of Things are revolutionizing the whole eHealth ecosystem. In 2012 Digital Healthcare data was estimated to be equal to 500 petabytes and in 2020 it was expected to be 25,000 petabytes [1]. In 2022 worldwide digital healthcare data is estimated to currently equal between 25 exa-bytes and 35 zeta-bytes, with an annual increase of between 1.2 and 2.4 exa-bytes per year[2]. Such a huge amount of health data is generated by a variety of lab systems and health information systems (e.g., EHRs)[3][2]. Epidemics and pandemics have created high level importance to the digital health and propelled to the ongoing developments with the transformation in

[1] Corresponding author*. E-mail: daniela.alderuccio@enea.it
[2] Elaboration by Sin [2] from IEEE Big Data source (https://bigdata.ieee.org/) , on 1 February 2022
[3] An Electronic Health Records (EHR) is an electronic version of a patient medical history (supported by the provider over time) with key heath information and administrative clinical data.

digital healthcare through online symptom checkers, remote patient monitoring tools, telehealth, patient portals, etc.

2. Health Knowledge

In the Health sector, Knowledge is defined as: *(i) Provider knowledge:* it typically contains both explicit (standard medical practice for a particular condition) and tacit[4] knowledge (practice and experience is internal knowledge and complement standard treatment); *(ii) Patient knowledge:* it is generally tacit (it is a patient's self-knowledge of current and past medical conditions); providers use this "health status" to diagnose, prescribe for and treat diseases; *(iii) Organization knowledge:* data (structured, semi-structured and unstructured data) and information available for providers and patients access. It often contains information collected from text-based materials, diagnostic systems, and other medical providers. Government and healthcare institutions are providers. They guarantee inclusive and easy access to healthcare services, for a healthier Society. Each government or healthcare institution has its own warehouse (silo) of public health information as well as confidential data. All these data are collected according to security and privacy issues.
Stakeholders in the Healthcare sector are patients, medical practitioners, hospital operators, pharma and clinical researcher, healthcare insurers [3]. Any knowledge created by one sector is important to all others. So, knowledge management in the healthcare sector must find a way to manage the creation, storage, sharing and use/reuse of this valuable information. COVID-19 Pandemic has dramatically accelerated the process and forced governments, public healthcare stakeholders and research institutions to collaborate and make available decades of stored usable, interoperable, searchable, and sharable according to the *once-only principle*. New sources (such as social media platforms, wearable devices, etc.,) have been used by Providers in addition to traditional sources (i.e., patient medical history, diagnostic/clinical trials data and drug information) with the aim to find relationships and pattern of interest among these heterogeneous sources. In this scenario, ENEA-CRESCO infrastructure faced the outbreak of COVID-19 improving the capability to analyse and to predict from huge amount of data, offering High Performance Data Analysis of Big Data (HPC/ HPDA) [4]. Social Media Analytics in ENEA focus on Knowledge Extraction in real-case scenario [5]. The challenge is to extract actionable knowledge from data, in order to perform predictive and prescriptive analysis, to support activities. The goal of knowledge management in healthcare is to provide decision-makers with the tools to turn information into a knowledge asset, transforming the organization: (i) into a place where new knowledge is generated and shared, (ii) into a learning organization, where information flows from ever-increasing sources and in great volume.

2.1 Big Data in the Health domain

Jee & Kim [6] redefined the characteristics of healthcare big data into three features: *Silo*, *Security* and *Variety*[5], instead of Volume, Velocity and Variety. Palanisamy and Jee & Kim [3, 6] stated that Big Data in the business sector differs from Big Data in Health domain[6]. Big Data in e-Health sector support comprehensive healthcare solutions such as clinical decision support, disease surveillance and public health monitoring and management. The traditional *disease-centric model* is now shifting towards a *patient-centric model*, as requested by National Recovery and Resilience Plan (PNRR) too, where an active participation of patients is needed. The challenges for healthcare involve sharing healthcare information[7] hosted in silos (warehouse) in order to provide data integration, to maintain the control over the data, to implement regulation on security and compliance and to transform the huge amount of

[4] Explicit knowledge: It is recorded and communicated through different mediums (print, audio, etc.). It can be transmitted quickly and easily from one individual to another and is organized systematically. Tacit knowledge: It involves a person's ability (or specialized inherent knowledge). Tacit knowledge can be achieved only through experience.
[5] *Silo* is databases having healthcare information maintained by stakeholders (i.e., hospitals). *Security* feature is related to the care needed to keep healthcare data. *Variety* shows the forms of healthcare data: structured, unstructured and semi-structured.
[6] Big Data in business sector has been used to identify consumers' behavioral patterns, to develop business services and solutions. [3]
[7] The goals are: (i) providing better citizen's healthcare services, (ii) improving medical treatment, (iii) enhancing easy and equal access to health services, (iv) improving security, speed, interoperability, analytics capabilities.

e-health data into actionable knowledge. We will show a pipeline of sequential steps to be performed (

Fig. 1), in order to process and analyse health data. This pipeline is designed on health data but could be standardized and then used as a model to be applied to other domains. As a first step, we extract specific knowledge for keyword identification and selection before crawling from open data coming from different sources (online news, websites, social media platforms, etc.). The second step is Data Crawling. Further steps are Data Stream including Text Analysis, validation, and Sentiment Analysis.

Fig. 1: *Pipeline*

3. Results

As a first step, we explore Twitter Trends (2020-2022), in order to select keywords, to integrate the semantic field of hashtags to be used for crawling and analysis tasks. In health domain, Twitter data might offer knowledge about patients' symptoms, opinions, etc. [7]. In our analysis we proceed exploring the semantic field of topics for keyword identification and selection, taking into account multi-language and space-time distribution. The first idea was to use the definition of the disease (SARS-cov 2- COVID-19) or virus denomination (coronavirus, rna-virus), but investigating deeply we found additional keywords. Then we use these keywords to start crawling task and then analyse results. In particular, in Twitter Trends we searched for the keyword to be used to select tweets in Italy from 16th to 18th March 2020. We found following trends related to pandemic, and we extracted following hashtags containing: virus denomination and sometime geo-localization: *(#coronavirusitalia, #coronavirusitaly, #COVID19italia, #covid19uk, #bergamo, #coronavirus-updates, #CoronaVirusUpdates,);* keyword linked to: the pandemic emergency (*#emergenzacovid19, #EmergenzaCovid19*); to social activities/actions supporting people (*#CoronaVirusChallenge, #flashmob, #flashmobitalia, #flashmobsonoro, #balconi, #PaesaggiDaCartolina, #stayhome-challenge);* to emotion to support (*#orgoglioitaliano, #DomaniUsciraIlSole, #CuraItalia, #OrgoglioItaliano, #celafaremo, #scrivoquelchesento, #DomaniUsciraIlSole);* to negative emotion (*#coronapocalypse);* to the disease, protection devices and recommended behaviours: (*#quarantinelife, #Mascherine, #mascherine);* to governmental rules: (*#decretocuraitalia, #CuraItalia);* to politicians: *(#GovernoConte, #governoconte, #IoStoConConte, #contedimettiti, #De Luca, #boris Johnson);* and other hashtags without any semantic correlations, that apparently did not have nothing in commons with the pandemic (*#leCose, #iorestoacasa, #unitaditalia).* Preliminary results show the trends of emotion (expectation, anxiety, fear, reaction, sadness, and joy public acceptance/not acceptance) and the narratives underlying those emotions during the different phases of pandemic by North, Centre, and South of Italy. The outcomes show the relationships and pattern of interest among these heterogeneous

sources of big data (providers and user-generated contents), and we formulate hypothesis on the dynamic of information spreading from hub to users, from the center to the periphery. These results are useful for management of health domain.

4. Conclusions

Digital Health Data provide an interesting scenario, in view of many applications such as personalized healthcare and public health, for a healthier Society[8]. The challenge to face is to transform the huge amount of health data into actionable knowledge, in order to perform predictive and prescriptive analysis, to support healthcare activities. Furthermore, real-time analysis of health data should be carried out, according to privacy and security laws [6]. In our research, we highlight the importance of selecting keywords before crawling tasks and of adopting a pipeline designed on the characteristics of the application domain. Before extracting, processing, and analysing health data using Text Mining methodologies, in this first exploratory study we adopted (i) a cross-linguistic semantic perspective exploring multilingual data, and enabling the selection of keywords and hashtags for crawling and analysis task; and (ii) we defined a pipeline to process Healthcare data. This pipeline could be standardized and used as a model to be applied to other domains. As a further step we will formulate hypothesis on the dynamics of information/knowledge spreading from institutional hub to users/patients, finding centre/periphery interactions, and among patients.

References

[1] J. Sun, C.K. Reddy. Big data analytics for healthcare. *Proceedings of the 19th ACM SIGKDD international conference on Knowledge discovery and data mining* (2013).

[2] P. Šín, A. Hokynková, M. Novakova; A. Pokorna, R. Krcˇ, J. Podroužek. Machine Learning-Based Pressure Ulcer Prediction in Modular Critical Care Data. *Diagnostics* 2022, 12, 850. Academic Editors: Keun Ho Ryu & Nipon Theera-Umpon - https://doi.org/10.3390/ diagnostics12040850 (2022) – cited IEEE Big Data. https://bigdata.ieee.org/ (accessed on Feb 2022)

[3] V. Palanisamy, R. Thirunavukarasu. Implications of big data analytics in developing healthcare frameworks - A review. *J. King Saud Univ. Comput. Inf. Sci.*, 31, 415-425.Science J. King Saud Univ. Comput. Inf. Sci. (2017)

[4] F. Iannone and HPC-CRESCO Team. ENEA HPC CRESCO in the time of Covid-19 and new Supercomputing Frontiers, *ENEA CRESCO in the fight against COVID-19* - ENEA - pp. 8-31, 2021 - ISBN:978-88-8286-415-6 (2021)

[5] D. Alderuccio, S. Migliori and ICT-HPC Team: Knowledge Extraction from Social Media Web Sources: Elements affecting Web Crawling and Data Analytics Tasks in ENEAGRID. *High Performance Computing on CRESCO Infrastructure: research activity and results 2019* , pp. 155-158 - ISBN: 978-88-8286-390-6 – ENEA *(*2020)

[6] K. Jee, GH. Kim. Potentiality of big data in the medical sector: focus on how to reshape the healthcare system. *Healthc Inform Res. 2013 Jun*;19(2):79-85. doi: 10.4258/hir.2013.19.2.79. Epub 2013 Jun 30. PMID: 23882412; PMCID: PMC3717441. (2013)

[7] B.A. Panuganti, A. Jafari, B. MacDonald, A.S. De Conde, Predicting COVID-19 Incidence Using Anosmia and Other COVID-19 Symptomatology: Preliminary Analysis Using Google and Twitter. *Otolaryngology – Head and Neck Surgery 2020,* Vol. 163(3) 491–497 The Author(s) - DOI: 10.1177/0194599820932128 - http://otojournal.org (2020).

[8] COM(2018) 233 https://eur-lex.europa.eu/legal-content/EN/TXT/PDF/?uri=CELEX:52018DC0233&from=EN

WRF-CHEM AIR QUALITY SIMULATIONS FOR AIRFRESH PROJECT

Beatrice Sorrentino[1], Alessandra De Marco[1], Alessandro Anav[1]

[1] *Italian National Agency for New Technologies, Energy and the Environment (ENEA), Italy*

ABSTRACT. To efficiently reduce air pollution in cities, municipalities and city planners urgently need a quantitative and concrete assessment of the role of urban trees in affecting air quality. In this study, we selected two front-runner cities: Aix-en-Provence in Southeastern France (143,000 inhabitants) and Florence in Italy (380,000 inhab.), where population is regularly exposed to high particles (PM2.5, PM10), nitrogen dioxide (NO2) and tropospheric ozone (O3) levels, exceeding the World Health Organization Air Quality Guidelines. This study is performed within the LIFE project AIRFRESH, which aims to produce new information and recommendations to be integrated into ambitious Urban Greening Plans and Air Quality plans. For these purpose, we use the coupled chemistry-climate model WRF-Chem firstly over European and Mediterranean scale domains then we run the model considering different afforestation scenarios at city-levels. This allows to qualify the difference in pollutants, and the effects of tree species in air pollution removal.

1 Introduction

In the context of the life AIRFRESH project "Air pollution removal by urban forests for a better human well-being" (LIFE19 ENV / FR / 00086), two front-runner cities have been selected: Aix-en-Provence in Southeastern France and Florence in Italy and two cities for replication: Naples and Zagreb.
The AIRFRESH project aims to:
i) estimate the air pollution removal capacity by a reforested test area in the selected cities;
ii) estimate and quantify the environmental and health benefits provided by urban tree at city-scale;
iii) propose recommendations for reforestation policies for attainment of the air quality standards in the case-study cities.
Nature-based solutions can be adopted to face urban challenges, i.e. air pollution and climate change effects mitigation. The project will produce new information and recommendations to be integrated into ambitious Urban Greening Plans and Air Quality plans, such as recommendations for reforestation policies (e.g. number and type of tree species to be planted) to avoid negative impacts of planting and to improve air quality for attainment of the standards in cities. In particular, the project, through the implementation of simulations on CRESCO, will evaluate the main air quality indicators (PM2.5, PM10, NO_2, O_3) in both front-runner cities. The estimation will be performed through a modeling approach, using a chemical transport model (CTM) at a resolution of 1 km, using different scenarios. Finally, by calculating the difference in pollutants between the different scenarios, air pollution removal will be quantified in the different cases.

2 Setup

To carry out the simulations we use the Weather Research and Forecasting (WRF) model coupled with chemistry (i.e. WRF-Chem). The model simulates the emission, transport, mixing, and chemical transformation of trace gases and aerosols simultaneously with the meteorology. The WRF-Chem model system offers different gas phase chemistry and aerosol parameterizations to simulate the atmospheric chemistry. We employed the MOZART (Model for OZone And Related chemical

Tracers) scheme to simulate the gas-phase chemistry, while the Model for Simulating Aerosol Interactions and Chemistry (MOSAIC) is used for the aerosol mechanism.
In order to have realistic meteorological conditions at city level, we use a triply-nested domain to downscale the forcing data from a coarse domain to fine scale city domains. For the first step we applied WRF-Chem (v4.2.2) over European domain, as shown in Fig.1: the model domain is projected on a Lambert conformal grid with an horizontal spatial resolution of 15 km and with 35 vertical levels extending from land surface up to 50 hPa.

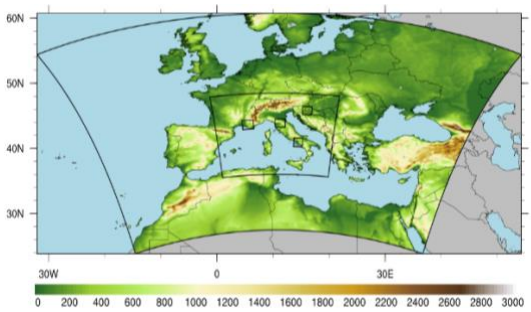

Fig.**1**: The figure shows nested domains used for simulations: european domain (15 km), intermediate domain (5 km), urban domains Aix-en-provence, Florence, Naples, Zagreb (1 km)

The time period chosen for the simulations is 2019 and the output frequency is 1 hour. For the meteorological forcing we used the ERA5 data from the European Centre for Medium-range Weather Forecast as boundary conditions. For the European domain we also use a method called spectral nudging that allows transmitting forcing information not only from the boundary conditions but also and directly within the domain; this allows for a more stable model increasing the consistency with the reanalysis. For the chemical boundary conditions CAM-chem is used, which is a component of the NCAR Community Earth System Model (CESM) and provide global tropospheric and stratospheric atmospheric composition. For the antropogenic emissions we used CAMS-GLOB-ANT data, for the fire emissions the FINN (Fire INventory from NCAR) inventory, while the biogenic emissions are calculated online by the WRF-Chem model through the MEGAN (Model of Emissions of Gases and Aerosols from Nature) model.
In order to perform these simulations, a few modifications have been made to the standard WRF-Chem versions. First of all, we used the Corine Land Cover (CLC) database as initial condition for land cover: in fact, unlike the standard dataset used by WRF (i.e. MODIS and USGS), the CLC allows to identify several urban features, like industrial areas or highly/low residential areas. These information are needed by the model when using the urban scheme over the city-domains. Besides, we modified the preprocessing of the MEGAN model. In the standard version, the biogenic emissions are computed from the spatial distribution of four plant functional types. This suggests that the landcover used by MEGAN is not directly related to the landcover used within WRF, thus any afforestation scenario does not directly affect the biogenic emissions. To avoid this issue we improved the MEGAN preprocessing and now the biogenic emissions are computed from the same landcover used by the model (i.e. CLC).
All the simulations are performed on CRESCO with a specific queue called “airfresh”. The WRF-Chem model has been compiled with the intel compiler (mpiifort) and ran over CRESCO6 using 384 CPUs for the European and Mediterranean domains, while 96 CPUs are used for the city domains. The domain decomposition has been achieved with MPI.

3 Main results

In this section, some of the preliminary results obtained from the simulation at European level are discussed. In Fig. 2 in the first boxes on the left are shown seasonal averages for NO2, from January to June, obtained with WRF-Chem. For comparison, we use chemistry boundary conditions used to run the model, namely the CAM-chem NCAR reanalysis (shown on the right boxes). It is observed that our simulation correctly reproduces the reanalyses but with a more resolved spatial pattern: for

example, it is possible to observe a NO2 maxima over England (around London), Europe and over Moscow. Comparing the simulation with in-situ data, in the lower boxes of Fig. 2, results suggest a general good agreement between WRF-Chem and observations, although in some sites there is a large mismatch due to differences in the scale (microscale for observations and mesoscale for modeling) and poorly reproducibility of urban air quality with a resolution of 15 km.

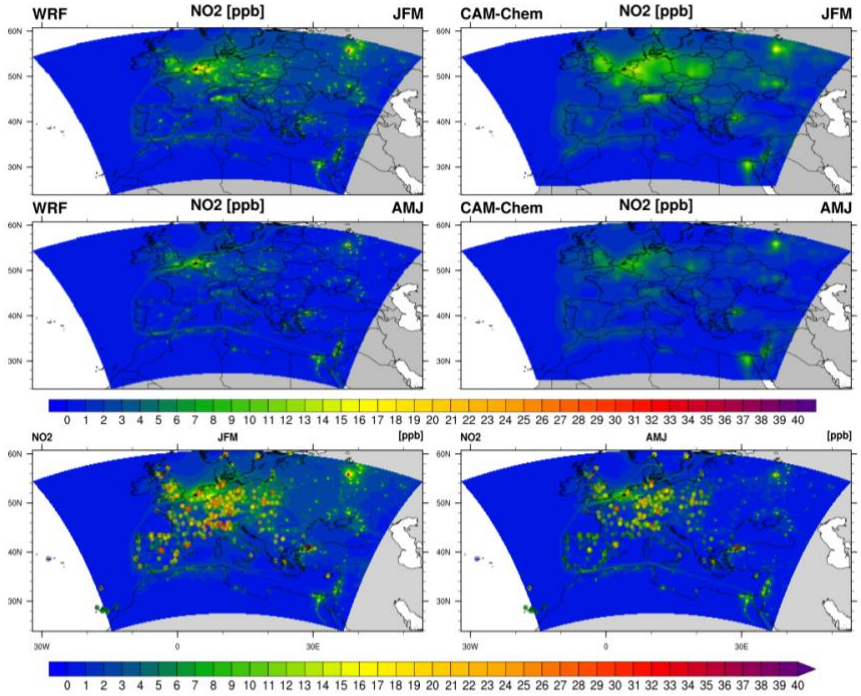

Fig.2: Left boxes show the seasonal averages for NO_2, in the upper box from January to March, in the lower box from April to June, the right boxes show the CAM-chem NCAR reanalyses for the same periods. The data of the measurement stations are shown in the two boxes at the bottom .

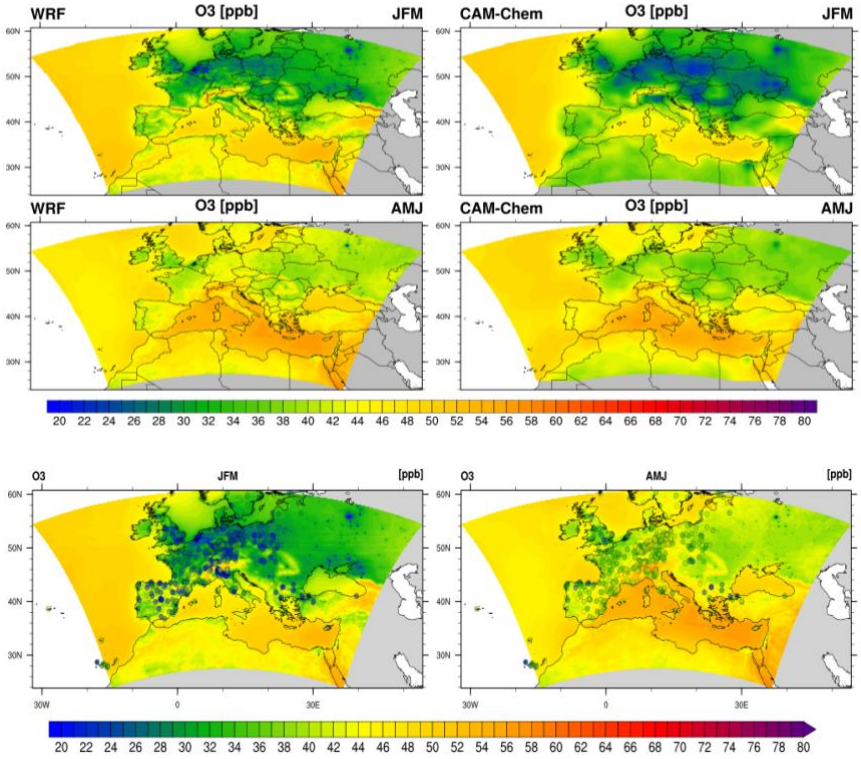

Fig.3: Left boxes show the seasonal averages for O_3, in the upper box from January to March, in the lower box from April to June, the right boxes show the CAM-chem NCAR reanalyses for the same periods. The data of the measurement stations are shown in the two boxes at the bottom.

Fig. 3 shows the results for ozone. It can be observed that WRF-Chem correctly reproduces the reanalysis spatial pattern. The comparison of simulated results with in-situ data points out that the model rightly reproduces the observations for the most remote stations and far from the cities. Concluding we observed that the model is able to correctly reproduce surface concentration of the studied species, so we are continuing with the nested domains, until urban simulations with different scenarios.

References:

Anav, A., Carillo, A., Palma, M., Struglia, M. V., Turuncoglu, U. U., and Sannino, G.: The ENEA-REG system (v1.0), a multi-component regional Earth system model: sensitivity to different atmospheric components over the Med-CORDEX (Coordinated Regional Climate Downscaling Experiment) region, Geosci. Model Dev., 14, 4159–4185, https://doi.org/10.5194/gmd-14-4159-2021, 2021.

De Marco A., Sicard P., Vitale M., Carriero G., Renou C., Paoletti E., (2015) Metrics of ozone risk assessment for Southern European forests: Canopy moisture content as a potential plant response indicator. *Atmospheric Environment,* 120, 182-190.

Fallmann J., Forkel R., Emeis S., Secondary effects of urban heat island mitigation measures on air Quality, https://doi.org/10.1016/j.atmosenv.2015.10.094, 2015.

Li H., Wolter M., Wang X., Sodoudi S., Impact of land cover data on the simulation of urban heat island for Berlin using WRF coupled with bulk approach of Noah-LSM, DOI 10.1007/s00704-017-2253-z, 2018.

Mills, G., et al. (2018) Tropospheric ozone assessment report: Present-day tropospheric ozone distribution and trends relevant to vegetation. Elem. Sci. Anth. 6, 47.

Sicard P., Crippa P., De Marco A., Castruccio S., Giani P., Cuesta J., Paoletti E., Feng Z., Anav A., High spatial resolution WRF-Chem model over Asia: Physics and chemistry evaluation, https://doi.org/10.1016/j.atmosenv.2020.118004, 2020.

AB INITIO STUDY OF THE ABSORPTION ENERGY OF Li_2S_X ON GRAPHENE

Mariarosaria Tuccillo[1], Annamaria Grippo[2], Priscilla Reale[3], Sergio Brutti[2]

[1] University of Rome La Sapienza, Dept. Chemical Engineering Materials and Environment, Piazzale Aldo Moro 5, Rome, Italy; [2] University of Rome La Sapienza, Dept. Chemistry, Piazzale Aldo Moro 5, Rome, Italy; [3]ENEA, Via Enrico Fermi 45, Frascati, Italy

In recent years, research is increasingly moving towards the development of alternative energy storage systems to the very popular Li-ion batteries. One of the most promising technologies turns out to be Li-S batteries. Sulfur is one of the most abundant elements in nature, unlike Li, and has a high theoretical capacity (~ 1657 mAh g^{-1}) and a high specific energy (~ 2600 Wh Kg^{-1}). [1]

The high capacity is based on the conversion reaction of sulfur to form lithium sulfide (Li_2S) by reversibly incorporating two electrons per sulfur atom, compared to one of an electron per transition metal ion in the oxide cathodes. [2]

Sulfur chemistry therefore offers several advantages, including a low operating voltage, greatly improving safety, low costs and eco-friendly nature. However, large-scale deployment is hampered by several technological challenges: Li-S systems under development still suffer from low efficiency due to factors such as the insulating nature of both sulfur (S_8) and lithium sulfide (Li_2S), dissolution of the active material, the large volumetric variation of the electropositive compartment (80%), which accompanies the electrochemical reactions and the known shuttle effect. [3]

In particular, the dissolution of material and the shuttle effect are both consequences of the high solubility of the reaction intermediates, lithium polysulphides (Li_2S_x), in the electrolyte based on ethereal solvents. There are several strategies to overcome these problems, one of which consists in the chemical adsorption of Li_2S_x on conductive matrices to suppress the shuttle effect and increase electron mobility. [4]

In this scenario, our goal was a first principles study of adsorption thermodynamics of lithium polysulphides (Li_2S_x) on graphene.

All calculations have been performed with the Vienna Ab-initio Simulation Package (VASP), [5] which performs periodic ab-initio quantum mechanical calculations within the Kohn-Sham density functional theory (DFT) framework, [6] with projector-augmented wave potentials and plane wave basis sets. We applied the generalized-gradient approximation (GGA) with the exchange–correlation density functional by Perdew, Burke and Ernzenhof (PBE). [7] In particular, Van der Waals (vdW) force correction was also considered for our calculation using the semi-empirical force field method (DFT-D3).

First, we have modelled four different graphene supercells, (2x2x1, 4x4x1, 6x6x1, 8x8x1), and the isolated of lithium polysulphides and elemental sulfur (S_8, Li_2S_8, Li_2S_7, Li_2S_6, Li_2S_5, Li_2S_4, Li_2S_3, Li_2S_2, Li_2S). Subsequently, tests were carried out for the choice of the best supercell on which to adsorb the molecules, so that there was no lateral interaction between the images of the molecule adsorbed in the adjacent cells. Therefore, all adsorption calculations were performed considering a 6x6x1 supercell and 13 Å of vacuum.

We optimized the structural parameters of supercells by relaxing iteratively the ion positions and the cell lattices without any symmetry constraints until the residual force on each atom was <0.01 eV $Å^{-1}$. We used a specific kinetic energy cut-off and a Γ-centered k-point mesh for each structure, based on convergence test.

To provide information on the nature of the bonds that are established between the surface and the Li_2S_x molecules, the charge density difference was calculated, considering eq. 1:

$\Delta\rho = \rho_{AB} - (\rho_A - \rho_B)$ (1)

where ρ_{AB} is the spatial distribution of the charge density in graphene with the adsorbed polysulfide, ρ_A that in the isolated polysulfide and ρ_B that in graphene.

Fig. 1 shows the optimized polysulphides structures. The adsorption energies were calculated considering the eq.2:

$E_{ads} = E_{C+Pol} - E_C - E_{Pol}$ (2)

where E_{ads} represents the adsorption energy, E_{C+Pol} the cohesion energy of the graphene-polysulfide system, E_C the cohesion energy of the isolated graphene and E_{Pol} the cohesion energy of the isolated polysulfide. Fig. 2 shows, as an example, the optimized structure of Li2S on graphene.

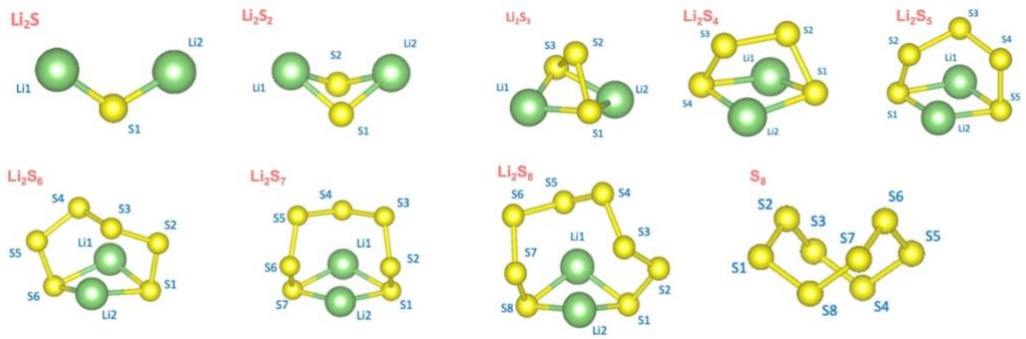

Fig. 1: Optimized polysulphide structures S_8, Li_2S_8, Li_2S_7, Li_2S_6, Li_2S_5, Li_2S_4, Li_2S_3, Li_2S_2, Li_2S. Color code: S yellow, Li light green.

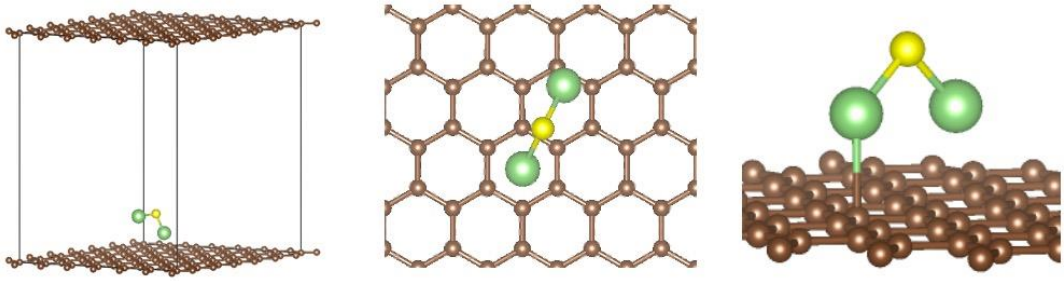

Fig. 2: Optimized Li_2S on surface graphene layer. Color code: S yellow, Li light green, C brown.

In table 1 we reported the adsorption energies with literature values [8], in parenthesis, for each molecule, and relevant C-Li/C-S distances between surface and molecules [9].

Table 1: Adsorption Energies (E_{ads}) calculated for each polysulphides, following eq.2, and relevant C-Li/C-S distances (d_{ads}) between surface and molecules.

Grafene-Li_2S_x	**E_{ads} (eV/molecule)**	**d_{ads} (Å)**
Li_2S	-0.679 (-0.60)	2.471 (2.01)
Li_2S_2	-0.770 (-0.58)	2.478 (2.13)
Li_2S_4	-0.530 (-0.50)	2.796 (2.46)
Li_2S_6	-0.751 (-0.68)	2.481
Li_2S_8	-0.814 (-0.78)	2.801 (2.54)
S_8	-1.051 (-0.75)	3.34

Our computational results are in good agreement with literature values. Li_2S_4 appears to be the least adsorbed species. The relevant aspect is that the most negative adsorption energies are those associated with S_8 and Li_2S_8, which are the most soluble species in the electrolytes of Li-S batteries. [10]
In order to provide a more detailed explanation of the different bonding character of C-Li/C-S in the different graphene polysulfide systems, the densities of states (DOS) and charge density difference were calculated. Fig. 3 shows, as an example, DOS and charge density difference for Li_2S on graphene.
From the analysis of the densities of the states and the distributions of the charge density it was possible to deduce that between polysulfides and graphene there is a delocalized charge densification, typical of weak-type interactions. Therefore, although in energy terms the interaction between the two species is not weak, it is a-directional and there is no formation of a real directional adsorption bond.

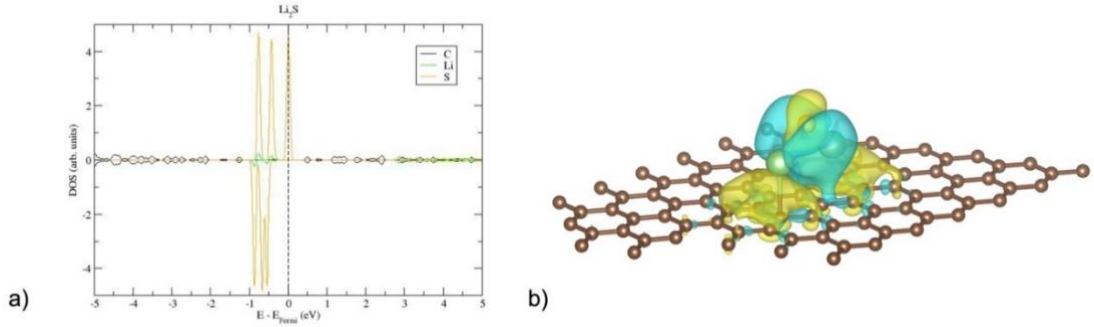

Fig. 3: a) Density of states (DOS) and b) charge density difference plot calculated for Li_2S adsorbed on graphene. Clouds in yellow indicate areas of charge densification (electron gain) while clouds in blue indicate areas with loss of charge (loss of electrons).

Overall this work presents a first principles study of the adsorption process of polysulphides on graphene, using the Density Functional Theory (DFT) method. Starting from the structural optimization of the species, structural and electronic optimization was carried out in order to evaluate the adsorption energies and to provide an explanation of the different bonding character. The trend of the adsorption energies obtained showed a more favorable interaction for the long-chain species (Li_2S_8 and S_8), a relevant aspect that would help to combat the solubility problem associated with these species. To explain in more detail the S-C and Li-C bond character, the density of the states and the distribution of the charge density of the different polysulphide-graphene systems were studied. The results confirmed the presence of interactions which are however weak and have a strongly a-directional character, so they do not involve the formation of a real covalent or ionic bond.
With the results obtained, the next step is to provide a valid mechanism for the reduction of polysulphides on the graphene surface, also subsequently implementing the theory level.

References

[1] J. A. R. Sheng and S. Zhang. A new direction for the performance improvement of rechargeable lithium/sulfur batteries, *Journal of Power Sources*, pp. 77-82, 2011.
[2] X. A. F. N. Ji. Advance in Li-S, *Journal of Materials Chemistry*, **20**, pp. 9821-9826, 2010.
[3] G. A.-C. J. S. G. D. L. B. Fongy C. Ionic vs electronic power limitations and analysis of the fraction of wired grains in LiFePO4 composite electrodes, *Journal Electrochem Socity*, **157**, pp. A885-A891, 2010.
[4] L. Ji X. L. A highly ordered nanostructured carbon-sulphur cathode for lithium-sulfur batteries, *Nat Mater*, **8**, pp. 500-506, 2009.

[5] Hafner, J.; Kresse, G. The Vienna AB-Initio Simulation Program VASP: An Efficient and Versatile Tool for Studying the Structural, Dynamic, and Electronic Properties of Materials. In *Properties of Complex Inorganic Solids*; Springer US, pp. 69–82, (1997)
[6] Perdew, J. P.; Burke, K.; Ernzerhof, M. Generalized Gradient Approximation Made Simple. *Physical Review Letters*, **18**, pp. 3865–3868, (1996).
[7] Becke, A. D. Density-Functional Thermochemistry. III. The Role of Exact Exchange. *The Journal of Chemical Physics* **98**, pp. 5648–5652, (1993).
[8] Y. W. Z. W. S. Z. F. R. Z. Y. C. Q. Zhang. Understanding the anchoring effect of two-dimensional layered materials for Lithium-Sulfur batteries, *Nano Lett.*, **15**, pp. 3780-3786, 2015.
[9] F. S. H. G. C. C. Z. P. H. N. D. C. C. Z. Yi. New insight into Li2S2/Li2S adsorption on the graphene bearing single vacancy: A DFT study, *Applied Surface Science*, 2019.
[10] J. R. A. Y. V. Milkhaylik. Polysulfide shuttle study in the Li/S battery system, *Journal of the Electrochemical Society*, **151**, pp. A1969-A1976, 2004.

TESTING THE SHIELDING SOLUTION FOR THE ABCS (ASTRO-BIO CUBESAT) PAYLOAD USING FLUKA ON CRESCO

N. Burgio[1*], A. Santagata[1]
[1]*ENEA, FSN-FIS-RNR, C.R. Casaccia, Roma, Italy*
**Corresponding author:nunzio.burgio@enea.it*

ABSTRACT. The AstroBio Cube Satellite (ABCS) will deploy within the inner Van Allen belt on the Vega C Maiden Flight launch opportunity of the European Space Agency. At this altitude, ABCS will experience radiation doses orders of magnitude greater than in low earth orbit, where CubeSats usually operate. To quantify the dose delivered to the payload and adopt a shielding solution, we need to define the contributions of geomagnetically trapped particles (electron and proton), Galactic Cosmic Rays (GCR ions), Solar Energetic Particle (SEP) within the ABCS orbit using the ESA's SPace ENVironment Information System (SPENVIS) and using the FLUKA (FLUktuierende KAskade - Fluctuating Cascade) code models the ABCS interaction with the orbital source. Such a design task is calculation intensive and requests an implementation of FLUKA in the "embarrassing parallel" modality on the CRESCO computational facility.

1 Introduction

AstroBio Cube Sat (ABCS) is a 3U CubeSat [1] designed and developed in partnership between INAF, Italian National Institute of Astrophysics, Sapienza University of Rome, and Alma Mater Studiorum University of Bologna, on the Vega C Maiden Flight launch opportunity offered by European Space Agency (ESA) with the support of the Italian Space Agency (ASI) [2]. The project aims to test an automated onboard laboratory in space environments. In-orbit validation of the proposed technology would represent a significant breakthrough for the autonomous execution of bio-analytical experiments in space. The ABCS will be deployed within the inner Van Allen belt (5830 km altitude). At this altitude, ABCS will experience radiation doses orders of magnitude greater than in the Low Earth Orbit, where CubeSats usually operate (see Fig 1). According to the calculation carried out with SPENVIS [3], the total flux intensity in the mission orbit is 1.41E+07 particles/cm^2/s.

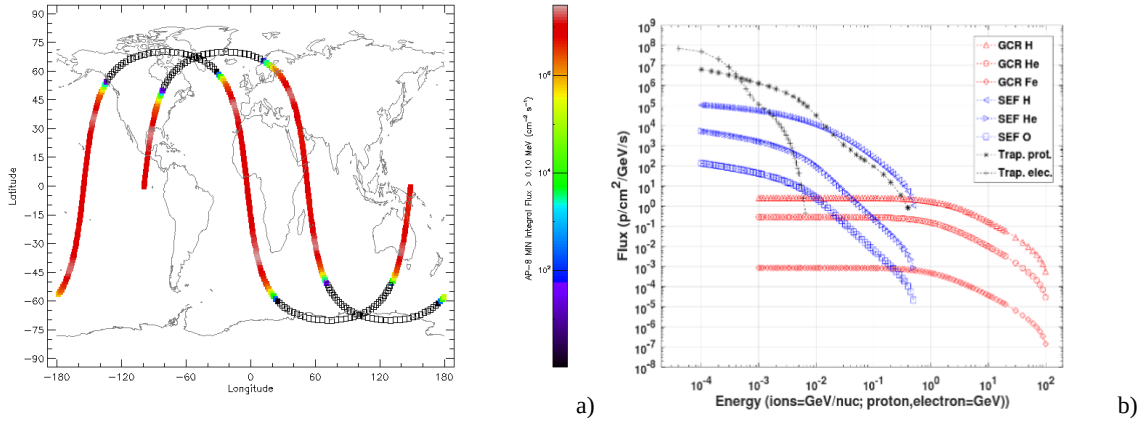

a) b)

Fig. 1: a) Satellite ground track on a world map with the proton flux intensity on logarithm chromatic scales: ABCS is subjected to the maximum flux intensity for a significant part of its orbit. b) Comparison of the energy differential fluxes of the source terms in the mission orbit. GCR ions emission are at the highest energies but with low flux. Trapped particles and SEP ions shows higher flux with lower energies.

Trapped particles (electron and proton) are the main component of the total flux. Solar Energetic Particles (SEP) and Galactic Cosmic Ray (GCR) are ions with atomic numbers Z from 1 to 92. The interaction of each kind of particle with the satellite structure generates a cascade of secondary particles with lower kinetic energy and a higher probability of interacting further within the satellite interior, releasing dose, causing damage to the material, and altering the subsystem's functionality. Consequently, we use FLUKA (FLUktuierende KAskade) [4] Monte Carlo code to cover the whole energy range of the considered particles that arrive up to the ultra-relativistic regime and implement the full-scale geometric layout of the satellite (Figure 2). Finally, to overcome the long computational time required for this kind of simulation, we decided to implement FLUKA in the embarrassing parallelism modality on the CRESCO cluster. This report aims to describe the FLUKA compilation modality and the implementation of the scripts to pre-process the input, launch the LSF jobs on CRESCO, and process the results.

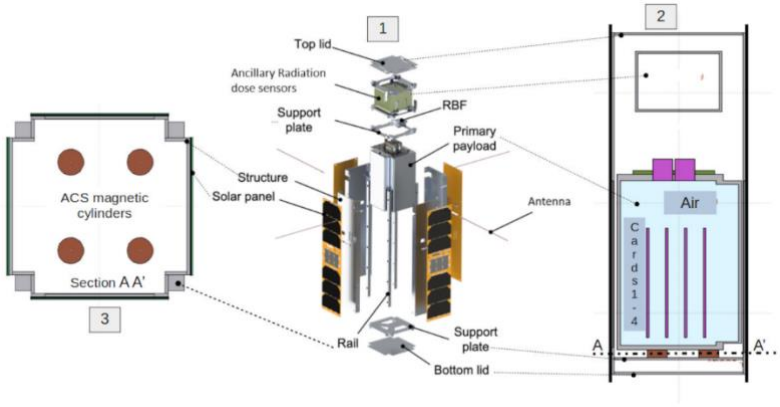

Fig. 2: Comparison of the satellite's exploded view (1) with the layout's sections obtained by FLAIR (FLUKA Advanced Interface) in the FLUKA model. The model layout retains only the geometrical features and the materials necessary for particle transport and shielding considerations. In particular, section (2) shows the pressurised primary payload, the ancillary radiation dose sensors box, and the upper and lower support plate. Section (3) shows the position of the Attitude Control System (ACS) magnetic cylinders

2 FLUKA installation and tune-up on CRESCO

The precision of the Monte Carlo results depends on the number of primary source particles used for the simulation [5]. Higher precision is generally obtained by increasing the number of primary particles at the cost of higher calculation time. We implement FLUKA on the high-performance computing system CRESCO [6] to shorten calculation time, executing the simulation in the "embarrassing parallel" [7] modality, resulting from several replicas of the same problem having different seeds for the pseudo-Random Number Generator (PseudoRNG). The results from each replica are like independent measurements of experimental quantities, and their mean μ and standard deviations σ are the final simulation results. We quantify the attained precision level using the relative error Er= σ/μ. In an embarrassing parallelism scheme, the overall number of primary particles P, connected with the simulation precision, is

$$P = N\,p; \quad \text{equation (1)}$$

with

N= number of CPU

p= number of particles per CPU (on which run a simulation replica)

P= overall number of particles in the simulation

This calculation methodology also allows the individual analysis of each source term (superposition approximation), optimising precision and simulation time by changing the number of particles and CPUs.

We successful compile and linked the FLUKA package version 4.2-2 using gfortran 9.1.1 under the devtoolset-9 environment recently installed on Linux CENTOS 7.8. To execute the simulations, we implement a bash script by which the user specifies the FLUKA input file, the requested number of CRESCO nodes, the number of tasks per node, the LSF queue, the desired version of FLUKA executable, and the optional auxiliary files. The bash script, invoking the stream editor awk, prepares N replicas of the input file, each having a different seed for the FLUKA's PseudoRNG, and saves it in a dedicated subdirectory, along with the auxiliary files. A set of scripts to launch a batch job on each requested node is then prepared and queued on LSF.

Table 1: Performance on CRESCO of the main set of simulations to assess the ABCS payload shielding

Source Term	number of particles per CPU (p)	Number of CPU per simulation (N)	Overall number of particles per simulation (P)	CPU time per particle (seconds)	Simulation execution time (hours)	Relative error ($E_r = \frac{\mu}{\sigma}$) x 100
Trapped Proton	4.00E+08	64	2.56E+10	5.43E-05	6.0	1.47%
Trapped Electron	4.00E+08	64	2.56E+10	5.03E-05	5.6	6.24%
GCR Proton	1.00E+07	64	6.40E+08	8.27E-04	2.3	1.14%
GCR α (^{4}He)	5.00E+06	64	3.20E+08	1.76E-03	2.4	1.26%
GCR ^{56}Fe	1.00E+05	192	1.92E+07	2.76E-01	7.7	1.21%
SEP Proton	1.00E+08	64	6.40E+09	1.81E-04	5.0	1.18%
SEP α (^{4}He)	1.00E+08	64	6.40E+09	1.64E-04	4.6	1.52%
SEP ^{16}O	1.00E+08	64	6.40E+09	2.75E-04	7.6	1.18%

At the end of the calculation, another set of bash scripts collected the N individual results, using some auxiliary codes of the FLUKA package, and computed the overall mean and the standard deviation of each estimated quantity. The resulting file can be processed further using FLAIR [8] or user-developed scripts to obtain the results in final forms.

Table 1 reports the parameters adopted to minimise the relative error, within a sustainable simulation time, for each source term used on the configuration. A detailed analysis of the optimisation of the estimator's relative error goes beyond the scope of the present paper. For example, the relative errors reported in the last columns of Table 1 deal with the absorbed doses in the ABCS payload. Their values are below the 2% of relative error except for trapped electrons that, due to their low mean emission energy, were severely attenuated by the satellite structure and the shielding materials yielding more dispersed values of the mean TID rate with a relative error ranging from 6% to 10% that is still acceptable for this type of simulation.

3 Results

Table 2 compares the FLUKA estimates of the dose rate delivered on a Print Circuit Board, identified as card 4, located within the ABCS payload, using progressively increasing shielding protection.

Table 2 – Estimated TID rate for card 4 in the progressive construction of the ABCS layout around the target components

Void configuration	Base configuration	Shielded configuration
7.43E-04 Gy/s	1.02E-06 Gy/s	7.98E-07 Gy/s
Shielding effectiveness, in term of dose reduction, relative to Void configuration	-99.86%	-99.89%

Shielding effectiveness relative to the Base configuration	--	-21.50%

The “Void” configuration is obtained setting to vacuum all the materials in the satellite model except for the ABCS payload air volume and the four cards, the “base” configuration refers to the satellite layout protection on the payload, and, finally, the “shielded” configuration as additive protection for the primary payload. According to Table 2 and Figure 3, the dose rate decreases by 99.86%, passing from the void to the base configuration and slightly decrease, even more, adding further shielding layers to the payload. However, due to the highly harsh radiative environment, we decided to implement the shielded configuration in the final satellite design to maintain the highest allowable safety margin.

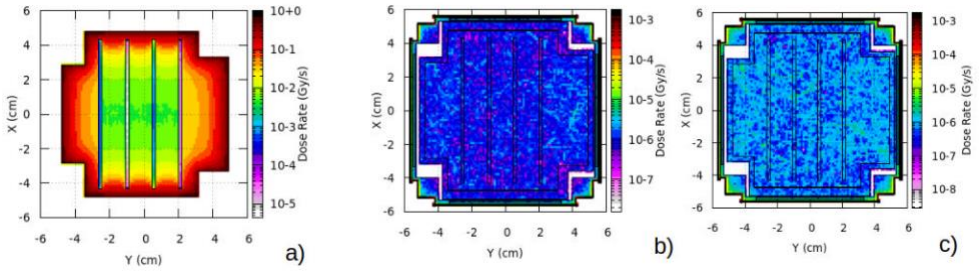

Fig.3: The comparison of the dose rate integrated on the Z-axis of the FLUKA reference system and reported on an X-Y cross-section of the satellite geometry (same as section 3 of Fig. 2 but at payload middle height): a) making void all the satellite components except the cards and the air in the payload; b) in the absence of the shielding; c) in the presence of the shielding; The progressive decrease of the dose rate with the shielding increase is apparent (See also Table 2 and text).

4 Conclusion

- FLUKA confirms its capability of simulating the complex interaction of mixed field space particles with matter.
- Implementing FLUKA on the CRESCO cluster increases the shielding design accuracy, maintaining low computational time.
- Pre- and post-processing allows a cross-checking of the results minimising the input errors.
- In 2022 the ABCS will be launched in Van Allen’s belt, and we will be able to compare our simulations outcome with the in-orbit measurement.

References

[1] https://www.nasa.gov/mission_pages/cubesats/index.html, accessed December 29 2021
[2] Agenzia Spaziale Italiana (ASI), https://www.asi.it, accessed December 29 2021
[3] https://www.spenvis.oma.be/ accessed December 29 2021
[4] G. Battistoni, et Al., Annals Nucl. Energy (2015) https://doi.org/10.1016/j.anucene.2014.11.007
[5] “Introduction to the Monte Carlo simulation of radiation transport”, Beginner online training, Spring 2020 https://indico.cern.ch/event/1012211/contributions/4247770/attachments/2254500/3825142/02_Introduction_to_Monte_Carlo_2021_online.pdf accessed December 29 2021
[6] F. Iannone et al., International Conference on High-Performance Computing & Simulation (HPCS), Dublin, Ireland, 2019, pp. 1051-1052, https://doi.org/10.1109/HPCS48598.2019.9188135
[7] D. Vrajitoru “Parallel and Distributed Programming” https://www.cs.iusb.edu/~danav/teach/b424/b424_23_embpar.html accessed December 29 2021
[8] Flair | The official CERN FLUKA website https://fluka.cern/documentation/examples/flair accessed December 29 2021

INTERATOMIC POTENTIALS FOR EVALUATION OF PuO_2 HEAT CAPACITY

Rolando Calabrese

ENEA, Safety and Sustainability of Nuclear Energy Division, I-40129, Bologna, Italy[9]

ABSTRACT. Mixed oxide fuel (MOX) for fast breeder reactor (FBR) is characterized by concentrations of PuO_2 of the order of 30 mol%. Properties relevant for safety and economic reasons such as thermal conductivity and melting temperature could markedly deviate from correlations validated for UO_2. Therefore, a careful determination of PuO_2 concentration effects on MOX fuel properties is mandatory. Concerning the heat capacity, plutonium dioxide concentration is accounted for by means of the Neumann-Kopp rule (NK). Nevertheless, a lack of experimental data at high temperature has led to a significant scatter of models' predictions in this temperature region. The author has performed MD calculations focused on the heat capacity of PuO_2 that showed the presence of a pre-melting transition and a noticeable effect of the formation energy of oxygen Frenkel pair (OFP) that is a key quantity in most recent models. A critical review performed on these results has suggested to revise coefficients of the interatomic potential and to employ a different modelling for heat capacity. Author has performed new MD calculations complying with these indications. Results have been used to reconsider conclusions derived from previous calculations and to discuss the curve of heat capacity recommended for PuO_2 and its correlation with a recent model used to determine the contribution of OFP defects to heat capacity.

1 Introduction

Concentrations of plutonium dioxide of MOX fuel designed for FBR are of the order of 30 mol% [1,2]. A lack of experimental measurements has raised questions on the heat capacity of PuO_2 in the high temperature domain extending from 2400 K up to the melting temperature. Some authors state that the excess heat capacity seen in actinide oxides is due to electronic disorder. Therefore, they support the hypothesis that in the high temperature region the heat capacity of PuO_2 should not increase because of the high formation energy required to create an electron-hole pair [3,4]. On the contrary, more recent models are based on the hypothesis that the formation of oxygen Frenkel pair defects (OFP) leads to a significant increase of PuO_2 heat capacity starting from 2000 K [2,5-6]. An analysis based on statistical mechanics has allowed to develop a correlation for evaluation of excess heat capacity due to OFP defects [6]. Recommendations have been developed in agreement with these findings [7]. This topic has been discussed by the author by means of MD calculations presented in [8] where a purpose-developed potential has been compared to the model published by Uchida et al. [9]. The author has performed a critical review of results presented in [8] identifying some aspects requiring a deeper analysis. The issues highlighted in our review are listed as follows:

- Deviation of about 10% of predictions from the curve of linear thermal expansion recommended for PuO_2;

[9] Corresponding author. E-mail: rolando.calabrese@enea.it

- Presence of an increase of heat capacity (interpreted as a pre-melting transition) in both the dilation and defects formation terms of the heat capacity model;
- Input value of the Grüneisen constant used in calculations.

The first bullet recalls that a significant deviation was noted between the results of MD calculations and the curve of thermal expansion recommended for PuO_2 [8]. This observation has highlighted the need for a refinement of the interatomic potential that could improve accuracy of predictions and robustness of conclusions. The second point deals with the model of heat capacity that has been applied in our previous calculations. The author has judged that a single quantity accounting for the pre-melting transition would be preferable for a better evaluation and interpretation of this phenomenon. The third issue concerns the value of the Grüneisen constant that was adopted in calculations (1.62) which is lower than most recent determinations and its use as an input parameter not well justified. The actions and changes implemented by the author to answer these issues are presented in following section. After this review, new MD calculations have been performed confirming the conclusions presented in our previous analysis [8,10]. In this paper we use our most recent results to discuss the correlation between the curve recommended for the heat capacity of PuO_2 [7] and the model for excess heat capacity proposed in [6]. MD calculations have been carried out by means of the LAMMPS code (v. 2019) [11]. Code runs have been carried out on the CRESCO6 cluster [12]. This machine supports the MPI message-passing library giving the opportunity to take advantage of the built-in parallel structure of the code. LAMMPS uses spatial-decomposition techniques to partition the simulation domain into small sub-domains of equal computational cost, one of which is assigned to each processor.

2 MD calculations

Interactions between atoms have been modelled by means of a Born-Mayer-Huggins pair potential (BMH). The analytical expression of BMH partially ionic is presented in Eq. 1. Each of the terms of Eq. 1 accounts for different types of interactions between ions: the first for long-range Coulombic, the second and the third for short-range interactions due to Pauli's repulsion principle and van der Waals forces, respectively. Values of ionicity are consistent with the effective electronic charges z_i and z_j; r_{ij} stands for the distance between ion *i* and ion *j*. A Morse potential accounts for the covalent bond between anion and cation; see Eq. 2. In this equation r_{ij}^* is the covalent bond length. D_{ij} and β_{ij} determine the depth and shape of potential.

$$U_{ij}(r_{ij}) = \frac{z_i z_j e^2}{4\pi\epsilon_0 r_{ij}} + A_{ij} exp\left(-\frac{r_{ij}}{\rho_{ij}}\right) - \frac{C_{ij}}{r_{ij}^6} \qquad (1)$$

$$U_{ij}(r_{ij}) = D_{ij}\{exp[-2\beta_{ij}(r_{ij} - r_{ij}^*)] - 2exp[-\beta_{ij}(r_{ij} - r_{ij}^*)]\} \qquad (2)$$

Two interatomic potentials named P1 and P2 have been applied in calculations. The first one (P1) is consistent with a model that has been developed by Uchida et al. relying on the measurements of PuO_2 thermal expansion [9]. The value of ionicity indicated by authors (0.565) sets the effective charges of plutonium and oxygen to +2.26 and to -1.13, respectively. A second potential (P2) has been developed by the author aiming at testing the effect of OFP formation energy on the heat capacity of PuO_2 [8]. In the light of outcomes of the review mentioned above, coefficients of the potential have been refined in order to improve accuracy of thermal expansion predictions and to achieve a reduction of the OFP formation energy for a better agreement with the values reported in the open literature [10]. New coefficients of P2 are listed in Tab. 1. Effective charges of plutonium and oxygen have been set to +2.02 and to -1.01, respectively. The use of these coefficients showed to markedly reduce the deviations noted in thermal expansion predictions with a decrease from 6.40 eV to 5.73 eV of the OFP formation energy [10]. Therefore, this new set of coefficients has allowed us to overcome the first observation mentioned in the introduction.

The model of heat capacity accounts for three contributions: phonon C_{ph}, dilation C_d, and formation of defects C_{df}; see Eq. 3 [13]. According to most recent indications in the open literature, we have assumed that the third term is strongly correlated with the creation of OFPs at high temperature.

$$C_p = C_{ph} + C_d + C_{df} \qquad (3)$$

The dilation term is presented in Eq. 4 where α is the volumetric thermal expansion, γ the Grüneisen constant and T the temperature.

$$C_d = \alpha\gamma C_{ph} T \qquad (4)$$

Table 1: Coefficients of the P2 interatomic potential.

Pair (BMH)	A_{ij} (eV)	ρ_{ij} (Å)	C_{ij} (eV·Å ^{6})
O-O	334895.0	0.178	140.0
Pu-Pu	490000.0	0.250	0.0
Pu-O	4580.0	0.252	0.0
Pair (Morse)	D_{ij} (eV)	β_{ij} (Å^{-1})	r_{ij}^* (Å)
Pu-O	0.30	2.	2.37

In our previous analysis we assumed that the Grüneisen constant is an input parameter and that the term of defects formation in Eq. 3 could be derived from the results of calculations [8]. In order to overcome the observations listed above we have adopted a different approach to modelling. We have assumed that the scope of MD calculations is focused on the first two terms of Eq. 3 while the third one is mostly due to configurational entropy of defects and described by the correlation presented in [6]. Therefore, we assume that Eq. 5 rules the correlation existing between C_p and C_{ph} [2].

$$C_p = C_{ph}(1 + \alpha\gamma T) \qquad (5)$$

C_p and α have been derived by means of calculations on the enthalpy and lattice constant performed in the NPT ensemble. The derivative of the total energy calculated in the NVT ensemble has allowed us to determine the phonon term C_{ph}. With this approach the increase of heat capacity noted at high temperature is fully accounted for by the dilation term and the Grüneisen constant is an outcome of calculations (from Eq. 5) and not an input as in [8]. This answers the last two points raised in our review.

The supercell used in calculations is composed of 40500 atoms arranged in a face-centered cubic lattice (*fcc*). The elementary cell, formed by 12 atoms, has been replicated 15x15x15 along the x, y, z orthogonal axes. Periodic boundary conditions have been applied. Energy minimization was performed by means of a steepest descent algorithm. The Nose-Hoover thermostat/barostat has been used to reach equilibrium (30 ps) [11]. MD calculations have been performed in the temperature interval extending from 300 K up to 2900 K.

3 Results

Details of results concerning linear thermal expansion, Grüneisen constant, and Bulk modulus have been recently presented in [10]. Here, we focus on a comparison between the curve of heat capacity recommended for PuO_2 and the correlation proposed by Konings and Beneš for the contribution of OFP defects to heat capacity [6,7]. This latter correlation is presented in Eq. 6.

$$C_{p,exc} = \frac{\Delta H_{OFP}^2}{\sqrt{2}RT^2} exp\left(\frac{-\Delta H_{OFP}}{2RT}\right) exp\left(\frac{\Delta S_{OFP}}{2R}\right) \qquad (6)$$

In Eq. 6 ΔH_{OFP} and ΔS_{OFP} are the enthalpy and entropy of oxygen Frenkel pair formation, R is the universal gas constant. Values of these quantities are 279 kJ mol^{-1} and 66.7 J mol^{-1} K^{-1} for the OFP enthalpy and entropy, respectively [6]. In Fig. 1 (left) we show the curve recommended for PuO_2 and the curve obtained by subtracting from the recommended the contribution of defects that is calculated according to Eq. 6. The resulting curve that is consistent with $(C_{ph} + C_d)$ of Eq. 3, is compared to the results obtained from MD calculations. Numerical results have been increased by about 17 J mol^{-1} K^{-1} that is the deviation noted between calculations and recommended values in the temperature interval 1000-1400 K. These curves are in good agreement up to 2500 K, thereafter MD calculations show a markedly increase not consistent with the recommended values. This result highlights that MD calculations do not account for a constant term that is usually associated with the Schottky effect due to the presence of additional energy levels for PuO_2 f-electrons [14]. Concerning the phonon and dilation terms, one can observe that the modelling adopted here shows good agreement with recommendations up to 2500 K. The presence of a pre-melting transition is confirmed with intensity increasing with decreasing formation energy of OFP defects [10]. In Fig. 1 (right) we show the curve proposed by Konings and Beneš and the difference between this correlation and the contribution of defects formation according to the results of calculations. This latter contribution has been determined by subtracting calculated $(C_{ph} + C_d)$ from recommended $(C_{ph} + C_d)$. These quantities are presented in Fig. 1 (left).

Up to 2500 K no contribution of defects is noted in calculations, thereafter the differences are rather constants and at higher temperature decrease. If we consider a shift of the calculated defects term equal to the value of recommended curve at 2500 K (about 70 J mol^{-1}K^{-1}) we note that up to 2650-2700 K calculations and recommendations are fairly consistent. In the concluding part predictions increase linearly at a higher rate than recommendations.

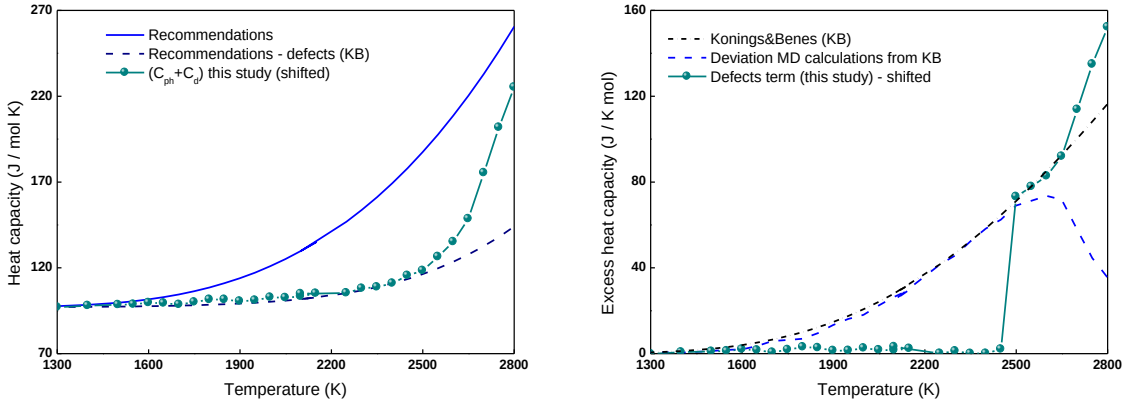

Fig.1: Comparison of recommended curves [6,7] with MD calculations (left); excess heat capacity due to defects formation: comparison of MD calculations at high temperature with the model in [6].

4 Discussion and conclusions

Results presented in Fig. 1 confirm that an additional term should be introduced in the model of heat capacity to account for the Schottky effect. MD calculations are not capable of predicting the contribution of defects below about 2500 K. From this temperature up to about 2650-2700 K recommendations and calculations are in fairly agreement. Beyond 2700 K calculations predict a linear increase of heat capacity that could be consistent with either a more intense phase of the pre-melting transition or the onset of melting transition. This point needs a deeper consideration. As aforementioned,

the increase of heat capacity predictions starts around 2500 K that is 88% of the melting temperature (2840 K). This observation supports the hypothesis that we are dealing with a pre-melting transition. A loosely correlation has been confirmed between the formation energy of OFP used in recommendations (2.9 eV) and the qualitative evaluations reported here. Our evaluations are rather consistent with the indications published in the open literature, however, the correlation proposed by Konings and Beneš predicts in this case negligible values of excess heat capacity. Therefore, we can observe that configurational entropy and coupling of defects contribute to reduce the formation energy of OFP markedly.

References

[1] A.K. Sengupta, K.B. Khan, J. Panakkal, H.S. Kamath, S. Banerjee, Evaluation of high plutonia (44% PuO_2) MOX as a fuel for fast breeder test reactor, *Journal of Nuclear Materials* **385**, pp. 173-177, (2009).

[2] M. Kato, T. Matsumoto, Thermal and Mechanical Properties of UO_2 and PuO_2, NEA/NSC/R(2015)2, pp. 172-177, OECD/Nuclear Energy Agency, Paris, (2015).

[3] J.K. Fink, Enthalpy and Heat Capacity of the Actinide Oxides, *International Journal of Thermophysics* **3**(2), pp. 165-200, (1982).

[4] J.-M. Bonnerot, Proprietes Thermiques des Oxydes Mixtes d'Uranium et de Plutonium, Ph.D. thesis, CEA-R-5450, (1988).

[5] J.H. Harding, D.G. Martin, P.E. Potter, Thermophysical and thermochemical properties of fast reactor materials, EUR 12402 EN, Commission of the European Communities, Luxemburg, (1989).

[6] R.J.M. Konings, O. Beneš, The heat capacity of NpO_2 at high temperatures: The effect of oxygen Frenkel pair formation, *Journal of Physics and Chemistry of Solids* **74**(5), pp. 653-655, (2013).

[7] R.J.M. Konings, O. Beneš, A. Kovăcs, D. Manara, D. Sedmidubsky, L. Gorokhov, V.S. Iorish, V. Yungman, E. Shenyavskaya, E. Osima, The Thermodynamic Properties of the f-Elements and their Compounds. Part 2. The Lanthanide and Actinide Oxides, *Journal of Physical and Chemical Reference Data* **43**, p. 013101, (2014).

[8] R. Calabrese, The Heat Capacity of PuO_2 at High Temperature: Molecular Dynamics Calculations, *Journal of Nuclear Engineering and Radiation Science* **8**(4), p. 041603, (2022), https://doi.org/10.1115/1.4054941.

[9] T. Uchida, T. Sunaoshi, K. Konashi, M. Kato, Thermal expansion of PuO_2, *Journal of Nuclear Materials* **452**, pp. 281-284, (2014).

[10] R. Calabrese, Heat Capacity of PuO_2 at High Temperature: a Comparison of Interatomic Potentials, Proc. Int. Conf. Nuclear Energy New Europe 2022, Portorož, Slovenia, September 12-15, Nuclear Society of Slovenia, paper 605 - under review -, (2022).

[11] S. Plimpton, Fast Parallel Algorithms for Short-Range Molecular Dynamics, *Journal of Computational Physics* **117**, pp. 1-19, (1995).

[12] High Performance Computing on CRESCO infrastructure: research activities and results 2019, Italian National Agency for New Technologies Energy and Sustainable Economic Development, Rome, (2020).

[13] K. Kurosaki, K. Yamada, M. Uno, S. Yamanaka, K. Yamamoto, T. Namekawa, Molecular dynamics study of mixed oxide fuel, *Journal of Nuclear Materials* **294**, pp. 160-167, (2001).

[14] L. Manes, in: Proc. 4th Int. Conf. Plutonium and Other Actinides, edited by W.N. Miner, Vol. 1, Santa Fe, New Mexico, October 5-9, p. 254, (1970).

HYDROGEN PRODUCTION BY MEANS OF STEAM METHANE REFORMING WITH CO_2 CAPTURE IN A CIRCULATING FLUIDIZED BED

Antonio Di Nardo, Giorgio Calchetti[1], Stefano Stendardo, Elisa Savuto

ENEA TERIN/PSU/IPSE Casaccia, Via Anguillarese 301, 00123 Roma

ABSTRACT. In this report we illustrate the modeling and simulation activities of a Dual Fluidized Bed (DFB) for hydrogen production and CO_2 capture, using a bifunctional catalyst/sorbents solid. The activities carried out were mainly focused on the study of a continuous process for hydrogen production from steam methane reforming (SMR), intensified by CO_2 capture through a $CaO/CaCO_3$ cycle (i.e. Sorption Enhanced Steam Methane Reforming SE-SMR). The double fluidized bed system consists of a carbonation reactor, where CO_2 capture is integrated in a single circuit with a calcination reactor in which the exhausted catalyst/sorbent is regenerated at high temperature. In this model, both the chemical kinetics of the SMR and CO_2 capture reactions were implemented. The main result is the confirmation of the solid material flow rate to be recirculated from the carbonator to the calciner (2.8 g/s) and the production of a gas flow at the exit of the carbonator with a fairly high purity in H_2, about 87.7%. The residual CH_4 is less than 2.5%, a sign that methane reforming and CO_2 capture take place effectively. Conversely, the methane conversion is around 90%.

1 Introduction

Currently more than 95% of the hydrogen, produced worldwide, derives from fossil fuels (natural gas and coal) and is responsible for the emission of about 830 Mt of CO_2 every year [1]. The SMR process is one of the most popular industrial processes for hydrogen production. In order to produce such a large quantity and meet the future massive demands of this gas, the scientific community has focused its efforts on the implementation of CO_2 capture systems in current production processes. The most promising method for large-scale hydrogen production is SE-SMR. This process is able to increase hydrogen production and lower operating process temperatures (650 °C). SE-SMR couples the SMR catalytic reactions with CO_2 capture at high temperature, through a "calcium looping" process (CaL). The SE-SMR process uses high temperature solid sorbents, for the simultaneous separation of CO_2 and the conversion of carbon-containing gases (CO and CH_4) into both H_2 and CO_2. This leads to an increase in conversion efficiency, because the CO_2 is separated at high temperatures (> 600 °C), with a more efficient use of heat. Such integration is not possible in technologies where the separation occurs at lower temperatures. The aim of the work is to study the SE-SMR process continuously in a double fluidized bed system, filled with bifunctional catalyst/sorbent particles. The numerical results obtained in this work will allow to effectively guide the experimental activities, with a considerable saving of time and technical and economic resources.

2 Simulations

This work addresses the kinetic and fluid dynamics aspects of the SE-SMR process, using the CPFD (Computational Particles Fluid Dynamics) [2]Barracuda® software. It is based on the MP-PIC (multiphase particle-in-cell method) model with a Lagrangian-Eulerian approach. The gaseous phase is treated as a continuous fluid with its own density, temperature and velocity, whereas the solid phase is modelled as a discrete Lagrangian phase. The two phases are fully coupled since solid and fluid turbulence, heat, mass and momentum exchanges are taken into account. The computational grid is made of approximately 1.5 million cells. The simulations were carried out on the ENEA CRESCO platform, on a machine equipped with a TESLA V100-PCIE-32GB GPU. Regarding the catalytic gas phase steam methane reforming reactions, the Numaguchi-Kikuchi model was used [3]. The model of Stendardo and Foscolo [4], was adopted for the $CaO+CO_2 \rightarrow CaCO_3$ carbon dioxide capture mechanism. In this model an approach called "shrinking core" is used for the propagation of the reaction front inside the particle. As regards the kinetic model of the $CaCO_3 \rightarrow CaO+CO_2$ calcination reaction, through which the regeneration of the exhausted sorbent takes place, it can be assumed that the reaction takes place uniformly inside the particle and a kinetic expression has been used, obtained using the "grain" model [5]. The double fluidized bed system (DFB) is schematized as in the figure 1, in which reactor A represents the carbonator, were the steam reforming reaction of methane takes place at 650° C, with simultaneous CO_2 capture by the sorbent. Reactor B is the calciner, which works at 950° C, were the sorbent is regenerated at high temperature. The two reactors are connected to each other to form a closed ring, by means of a connecting element called loop seal (calciner → carbonator) and by an inclined tube (carbonator → calciner).

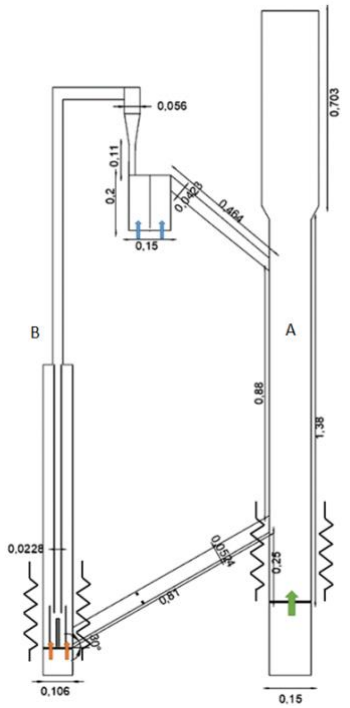

Fig.1: DFB scheme.

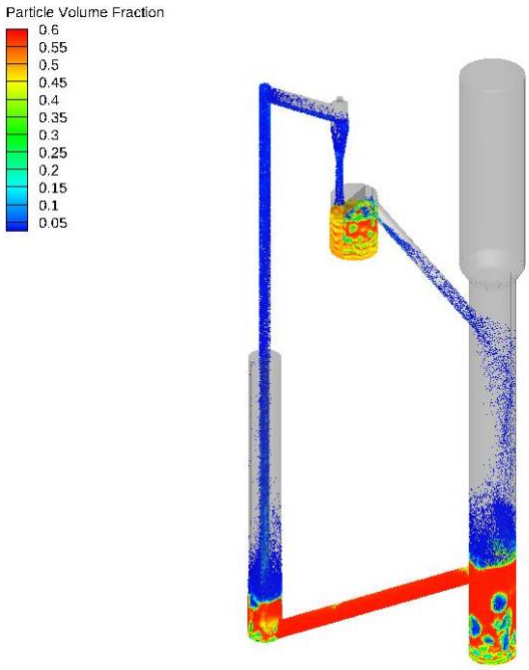

Fig 2: Instantaneous particle volume fraction in the DFB.

The carbonator works in a bubbling fluidization regime, while the calciner is partially bubbling, to ensure the necessary residence times for calcination and partially dragged, to allow the circulation of the solid material. The operating conditions of the DFB are summarized in Table 1. To ensure the maintenance of the desired temperatures in the two reactors, it is necessary to supply heat by means of electric heaters placed at the base. For this purpose, a temperature value of 1127 °C and 677 °C respectively was set for the internal wall of the calciner and the carbonator, verifying that the heat released by them was consistent with the thermal demands calculated in previous studies [6].The bifunctional particles used in this study are composed of 60% CaO, 10% Ni by mass and an inert support and have a diameter of 500 µm.

Table 1: Simulation input data

Carbonator	
Fluidization gas flow	$1.114*10^{-3}$kg/s
Fluidization gas temperature	450 °C
Fluidization gas composition (%mol)	25% CH_4 75% H_2O
Wall heat power input	677 °C
Hold up	4.6 kg
Calciner	
Fluidization gas flow	$1.169*10^{-3}$kg/s
Fluidization gas temperature	450 °C
Fluidization gas composition	CO_2
Nozzle gas flow	$1.25*10^{-3}$ kg/s
Nozzle gas input temperature	574 °C
Nozzle gas composition	CO_2
Wall heat power input	1127 °C
Hold up	1 kg
Loop seal	
Recycle chamber gas flow	$2.131*10^{-4}$ kg/s
Supply chamber gas flow	$1.421*10^{-4}$ kg/s
Gas input Temperature	450 °C
Gas composition	H_2O

The thermal inputs required are approximately 1.87 kW and 3.82 kW, for the carbonator and calciner respectively. In the figure 2 the volumetric fraction of the solid in the entire system is shown. The important data is represented by the confirmation of the exhausted sorbent value that must feed the calciner within the DFB. The mass flow rate is 2.8 g/s, in accordance with design request [6] and is able to guarantee a H_2 flow rate of approximately 73.5 Nl/min. From the chemical point of view, as shown in Figure 3, an output gas flow with a high H_2 percentage, approximately 87.7%, is obtained from the carbonator; the residual CH_4 is less than 2.5%, a clear indication that methane reforming reactions and CO_2 capture take place effectively.

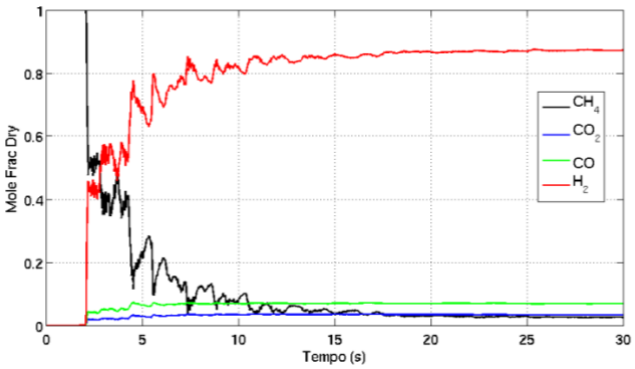

Fig 3: Gas composition from the carbonator.

Conversely, the methane conversion is around 90%. Figure 4 shows the distribution of the pressure calculation points along the entire system and the relative pressure polygon. The gas mass flow rate through the inclined connection pipe is approximately 1.53e-7 kg/s, i.e. less than 0.1 Nl/min, and the composition of the gas leaving the calciner is composed of 99.99% CO_2; the gas leakage from the carbonator to the calciner is so small that it therefore does not affect the operation of the two-reactor system.

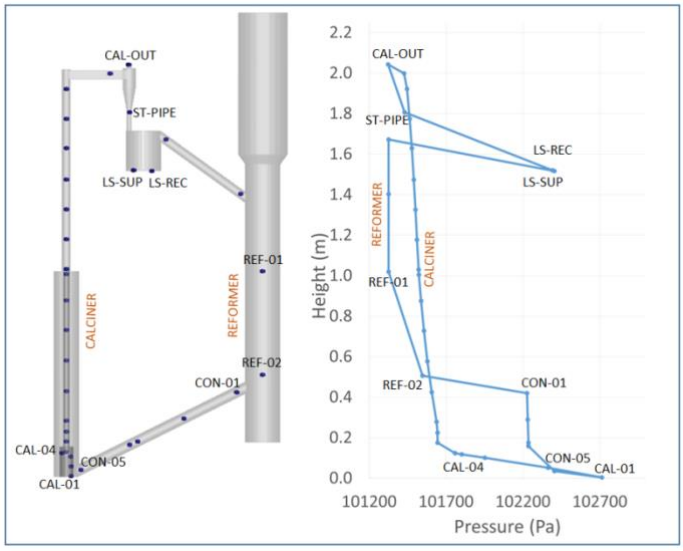

Fig. 4: Time averaged pressure profile along the dual fluidized bed loop.

3 Conclusions

The complete DFB model allowed the calculation of the solid flow and to verify how this value is congruent with the one necessary (2.8g /s) from the calciner to the carbonator to have an H_2 flow rate of about 73.5 Nl/min of H_2. From a chemical point of view, from the carbonator an output gas flow is obtained with a high percentage of H_2, about 87.7%; the residual CH_4 is less than 2.5%, a sign that methane reforming reactions and CO_2 capture take place effectively. Conversely, the methane conversion is around 90%. The results obtained in this work were used for the subsequent sizing of the calciner and of the elements connecting it to the carbonator. The calculation of the pressure drop across the calciner, the carbonator and in each of the above connection elements made it possible to verify the balance of the hydrodynamic forces by closing the pressure polygon.

References

[1] IEA, 2019. The Future of Hydrogen. Seizing today's opportunities. Report prepared by the IEA for the G20, Japan. https://www.iea.org/topics/hydrogen/.

[2] Snider, D. M., Clark, S. M., O'Rourke, P. J., 2011. Eulerian–Lagrangian method for three dimensional thermal reacting flow with application to coal gasifiers. Chem. Eng. Sci. 66, 1285-1295. https://doi.org/10.1016/j.ces.2010.12.042.

[3] Numaguchi, T., Kikuchi, K., 1988. Intrinsic Kinetics And Design Simulation In A Complex Reaction Network: Steam-Methane Reforming. Chem. Eng. Sci. 43, 2295-2301. https://doi.org/10.1016/0009-2509(88)87118-5.

[4] Stendardo, S., Foscolo, P.U., 2009. Carbon dioxide capture with dolomite: A model for gas–solid reaction within the grains of a particulate sorbent. Chem. Eng. Sci. 64, 2343-2352, 2009.https://doi.org/10.1016/j.ces.2009.02.009.

[5] Fang, F., Li, Z. S., Cai, N. S., 2009. Experiment and Modeling of CO2 Capture from Flue Gases at High Temperature in a Fluidized Bed Reactor with Ca-Based Sorbents. Energy Fuels 23, 207-216. https://doi.org/10.1021/ef800474n.

[6] Savuto E, Di Carlo A. Modellazione e simulazione di un calcinere per un sistema a doppio letto fluido per la cattura della CO_2 mediante sorbenti solidi a base di calcio. RdS/PTR/2020/079.

THE EFFECT OF HYDROGEN AND EXHAUST GAS RECIRCULATION ON NOX FORMATION IN LAMINAR AND TURBULENT CH4/H2/AIR FLAMES AT 25 BAR

D.Cecere[1*], S.Carpenella[1], E.Giacomazzi[1]

[1]*ENEA, DTE-PCU-IPSE, S.P. 081, Via Anguillarese 301, 00123, Rome, Italy*

ABSTRACT. The aim of this work is to investigate the effect of Exhaust Gas Recirculation (EGR) on NOx emissions in a CH4/H2/air combustion at 25 bar, with an Equivalence Ratio Φ = 0.7, in laminar and turbulent partially premixed flames.
Numerical simulations of twenty premixed and partially premixed counterflow flames with H2 percentages ranging from 0% to 100%, with and without EGR, were carried out. A sensitivity analysis showed that the thermal path is the main responsible for the NOx production. An H2 enrichment leads to an increase in NOx emissions. However, the addition of the exhaust gas decreases the flame temperature and therefore NOx decreases as well.
In addition, four turbulent slot jet flames with a CH4/H2/Air/EGR premixed central core and air/EGR as coflow were studied using Large Eddy Simulations (LES).
The four turbulent flames were simulated in a 2D domain with 0% and 50% hydrogen concentration, with and without EGR. The presence of hydrogen reduces CO2 emissions, but at the same time increases the NO concentration.
However, the introduction of exhaust gas recirculation leads to a NO reduction as in laminar flames.
Hence, the results obtained in this work show that at high pressure, the enrichment of hydrogen in the EGR mode, leads to lower NOx emissions.

1 Introduction

In order to homogenize contributions to CRESCO Project Progress Report 2021 and speed up the Nowadays, the necessity to lower CO2 emissions has driven to a new structure of the energy system, characterized by an increasing share of renewable sources of energy supported by the back-up service of gas turbines, and in which hydrogen can play an important role in the transition towards a low-carbon economy.
This scenario opens new research areas, also for gas turbines: in fact, aiming to feed them with blends of natural gas having an increasing hydrogen content, it is necessary to develop new technologies able to maintain low NOx emissions without efficiency loss.
Lean premixed dry combustion is an established technology for stationary gas turbines fueled by natural gas to achieve lower emissions and higher efficiency. It is the target combustion technology also for hydrogen blends, but new solutions for its implementation are required to control NOx and CO, the main regulated pollutants for stationary gas turbines [1]: Exhaust Gas Recirculation can be one of the solutions.
It has been shown that in diffusion flames hydrogen enrichment can improve flame stability and reduce CO2 emissions, but it increases NO production [2]. The net effect of hydrogen enrichment on NO formation in a hydrocarbon diffusion flame depends on the relative variations of the thermal and prompt paths [2].
In this work, the effect of EGR, i.e. CO2 and H2O dilution, on NOx emissions in a CH4/H2/air combustion at 25 bar, with an Equivalence Ratio Φ = 0.7, is analyzed in laminar premixed, laminar

Corresponding author. E-mail: donato.cecere@enea.it

partially premixed counterflow diffusion flames and turbulent partially premixed flames in a simple slot configuration to mimic air dilution in a gas turbine combustor.
A specific reduced kinetic scheme was developed from the complete POLIMI scheme [3] for the production of NOx at the specific equivalence ratio of $\Phi = 0.7$ and different H2 concentration levels without losing accuracy in temperature and product species concentrations. In this way LES simulations times can be significantly reduced.
Numerical simulations of twenty premixed and partially premixed counter flow flames with H2 percentages ranging from 0% to 100%, with and without EGR, were carried out by means of Opensmoke++ code [3]. In addition, four LES were simulated in a 2D domain by means of the in-house parallel code HeaRT [4] and ENEA's supercomputing facility CRESCO [5] (using 2000 processors per day), with 0% and 50% hydrogen concentration, with and without EGR. In the first two flames, named F1 and F2, the fuel is composed only by CH4. In the other two flames, named F3 and F4, the fuel is a mixture of 50% CH4 and 50% H2 The exhaust gases are premixed with both fuel and oxidizer in F2 and F4 flames.
The mixture was considered at 800 K, considering usual preheating temperatures in gas turbines, internal combustion engines and recirculating furnaces.

2 Results and discussion

2.1 NO Analysis in Premixed and Partially Premixed Flames

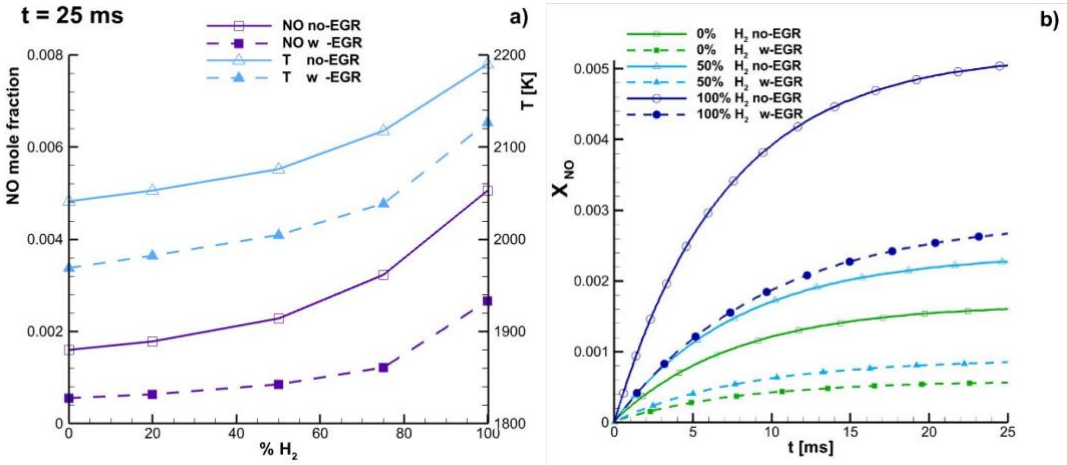

Fig.1: a) Premixed maximum temperature and NO mole fractions profiles with EGR and without EGR as a function of H2 concentration. b) NO mole fraction versus the residence time at different hydrogen composition, with and without EGR

Maximum NO mole fractions at residence time t = 25ms are reported in Fig. 1a. The NO mole fraction peak increases from 0% to 100% H2 by approximately 68%. The EGR dilution decreases NO in all percentages of hydrogen, in particular, NO mole fraction peak decreases by nearly 65% without hydrogen and 48% with 100% hydrogen composition. Note that an increase of temperature leads to an higher NO production, because the thermal path is the main NO formation mechanism. The reactions of this mechanism require a high activation energy, so high temperatures are required to activate them. Fig. 1b shows that NO mole fraction increases with the residence time and it achieves a constant value around 25ms. Each flame has a NO reduction when is diluted with EGR. In particular, there is a NO decrease of 65%, 63% and 48% for the flames with 0%, 50% and 100% of hydrogen composition respectively. It is interesting to note that the flame with composition of 50% H2 and with

* Corresponding author. E-mail: v.dalessandro@univpm.it

EGR (light blue dashed line) has a lower NO production than the flame without hydrogen and without EGR (green solid line) as well. Hence, despite hydrogen composition is increased, the NO production is decreased due to EGR.

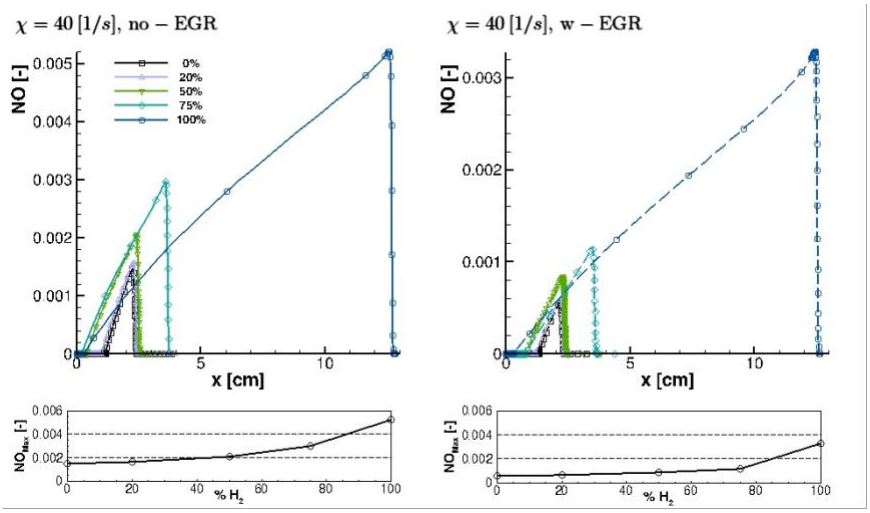

Fig.2: Partially premixed NO mass fractions profiles without EGR (top-left) and with EGR (top-right) at global strain of 40 1/s. and different H2/CH4 concentrations. Maximum NO mass fractions without (bottom-left) and with (bottom-right) EGR

EGR addition affects the partially premixed flame (PPF) speed as well as the flame structure reducing the peak flame temperature and thereby with favorable impact on the pollution emissions formation such as carbon monoxide (CO), unburned hydrocarbon and NOx production (see Fig.2). Fig.2 shows the evolution of the calculated maximum NO mole fractions as a function of H2 concentration without and with EGR. They show that hydrogen addition induces an increase of the NO mole fraction by roughly a factor of 3 as the flame temperature increases. In the EGR addition case (Fig.2), the NO mole fraction peak profile is reduced by approximately 50%. So one of the main advantage of hydrogen addition is to allow stabilization of lean EGR diluted flames (by increasing laminar flame velocity) while producing less NO.

2.2 The influence of hydrogen and EGR in turbulent flames

The configuration of the turbulent test cases defined for this study is a 2D unconfined premixed slot-burner flame at 25 bar pressure. It consists of a central slot-jet of premixed reactants surrounded on both longer sides by two coflowing jets. The central jet is a lean (equivalence ratio $\Phi = 0.7$) mixture of methane, hydrogen and air (air/exhaust gases) with fuel molar fractional distribution of 0% H2 and 100% CH4 for the flames F1-F2, and of 50% H2 and 50% CH4 for the flame F3-F4.
Left side of Fig.3 shows the average temperature field of flame F4. The central core has the highest temperature, hence there will be higher NOx production in this region. For this reason it has been analyzed the temperature, NO and NO2 mass fraction trends as function of height z, at fixed y = 0.0m, for all four flames. This is showed on the right side of Fig.3. Note that at $z < 0.03$m, the flames with EGR have a higher temperature, however after the reaction zone the flames with hydrogen have a higher temperature. As seen in laminar flames, the main mechanism of NOx formation is the thermal path and this is confirmed by the NO trend. At low heights there is a higher NO production in the flames with EGR, because at low residence times the temperature has not yet stabilized at high values and therefore the prompt path formation mechanism predominates, characterized by chemical

reactions with carbon.

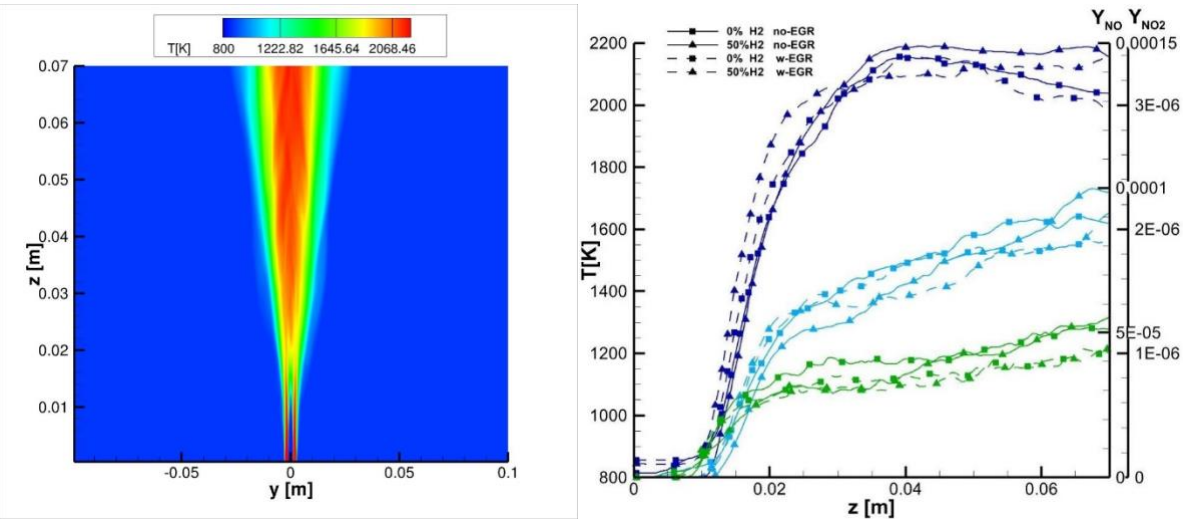

Fig.3: Left side: Temperature average field of flame F4 - Right side: Temperature (blue line), NO mass fraction (light blue line) and NO2 mass fraction (green line) average trends along z.

Once the temperature stabilizes at its maximum value, there is a strong rise in NO production in the flames with hydrogen. Thus, the hydrogen enrichment causes an increase of NO as the residence time increases. In contrast, EGR dilution leads to a lower NO production by about 10% and a lower NO2 production by about 25% at the exit of the combustor. Thus, the results of the turbulent flames confirm the trends shown by the laminar flames, even if with different percentage values.

Acknowledgments

The computing resources and the related technical support used for this work have been provided by CRESCO/ENEAGRID High Performance Computing infrastructure and its staff [5]. CRESCO/ENEAGRID High Performance Computing infrastructure is funded by ENEA, the Italian National Agency for New Technologies, Energy and Sustainable Economic Development and by Italian and European research programmes (see http://www.cresco.enea.it/english).

References

[1] T.C.Lieuwen , M.Chang, A.Amato, “Stationary gas turbine combustion: Technology needs and policy considerations”, Combustion Flame 160 (8) ,1311–1540 (2013).
[2] H.Guo, W.S. Neill, “A numerical study on the effect of hydrogen/reformate gas addition on flame temperature and NO formation in strained methane/air diffusion flames”, Comb. and Flame 156, 477-483 (2009).
[3] Cuoci A., Frassoldati A., Faravelli T., Ranzi E., “OpenSMOKE++: An object-oriented framework for the numerical modeling of reactive systems with detailed kinetic mechanisms”, Computer Physics Communications, 192, pp.237-264 (2015).
[4] D. Cecere, E. Giacomazzi, N.M. Arcidiacono, F.R. Picchia, et al.,“Direct numerical simulation of turbulent lean premixed CH4/H2-Air slot flame”, Combustion and Flame 165, 384-401 (2016).
[5] Iannone, F. and et al., “CRESCO ENEA HPC clusters: a working example of a multifabric GPFS Spectrum Scale layout”, Proc. Int. Conf. on High Performance Computing and Simulation, 1051-1052 (2019).

MONTE CARLO TRANSPORT CALCULATIONS SUPPORTING IRRADIATION EXPERIMENTS IN N_TOF FACILITY AT CERN

Patrizio Console Camprini[1*]

[1]*ENEA, Fusion and Technology for Nuclear Safety and Security Department, 40129, Bologna, Italy*

ABSTRACT. Neutron detectors are essential tools in many research fields, as nuclear, particle and astroparticle physics with applications in radiotherapy and radiation safety. Within the n_TOF experiment at CERN, neutron irradiation conditions are utilized also to develop and test innovative neutron detection techniques and instrumentations. In particular, neutron-based experimental techniques are related to the detection of charged particle or electromagnetic radiation which are originated along neutron-induced reactions. An effective description of fast neutrons is obtained often through the neutron-proton elastic scattering reaction. In fact, the ionization induced by the recoil protons in a hydrogenous material provides the basic information for the design of neutron detectors. In the framework of this study, a novel recoil-proton track imaging system in which the light deriving from a fast scintillation signal is used to perform a complete reconstruction in space and time of the event. In particular, the RIPTIDE (RecoIl Proton Track Imaging DEtector) detector consists in an innovative system which combines a plastic scintillator with imaging devices based on CMOS technology. The present study is composed by preliminary Monte Carlo simulations performed by means of Geant4 code in order to in principle evaluate the production of optical photons inside the irradiation volume and to estimate the capacity of the sensors to collect them onto the external surfaces.

1 The recoil proton track imaging RIPTIDE detector

Neutron detectors – both classified as slow or fast - are devices in which the detection efficiency depends on the probability of neutron interaction into the conversion layer and the escape probability of the reaction products. For this reason, a continuous effort is being spent by the international agencies such as the International Atomic Energy Agency (IAEA) and the cross-section evaluation working groups in order to establish a series of suitable cross-sections, referred to as neutron cross-section standards to be used as reference in neutron experiments. Though such converters are extensively used for environmental dosimetry, neutron-beam flux, energy measurements and beam profiling. They are not able to provide neutron tracking, i.e. complete momentum reconstruction of the detected neutrons.

When fast neutrons are involved, kinematical properties of two-particle reaction make neutron tracking possible. In this context, the neutron-proton (n-p) elastic scattering represents the simplest and promising interaction to be applied, as widely reported in the literature. Consequently, several state-of-the-art approaches have been recently proposed with the aim of tracking neutrons by using n-p single

and double interaction. This kind of detectors are referred to as Recoil Proton Track Imaging (RPTI) systems.

The basic tool for neutron momentum reconstruction in RPTI detectors is the two-body kinematics. In fact, in the n-p elastic scattering the neutron energy E_n is related to the proton recoil angle and energy (θ_p and E_p) by the classical formula $E_n = E_p / \cos^2(\theta_p)$. Proposed RPTI detectors in literature exploiting this relationship can face limitations in terms of detection efficiency, complexity, cost, and final implementation. The obtained result is strictly related to the density of the gaseous scintillator, magnifying proton ranges.

Current limitations of RPTI systems can be largely mitigated by the detection system here proposed: a RecoIl Proton Track Imaging Detector (RIPTIDE). The system is based on a detection concept joining, at the same time, a simple and scalable layout with a low-cost technical implementation.

With no doubt, the n-p elastic scattering reaction is the most used reaction in fast neutron detectors and neutron metrology. This is not surprising since the differential cross-section is considered as a standard up to 20 MeV and a primary reference up to 350 MeV. Clearly, the good knowledge of n-p elastic total and differential cross-sections are crucial ingredients for a reliable efficiency determination by Monte Carlo simulations and several publications can be found in the literature for its correct implementation (see for instance refs. [1, 2]) in Monte Carlo codes such as Geant4 [3, 4].

2 Preliminary Monte Carlo simulations for RIPTIDE detector

A detector sketch describing the RIPTIDE working principle is shown in figure 1. More in detail, the basic idea relies on recording a snapshot of the scintillation light produced by protons originated from n-p elastic (single or multiple) scattering in a plastic scintillator.
The three-dimensional proton-recoil track reconstruction is obtained by 2D projections on orthogonal planes. Therefore, the central plastic scintillator (active volume) is surrounded by three (or more) optical systems coupled either to CMOS or Micro Channels Plates (MCP) imaging devices.

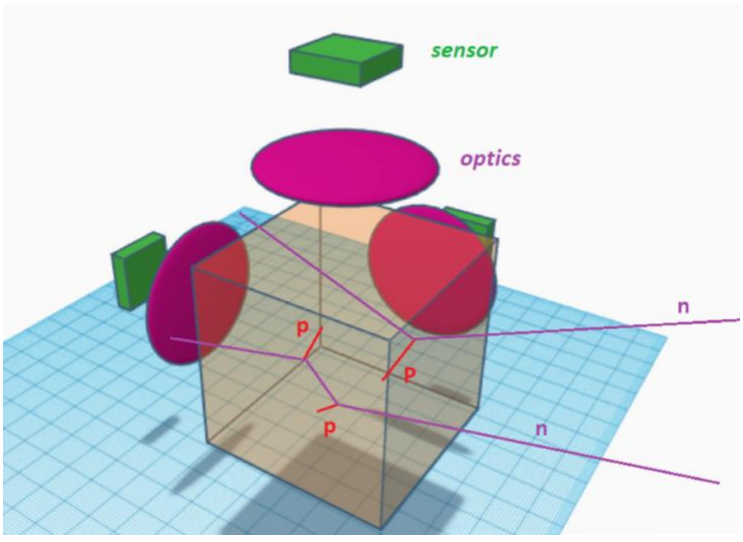

Figure 1. Working principle for the RIPTIDE neutron detector

From the geometrical point of view, the neutron momentum can be reconstructed in the 3D active volume of RIPTIDE in two cases:

• Single n-p scattering, by knowing the primary vertex of neutron
• Double or multiple n-p scattering in the detector active volume.

In summary, by stereoscopically imaging the recoil-proton tracks and correlating the spatial information with the time information, the proposed apparatus can provide neutron spectrometry capability and, at the same time, enable specific energy loss analysis along the track. Consequently, the proposed system makes it possible to retrieve the neutron direction and energy, without spoiling the intrinsic efficiency of the detection volume (plastic scintillator). In addition, particle discrimination can be obtained by spatial and topological event reconstruction, which is a crucial feature in neutron detection. Note that large efficiencies can be achieved by a full-scale detector, once the scalability of the here-proposed demonstrator will be proved.

Available or proposed fast-neutron detectors with imaging capabilities provide promising perspective in the field of nuclear and particle physics and related applications. However, proton-recoil track imaging is still far from being considered a well-established technique. To face this deficiency, a prototype is under design phase, to demonstrate the possibility to reconstruct with sufficient precision the tracks and the vertices of neutron interactions with the hydrogen contained in a plastic scintillator.

The technological challenge imposed by a suitable optical readout joins with the requirements to get high data transfer rate capability from the imaging devices and the associated electronics. At the present stage, detector design is ongoing in terms of efficiency and particle tracking by tuning and cross-checking Monte Carlo simulations.

Geant4 simulations have been prepared and detector model for simple cubic sensitive volume has been used to investigate the performance obtainable by the device. Particle tracking of neutron beam has been simulated through proton recoil and subsequent optical photon generation by means of the scintillation properties of the plastic material in the volume.

In summary, RIPTIDE aims at establishing a novel neutron detection technique towards a new class of detectors with an unprecedented efficiency and timing properties, together with track-reconstruction capabilities, if successful, this innovative approach can represent a cutting-edge technology for several scientific, medical, and industrial applications.

Acknowledgement

The author thanks the INFN (National Institute for Nuclear Physics) – Bologna Section – for the collaboration concerning n_TOF facility and all the information to prepare the calculations.
Simulations were performed through the CRESCO supercomputing facility since large HPC techniques and massive computing environment were necessary to achieve these calculations.

References

[1] N. Terranova et al., Monte Carlo simulations and n-p differential scattering data measured with proton recoil telescopes, EPJ Web Conf. 239 (2020) 01024

[2] A. Manna et al., Setup for the measurement of the 235 U(n, f) cross-section relative to n-p scattering up to 1 GeV, EPJ Web Conf. 239 (2020) 01008
[3] S. Agostinelli et al., Geant4 — a simulation toolkit, Nucl. Instrum. Meth. A 506 (2003) 250
[4] J. Allison et al., Recent developments in Geant4, Nucl. Instrum. Meth. A 835 (2016) 186

TOWARDS CFD-PBE SIMULATION OF AIRBORNE TRANSPORT OF MUCOSALIVARY FLUID

Valerio D'Alessandro[1*], Matteo Falone[1], Luca Giammichele[1] and Renato Ricci[1]

[1]*Università Politecnica delle Marche, Dipartimento di Ingegneria Industriale e Scienze Matematiche, Via Brecce Bianche 12, 60131, Ancona, Italy*

ABSTRACT. COVID–19 pandemic promoted a lot of research activities in relation to airborne diffusion of saliva micro-droplets which travel into atmospheric air through a thermo-fluid dynamic interaction with it. One of the main areas of lack concerns the modelling of mucosalivary fluid complex nature and its interaction with environment in respiratory activities. Specifically, this is a key element to predict small diameters dry nuclei formation. For this reason, in this work we discuss the impact of velocity boundary conditions at the mouth print as well as the effect of the correlations for mass transfer coefficient evaluation, adopting a multi–scale modelling approach which couples the Population Balance Equation with the particle–source–in–cell (PSI–Cell) method.

1 Introduction

SARS–CoV–2 virus, responsible of COVID–19 pandemic, still has a great impact on our daily life. The disease spread involves several infection mechanisms, however SARS–CoV–2 virus airborne transport through saliva droplets was recognized as the dominant one, [1].

Droplets carrying pathogens evolve in the environment as result of inertia, gravity, buoyancy, aerodynamic drag, and evaporation, [2]. This latter is the responsible of non–volatile dry nuclei formation because of the continuous droplets' mass reduction that produces droplet nuclei, [3].

Considering that the human saliva is a complex water solution also consisting of sodium chloride, solvent evaporation can lead to a condition of a supersaturated solution which, in turns, triggers nuclei crystallization and their growth, [4]. The described process produces solid dry particles often characterized by small diameters, that could remain airborne for a more significant period if compared with larger droplets, [5]. In this context, it is evident that a proper understanding of evaporation/crystallization process as well as a correct modeling of respiratory activities are needed for the evaluation of guidelines on social distancing, face mask wearing, and the implementation of new practices in daily social life.

For this reason, this work aims to evaluate the impact of velocity boundary conditions at the mouth print as well as the effect of the correlations for mass transfer coefficient evaluation on saliva droplets' dynamics during coughing, adopting a multi-scale computational model, relying on the well-established OpenFOAM library.

2 Governing Equations

The numerical computations rely on an Eulerian-Lagrangian approach, in which the particle-source-in-cell (PSI-Cell) method [6] is adopted to couple the coexisting phases. Moreover, NaCl crystallization kinetics is modeled introducing the Population Balance Equation (PBE) within the Lagrangian frame, at droplet level.

Eulerian phase was modeled using compressible Reynolds Averaged Navier-Stokes equations, where the system closure is provided by standard constitutive equations for Newtonian fluids, while the SST k-ω model is adopted as turbulence model. Finally, source terms in mass, momentum, energy, and chemical specie mass fraction equations ensure Lagrangian and Eulerian phases coupling, [7].

Lagrangian framework is used to describe saliva droplets that, in our approach, are grouped in parcels for sake of computational efficiency. The particles laden into the domain have initial diameters that follow the Rosin-Rammler distribution, calibrated as in [7]. Moreover, the considered diameter's range is such that pressure, virtual mass and Brownian forces can be neglected, [8], thus, the parcels experiences only gravity, buoyancy, and aerodynamic drag forces. The last contribution is evaluated adopting standard Putnam correlation for spheres, [9]. For each parcel trajectory, momentum, mass, and energy equations are solved. The convective heat transfer and mass transfer coefficients are evaluated starting from Nusselt (Nu) and Sherwood (Sh) numbers, that, in this work, are obtained using Ranz–Marshall [10] and Clift [11] approaches. The adopted correlations are summarized in Tab.1, where Re_d is the Reynolds number evaluated on the particle's diameter, while Pr and Sc represent Prandtl and Schmidt numbers, respectively.

Table 1: Correlations for Nusselt and Sherwood numbers.

	Nu	**Sh**
Ranz–Marshall	$2 + 0.6{Re_d}^{0.6} Pr^{\frac{1}{3}}$	$2 + 0.6{Re_d}^{0.6} Sc^{\frac{1}{3}}$
Clift	$(1 + Re \cdot Pr)^{\frac{1}{3}} \cdot max\left[1, {Re_d}^{0.77}\right]$	$(1 + Re \cdot Pr)^{\frac{1}{3}} \cdot max\left[1, {Re_d}^{0.77}\right]$

In this study we have considered mucosalivary fluid as solution of water and sodium chloride. Therefore, PBE is solved at parcel level to consider NaCl crystallization kinetics. Furthermore, a coupling strategy between PSI–Cell and PBE allows to model micro-scale particles behaviour induced by meso-scale thermo-fluid dynamic phenomena.
Starting from semi-discrete PBE proposed by Woo el al., [12], and considering the parcel-averaged crystal mass, $N_{w,j}$, its evolution in time can be evaluated as follow:

$$\frac{dN_{w,j}}{dt} = -\frac{\rho_c k_v}{\Delta r}\left(r^4_{j+1/2} - r^4_{j-1/2}\right) max\,(sign\,\Delta c, 0) \times \left[G_{j+1/2}\left(f_j + \frac{\Delta r}{2}(f_r)_j\right) - G_{j-1/2}\left(f_{j-1} + \frac{\Delta r}{2}(f_r)_{j-1}\right)\right] + B|_{j=0} \quad (1)$$

where G_j is the growth rate, r_j is the particle internal coordinate, r_{j0} is the particle internal coordinate for a crystal nucleus, δ is the Dirac function, and B is the nucleation rate, $\Delta c = c - c^*$ is supersaturation, while c and c* are the NaCl concentration and its solubility in pure water. G_j and B values in eq. (1) are obtained from literature experimental data [13, 14].
Eq. (1), can be also used to calculate the total mass, m_{cr}, and the radius, r_N, of the droplets' dry nucleus:

$$m_{cr} = \pi \frac{D_p^3}{6} \sum_j N_{w,j}\,, \qquad r_N = \frac{\sum_j N_{w,j} r_j^4}{\sum_j N_{w,j}\, r_j^3} \quad (2)$$

3 Numerical approximation

The unstructured, cell-centered finite volume approach available within OpenFOAM library was adopted to achieve the carrier phase governing equations solution.
A linear-upwind scheme was used for convective terms approximation, while standard central schemes for diffusive contributions are adopted. Furthermore, the Pressure-Implicit with Splitting Operators (PISO) procedure was employed for pressure–velocity coupling. Time integration technique relies on an implicit, three level, second-order scheme.
Lagrangian phase mass and momentum equations were solved using a backward Euler scheme for time-integration, whereas energy equation was solved analytically. An explicit Strong Stability Preserving Runge-Kutta (SSPRK) having 9 stages and 5-th order of accuracy was adopted for PBE time-integration to avoid blow-up of the computations.

3.1 Initial and boundary conditions

In the present work, a 3D computational domain having length L = 4 m, a width W = 1 m, and a height H = 3 was considered. It represents an open-air volume starting from the mouth print of a standing

coughing person, [7]. The human cough was simulated by means of two different strategies of fluid and parcels injection at the mouth print boundary as showed in Fig. 1. In the first one, a stepped velocity equal to 8.5 m/s, was assumed to mimic the respiratory event over 0.12 s basing on the measurements carried by Scharfman et al. [15]. Secondly, following Cortellessa et al. [16], a sinusoidal approximation of breathing combined with a velocity peak is adopted to simulate a real–life condition. In particular, the sinusoidal velocity profile has amplitude of 1 m/s and a frequency of 0.2 Hz, while the coughing effect is modeled by means of a peak in velocity of 5 m/s. The initial total mass of saliva droplets laden into the domain during the cough event is 7.7 mg and a completely diluted NaCl/water solution consisting in 1% of NaCl was adopted for the saliva chemical composition. An environmental initial temperature of 20° C and a relative humidity fixed at 50% were considered. The ground is set at 25° C, while the air and droplets ejected by coughing are at 34° C.

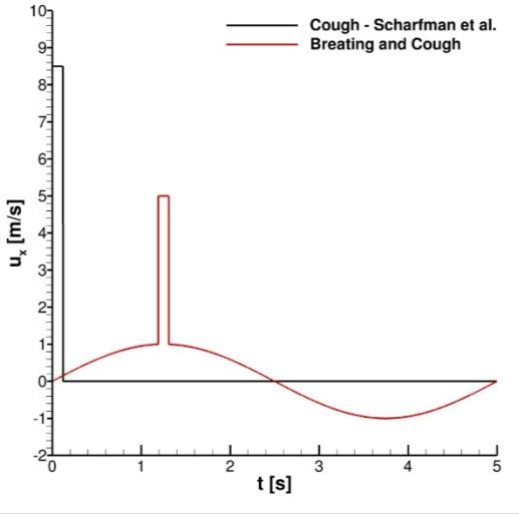

Fig. 1: Velocity adopted at the mouth print.

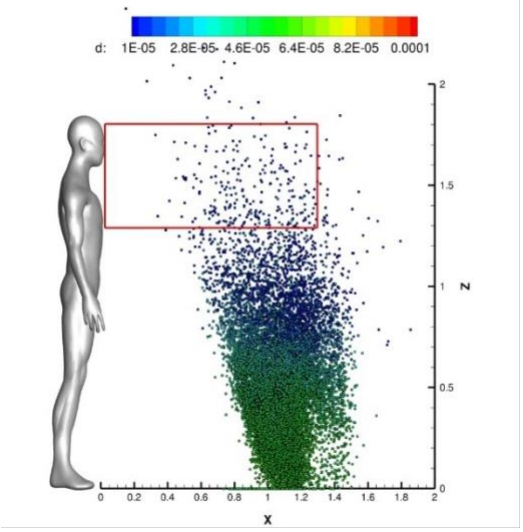

Fig. 2: Cloud representation at t = 10 s.

4 Results

In this section the numerical results referred to the saliva droplets produced during coughing are presented. In particular, the impact of the different velocity profiles at mouth print boundary as well as the overall effect of the different correlations considered for particles' Nu and Sh numbers evaluation are discussed. Some cloud characteristics are computed to investigate its diffusion, i.e., (i) the cloud center of mass, $\boldsymbol{G}$, and (ii) particles weighted average diameter, D_{10} , defined as:

$$\boldsymbol{G} = (x_G, y_G, z_G,) = \frac{\sum_{i=1}^{\widehat{N_p}(\Omega_0)} m_{P,i}\boldsymbol{x}_{P,i}}{\sum_{i=1}^{\widehat{N_p}(\Omega_0)} m_{P,i}}, \qquad D_{10} = \frac{\sum_{i=1}^{\widehat{N_p}(\Omega_o)} N_{P,i}D_{P,i}}{\sum_{i=1}^{\widehat{N_p}(\Omega_0)} N_{P,i}} \tag{3}$$

where $N_p(\Omega_0)$ is the number of parcels laden in the overall domain, Ω_0, in a given time instant. It is worth noting that x-axis is associated to stream-wise direction, y-axis represent the transverse direction, while z is the vertical one.

A representation of the computed cloud for a cough ejection modeled with the stepped velocity profile is reported in Fig. 2. It is very easy to note that also after 10 s from the particles ejection, a significant number of droplets still persists in a risky zone for a possible receiver standing in front of the emitter. This is due to the combined effects of evaporation/crystallization processes that leads to solid dry nuclei formation that can have suspension time of several minutes. This evidence corroborates the importance of accurately studying the cough features in terms of initial velocity and evaporation mechanism.

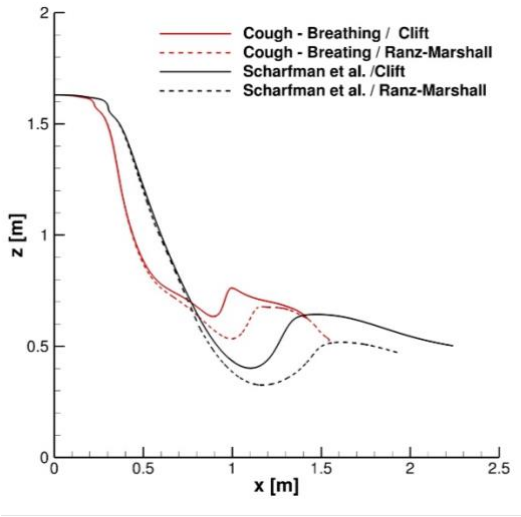

Fig. 3: Saliva cloud center of mass trajectory.

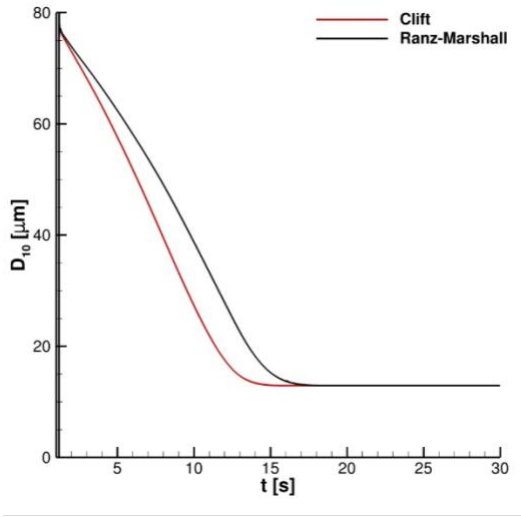

Fig. 4: D_{10} time–history.

Fig. 3 puts in evidence that both velocity boundary condition adopted at the mouth print and Nu/Sh approaches affect the saliva cloud's center of mass. In particular, Clift correlations produce an higher average center of mass height from the ground due to reduced evaporation rate of Clift correlations if compared with Ranz–Marshall ones. On the other hand, it is worth noting that that stepped velocity BC produces an average z_G lesser than coughing/breathing configuration because of the particles' momentum laden into the domain. Indeed, in the stepped approach, particles have a velocity equal to 8.5 m/s, while in the other configuration particles' velocity during cough is 5 m/s. Thus, it is straightforward that from transmission risk point of view, coughing/breathing approach coupled with Clift correlations is more conservative and relevant.

Finally, Fig. 4 provides the time history of the D_{10} calculated using eq. 3. Both Clift and Ranz-Marshall correlations lead to the same terminal diameter that is locked because of the formation of dry particles nuclei. From the evaporation process point of view, Clift and Ranz-Marshall approaches differ only for the time required to reach terminal diameter because they impose different evaporation rates. In this context, we want to empathize that the ratio between terminal diameter and the initial one, D/D_0, is 0.161 which is in a good agreement with literature data provided by Lieber et. al [17].

5 Conclusions

In this paper, we investigate: (i) the impact of velocity boundary conditions at the mouth print; (ii) the effect of the correlations for mass transfer coefficient evaluation. In particular we focused on saliva droplets' dynamics during coughing. An Eulerian–Lagrangian model is adopted to study the spreading of a saliva droplets' cloud deriving from coughing. Furthermore, a multi-scale mathematical model which couples PSI-Cell method and PBE solution within each Lagrangian particle is employed to predict NaCl crystallization kinetics effect.

It was showed that Clift correlations for Nusselt and Sherwood numbers, results in an higher average center of mass height from the ground due to reduced evaporation rate if compared with Ranz–Marshall approach. Moreover, we have also noted that velocity time–histories applied at inlet boundary strongly affect saliva cloud evolution. In particular, the adoption of a sinusoidal approximation of breathing combined with a velocity peak produces a saliva droplets cloud having a z_G higher than the one deriving from a stepped velocity profile. The obtained results suggest that from transmission risk point of view, coughing/breathing approach coupled with Clift correlations is more relevant.

Finally, the presented approach can be considered sufficiently reliable since numerical data put in evidence a satisfactory agreement with experimental literature data produced on real human saliva.

Acknowledgments

The authors want to acknowledge “Associazione Nazionale Big Data” that awarded this research work within COVID-19–Fast access to the HPC supercomputing facilities program. We acknowledge ENEA for awarding us access to CRESCO6 based at Portici.

References

[1] R. Zhang, Y. Li, A. L. Zhang, Y. Wang, and M.J. Molina. Identifying airborne transmission as the dominant route for the spread of COVID-19. Proceedings of the National Academy of Sciences of the United States of America 2020, 117, 14857 – 14863.
[2] X. Xie, Y. Li, A.T.Y. Chwang, P.L. Ho, and W.H. Seto. How far droplets can move in indoor environments - revisiting the Wells evaporation-falling curve. Indoor Air 2007, 17, 211– 225.
[3] L. Liu, J. Wei, Y. Li, and A. Ooi. Evaporation and dispersion of respiratory droplets from coughing. Indoor Air 2017, 27, 179–190.
[4] M.E. Rosti, S. Olivieri, M. Cavaiola, A. Seminara, and A. Mazzino. Fluid dynamics of COVID-19 airborne infection suggests urgent data for a scientific design of social distancing. Sci Rep–UK 2020, 10, 22426.
[5] L. Bourouiba. Turbulent Gas Clouds and Respiratory Pathogen Emissions: Potential Implications for Reducing Transmission of COVID-19. JAMA 2020, 323, 1837 – 1838.
[6] C. T. Crowe, M. P. Sharma, and D. E. Stock. The particle-source-in cell (PSI-Cell) model for gas-droplet flows. J. Fluids Eng. 99, 325–332, (1977).
[7] V. D'Alessandro, M. Falone, L. Giammichele, and R. Ricci. Eulerian–Lagrangian modeling of cough droplets irradiated by ultraviolet–C light in relation to SARS-CoV-2 transmission. Phys. Fluids 33, 031905, (2021).
[8] G. Busco, S. Yang, J. Seo, and Y.A. Hassan. Sneezing and asymptomatic virus transmission. Phys. Fluids 2020, 32, 073309. 342
[9] A. Putnam. Integratable form of droplet drag coefficient. ARS J. 1961, 31, 1467 – 1468.
[10] W.E. Ranz, ad W.R. Marshall. Evaporation from drops. Chem. Eng. Prog. 1952, 48, 141 – 146.
[11] R. Clift, J.R. Grace, and M.E. Weber. Bubbles, Drops, and Particles; Dover, 2005.
[12] X.Y. Woo, R.B.H. Tan, P.S. Chow, and R.D. Braatz. Simulation of Mixing Effects in Antisolvent Crystallization Using a Coupled CFD-PDF-PBE Approach. Cryst Growth Des 2006, 6, 1291–1303.
[13] J. Desarnaud, H. Derluyn, J. Carmeliet, D. Bonn, and N. Shahidzadeh. Metastability Limit for the Nucleation of NaCl Crystals in Confinement. J. Phys. Chem. Lett. 2014, 5, 890–895.
[14] A. Naillon, P. Joseph, and M. Prat. Sodium chloride precipitation reaction coefficient from crystallization experiment in a microfluidic device. J Crys Growth 2017, 463, 201–210.
[15] B.E. Scharfman, A.H. Techet, J.W.M. Bush, and L. Bourouiba. Visualization of sneeze ejecta: steps of fluid fragmentation leading to respiratory droplets. Exp Fluids 2016, 57, 24.
[16] G. Cortellessa, L. Stabile, F. Arpino, D.E. Faleiros, W. van den Bos, L. Morawska, G. Buonanno. Close proximity risk assessment for SARS-CoV-2 infection. Sci. Total Environ. 2021, 794, 148749.
[17] C. Lieber, S. Melekidis, R. Koch, and H.J. Bauer. Insights into the evaporation characteristics of saliva droplets and aerosols: Levitation experiments and numerical modeling. J. Aerosol Sci. 2021, 154, 105760.

PRELIMINARY CFD INVESTIGATION OF A MONOLITHIC SMR REACTOR CORE

Roberto Da Vià[10*], Francesco Lodi[1], Giacomo Grasso[1]

[1]*ENEA FSN-SICNUC-PSSN, C.R. "E. Clementel", via Martiri di monte sole 4, 40129 Bologna, Italy*

ABSTRACT. A preliminary hydraulic study by Computational Fluid Dynamics (CFD) has been performed to investigate the mass flow rate distribution among the subchannels of a small modular Lead Fast Reactor monolithic core. Two different core geometries have been studied, with the intent of decreasing the bypass mass flow rate occurring on the outer zone of the core. A fork of the open-source CFD code OpenFOAM, developed at ENEA within the PSSN laboratory, has been used to perform the simulations on ENEA CRESCO6 High Performing Computing system.

1 Introduction

Liquid-metal-cooled fast reactors represent one of the most promising technologies, in the field of nuclear power plants, to fulfil the requirements of energy production in terms of sustainability, safety and with a reduced impact on the environment [1]. In this context, many reactor configurations are being studied, with produced electrical power ranging from few MW up to GW [2]. The lower segment of power generation (up to 300 MW) is the target area of Small Modular Reactors [3]. These represent a new emerging generation of reactors with compactness and modularity being key aspects of their design, as they would help the standardization of components, with a possible reduced time and effort for licensing, and the serialization of the production, with a sensible decrease in the cost of fabrication [4].

In the past, ENEA collaborated with Hydromine Nuclear Energy S.à.r.l. in designing innovative Transportable and Long-lived Lead Fast Reactors (LFRs), labelled as LFR-TL-X, with X being the target produced electrical power in MW. For LFRs, fuel pins are usually arranged in fuel assemblies enclosed in hexagonal wrappers, and the whole core is made of several fuel assemblies. To enhance the compactness of the core, for the LFR-TL-X the fuel pins are arranged, with a triangular lattice, in a monolithic cylindric bundle of pins [3]. With this strategy the reactor core consists of a unique fuel assembly with thousands of fuel pins – a "monolith" – that never needs to be replaced for the entire duration of the plant life, in the so-called battery approach. As the coolant mass flow rate (hereinafter labelled as mfr) is not distributed among fuel assemblies, it is important to keep the mfr distribution as uniform as possible among the sub channels, to guarantee a proper cooling of the fuel pins. As for the design process of all nuclear reactors, a reliable characterization of the thermal hydraulics of the core is essential to verify that all the constraints, which are set by safety margins, are verified.

In the present study a preliminary hydraulic investigation of a simplified model of the LFR-TL-5 has been performed by means of CFD simulations using OpenFOAM, targeting the mass flow rate distribution among the different subchannels of the monolithic reactor core.

[10] * Corresponding author. E-mail: roberto.davia@enea.it

2 The software

Thermal hydraulic studies, with reliable predictions of fluid flow patterns, pressure losses and thermal fields, are a fundamental step in the design process of a nuclear reactor core. Liquid metals are an attractive type of coolant fluids and represent a challenging task for the heat transfer modelling, due to their low Prandtl number values (order of magnitude of 0.01, namely high thermal diffusion and low kinematic viscosity values). Due to this peculiarity, models for turbulent heat transfer that are normally and successfully used (hence that are present in every opensource and commercial CFD code) in simulations of air and water cannot be used in simulations of liquid metals as they would overpredict the heat transfer.

Within the PSSN laboratory of the FSN-SICNUC ENEA division, a fork of the OpenFOAM v9 [5] opensource CFD code has been developed to extend the selection of dynamical and thermal turbulence models, as well as other useful features. At the present status the major implementations involve the four parameters turbulence model [6], the algebraic heat flux model [7] and an innovative application for boundary layer addition through a compression and extrusion operations applied to existing meshes, so to provide a 100% coverage of boundary layer addition on selected boundaries. The code is hosted on a private gitlab project and its installation is handled using SPACK [8], so to facilitate the portability on different platforms.

3 The geometrical and computational model

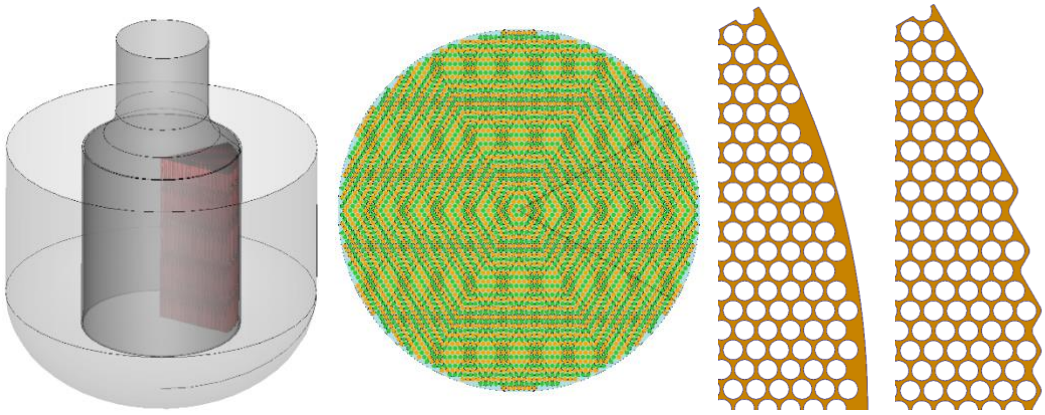

Fig. 1: From left to right: a sketch of the LFR-TL-5 model, with fuel pins of the 60° degrees sector highlighted in red; the entire fuel pin distribution in the monolithic core, with the highlighted boundary of the periodic 60° degrees sector; the lateral subchannels as realized by the original inner vessel profile and by the new introduced barrel component.

The simplified geometrical model of LFR-TL-5, considered for the current analysis, is shown on the left of Figure 1. The outer part of the domain represents a downcomer channel of the liquid lead, while the inner part represents the monolithic core. In the simplified model only the bare fuel pins are considered in the monolithic core, without any spacer means. Under this assumption, the core can be divided into 6 sectors having a rotation symmetry with respect of the vertical axis passing through the central fuel pin. The fuel pins of a single sector are highlighted in red in the left frame of Fig.1, together with the whole fuel pin lattice, with approximately 4400 fuel pins and with black lines showing the boundary of a single sector. Additionally, a second geometry has been considered and simulated, with the main and only difference being the adoption of a barrel structure in between the outer pin layer and the inner vessel. The barrel profile is designed to be tangent to groups of adjacent fuel pins, with a pin-to-barrel normal distance equal to the distance among adjacent pins. The profiles of the original inner vessel and of the barrel component are shown on the right of Figure 1. The role of the barrel is to limit the bypass mass flow rate in the outer subchannels.

The CAD models of the geometry were built using the SALOME – GEOM module. Polyhedral meshes of one 60° degrees sector of the geometry were computed starting from tetrahedral meshes generated with the Netgen algorithm from the SALOME – SMESH module and subsequently converted to polyhedral elements with the polyDualMesh application provided by OpenFOAM. The generated meshes consists of approximately 11 million cells.

4 Results

Steady state isothermal simulations have been performed for the two geometries presented above, using the standard k-w SST turbulence model implemented in OpenFOAM. At the inlet section (at the beginning of the downcomer channel) the mfr is set (283.7 kg/s) together with turbulent quantities representative of the Reynolds number of the fluid flow at that section (3.16E5). On the vertical surfaces that represent the boundary of the 60° degrees sector, cyclic boundary conditions are set, while no slip boundary conditions are imposed on all the wall surfaces. On the outlet section a simple zeroGradient condition is set.

Table 1: Comparison of bypass mass flow rate percentage and average inner subchannels (sch) mass flow rate between the original and the barrel cases

Plane ID	-	1	2	3	4	5	6
Axial location	[m]	0.51	0.71	0.91	1.11	1.31	1.51
Orig, bypass mfr %	-	4.3	8.9	10.3	11.3	12.1	12.7
Barrel, bypass mfr %	-	3.0	3.9	4.2	4.4	4.5	4.6
Orig, avg inner sch mfr	[kg/s]	0.170	0.162	0.159	0.158	0.156	0.155
Barrel, avg inner sch mfr	[kg/s]	0.178	0.176	0.175	0.175	0.175	0.175

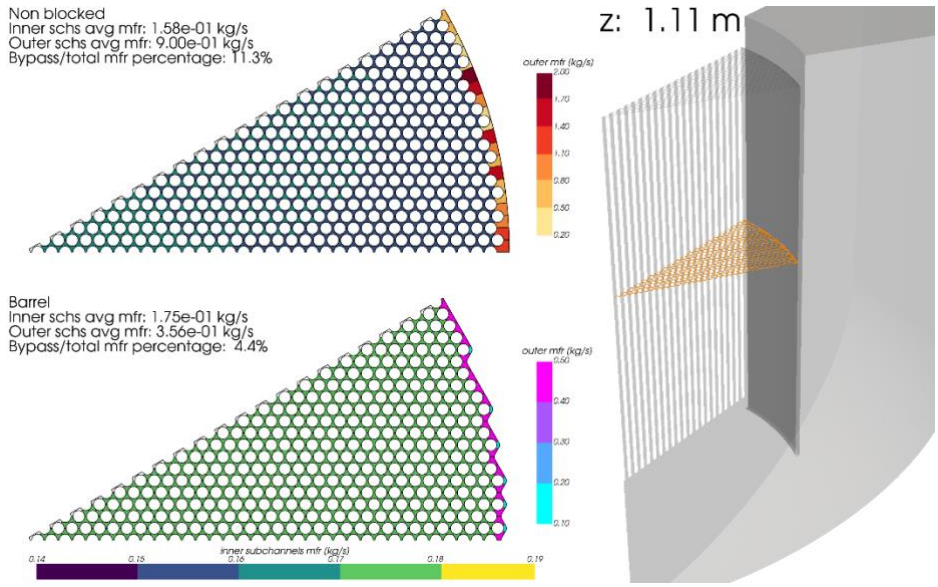

Fig. 2: Comparison of obtained results between the original geometry (inner vessel) and the core with the barrel in between the outer layer of fuel pins and the inner vessel. The subchannel mfr distribution is plotted with different scales for inner and outer subchannels.

The fuel pin length is of 1 meter. The average coolant mfr of inner subchannels and the bypass mfr percentage, calculated with respect to the total mfr, have been monitored on 6 cross section planes, starting from the fuel pin bottom section and spanning every 20 cm. The results are reported in Table 1. The bypass mfr is computed as the difference between the total mfr flowing in the outer channels (between the fuel pins and the inner vessel) and the theoretical mfr required to properly cool those subchannels (i.e., to ensure the nominal temperature rise), in the case of uniform heat generation among all the fuel pins. Starting from the first monitoring plane, the bypass mfr grows with the axial direction, with a migration of coolant mfr from the inner channels to the outer zone. This effect is highly

accentuated in the original case, while, with the adoption of the barrel, the bypass mfr reaches a maximum value of 4.6%, instead of 12.7%. This difference in the bypass mfr is reflected in the average coolant mfr values of the inner subchannels. For the original case, starting from an average mfr value of 0.170 kg/s, at the outlet section the average mfr value is equal to 0.155 kg/s, with a decrease of 8.8%. With the adoption of the barrel, the mass flow rate changes from 0.178 kg/s to 0.175 kg/s, with a decrease of 1.7% from inlet to outlet section. A graphical representation of the data provided in Table 1, for the axial plane at z=1.11 m, is shown in Figure 2.

5 Conclusions

A preliminary CFD analysis of a simplified model of a monolithic lead-cooled SMR core has been performed using a custom fork of OpenFOAM on ENEA CRESCO6 HPC system. The goal of the simulation has been to evaluate the mass flow rate distribution among the core subchannels, investigating the amount of bypass flow occurring on the outer zone of the core, between the outer fuel pins and the cylindrical inner vessel. The results showed that with the adoption of a simple barrel geometry, in between the outer fuel pins and the inner vessel, it is possible to contain the amount of bypass mass flow rate, allowing thus to keep a more uniform coolant mass flow rate in the inner subchannels.

References

[1] OECD/NEA. Technology Roadmap Update for Gen. IV Nuclear Energy Systems (2014).
[2] A. Alemberti et al. Lead-cooled Fast Reactor (LFR) Risk and Safety Assessment White Paper, Revision 8 April 2014
[3] IAEA, Advances in small modular reactor technology developments (2018), International Atomic Energy Agency, A Supplement to: IAEA Advanced Reactors Information System (ARIS) (2018)
[4] Esam MA. Hussein, Emerging small modular nuclear power reactors: a critical review**,** Phys Open, 5 (2020), Article 100038
[5] Official OpenFOAM v9 github repository: https://github.com/OpenFOAM/OpenFOAM-9
[6] R. Da Vià and S. Manservisi, "Numerical simulation of forced and mixed convection turbulent liquid sodium flow over a vertical backward facing step with a four parameter turbulence model," International Journal of Heat and Mass Transfer, vol. 135, pp. 591–603, 2019.
[7] A. Shams et al., "Assessment and calibration of
an algebraic turbulent heat flux model for low-prandtl fluids," International Journal of Heat and Mass Transfer, vol. 79, pp. 589–601, 2014.
[8] Todd Gamblin et al., The Spack Package Manager: Bringing order to HPC software chaos, Supercomputing 2015, Austin, Texas

HETEROGENOUS DYNAMIC OF MOLECULAR ROTORS IN PERIODIC MESOPOROUSE ORGANOSILICA

Antonio De Nicola[1*], Giuseppe Milano[2], Angiolina Comotti[3] and Piero Sozzani[3]

[1]*Scuola Superiore Meridionale, Largo San Marcellino 10, 80138 Napoli, Italy*
[2]*Department of Chemical, Materials and Production Engineering, University of Naples Federico II, Piazzale Tecchio 80, 80125 Naploli, Italy*
[3]*Department of Materials Science, University of Milano - Bicocca, Via R. Cozzi 55, Milano, Italy*

ABSTRACT. Porous organosilicas, comprising p-phenylene rotators pivoted onto a siloxane scaffold, were modelled using molecular dynamics (MD) simulations. The motions observed in the MD simulations, long run on microsecond scale, support a multiple-site model for rotor reorientations. Computed motional frequencies revealed a complex rotatory mechanism composed of an ultra-fast oscillation motion (about 30°) and a slow and fast 180° flip reorientation. Adopting a multiple-site model provides a more accurate simulation of the 2H-NMR spectra and a rationalization of their temperature dependence.

1 Introduction

The fabrication of materials containing rotors which are arranged in ordered 3D array gained increased interest since rotary motion is a key future in both, biological1 and artificial applications. The crystalline periodic mesoporous organosilica (PMOs) have two valuable features combined in a single material, ultra-fast molecular rotors and a robust porous 3D framework. The presence of rotors, responsive to chemical stimuli, joint with the low density and high surface area makes PMOs an ideal candidate for the fabrication of new material for applications in several areas, including: gas storage, selective adsorption, confined polymerization, molecular rotors, catalysis, water adsorption and desalination. The first successful synthesis of bridge-bonded species $(RO)_3Si\text{-}R\text{-}Si(OR)_3$ was reported, independently, by Inagaki [1] and Asefa[2] groups in 1999. The most diffuse and common synthetic strategy to produce PMOs materials is based on the so called "sol-gel" process.[3] A variety of phisico-chemical properties such as accessible free volume or hydrophobicity can be controlled through chemical modification of R groups.

The periodic 3D structure of PMOs, obtained with sol-gel process, exhibit simultaneous molecular and mesoscale orders. The PMOs show also the presence of regular pores and nanochannels. In particular, the structure of PMOs consists of a siloxane framework characterized by the presence of organic parts connecting inorganic layers trough Si-C bonds. In this contest, the periodic structure of p-phenylensilica (PPS) is arranged in a hexagonal array, owns the adequate framework architecture to allow to organic molecules to behave as molecular rotors. More in detail, ordered arrays of PPS consist of two adjacent siloxane layers bridged by p-phenylene units, while, two adjacent silicon atoms are connected with an Si-O-Si bond (see Figure 1b-c).

The aim of the work is to understand and clarify the rotation motion in PPSs materials, combining the computational Molecular Dynamics (MD) and experimental 2H-NMR techniques.

2 Atomistic Model and MD Method

The MD technique was used, by using atomistic model, to investigate the dynamic of the rotation of p-phenylen units. The system model used in MD simulations consists of a periodic p-phenylensilica structure miming a wall of PPS framework. In particular, the simulated structure is made of 10 siloxane layers each of them containing 11 silicon atoms arranged in two rows of 6 and 5 Si atoms and connected through Si-O-Si bonds. Two consecutive layers are bridged by p-phenylene units (Figure 1b). In total, the simulated structure counts for 110 p-phenylene units, each of them marked according the position assumed in a layer.

We adopt the atomistic model, based on OPLS-AA force-field,[4] optimized and validated to reproduce the periodicity of PPS meso structure.[6] Moreover, in the model we used the energy barrier of the torsional angle , involved in the rotation of p-phenylene units, is optimized by DFT calculation performed on structures representative of PPS (angle definition in Figure 1d). Five independent MD simulations at 5 different temperatures, from 270 to 500 K, were performed. All the simulations were done in the NVT ensemble with a time step of 2 fs by using GROMACS package 4.5.4. The temperature was controlled by Berendsen thermostat with a coupling time τ_T of 10 fs. The energy of all the initial configurations was minimized by using the steep-descent algorithm (500 steps). In the production runs, after energy minimization, all bonds were constrained by using LINCS algorithm.

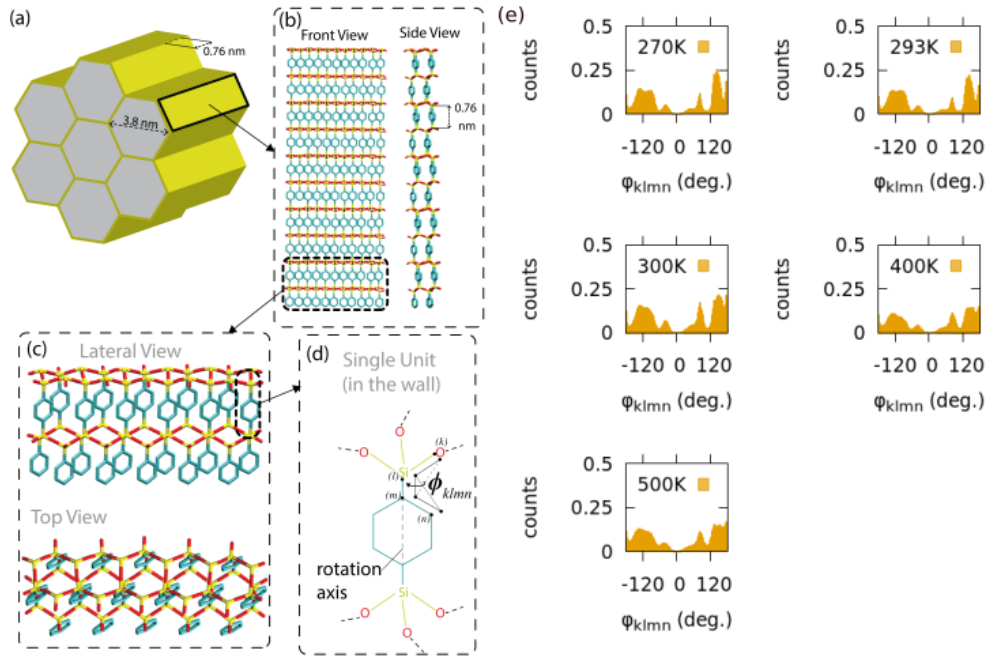

Figure 1. (a) Schematic representation of the hexagonal array of the mesoporous p-phenylensilica. The nanochannels diameter of 3.8 nm and the characteristic layer spacing of 0.76 nm are reported in the scheme. (b) Font and lateral view of the atomistic model representing the periodic section of a wall of PPS. (c) Magnification of lateral and top view of two siloxane rows constituting the periodic wall is reported. (d) Chemical structure of a single p-phenylene unit. The rotation axis and the dihedral angle ϕ are both indicated in figure. Silicon atoms are reported in yellow, while, oxygen and carbons in red and green, respectively. Hydrogen atoms are not explicitly reported for clarity. (e) Dihedral angle ϕ distributions calculated from MD simulations at different temperatures.

3 Results

Based on the mechanism proposed in the previous works of Comotti et al.,[6] the p-phenylene rings reorientation has been investigated by analyzing the MD trajectories a different temperature ranging from 270 to 500 K. The distributions of the dihedral angle (see Figure 1d) defining the p-phenylene ring orientation are reported in Figure 1e. In the limit of simulation time, the calculated dihedral distributions are not symmetric. The observed behaviours indicate a nonhomogeneous sampling of angle space for each one of the110 p-phenylene. Moreover, at higher temperatures broader peaks and more homogeneous distributions are found. The qualitative and qualitative differences in the different motions of p-phenylene rings can be examined by looking at behaviours of single rings. We found three qualitative different motions of p-phenylene rings which can be categorized as: i) rings without 180º flipping motion which only fluctuate (librations with and amplitude of ± 30º) around at certain ϕ_{klmn} angle. ii) rare flipping events. These rings have many fluctuations around a certain value of ϕ_{klmn}, and, less frequently, the 180º flipping rotations take place. iii) freely rotating rings. For these rings the fluctuation around a certain value of ϕ_{klmn} is the most probable event, but, a wider range of dihedral angle space is explored. Analyzing the occurrence frequency of ring fluctuation, at different five temperatures, we found that librations of of ± 15-30º of amplitude are always very fast at all investigated temperatures occurring on timescale lower or equal to one nanosecond. In particular, in the slower cases (at 270-293 K) the libration times are distributed between 200 and 600 ps, while at higher temperatures (300-500 K) the times range from 100 and 300 ps, see Figure 2A. These results are in agreement with a regime of fast librations of the p-phenylene rings having an amplitude of ± 15-30º. Instead, the dynamic behaviour of the180º flip motion is qualitatively different. We can distinguish two motions, One in which the 180º reorientation is fast (timescale ≈ 0.5 μs), and a second one with slower dynamic occurring on timescale > 1 μs (see Figure 2B). Variable temperature 2H NMR spectra allowed to collect information about C-Si bonds reorientation within the frequency range $10^8 – 10^3$ Hz and detect the angles explored during their angular displacement. Thus, NMR spectroscopy is a method of choice to provide experiments sensitive to dynamics comparable to MD modelling results. In addition to the spectra recorded below room temperature down to 200 K, a new series of spectra was performed at higher temperature, up to 450 K. The dramatic spectral change in the low-temperature range could be simulated by appropriate p-phenylene ring rotation frequencies, with 180° flip rotation as the fundamental phenomenon. However, the more complex mechanisms depicted by MD modelling must be taken into account to guide the NMR spectra simulations. Especially at high temperatures fast and large oscillations (>10^8 Hz) oscillations are apparent in the spectra, which showed a peculiar profile with an overall restricted width, as compared to a plain fast 180°-flip reorientation. Such further restriction was accurately simulated by the exploration of angles from ±15° to ± 30º by increasing temperature. Spectral shoulder sliming and singularities were accurately reproduced by a fast 4-site model combining such angles with a 0° and 180° average positions, in agreement with the proposed MD model. Additionally, the spectra revealed a persistent 20% slow motion (10^5 Hz) even at 450 K: a clear indication of the simultaneous presence of slow and fast ring reorientations, as observed in molecular dynamics.

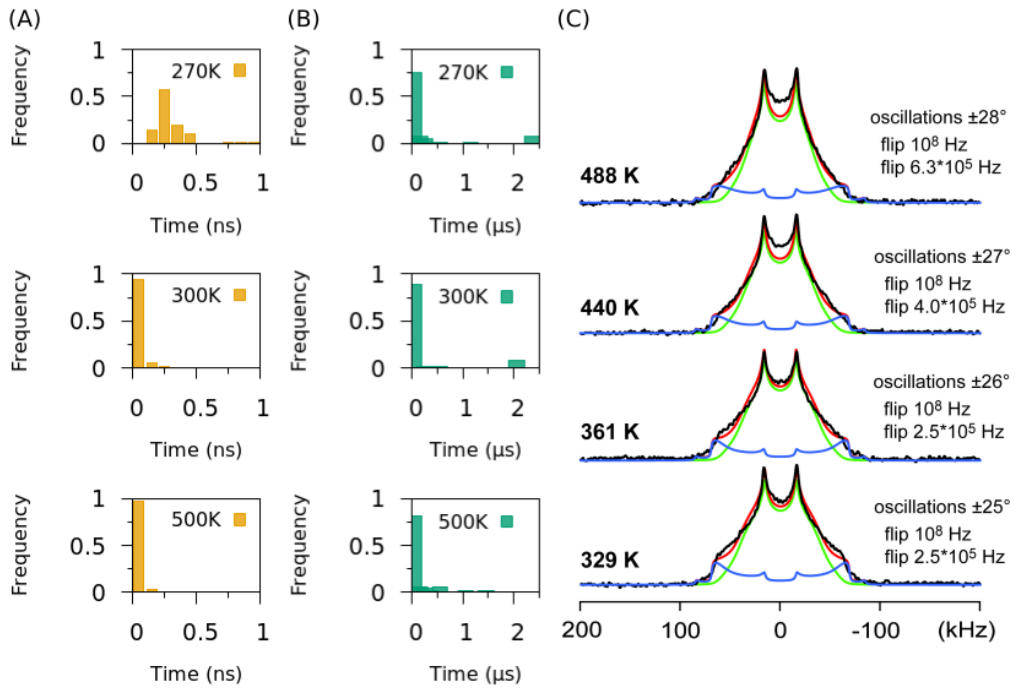

Figure 2. (A) Relative occurrence frequency of ring fluctuation ± 30º calculated in a temperature range from 270 to 500 K. (B) Relative occurrence frequency of ring flipping 180º motion calculated in a temperature range from 270 K to 500 K. (C) Simulations of 2H NMR spectra of perdeutero-PSS at distinct temperatures. The fast component (k=108 Hz) is coupled with increasing oscillations (from ±25° to ± 30°) on increasing temperature (green line). The slow two site 180° flip reorientation (k=2.5 *105 Hz) and the total simulated spectra are highlighted in blue and red, respectively.

References

[1] Inagaki, S.; Guan, S.; Fukushima, Y.; Ohsuna, T.; Terasaki, O. Novel Mesoporous Materials with a Uniform Distribution of Organic Groups and Inorganic Oxide in Their Frameworks. J. Am. Chem. Soc. **1999**, 121 (41), 9611–9614.

[2] Asefa, T.; MacLachlan, M. J.; Coombs, N.; Ozin, G. A. Periodic Mesoporous Organosilicas with Organic Groups inside the Channel Walls. Nature **1999**, 402 (6764), 867–871.

[3] Teng, Z.; Li, W.; Tang, Y.; Elzatahry, A.; Lu, G.; Zhao, D. Mesoporous Organosilica Hollow Nanoparticles: Synthesis and Applications. Adv. Mater. **2019**, 31 (38), 1–24.

[4] Jorgensen, W. L.; Mcdonald, N. A. Development of an All-Atom Force Field for Heterocycles. Properties of Liquid Pyridine and Diazenes'; **1998**; Vol. 424

[5] De Nicola, A.; Correa, A.; Comotti, A.; Sozzani, P.; Milano, G. Atomistic Model of Realistic Crystalline Mesoporous Organosilica Materials Including Nanochannels. J. Phys. Chem. C **2018**, 122 (31), 17825–17835.

[6] Comotti, A.; Bracco, S.; Valsesia, P.; Beretta, M.; Sozzani, P. Fast Molecular Rotor Dynamics Modulated by Guest Inclusion in a Highly Organized Nanoporous Organosilica. Angew. Chemie - Int. Ed. **2010**, 49 (10), 1760–1764.

POLYMER PHYSICS AND COMPUTATIONAL METHODS ALLOW TO INVESTIGATE THE PRINCIPLES OF 3D GENOME ORGANIZATION

Francesca Vercellone[1], Alex Abraham[1], Mattia Conte[2], Simona Bianco[1], Andrea Maria Chiariello[1] and Andrea Esposito[1*]

[1]*Dipartimento di Fisica, Università di Napoli Federico II, and INFN Napoli, Complesso Universitario di Monte Sant'Angelo, 80126, Naples, Italy*

[2]*Berlin Institute for Medical Systems Biology, Max-Delbrück Centre (MDC) for Molecular Medicine, 10115 Berlin, Germany*

[*]*Corresponding author. Email: andrea.esposito@na.infn.it*

ABSTRACT.

Novel technologies are shedding light on the three-dimensional (3D) structure of chromosomes within the eukaryotic cell nucleus. Such experiments have led to the discovery of topological structural properties of chromosomes, describing a picture in which the genome is folded in complex spatial structures in order to bring genes and their regulators into close spatial proximity. However, the molecular mechanisms that guide such organization are still partially unknown. Quantitative, theoretical models from Polymer Physics are helping to decrypt the mechanical rules of DNA 3D folding. Here, we report on two recent studies in which we show that those models can be further refined by considering independent data, i.e., epigenetics, and the coexistence of different molecular mechanisms. We also point out that efficient algorithms and large-scale computational resources are necessary to improve the accuracy of the models which, in turn, will advance our understanding of DNA 3D folding.

1. Introduction

Recent molecular biology techniques, such as Hi-C [1], GAM [2], and SPRITE [3], have revealed that chromosomes are folded in the cell nucleus in complex, non-random three-dimensional (3D) conformations. For example, it has been shown that they are organized in megabase-sized domains of self-interaction, called TADs [4,5], which, while having a complex inner structure [6], also interact among themselves in a hierarchical fashion, forming higher order structures (e.g., metaTADs and compartments) that can span entire chromosomes [7]. Such a complex spatial arrangement has been demonstrated to be crucial for transcriptional regulation by bridging, for example, regulatory elements and their target genes into close spatial proximity [8], and its disruption has been associated to disease [9]. However, the physical mechanisms underlying genome folding remain mostly unknown. In this context, principled approaches based on the laws of physics and large-scale numerical simulations are key tools to make sense of those complex contact patterns. Among the others, the Strings and Binders Switch (SBS) polymer physics model [10,11], describes a scenario in which a genomic region is represented as a self-avoiding string of beads having attachment sites for cognate binding molecules, which can form loops by bridging pairs of polymer sites, shaping in this way the polymer 3D structure. The arrangement of binding sites that best reproduces an input contact matrix can be found, i.e., via machine-learning-based approaches as, for instance, the recently developed PRISMR method [12]. In this way, we obtain the specific polymer model of the genomic region of interest. After that, massive, parallel Molecular Dynamics simulations are run to build an ensemble of 3D structures that quantitatively describe the studied region, a highly computationally demanding step in which efficient calculus infrastructures are crucial [13]. Here, we review two recent results in which the SBS model is

extended to accommodate known biological players, such as chromatin epigenetic modifications [14] and loop-extruding factors [15] to progress our understanding of the mechanisms of 3D genome folding.

2. The polymer physics-based SBS model and its implementation

In the SBS model a genomic region is represented as a self-avoiding string of beads having specific attachment sites (binding sites) for diffusive binding molecules (binders) **(Fig. 1A)**. The bead-binder interaction is highly specific, in the sense that only same-colored bead-binder pairs interact, and many interaction types (colors) are allowed. The system evolves under just the laws of physics and its dynamics can be studied, for instance, by Molecular Dynamics (MD) simulations using standard interaction potentials described in classical polymer physics studies [11,13]. Specifically, the Langevin equation of motion are solved with a standard Verlet integrator by the use of the LAMMPS software [16]. The intricate network of interactions between beads and binders drives the system's folding through a phase separation mechanism **(Fig. 1B)**. According to polymer physics [17], the system moves from a randomly open conformational state (coil) to a more compact, globular phase as soon as the binders' concentration (or affinity strength with polymer sites) exceeds a threshold value.
The SBS model can be specialized to study real genomic regions whose associated contact matrix present non-trivial patterns of interaction domains. To this aim, we have developed a computational method called PRISMR [12], which takes the contact matrix of the considered genomic region as input and, based on a simulated annealing Monte Carlo method, returns as output the minimum number of different colors and their precise arrangement along the polymer chain which best reproduces the input dataset within a given accuracy **(Fig. 1C)**. After obtaining the optimal SBS model, we run extensive MD simulations to obtain a thermodynamic ensemble of polymer models, which allows us to examine the dynamics and equilibrium characteristics of the system. Depending on the size of the investigated polymer model, it may take many hours to execute a thorough simulation of the system from the coil to the globular state. Hence, high-Performance Computing (HPC) resources play a fundamental role in this approach. The SBS model has been used to correctly describe the 3D organization of several important genomic regions in both human and mouse cells [2,12,18–20]. While the SBS model relies on the equilibrium process of phase-separation, recent advances in the field have also revealed that an off-equilibrium, energy-burning active process called loop-extrusion is a significant contributor in determining chromosome 3D structure [21]. Although there have been models based only on the loop-extrusion mechanism to explain and understand its role in the genome spatial organization [22–24], it is not certain how it functions in coordination with phase-separation to drive the folding. Here, we also review a recent development in which we integrate the SBS and the loop-extrusion mechanisms in the same context and study their combined effect at the level of single-molecules [15].

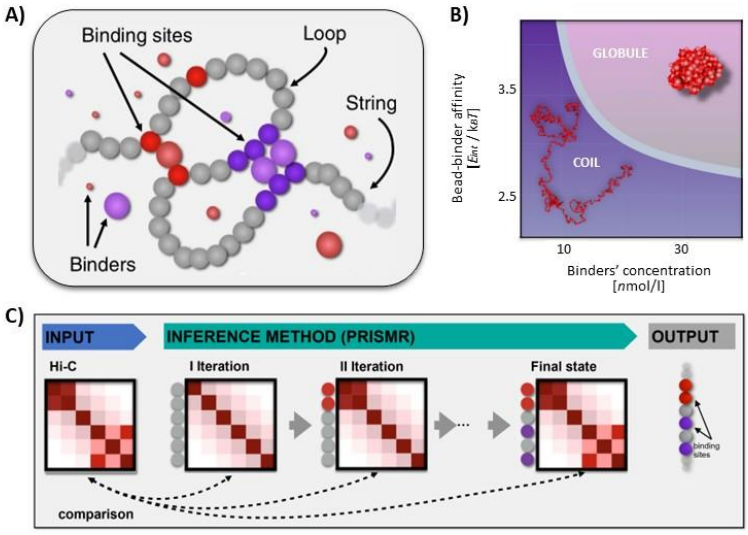

Fig.1: A) In the Strings and Binders Switch (SBS) model, the process of folding is guided by homotypic interaction between binding sites and cognate diffusing binders. The interaction between a binder and a binding site is specific: only bead-binder pairs of the same color can interact. **B)** SBS phase diagram: depending on the values of binders' concentration and affinity strength with binding sites, the polymer undergoes a coil-globule transition. **C)** Sketch of the PRISMR procedure: starting from a random polymer, PRISMR takes as input the experimental contact matrix (i.e., Hi-C) of a genomic region and minimizes, through an iterative procedure, the distance between the predicted and the experimental contact matrix. Adapted from [11].

3. Exploration of chromatin folding and its link with epigenetics, loop-extrusion and phase-separation mechanisms

As discussed in the previous section, the PRISMR algorithm infers from an experimental contact matrix the distribution of binding sites along the SBS polymer that best describes the matrix itself. We performed a genome-wide PRISMR on Hi-C data in human GM12878 B-lymphoblastoid cells at 5 kb resolution [14,21]. The model contact matrices, obtained for all chromosomes at the same 5 kb resolution, are found to be in good agreement with the experiments, with a mean Pearson correlation r=0.94. Then, in order to obtain a molecular characterization of the inferred binding domains (the same-colored binding sites), we correlated their genomic positions to histone mark tracks available from the ENCODE database [25] for the studied cell line **(Fig. 2A)**. Specifically, here we used the PRISMR-derived binding domains from even-numbered chromosomes to compute such correlations to later test the resulting barcode connecting binding domains and epigenetics by predicting the structure of odd-numbered chromosomes. We found that, across chromosomes, each binding domain correlates with a distinct, specific combination of epigenetic marks rather than with a single one. We also found that the genome-wide inferred binding domains fall into nine epigenetic classes **(Fig. 2B)** that closely match functional chromatin states identified in linear segmentation studies [26–30]. The first three classes have a high correlation with active chromatin marks, although they are not the same from an epigenetic perspective. While class 1 is exclusively enriched for active marks, classes 2 and 3 are additionally enriched in H3K9me3. Also, when compared to class 2, class 3 has a greater link with H3K4me1, a histone mark associated with active enhancer regions. Class 4 features the typical bivalent chromatin signature, with H3K27me3 coupled with active marks. Classes 5 and 6 are highly correlated with H3K27me3 and may be responsible for the experimentally observed self-interacting regions of PRC-repressed chromatin [31]. Classes 7 and 8 exhibit a lack of active marks, although class 7 displays a link with H3K9me3, a mark normally associated with constitutive heterochromatin and a lack of TF binding, explaining the tendency of heterochromatin regions to cluster in space. Finally, class 9 (called "low signal") has a very low correlation with histone marks that are available. To test our code's predictive power, in a reverse approach, we correlate the epigenetic profiles of the binding domains from even chromosomes with epigenetic signals from odd chromosomes to identify the binding sites of the latter. Next, we use the SBS polymer model to predict 3D structures and contact matrices of odd chromosomes to be compared against independent Hi-C data. We find comparatively high correlation values between the epigenetic-predicted contact matrices and the corresponding experiments (i.e., for chromosome 19 we obtain Pearson r=0.91, genomic distance corrected Pearson r'=0.47; for chromosome 21 r=0.91, r'=0.63) **(Fig. 2C)**. Summarizing, the epigenetic code of binding domains can predict de novo chromatin conformations by associating specific sets of epigenetic signals to distinct types of binding sites, demonstrating that the inferred combinatorial 1D arrangement of binding sites contains accurate architectural information.

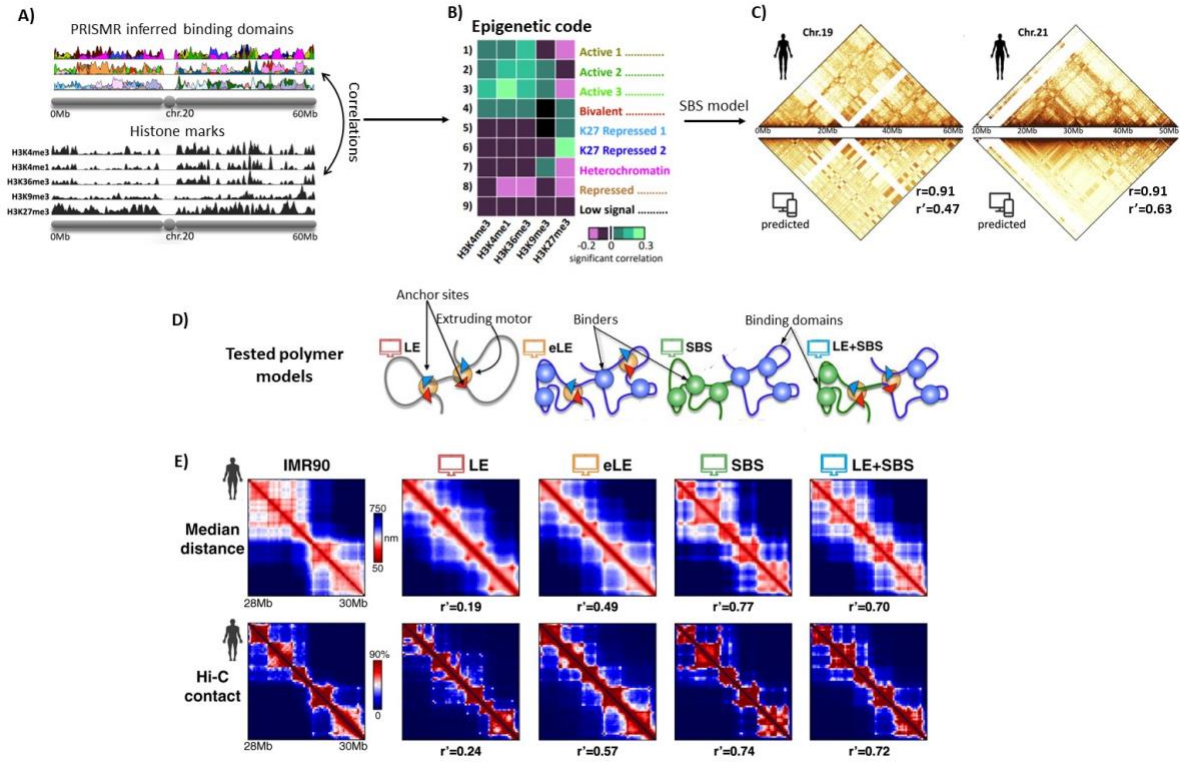

Fig.2: A) Top: different types of binding sites (binding domains) inferred by PRISRM for chromosome 20. For visualization purposes, the different domains, each represented by a different color, are drawn in groups of 10 in different rows. Bottom: binding domains have specific correlations with a set of histone marks. **B)** According to such correlations, binding domains cluster in nine main epigenetic classes, the centroid of which is shown in the heatmap. **C)** Using the epigenetic code, 3D structures can be successfully predicted for independent chromosomes. Here we show our results for chromosomes 19 and 21. **D)** All polymer models considered in our study. Loop-Extrusion (LE): polymer sites do not interact, and active motors extrude loops until encountering another motor or CTCF anchor points with opposite orientation; extended Loop-Extrusion (eLE): anchor sites may vary among the ensemble of single molecules, thus mimicking the epigenetic heterogeneity of single cells; Strings and Binders Switch (SBS) model, previously discussed; a hybrid polymer model (LE+SBS) where in a single molecule both eLE and SBS act at the same time. **E)** Microscopy median distance (top) and bulk Hi-C (bottom) data are compared to the corresponding model results in the studied IMR90 locus. The different models have high correlations with experiments, but the simple LE model is significantly inferior among the others. Adapted from [14,15].

Next, we explored a model that combines the loop-extrusion mechanism with the SBS model. We compared the multiplexed fluorescent microscopy data available on the human loci in IMR90 and HCT116 cells [32] against the hybrid model as well as the pure loop-extrusion and SBS models, to understand the relationship between loop-extrusion and phase separation. In this study, the loop-extrusion was modelled using extruding motors that randomly bind to the SBS polymer and extrude the polymer to create loops. The extrusion is halted only when they encounter either an extrusion anchor point or another extruding motor. Each anchor point blocks only either a forward or a backward moving extruding motor. This orientation as well as the position of anchor points are identified through the FIMO motif finding analysis [33] on the peaks of ChIP-Seq data for the CTCF protein complex from the ENCODE epigenomic database [25]. The model was implemented in the HOOMD-Blue molecular dynamics (MD) package [34] made for Python, while pure SBS model was implemented in LAMMPS [16]. For each of the 10^7 MD time steps used in the simulations, the software computes force and velocity for all the particles (around 10^3 particles for each system), making high-performance computing (HPC) resources from ENEA-CRESCO [35] a necessity for the study. The results from the simulations unambiguously showed that the loop-extrusion mechanism can indeed co-exist with phase separation in shaping the 3D genome architecture. At first, to systematically understand loop-extrusion,

we used a primitive loop-extrusion (LE) model, where the underlying polymer doesn't self-interact and instead interacts only through the extruding motors. We then developed an extended loop-extrusion (eLE) model, where the anchor sites may vary among the ensemble of single molecules, thus mimicking the epigenetic differences of single cells. Unlike the LE model, where all the anchor sites found in the FIMO analysis were used, in eLE model only the optimal anchor sites that best reproduce the experimental contact data were included. Finally, a hybrid model where both eLE and SBS acts on the single molecule was considered, along with the simple SBS model of the studied loci **(Fig. 2D)**. The HPC simulations showed that both the loop-extrusion and phase-separation based models can reproduce ensemble-averaged microscopy data and bulk Hi-C contact data, with the simple LE model being significantly inferior among the cohort **(Fig. 2E)**. They both can faithfully explain the single-cell chromatin conformations and higher order contacts, as evidenced by the single-molecule analyses [15]. However, the phase-separation models were better at explaining the cell-to-cell variability and the globular structures in the studied loci. This variability arises out of the thermodynamic degeneracy of the folded polymer and the epigenetic variations among the cells, indeed the LE+SBS model, which takes into account both these features of chromatin, was better at capturing the overall contact data as well as the triple contact data for the studied loci. This shows that the loop-extrusion and phase-separation can co-exist at single molecule level.

4. Conclusions

Thanks to recent developments in Molecular Biology, we have now access to a wealth of 3D genome data that are opening the way to investigate the mechanisms underlying such a complex organization. In this report, we showed that models based on polymer physics and machine learning are able to reproduce the 3D structure of real genomic regions, both at specific loci and genome wide. We found, in particular, that the binding domains inferred from the genome wide model exhibit a non-trivial correlational pattern with a specific combination of histone marks, characterizing their molecular nature. The model, based on the thermodynamic mechanism of phase separation, is general enough to be extended to accommodate other molecular processes, such as the off-equilibrium loop extrusion. The combined model still captures very well cell to cell variability and explains the ensemble-averaged data even better than the pure models alone. To push further our understanding of the 3D genome principles, we need more accurate models in which many molecular processes are taken into account simultaneously. This directly impact the computational effort needed to run the simulation of such systems. For these reasons, High Parallel Computing resources from ENEA [35] are fundamental to efficiently run accurate Molecular Dynamics simulations and represent a key tool for this research field.

References

1. Lieberman-Aiden, E.; Van Berkum, N.L.; Williams, L.; Imakaev, M.; Ragoczy, T.; Telling, A.; Amit, I.; Lajoie, B.R.; Sabo, P.J.; Dorschner, M.O.; et al. Comprehensive mapping of long-range interactions reveals folding principles of the human genome. *Science (80-.).* **2009**, *326*, 289–293, doi:10.1126/science.1181369.
2. Beagrie, R.A.; Scialdone, A.; Schueler, M.; Kraemer, D.C.A.; Chotalia, M.; Xie, S.Q.; Barbieri, M.; De Santiago, I.; Lavitas, L.M.; Branco, M.R.; et al. Complex multi-enhancer contacts captured by genome architecture mapping. *Nature* **2017**, *543*, 519–524, doi:10.1038/nature21411.
3. Quinodoz, S.A.; Ollikainen, N.; Tabak, B.; Palla, A.; Schmidt, J.M.; Detmar, E.; Lai, M.M.; Shishkin, A.A.; Bhat, P.; Takei, Y.; et al. Higher-Order Inter-chromosomal Hubs Shape 3D Genome Organization in the Nucleus. *Cell* **2018**, *174*, 744-757.e24, doi:10.1016/j.cell.2018.05.024.
4. Dixon, J.R.; Selvaraj, S.; Yue, F.; Kim, A.; Li, Y.; Shen, Y.; Hu, M.; Liu, J.S.; Ren, B. Topological domains in mammalian genomes identified by analysis of chromatin interactions. *Nature* **2012**, *485*, 376–80, doi:10.1038/nature11082.
5. Nora, E.P.; Lajoie, B.R.; Schulz, E.G.; Giorgetti, L.; Okamoto, I.; Servant, N.; Piolot, T.; Van Berkum, N.L.; Meisig, J.; Sedat, J.; et al. Spatial partitioning of the regulatory landscape of the

X-inactivation centre. *Nature* **2012**, *485*, 381–385, doi:10.1038/nature11049.
6. Phillips-Cremins, J.E.; Sauria, M.E.G.; Sanyal, A.; Gerasimova, T.I.; Lajoie, B.R.; Bell, J.S.K.; Ong, C.T.; Hookway, T.A.; Guo, C.; Sun, Y.; et al. Architectural protein subclasses shape 3D organization of genomes during lineage commitment. *Cell* **2013**, doi:10.1016/j.cell.2013.04.053.
7. Fraser, J.; Ferrai, C.; Chiariello, A.M.; Schueler, M.; Rito, T.; Laudanno, G.; Barbieri, M.; Moore, B.L.; Kraemer, D.C.; Aitken, S.; et al. Hierarchical folding and reorganization of chromosomes are linked to transcriptional changes in cellular differentiation. *Mol. Syst. Biol.* **2015**, *11*, 852–852, doi:10.15252/msb.20156492.
8. Dekker, J.; Mirny, L. The 3D Genome as Moderator of Chromosomal Communication. *Cell* **2016**, *164*, 1110–1121, doi:10.1016/j.cell.2016.02.007.
9. Lupiáñez, D.G.; Kraft, K.; Heinrich, V.; Krawitz, P.; Brancati, F.; Klopocki, E.; Horn, D.; Kayserili, H.; Opitz, J.M.; Laxova, R.; et al. Disruptions of topological chromatin domains cause pathogenic rewiring of gene-enhancer interactions. *Cell* **2015**, *161*, 1012–1025, doi:10.1016/j.cell.2015.04.004.
10. Barbieri, M.; Chotalia, M.; Fraser, J.; Lavitas, L.-M.; Dostie, J.; Pombo, A.; Nicodemi, M. Complexity of chromatin folding is captured by the strings and binders switch model. *Proc. Natl. Acad. Sci.* **2012**, *109*, 16173–16178, doi:10.1073/pnas.1204799109.
11. Chiariello, A.M.A.M.; Annunziatella, C.; Bianco, S.; Esposito, A.; Nicodemi, M. Polymer physics of chromosome large-scale 3D organisation. *Sci. Rep.* **2016**, *6*, doi:10.1038/srep29775.
12. Bianco, S.; Lupiáñez, D.G.; Chiariello, A.M.; Annunziatella, C.; Kraft, K.; Schöpflin, R.; Wittler, L.; Andrey, G.; Vingron, M.; Pombo, A.; et al. Polymer physics predicts the effects of structural variants on chromatin architecture. *Nat. Genet.* **2018**, *50*, 662–667, doi:10.1038/s41588-018-0098-8.
13. Annunziatella, C.; Chiariello, A.M.; Esposito, A.; Bianco, S.; Fiorillo, L.; Nicodemi, M. Molecular Dynamics simulations of the Strings and Binders Switch model of chromatin. *Methods* 2018, *142*, 81–88.
14. Esposito, A.; Bianco, S.; Chiariello, A.M.; Abraham, A.; Fiorillo, L.; Conte, M.; Campanile, R.; Nicodemi, M. Polymer physics reveals a combinatorial code linking 3D chromatin architecture to 1D chromatin states. *Cell Rep.* **2022**, *38*, 110601, doi:10.1016/J.CELREP.2022.110601.
15. Conte, M.; Irani, E.; Chiariello, A.M.; Abraham, A.; Bianco, S.; Esposito, A.; Nicodemi, M. Loop-extrusion and polymer phase-separation can co-exist at the single-molecule level to shape chromatin folding. *Nat. Commun.* **2022**, *13*, 2021.11.02.466589, doi:10.1038/s41467-022-31856-6.
16. Plimpton, S. Fast parallel algorithms for short-range molecular dynamics. *J. Comput. Phys.* **1995**, *117*, 1–19, doi:10.1006/jcph.1995.1039.
17. De Gennes, P.G. Scaling concepts in polymer physics. Cornell university press. *Ithaca N.Y.*, **1979**, doi:10.1163/_q3_SIM_00374.
18. Bianco, S.; Annunziatella, C.; Andrey, G.; Chiariello, A.M.; Esposito, A.; Fiorillo, L.; Prisco, A.; Conte, M.; Campanile, R.; Nicodemi, M. Modeling Single-Molecule Conformations of the HoxD Region in Mouse Embryonic Stem and Cortical Neuronal Cells. *Cell Rep.* **2019**, *28*, 1574-1583.e4, doi:10.1016/j.celrep.2019.07.013.
19. Chiariello, A.M.; Bianco, S.; Oudelaar, A.M.M.; Esposito, A.; Annunziatella, C.; Fiorillo, L.; Conte, M.; Corrado, A.; Prisco, A.; Larke, M.S.C.; et al. A Dynamic Folded Hairpin Conformation Is Associated with α-Globin Activation in Erythroid Cells. *Cell Rep.* **2020**, *30*, 2125-2135.e5, doi:10.1016/j.celrep.2020.01.044.
20. Conte, M.; Fiorillo, L.; Bianco, S.; Chiariello, A.M.; Esposito, A.; Nicodemi, M. Polymer physics indicates chromatin folding variability across single-cells results from state degeneracy in phase separation. *Nat. Commun.* **2020**, *11*, 3289, doi:10.1038/s41467-020-17141-4.
21. Rao, S.S.P.P.; Huntley, M.H.; Durand, N.C.; Stamenova, E.K.; Bochkov, I.D.; Robinson, J.T.; Sanborn, A.L.; Machol, I.; Omer, A.D.; Lander, E.S.; et al. A 3D map of the human genome at kilobase resolution reveals principles of chromatin looping. *Cell* **2014**, *159*, 1665–80, doi:10.1016/j.cell.2014.11.021.

22. Sanborn, A.L.; Rao, S.S.P.; Huang, S.-C.; Durand, N.C.; Huntley, M.H.; Jewett, A.I.; Bochkov, I.D.; Chinnappan, D.; Cutkosky, A.; Li, J.; et al. Chromatin extrusion explains key features of loop and domain formation in wild-type and engineered genomes. *Proc. Natl. Acad. Sci.* **2015**, *112*, E6456–E6465, doi:10.1073/pnas.1518552112.
23. Fudenberg, G.; Imakaev, M.; Lu, C.; Goloborodko, A.; Abdennur, N.; Mirny, L.A. Formation of Chromosomal Domains by Loop Extrusion. *Cell Rep.* **2016**, *15*, 2038–2049, doi:10.1016/j.celrep.2016.04.085.
24. Banigan, E.J.; Mirny, L.A. Loop extrusion: theory meets single-molecule experiments. *Curr. Opin. Cell Biol.* 2020, *64*, 124–138.
25. Dunham, I.; Kundaje, A.; Aldred, S.F.; Collins, P.J.; Davis, C.A.; Doyle, F.; Epstein, C.B.; Frietze, S.; Harrow, J.; Kaul, R.; et al. An integrated encyclopedia of DNA elements in the human genome. *Nature* **2012**, *489*, 57–74, doi:10.1038/nature11247.
26. Boettiger, A.N.; Bintu, B.; Moffitt, J.R.; Wang, S.; Beliveau, B.J.; Fudenberg, G.; Imakaev, M.; Mirny, L.A.; Wu, C.T.; Zhuang, X. Super-resolution imaging reveals distinct chromatin folding for different epigenetic states. *Nature* **2016**, *529*, 418–22, doi:10.1038/nature16496.
27. Ernst, J.; Kheradpour, P.; Mikkelsen, T.S.; Shoresh, N.; Ward, L.D.; Epstein, C.B.; Zhang, X.; Wang, L.; Issner, R.; Coyne, M.; et al. Mapping and analysis of chromatin state dynamics in nine human cell types. *Nature* **2011**, *473*, 43–49, doi:10.1038/nature09906.
28. Gifford, C.A.; Ziller, M.J.; Gu, H.; Trapnell, C.; Donaghey, J.; Tsankov, A.; Shalek, A.K.; Kelley, D.R.; Shishkin, A.A.; Issner, R.; et al. Transcriptional and epigenetic dynamics during specification of human embryonic stem cells. *Cell* **2013**, *153*, 1149–1163, doi:10.1016/j.cell.2013.04.037.
29. Ho, J.W.K.; Jung, Y.L.; Liu, T.; Alver, B.H.; Lee, S.; Ikegami, K.; Sohn, K.A.; Minoda, A.; Tolstorukov, M.Y.; Appert, A.; et al. Comparative analysis of metazoan chromatin organization. *Nature* **2014**, *512*, 449–452, doi:10.1038/nature13415.
30. Javierre, B.M.; Sewitz, S.; Cairns, J.; Wingett, S.W.; Vï¿½rnai, C.; Thiecke, M.J.; Freire-Pritchett, P.; Spivakov, M.; Fraser, P.; Burren, O.S.; et al. Lineage-Specific Genome Architecture Links Enhancers and Non-coding Disease Variants to Target Gene Promoters. *Cell* **2016**, *167*, 1369-1384.e19, doi:10.1016/j.cell.2016.09.037.
31. Kundu, S.; Ji, F.; Sunwoo, H.; Jain, G.; Lee, J.T.; Sadreyev, R.I.; Dekker, J.; Kingston, R.E. Polycomb Repressive Complex 1 Generates Discrete Compacted Domains that Change during Differentiation. *Mol. Cell* **2017**, *65*, 432-446.e5, doi:10.1016/j.molcel.2017.01.009.
32. Bintu, B.; Mateo, L.J.; Su, J.-H.H.; Sinnott-Armstrong, N.A.; Parker, M.; Kinrot, S.; Yamaya, K.; Boettiger, A.N.; Zhuang, X. Super-resolution chromatin tracing reveals domains and cooperative interactions in single cells. *Science (80-.).* **2018**, *362*, eaau1783, doi:10.1126/science.aau1783.
33. Grant, C.E.; Bailey, T.L.; Noble, W.S. FIMO: scanning for occurrences of a given motif. *Bioinformatics* **2011**, *27*, 1017–1018, doi:10.1093/BIOINFORMATICS/BTR064.
34. Anderson, J.A.; Glaser, J.; Glotzer, S.C. HOOMD-blue: A Python package for high-performance molecular dynamics and hard particle Monte Carlo simulations. *Comput. Mater. Sci.* **2020**, *173*, 109363, doi:10.1016/J.COMMATSCI.2019.109363.
35. Iannone, F.; Ambrosino, F.; Bracco, G.; De Rosa, M.; Funel, A.; Guarnieri, G.; Migliori, S.; Palombi, F.; Ponti, G.; Santomauro, G.; et al. CRESCO ENEA HPC clusters: a working example of a multifabric GPFS Spectrum Scale layout. In Proceedings of the CRESCO ENEA HPC clusters: a working example of a multifabric GPFS Spectrum Scale layout; 2019; pp. 1051–1052.

ANTIVIRAL POTENTIAL OF TEA TREE OIL AGAINST CORONAVIRUSES: EXPERIMENTAL AND SIMULATION EVIDENCE

Alice Romeo[1], Federico Iacovelli[1] and Mattia Falconi[1*]

[1]*Department of Biology, University of Rome Tor Vergata, Via della Ricerca Scientifica 1, 00133 Rome, Italy*[11]

ABSTRACT. The rapid diffusion of the COVID-19 pandemic renewed the interest in developing novel disinfectant materials to limit virus spread among the population. Melaleuca alternifolia essential oil, named Tea tree oil (TTO), is widely known for its antibacterial, antifungal and antiviral properties. TTO is supposed to act by inhibiting virus entry and fusion with the host cell, interfering with the structural dynamics of the protein and membrane components of the viral envelope. In this study, for the first time, we demonstrated the virucidal effects of this oil against two SARS-CoV-2 surrogate models, the feline coronavirus (FCoVII) and the human coronavirus OC43 (HCoV-OC43). Then, we evaluated the possible effects of representative TTO compounds (terpinen-4-ol, γ-terpinene, and 1,8-cineole) on the outer surface of SARS-CoV-2 through GaMD simulations of a SARS-CoV-2 envelope portion, including a complete model of the Spike glycoprotein inserted in the membrane. Overall, the obtained results prompted us to hypothesize a potential use of TTO as a safe and effective natural disinfectant agent against coronaviruses.

Introduction

The use of disinfectants has become a worldwide daily practice since the beginning of the COVID-19 pandemic. Because of their lipid membrane, enveloped viruses like SARS-CoV-2 are more susceptible than naked viruses to external conditions and disinfectant products [1]. Several disinfectant agents have shown efficacy against highly pathogenic coronaviruses like MERS-CoV, SARS-CoV-1 and SARS-CoV-2 [1–3]. Their virucidal effect is mostly based on protein denaturation and the disruption of the viral lipid envelope, thanks to their amphiphilic properties facilitating their entry into lipid membranes [1,2]. During the COVID-19 pandemic, the WHO and FDA recommended the use of alcohol-based sanitizers to counteract SARS-CoV-2 diffusion, but prolonged and excessive use of these products was demonstrated to cause skin dryness and damage, favouring the entry of other harmful microbes [4–6]. This risk, mainly associated with liquid preparations, could be reduced by using foam or gel formulations, but the applied volume and required drying time of these products deeply affect their efficacy [2]. Possible environmental impacts caused by the increased use of these chemicals are also a concern [4]. On the other hand, many natural compounds possess known antimicrobial properties and could represent a potential non-toxic and biodegradable alternative to disinfectants [6]. In particular, essential oils extracted from aromatic herbs or plants showed antiviral activity against coronaviruses, including SARS-CoV-1, and their possible use also against SARS-CoV-2 was hypothesized [7].

The extract of the Melaleuca alternifolia tree, commonly called Tea tree oil (TTO), possesses well-known antibacterial, antifungal, and antiviral properties [8–11]. In particular, its lipophilic nature

[11] Corresponding author. E-mail: falconi@uniroma2.it.

enables penetration into the skin and its topical use as a treatment for mucosal and cutaneous infections [8,12,13]. Notably, TTO-based handwash formulations have been evaluated as possible disinfectants in health care settings, showing that either a product with 5% TTO and 10% alcohol, or a solution of 5% TTO in water, reduced bacterial proliferation significantly more than soft soap [14]. Another recent randomized trial also suggested that a 10% TTO disinfectant induced a higher antimicrobial effect than an 83% alcohol-based gel disinfectant or a benzalkonium chloride foam disinfectant [15]. Considering this evidence, we proposed the use of TTO as a novel natural disinfectant agent against coronaviruses, evaluating its possible efficacy against SARS-CoV-2 using computational and experimental techniques.

1 Methods

1.1 Experimental methods

All the experiments described have been performed in the Laboratory of Virology (Department of Molecular Medicine) of the Sapienza University of Rome.

Different TTO-EtOH formulations, characterized by scalar TTO and EtOH concentrations, were used to carry out the in vitro virucidal assays. TTO dilutions (3.33%, 0.66%, and 0.13%) were obtained starting from pure TTO (Sigma-Aldrich W390208), while that of EtOH (5.33%, 1.06%, and 0.21%) were produced starting from 80% of EtOH in distilled water (Merck K35016883). γ-terpinene (Sigma-Aldrich 223190), 1,8-cineole (Sigma-Aldrich PHR1828) and terpinen-4-ol (Sigma-Aldrich W224820) were diluted as described for pure TTO at 3.33% and 0.66%. The disinfectant ISACLEAN® (Cantel Medical S.R.L.), a product with proven virucidal effects, was used as a reference agent (composition: isazone, benzalkonium chloride 50%, chlorhexidine gluconate, and isopropanol). Vero E6 (African green monkey kidney cells) and CRFK (Crandell–Rees feline kidney) cell lines were employed in the assays. The coronaviruses feline coronavirus (FCoVII) was propagated in CRFK cells, while human coronavirus OC-43 (HCoV-OC43) was propagated in Vero E6 cells. Both viruses can be handled at Biosafety Level 2 (BSL-2).

Virucidal activity assays were performed in three intervals (5, 15, and 30 min) of contact of the viruses with the different products, using fixed amounts of FCoVII (6 Log TCID50/mL) and HCoVOC43 (5 Log RNA copies/mL) and mixing 100 µL of each virus with 100 µL of each formulation. Virus controls with 100 µL medium in place of the tested products were included. At the end of the exposure times, virucidal activity was stopped by adding 900 µL of ice-cold cell culture medium and virus titers were determined using end point dilution titration in microtiter plates (FCoVII/ CRFK cells) or RT/Real Time PCR (HCoV-OC43/ Vero E6 cells). Viral titer reduction of both coronaviruses was calculated as the difference between the virus titers after exposure with TTO and the control virus titer (medium). Further details on the experimental materials and methods can be found in the paper [16].

1.2 Simulation methods

1.2.1 Gaussian Accelerated Molecular Dynamics simulations

Gaussian Accelerated Molecular Dynamics (GaMD) simulations were performed using a complete model of the SARS-CoV-2 Spike glycoprotein in prefusion conformation, with its RBDs in closed configuration, including known glycosylation and palmitoylation sites [17]. Topology and coordinate files for the protein, inserted in a 230x230 Å membrane, were generated using the Membrane Builder tool of CHARMM-GUI (https://www.charmm-gui.org/) and the CHARMM36m force field for proteins [18], lipids [19], and carbohydrates [20]. The same membrane composition employed by Woo and co-workers was chosen to mimic the viral envelope [17]. An initial simulation of the protein-membrane system was first carried out to equilibrate the system. Protein and membrane were inserted in a rectangular box filled with TIP3P water molecules [21] and then neutralized with 0.15 M of NaCl ions.

The system was first minimized in ten runs, each including 2000 steps to remove unfavorable interactions. A constraint of 20.0 kcal/mol was initially applied on each atom, sequentially halved in the subsequent runs, and finally removed in the last. The minimized system was then thermalized in a canonical ensemble (NVT) using a timestep of 1.0 fs, gradually increasing the temperature from 0 to 310 K every 30 ps using Langevin dynamics [22] and applying a constraint of 5.0 kcal/mol on protein and membrane atoms. The system was then equilibrated in an anisotropic NPT (NPT-A) ensemble using the Nosè–Hoover Langevin piston method [23,24] and a constant pressure of 1.0 atm, gradually releasing the constraints applied on the protein and membrane every 250.0 ps during a 2250.0 ps run. Then, the timestep was increased to 2.0 fs and the system was simulated for 10.0 ns using classical MD before starting a 150 ns dual-boost GaMD simulation [25]. The GaMD procedure included 2.0 ns of classical MD preparation, 50.0 ns of GaMD equilibration, and 100.0 ns of GaMD production. The upper and lower limits for the standard deviation of the total boost potential were kept to 6.0 kcal/mol as default. The PME method was used to calculate electrostatic interactions [26], while the cut-off for nonbonded interactions was set to 12.0 Å. At the end of this simulation, a representative frame of the protein–membrane system was extracted from the trajectory production phase using the cluster module of GROMACS 2020 [27]. This equilibrated structure was then used as a starting point for two other simulations, performed in the absence or presence of several molecules of three representative components of TTO (γ-terpinene, terpinen-4-ol, and 1,8-cineole), randomly distributed around the Spike using the Packmol program [28]. Compound's structures were retrieved from the PubChem database (https://pubchem.ncbi.nlm.nih.gov/), while their parameters were generated using the CGenFF program (https://cgenff.umaryland.edu) and the CHARMM general force field [29]. Topologies and coordinates files for the new systems were obtained using the VMD program [30], solvating the structures in rectangular boxes of TIP3P water molecules and neutralizing them with 0.15 M of NaCl ions. The same minimization and equilibration protocol was applied, except that a shorter NPT-A equilibration of 1500.0 ps was performed prior to the 10.0 ns of classical MD. Then, 150.0 ns dual-boost GaMD simulations were carried out as previously described for both systems. All simulations were performed using the NAMD 2.13 program [31] on the ENEA CRESCO6 HPC cluster [32], saving systems coordinates every 1000 steps.

1.2.2 Trajectory analysis

Principal component analysis (PCA) [33] was performed on the Spike Cα atoms using the GROMACS 2020 program [27]. Correlation plots were generated using a custom Python script. Membrane thickness was evaluated using the VMD MEMBPLUGIN Tool [34], while salt bridges were analyzed using the VMD Salt Bridges Tool [30]. Binding persistence of TTO molecules with each Spike domain was analyzed using a custom Tcl script in VMD, setting the distance threshold for identifying a contact to 4.0 Å. Radial distribution functions (RDFs) for the three TTO molecules were calculated using the GROMACS 2020 program, setting the Spike Cα atoms as reference set of positions. Plots were generated using custom Python scripts.

2 Experimental results

2.1 Virucidal activity of TTO against FCoVII and HCoV-OC43

Virucidal effects of different products were evaluated against the coronaviruses FCoVII (in CRFK cells) and HCoV-OC43 (in Vero E6 cells): three TTO/EtOH formulations (3.33/5.33%, 0.66/1.06%, 0.13/0.21%), an EtOH formulation (5.33%), a reference disinfectant ISACLEAN® (Cantel Medical S.R.L.), and formulations of three individual TTO components (γ-terpinene, 1,8-cineole and terpinen-4-ol), diluted at 3.33% and 0.66%. Results showed that at the highest concentration tested (3.33% TTO / 5.33% EtOH), the TTO-EtOH formulation possesses a strong virucidal activity against the replication

of both FCoVII and HCoV-OC43. In particular, a ≥99.97% and 83.41% reduction in virus titers was observed for FCoVII and HCoV-OC43, respectively, already after 5 min exposure. A 95.83% inhibition of HCoV-OC43 titer was reached after 30 min (Table 1). Instead, for both viruses, moderate or no virucidal effects were recorded for lower concentrations of the TTO-EtOH formulation. Instead, treatment with only a 5.33% EtOH formulation induced no effects on virus replication (Table 1), suggesting that the virucidal effect observed for the TTO-EtOH product should be mainly attributed to TTO, or a synergistic activity of both components. As a reference, TTO virucidal activity was compared to that of the common disinfectant ISACLEAN®, which induced a reduction ≥99% in virus titers of both coronaviruses after 5 min of contact (Table 1). The same effect was observed in FCoVII when exposed to the TTO-EtOH formulation already after 5 min, while a similar reduction is observed only after 30 min for HCoV-OC43.

To identify specific molecules responsible for TTO efficacy, three of the major components of TTO (γ-terpinene, 1,8-cineole, and terpinen-4-ol) were individually tested against FCoVII and HCoV-OC43, using the same virucidal assay (Table 1). At the highest concentration tested (3.33%), all three compounds show a strong time-dependent virucidal activity against both coronaviruses. In particular, terpinen-4-ol showed the strongest effects against both viruses at any time point tested (5, 15, and 30 min), with a ≥99.0% reduction of virus titers already after 5 min contact. On the other hand, γ-terpinene can decrease FCoVII and HCoV-OC43 titers by 90.00% and 87.11%, respectively, only after 15 min. After 30 min of contact with γ-terpinene, ≥90.00% virus inactivation can be observed for both coronaviruses. Concerning 1,8-cineole, this compound can induce a 91.09% reduction in HCoV-OC43

	FCoVII (CRFK cells) (Log TCID50/ml)	**HCoV-OC43** (Vero E6 cells) (Log RNA copies/ml)

titer already after 5 min, while a 96.84% reduction of FCoVII titer is observed after 30 min. Lower concentrations of the TTO individual components tested resulted in a reduced efficacy against the two coronaviruses.

Table 1: Virucidal activity of the different formulations evaluated against FCoVII and HCoV-OC43. For all products, only the highest concentrations tested have been reported.

3 Computational results

Considering the promising experimental results obtained for the FCoVII and HCoV-OC43 coronaviruses, we hypothesized that TTO could also exert a similar virucidal activity against SARS-CoV-2. Therefore, to validate this hypothesis and elucidate its atomistic details, a portion of the SARS-CoV-2 envelope, including the Spike glycoprotein was simulated for 150.0 ns using the GaMD method, in the presence of several molecules of the three representative TTO compounds (γ-terpinene, 1,8-cineole and terpinen-4-ol) (Fig. 1). This target site was chosen since antiviral activity of TTO is generally mainly attributed to the inhibition of viral attachment and fusion to host cells, involving the impairment of key envelope macromolecules [9,11].

Tested product (%)	Time (min)	Virus exposed	Virus control	RV	Virus Inactivation (%)	Virus exposed	Virus control	RV	Virus Inactivation (%)
TTO-EtOH* (3.33, 5.33)	5	<0.50	4.00	≥3.50	≥99.97*	2.58	3.36	0.78	83.41
	15	<0.50	4.00	≥3.50	≥99.97*	2.56	3.28	0.72	80.96
	30	<0.50	4.00	≥3.50	≥99.97*	2.78	4.16	1.38	95.83
EtOH (5.33)	5	ND	ND	ND	ND	ND	ND	ND	ND
	15	ND	ND	ND	ND	ND	ND	ND	ND
	30	4.00	4.00	0.00	0.00	4.12	4.05	0.00	0.00
ISACLEAN®	5	<0.50	3.50	≥3.00	≥99.90*	1.90	4.03	2.13	99.26
terpinen-4-ol (3.33)	5	<0.50	3.00	≥2.50	≥99.68*	2.24	4.39	2.15	99.29
	15	<0.50	3.00	≥2.50	≥99.68*	2.23	4.39	2.15	99.30
	30	<0.50	3.00	≥2.50	≥99.68*	1.97	4.39	2.42	99.62
γ-terpinene (3.33)	5	2.50	3.00	0.50	68.38	3.91	4.39	0.48	66.88
	15	2.00	3.00	1.00	90.00	3.50	4.39	0.89	87.11
	30	2.00	3.00	1.00	90.00	3.35	4.39	1.04	90.87
1,8-cineole (3.33)	5	2.50	3.00	0.50	68.38	3.34	4.39	1.05	91.09
	15	2.50	3.00	0.50	68.38	3.02	4.39	1.37	95.73
	30	1.50	3.00	1.50	96.84	2.90	4.39	1.49	96.76

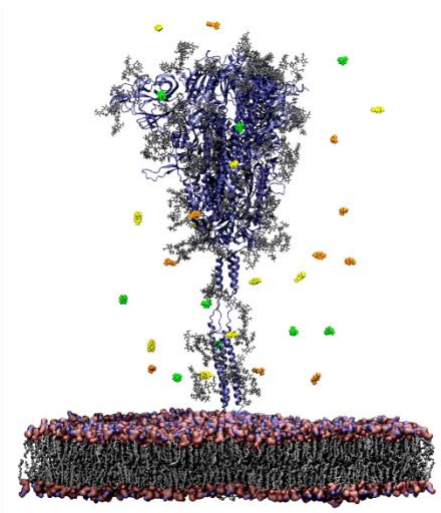

PubChem CID	Name	2D structure
7461	γ-terpinene	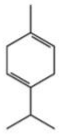
11230	terpinen-4-ol	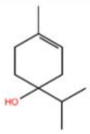
2758	1,8-cineole	

Fig.1: Simulation system described in this work. The Spike glycoprotein is shown as blue cartoon and its glycans as grey sticks. Membrane polar heads are shown as surface, colored by atom type, while lipid tails are displayed as grey sticks. TTO compounds are shown as spheres (γ-terpinene: orange, terpinen-4-ol: yellow, 1,8-cineole: green). On the right, 2D molecular structures and PubChem IDs of the compounds are reported in a table.

3.1 TTO influence on the viral envelope

During the simulation, we observed the insertion in membrane of six TTO compounds, including two 1,8-cineole, one γ-terpinene, and three terpinen-4-ol (Fig. 2A,B). Subsequent analyses on the membrane showed how the presence of these molecules determined a clear change in membrane thickness (Fig. 2B). In particular, during the second half of the GaMD production phase (from about 100.0 ns until the end of the simulation), membrane thickness showed a marked increase of about 0.7 Å in the system with TTO (Fig. 2B). At this timepoint, one γ-terpinene, two 1,8-cineole and one terpinen-4-ol molecules were inserted in membrane, and the timing of the observed shift approximately corresponds to the γ-terpinene reaching the opposite membrane leaflet and the 1,8-cineole and terpinen-4-ol molecules inserting deeper into the membrane. Notably, γ-terpinene is the only compound diffusing to the other membrane leaflet. It also shows lateral movements, suggesting that its structure and hydrophobicity allow it to fluctuate more easily within this lipid environment. Following these events, the thickness shift is stably maintained until the end of the simulation, and other two terpinen-4-ol molecules enter the membrane, although one of them diffuses again in the solvent during the last trajectory frames (Fig. 2B). Accordingly, 2D thickness maps, representing averaged membranes thickness profiles along the z-axis, outlined an altered thickness pattern in the presence of TTO compounds, with the appearance of wider regions of higher thickness in the viral membrane with respect to the reference (Fig. 2C).

Despite the limited size of the simulated system, adopted to stem the computational costs, results indicate that the inhibition mechanism mediated by TTO compounds involves an alteration of the physical properties and structural organization of the viral envelope.

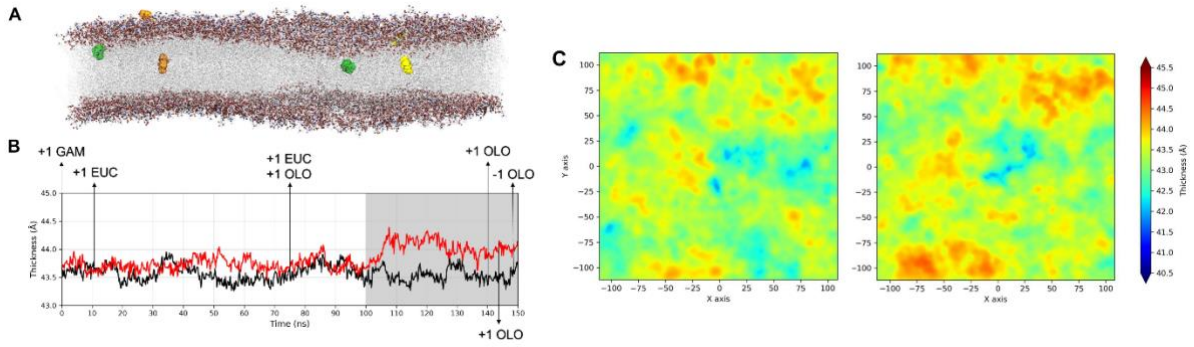

Fig.2: A) Final frame extracted from the 150 ns trajectory, showing the insertion of the γ-terpinene (orange), terpinen-4-ol (yellow), and 1,8-cineole (green) molecules, shown as spheres, within the viral membrane bilayer. B) Membrane thickness, calculated as a function of the simulation time in the absence (black line) or presence (red line) of the TTO molecules. Arrows indicate the timepoints of compounds entry (+1) or exit (−1). The grey background highlights the observed thickness shift. C) 2D thickness heatmaps calculated for the viral membrane in the absence (left plot) or presence (right plot) of TTO compounds.

3.2 Interaction analysis of TTO compounds with the Spike glycoprotein

Interactions of TTO compounds with the SARS-CoV-2 Spike glycoprotein were analysed, taking into consideration their influence on the structural dynamics of the protein (Fig. 3).

Results showed that γ-terpinene is the compound more frequently and persistently binding to the S surface (Fig. 3A). In particular, one γ-terpinene molecule binds the Spike RBD (residues 319-541) for 85.4% of the simulation time, suggesting a high affinity between the compound and this key protein region (Fig. 3A and 4A). Notably, the achieved binding site corresponds to a known fatty acid binding pocket (residues 330–470 and 500–515), located at each RBD of the Spike trimer [35]. The binding of linoleic acid to these regions was shown to reduce Spike-ACE2 interactions in vitro, inducing a higher rigidity in the S1 trimer [35,36]. During our simulations, we also observed the binding of two terpinen-4-ol molecules at the interface of the other two fatty acids binding pockets (Fig. 3A and 4B,C), as expected, given the structural similarity between γ-terpinene and terpinen-4-ol. Binding of compounds to these regions suggests that, as observed for linoleic acid, they could interfere to some extent with RBD transition to the open conformation and thus decrease the likelihood of Spike interactions with ACE2. In particular, as the simulation also suggests, the insertion of γ-terpinene within this mostly hydrophobic pocket should be more favored than that of terpinen-4-ol, given the stronger hydrophobic character of γ-terpinene.

Moreover, one γ-terpinene molecule also binds to a region spanning between the S2′ cleavage site and the fusion peptide (FP) region (residues 808–837), for about 92.2% of the simulation time, also contacting a segment of the HR1 region (residues 920–970) for 74.2% of the simulation (Fig. 3A). Accessibility of the S2′ cleavage site for protease priming is crucial to initiate the Spike conformational changes, since its cleavage leads to the exposure of the FPs and their insertion in the cell membrane [37]. Therefore, binding of γ-terpinene to this region could sterically interfere with S2-protease interactions and interrupt the subsequent chain of events. Moreover, the small size of γ-terpinene allowed for its insertion within the Spike surface, reaching the FP region, suggesting that this molecule could also easily find an entry path to the central helical region or internal cavity of the Spike. This suggests the potential entry and aggregation of a cluster of γ-terpinene molecules within the internal pocket, which could represent another possible strategy to interfere with Spike conformational changes. In fact, the presence of a strong steric hindrance within viral fusion proteins' internal regions has already been demonstrated to be effective in inhibiting the respiratory syncytial virus (RSV) entry into cells

[38], and has also been hypothesized to apply to SARS-CoV-2 in a previous paper of our group [39]. Finally, γ-terpinene also binds to the HR2 helix bundle (residue 1163 to 1202) (Fig. 3A) for 39.4% of the simulation time, detaching before the end of the simulation.

On the other hand, several 1,8-cineole molecules contact the S surface, mostly binding to its NTDs, but only establishing transient interactions that persisted from about 3.2 to 48.1% of the simulation time (Fig. 3A). Similarly, while terpinen-4-ol molecules can closely contact the RBD fatty acids pocket (Fig. 4B,C), as already described, they only transiently interact with other regions of the Spike, such as the NTD and HR2 (Fig. 3A).

Molecules' distribution around the Spike protein was further analysed by calculating, for the entire trajectory, the radial distribution functions (RDFs) of γ-terpinene, 1,8-cineole, and terpinen-4-ol (Fig. 3B). This analysis measured how molecules' densities change as a function of their distance from the Spike surface. Results highlighted that γ-terpinene molecules are strongly attracted toward the protein, arranging close to the structure and forming a sharp density peak around 0.8–1.0 nm from its surface (Fig. 3B). Instead, 1,8-cineole and terpinen-4-ol are less distributed around the Spike surface, with molecules diffusing up to 10.0 nm away from the protein (Fig. 3B). Overall, these data confirm the results Fig. 3A, suggesting that 1,8-cineole and terpinen-4-ol molecules mainly fluctuate in the solvent without achieving specific interactions on the protein surface.

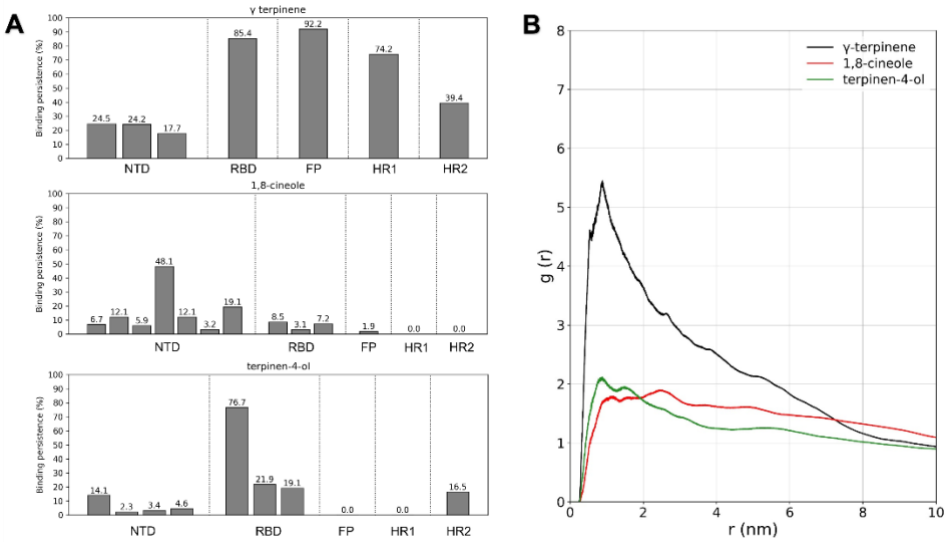

Fig. 3: A) Binding persistence of TTO molecules with different Spike functional domains during the simulation. For each domain, the number of bars represents the number of bound molecules, while the height of the bars indicates the percentage of simulation time in which the molecule was in contact with the domain also reported on top of bars. (NTD: N-terminal domain, RBD: receptor binding domain, FP: fusion peptide, HR1: heptad-repeats 1, and HR2: heptad-repeats 2). B) RDFs calculated for the three TTO compounds over the Spike surface during the 150 ns trajectory.

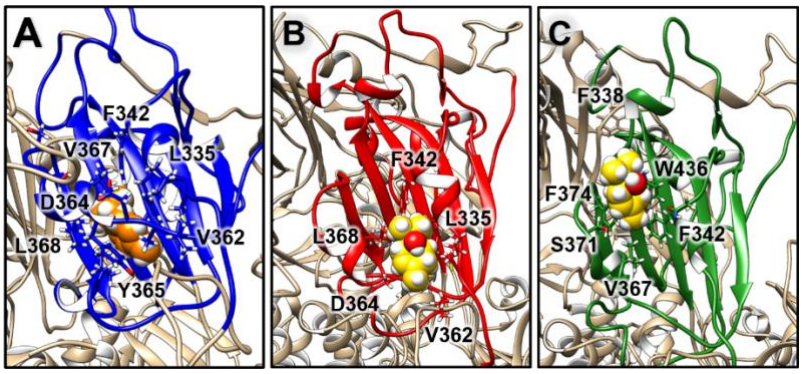

Fig.4: Binding poses observed for A) γ-terpinene (orange) and B,C) terpinen-4-ol (yellow) on the Spike fatty acids binding pockets located on the three protein RBDs (highlighted in blue, red, and green).

3.3 Structural effects of TTO compounds on Spike mobility

Protein motions were further analysed through principal component analysis (PCA) [33] to evaluate if interaction with TTO compounds and the identified alterations in membrane thickness also influenced the Spike protein mobility and structural dynamics. Dynamic cross-correlation plots, obtained using a custom Python script, showed that the presence of TTO compounds can influence the protein's NTD (residues 1-303) and RBD (residues 319-541) correlation patterns in all three monomers, particularly inducing a general increase in negatively correlated motions and a decrease in positively correlated motions in the the three RBDs (Fig. 5). Moreover, different patterns of positively correlated motions between the three monomers are present in the S2 subunits of the two systems. Positively correlated motions between the S CTDs (residues 1200–1273) and the RBDs also present different patterns in the two conditions, and in all three S monomers there is an increase in the strength of negatively correlated motions between the CTDs and different regions of the S2 subunit (residues 700–1200), including the HR1 and HR2 domains (Fig. 5). Being the CTD region close to the membrane, its altered behavior suggests that the increase in membrane thickness could have influenced S structural dynamics.

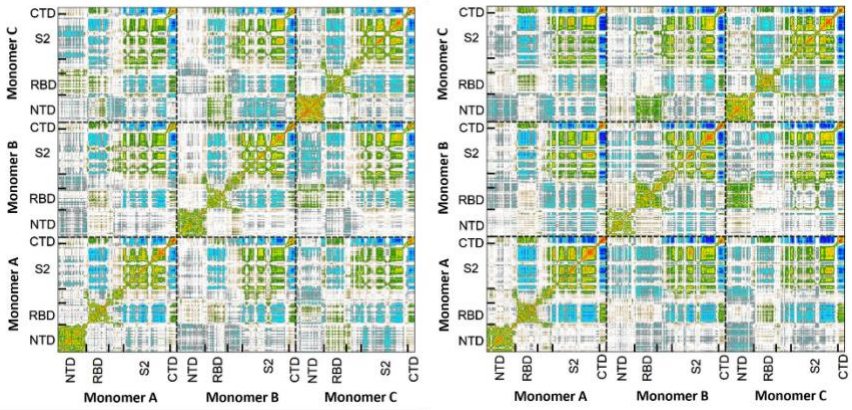

Fig.5: Correlation plots obtained for the Spike protein Cα atoms in the absence (left) or presence (right) of TTO compounds.

Salt bridge networks stabilizing the different S domains have been analyzed to better explain the observed differences. Salt bridges strongly influence protein motion and flexibility; therefore, the presence or absence of these electrostatic interactions can structurally influence the protein conformation, subsequently affecting the overall protein function [40]. This analysis revealed that the Spike NTDs, RBDs, and CTDs show the appearance and disappearance of several salt bridges in the

presence of TTO, while most of the salt bridges which are conserved in both simulations show different percentages of persistence [16]. However, 5 highly stable salt bridges (R290-R273, E169-K129, D53-K195, D398-R355, and D442-R509) can still be observed in the NTD and RBD of each of the three S monomers. Remarkably, ionic interactions between D290-R273 and D398-R355 are associated with RBD stability in closed conformation [41]. On the other hand, in the presence of TTO, the HR2 domain only shows the appearance of two additional salt bridges and minor variations in the other salt bridges' persistence, while negligible differences were observed for the HR1 domain in both conditions.

4 Discussion

Considering the structural similarities between different coronaviruses [42] and the promising experimental results obtained on the FCoVII and HCoV-OC43 coronaviruses, we evaluated the hypothesis that the strong antiviral activity exerted by TTO and its individual components could also be extendable to SARS-CoV-2. For this reason, we performed GaMD simulations to explain a possible inhibition mechanism carried out by TTO on the outer region of the SARS-CoV-2 envelope. Concerning the effects of TTO on the membrane, simulations confirmed that the three compound types can easily enter the viral bilayer and alter its thickness profile (Fig. 2). Therefore, their insertion could lead to a modification in the molecular organization of the viral envelope, in turn influencing the efficiency of the viral–cell membrane fusion process. Indeed, a similar mechanism was already proposed in literature to explain TTO antimicrobial properties, since its lipophilic terpene components tend to partition into bilayers disrupting their typical structure and function [43].

Interaction analyses and RDF calculations showed that γ-terpinene has a stronger attraction toward the Spike surface than terpinen-4-ol or 1,8-cineole (Fig. 3 A,B). In particular, several γ-terpinene molecules were persistently bound to the Spike protein during the simulation (Fig. 3), influencing the protein's structural correlation patterns and salt bridges networks and specifically targeting four key structural regions of S (the RBD domain, the S20/FP cleavage protease site, the HR1 helical region, and the HR2 helix bundle). Since all these domains are crucial in the process of membranes fusion, we hypothesize that the antiviral mechanism of γ-terpinene may influence virus entry at different levels, altering the specific sequence of events characterizing this process (receptor recognition, Spike cleavage and activation, fusion peptide insertion, and HR1 and HR2 assembly into the pore-inducing 6-HB) [37]. Remarkably, this observation is supported by an experimental work on the enveloped virus HSV-1, in which γ-terpinene induced a >96% reduction in plaque formation if pre-incubated with the virus, while terpinen-4-ol and 1,8-cineole had a lower efficacy [11]. Notably, γ-terpinene binding site on the Spike RBD corresponds to a known fatty acids binding pocket, where linoleic acid binding was shown to increase the inter-subunit contacts between the three RBDs, resulting in a more rigid S1 trimer and in a reduction of S-ACE2 interactions in vitro [35,36]. Moreover, two terpinen-4-ol molecules were also capable of binding this same region, although not completely inserting within the binding pocket. Differently from the other two TTO components evaluated, 1,8-cineole did not show any particular affinity for the S protein, but it could quickly enter the viral membrane (Fig. 2,3). This agrees with the TTO inhibition mechanism proposed for the methicillin-resistant S. aureus (MRSA), in which the essential oil can strongly destabilize the bacterial membrane, mainly when using 1,8-cineole alone [10]. This suggests that the antimicrobial activity of this compound may be specifically directed towards membranes, allowing for their destabilization and permeabilization, and facilitating the entry of other active components.

Despite the absence of a direct experimental confirmation of TTO efficacy on SARSCoV-2, its potential effects on this virus may be reasonably inferred from the simulation results and are also supported by the experiments on surrogate coronavirus models (e.g., FCoVII and HCoV-OC43) (Table 1), which have been commonly exploited during the pandemic to avoid the costs and biosafety concerns related to SARS-CoV-2 manipulation [44,45].

In conclusion, this study experimentally demonstrated for the first time the strong in vitro virucidal activity of a low TTO concentration and its individual components against two coronaviruses. Considering the promising results obtained through GaMD simulations, we hypothesize that this formulation could also be effective against SARS-CoV-2, suggesting its use as a safe disinfectant agent limiting the spread of enveloped pathogens.

Acknowledgments

The computing resources and the related technical support used for this work have been provided by CRESCO/ENEAGRID High Performance Computing infrastructure and its staff [32]. CRESCO/ENEAGRID High Performance Computing infrastructure is funded by ENEA, the Italian National Agency for New Technologies, Energy and Sustainable Economic Development and by Italian and European research programmes, see http://www.cresco.enea.it/english for information.

References

[1] Q. Lin, J.Y.C. Lim, K. Xue, P.Y.M. Yew, C. Owh, P.L. Chee, X.J. Loh. Sanitizing agents for virus inactivation and disinfection. *View*. **1**, p. e16, (2020).

[2] D. Singh, K. Joshi, A. Samuel, J. Patra, N. Mahindroo. Alcohol-based hand sanitizers as first line of defense against SARS CoV-2: A review of biology, chemistry and formulations. *Epidemiol. Infect.* **148**, p. e229, (2020).

[3] K.H. Chan, S. Sridhar, R.R. Zhang, H. Chu, A.F. Fung, G. Chan, J.W. Chan, K.W. To, I.N. Hung, V.C. Cheng, K.Y. Yuen. Factors affecting stability and infectivity of SARS-CoV-2. *J. Hosp. Infect.* **106**, pp. 226–231, (2020).

[4] A. Mahmood, M. Eqan, S. Pervez, H.A. Alghamdi, A.B. Tabinda, A. Yasar, K. Brindhadevi, A. Pugazhendhi. COVID-19 and frequent use of hand sanitizers; human health and environmental hazards by exposure pathways. *Sci. Total Environ.* **742**, p. 140561, (2020).

[5] J.L.J. Jing, T.P. Yi, R.J.C. Bose, J.R. McCarthy, N. Tharmalingam, T. Madheswaran. Hand sanitizers: A review on formulation aspects, adverse effects, and regulations. *Int. J. Environ. Res. Public Health.* **17,** p. 3326, (2020).

[6] A. Daverey, K. Dutta. COVID-19: Eco-friendly hand hygiene for human and environmental safety. *J. Environ. Chem. Eng.* **9**, p. 104754, (2021).

[7] A.R. Wani, K. Yadav, A. Khursheed, M.A. Rather. An updated and comprehensive review of the antiviral potential of essential oils and their chemical constituents with special focus on their mechanism of action against various influenza and coronaviruses. *Microb. Pathog.* **152**, p. 104620, (2021).

[8] C.F. Carson, K.A. Hammer, T.V. Riley. Melaleuca alternifolia (Tea Tree) Oil: a Review of Antimicrobial and Other Medicinal Properties. *Clin. Microbiol. Rev.* **19**, pp. 50–62, (2006).

[9] X. Li, S. Duan, C. Chu, J. Xu, G. Zeng, A. Lam, J. Zhou, Y. Yin, D. Fang, M. Reynolds, H. Gu, L. Jiang. Melaleuca alternifolia Concentrate Inhibits in Vitro Entry of Influenza Virus into Host Cells. *Molecules.* **18**, pp. 9550–9566, (2013).

[10] C.F. Carson, B.J. Mee, T.V. Riley. Mechanism of action of Melaleuca alternifolia (tea tree) oil on Staphylococcus aureus determined by time-kill, lysis, leakage, and salt tolerance assays and electron microscopy. *Antimicrob. Agents Chemother.* **46**, pp. 1914–1920, (2002).

[11] A. Astani, J. Reichling, P. Schnitzler. Comparative study on the antiviral activity of selected monoterpenes derived from essential oils. *Phyther. Res.* **24**, pp. 673-679, (2010).

[12] C.F. Carson, L. Ashton, L. Dry, D.W. Smith, T.V. Riley. Melaleuca alternifolia (tea tree) oil gel (6%) for the treatment of recurrent herpes labialis. *J. Antimicrob. Chemother.* **48**, pp. 450-451, (2001).

[13] C. Giordani, A. Molinari, L. Toccacieli, A. Calcabrini, A. Stringaro, P. Chistolini, G. Arancia, M. Diociaiuti. Interaction of Tea Tree Oil with Model and Cellular Membranes. *J. Med. Chem.* **49**, pp. 4581–4588, (2006).
[14] S. Messager, K.A. Hammer, C.F. Carson, T.V. Riley. Effectiveness of hand-cleansing formulations containing tea tree oil assessed ex vivo on human skin and in vivo with volunteers using European standard EN 1499. *J. Hosp. Infect.* **59**, pp. 220–228, (2005).
[15] B.H. Youn, Y.S. Kim, S. Yoo, M.H. Hur. Antimicrobial and hand hygiene effects of Tea Tree Essential Oil disinfectant: A randomised control trial. *Int. J. Clin. Pract.*, **75**, p. e14206, (2021).
[16] A. Romeo, F. Iacovelli, C. Scagnolari, M. Scordio, F. Frasca, R. Condò, S. Ammendola, R. Gaziano, M. Anselmi, M. Divizia, M. Falconi. Potential Use of Tea Tree Oil as a Disinfectant Agent against Coronaviruses: A Combined Experimental and Simulation Study. *Molecules*. **27**, p. 3786, (2022).
[17] H. Woo, S.J. Park, Y.K. Choi, T. Park, M. Tanveer, Y. Cao, N.R. Kern, J. Lee, M.S. Yeom, T.I. Croll, C. Seok, W. Im. Developing a Fully Glycosylated Full-Length SARS-CoV-2 Spike Protein Model in a Viral Membrane. *J. Phys. Chem. B.* **124**, pp. 7128–7137, (2020).
[18] J. Huang, S. Rauscher, G. Nawrocki, T. Ran, M. Feig, B.L. De Groot, H. Grubmüller, A.D. MacKerell. CHARMM36m: An improved force field for folded and intrinsically disordered proteins. *Nat. Methods.* **14**, pp. 71–73, (2016).
[19] J.B. Klauda, R.M. Venable, J.A. Freites, J.W. O'Connor, D.J. Tobias, C. Mondragon-Ramirez, I. Vorobyov, A.D. MacKerell, R.W. Pastor. Update of the CHARMM All-Atom Additive Force Field for Lipids: Validation on Six Lipid Types. *J. Phys. Chem. B.* **114**, pp. 7830–7843, (2010).
[20] O. Guvench, S.S. Mallajosyula, E.P. Raman, E. Hatcher, K. Vanommeslaeghe, T.J. Foster, F.W. Jamison, A.D. MacKerell. CHARMM Additive All-Atom Force Field for Carbohydrate Derivatives and Its Utility in Polysaccharide and Carbohydrate–Protein Modeling. *J. Chem. Theory Comput.* **7**, pp. 3162–3180, (2011).
[21] W.L. Jorgensen, J. Chandrasekhar, J.D. Madura, R.W. Impey, M.L. Klein. Comparison of simple potential functions for simulating liquid water. *J. Chem. Phys.* **79**, pp. 926–935, (1983).
[22] N. Goga, A.J. Rzepiela, A.H. De Vries, S.J. Marrink, H.J.C. Berendsen. Efficient algorithms for langevin and DPD dynamics. *J. Chem. Theory Comput.* **8**, pp. 3637–3649, (2012).
[23] S.E. Feller, Y. Zhang, R.W. Pastor, B.R. Brooks. Constant pressure molecular dynamics simulation: The Langevin piston method. *J. Chem. Phys.* **103**, pp. 4613–4621, (1995).
[24] G.J. Martyna, D.J. Tobias, M.L. Klein. Constant pressure molecular dynamics algorithms. *J. Chem. Phys.* **101**, pp. 4177–4189, (1994).
[25] Y. Miao, V.A. Feher, J.A. McCammon. Gaussian Accelerated Molecular Dynamics: Unconstrained Enhanced Sampling and Free Energy Calculation. *J. Chem. Theory Comput.* **11**, pp. 3584–3595, (2015).
[26] T. Darden, D. York, L. Pedersen. Particle mesh Ewald: An N·log(N) method for Ewald sums in large systems. *J. Chem. Phys.* **98**, pp. 10089–10092, (1993).
[27] M.J. Abraham, T. Murtola, R. Schulz, S. Páll, J.C. Smith, B. Hess, E. Lindah. Gromacs: High performance molecular simulations through multi-level parallelism from laptops to supercomputers. *SoftwareX*. **1–2**, pp. 19–25, (2015).
[28] L. Martínez, R. Andrade, E.G. Birgin, J.M. Martínez. PACKMOL: A package for building initial configurations for molecular dynamics simulations. *J. Comput. Chem.* **30**, pp. 2157–2164, (2009).
[29] K. Vanommeslaeghe, E. Hatcher, C. Acharya, S. Kundu, S. Zhong, J. Shim, E. Darian, O. Guvench, P. Lopes, I. Vorobyov, A.D. Mackerell. CHARMM general force field: A force field for drug-like molecules compatible with the CHARMM all-atom additive biological force fields. *J. Comput. Chem.* **31**, pp. 671–690, (2010).

[30] W. Humphrey, A. Dalke, K. Schulten. VMD: Visual molecular dynamics. *J. Mol. Graph*. **14**, pp. 33-38, (1996).
[31] J.C. Phillips, R. Braun, W. Wang, J. Gumbart, E. Tajkhorshid, E. Villa, C. Chipot, R.D. Skeel, L. Kalé, K. Schulten. Scalable molecular dynamics with NAMD. *J. Comput. Chem.* **26**, pp. 1781–1802, (2005).
[32] F. Iannone, F. Ambrosino, G. Bracco, M. De Rosa, A. Funel, G. Guarnieri, S. Migliori, F. Palombi, G. Ponti, G. Santomauro, P. Procacci. CRESCO ENEA HPC clusters: A working example of a multifabric GPFS Spectrum Scale layout. *2019 Int. Conf. High Perform. Comput. Simulation, HPCS 2019*. pp. 1051-1052, (2019).
[33] A. Amadei, A.B.M. Linssen, H.J.C. Berendsen. Essential dynamics of proteins. *Proteins Struct. Funct. Genet.* **17**, pp. 412-425, (1993).
[34] R. Guixà-González, I. Rodriguez-Espigares, J.M. Ramírez-Anguita, P. Carrió-Gaspar, H. Martinez-Seara, T. Giorgino, J. Selent. MEMBPLUGIN: studying membrane complexity in VMD. *Bioinformatics*. **30**, pp. 1478-1480, (2014).
[35] C. Toelzer, K. Gupta, S.K.N. Yadav, U. Borucu, A.D. Davidson, M. Kavanagh Williamson, D.K. Shoemark, F. Garzoni, O. Staufer, R. Milligan, et al. Free fatty acid binding pocket in the locked structure of SARS-CoV-2 spike protein. *Science*. **370**, pp. 725-730, (2020).
[36] D.K. Shoemark, C.K. Colenso, C. Toelzer, K. Gupta, R.B. Sessions, A.D. Davidson, I. Berger, C. Schaffitzel, J. Spencer, A.J. Mulholland. Molecular Simulations suggest Vitamins, Retinoids and Steroids as Ligands of the Free Fatty Acid Pocket of the SARS-CoV-2 Spike Protein. *Angew. Chemie Int. Ed.* **60**, pp. 7098-7110, (2021).
[37] T. Tang, M. Bidon, J.A. Jaimes, G.R. Whittaker, S. Daniel. Coronavirus membrane fusion mechanism offers a potential target for antiviral development. *Antiviral Res.* **178**, p. 104792, (2020).
[38] M.B. Battles, J.P. Langedijk, P. Furmanova-Hollenstein, S. Chaiwatpongsakorn, H.M. Costello, L. Kwanten, L. Vranckx, P. Vink, S. Jaensch, T.H.M. Jonckers, et al. Molecular mechanism of respiratory syncytial virus fusion inhibitors. *Nat. Chem. Biol.* **12**, pp. 87–93, (2016).
[39] A. Romeo, F. Iacovelli, M. Falconi. Targeting the SARS-CoV-2 spike glycoprotein prefusion conformation: virtual screening and molecular dynamics simulations applied to the identification of potential fusion inhibitors. *Virus Res.* **286**, p. 198068, (2020).
[40] S. Kumar, R. Nussinov. Close-Range Electrostatic Interactions in Proteins. *ChemBioChem*. **3**, p. 604, (2002).
[41] J. Warwicker. A model for pH coupling of the SARS-CoV-2 spike protein open/closed equilibrium. *Brief. Bioinform.* **22**, pp. 1499–1507, (2021).
[42] P.S. Masters. The Molecular Biology of Coronaviruses. *Adv. Virus Res.* **65**, pp. 193-292, (2006).
[43] J. Sikkema, J.A. de Bont, B. Poolman. Mechanisms of membrane toxicity of hydrocarbons. *Microbiol. Rev.* **59**, pp. 201-222, (1995).
[44] Y. Gao, X. Liang, Q. Wang, S. Zhang, H. Zhao, K. Wang, G. Hu, W.J. Liu, F. Gao. Mind the feline coronavirus: Comparison with SARS-CoV-2. *Gene.* **825**¸ p. 146443, (2022).
[45] E.E. Schirtzinger, Y. Kim, A.S. Davis. Improving human coronavirus OC43 (HCoV-OC43) research comparability in studies using HCoV-OC43 as a surrogate for SARS-CoV-2. *J. Virol. Methods.* **299**, p. 114317, (2022).

AB INITIO STUDY OF AN OCTANE MOIETY ADSORBED ON H- AND CL- FUNCTIONALIZED SILICON NANOWIRES

Barbara Ferrucci[1*], Francesco Buonocore[2], Simone Giusepponi[2], Massimo Celino[2]

[1]*ENEA, Bologna Research Centre, I- 40129 Bologna, Italy*

[2]*ENEA, Casaccia Research Centre, I-00123 Rome, Italy*

ABSTRACT. The silicon nanowires (SiNWs) surfaces' oxidation is a phenomenon affecting the SiNWs-based nanodevices performances. Surface functionalization is one of the best techniques to modify the overall electronic properties of SiNWs. To this end, Silicon atoms at the SiNW surface can be terminated with a variety of molecules bearing covalent interfacial bonds, among these Si-C bonds are exploited to reduce tendency to the oxidation of the SiNWs. In this study, we performed DFT calculations employing Quantum Espresso ab-initio simulation package to investigate surface oxidation resistance of SiNWs fully functionalized with H- and Cl- atoms and with C_8H_{17} alkane molecule adsorbed on the (111) or (110) surface. The results show that the Si-C bonds on the surface can enhance protection against oxidation without substantial modification of the electronic properties.

1 Introduction

Silicon nanowires are attractive materials for use in numerous applications due to their unique optical, mechanical, and electrical properties. However, they can achieve a better performance by adjusting their surface properties with organic/inorganic compounds. For many specific device settings, the protection of the SiNWs surfaces against oxidation is a key issue. Bashouti et al. [1] showed that chlorination/alkylation process for functionalizating SiNWs with C_1-C_6 alkyl chains provides surface oxidation resistance that depends on the chain length and molecular coverage.

In this study, we investigate the effect of an octane moiety, C_8H_{17}, adsorbed on the (111) or (110) surface of a fully hydrogen- and chlorine-functionalized SiNW oriented along the <112> direction. The choice of the octane moiety as adsorbed molecule was made because of its length that well fits the objective to investigate the variation of some structural parameters such as rotation and/or alignment of the molecule with respect the SiNW surfaces. We calculated the energetics and electronic properties of the system to compare the effect of the position of the adsorbed molecule on different surfaces. DFT models were established to find the optimized geometry and calculate the formation energy of the systems.

2 Methods

Calculations were performed within the periodic density functional theory (DFT) as implemented in the PWscf (plane-wave self-consistent field) code of the QUANTUM ESPRESSO package [2], compiled with Intel Fortran compiler, Math Kernel Library (MKL) and Message Passing Interface (MPI) parallelization on the Cresco6 cluster of the high-performance computer facility CRESCO [3], with a good scalability up to hundreds of cores. The exchange-correlation energies were treated with the Perdew, Burke and Enzerholf (PBE) functional [4]. For the investigated systems the electron–ion interactions were described by the ultra-soft Vanderbilt pseudopotentials [5] using an energy cut-off of

*Corresponding author. E-mail: barbara.ferrucci@enea.it

40 Ry, and a charge density of 400 Ry. The force and energy threshold have been imposed equal to 1.0E-4 Ry/Bohr and 1.0E-5 Ry respectively. The Brillouin zone of the system was sampled by 1×1×8 k-points in the z direction.
Using a supercell periodic along the <112> direction, we modelled a SiNW enclosed with the (111) and (110) facets and fully functionalized with hydrogen (H) and chlorine (Cl) atoms. Each SiNW consists of 192 atoms of Si, and 79 atoms of H or Cl at the top sites of the nanowire surface. An octane moiety adsorbed on the two different surfaces of each system has been modelled obtaining the following systems:

- [(111)_C_8H_{17}]-H-SiNWs (fully hydrogenated SiNW with hydrogen and with the octane moiety adsorbed on the (111) surface)
- [(110)_C_8H_{17}]-H-SiNWs (fully hydrogenated SiNW with the octane moiety adsorbed on the (110) surface)
- [(111)_C_8H_{17}]-Cl-SiNWs (fully chlorinated SiNW with the octane moiety adsorbed on the (111) surface)
- [(110)_C_8H_{17}]-Cl-SiNWs (fully chlorinated SiNW with the octane moiety adsorbed on the (110) surface).

For each system the formation energy, the bond dissociation energy, the electronic band structure, the partial density of states (PDOS), and the differential charge density have been calculated.
As we have shown in the previous report [5], once the orientation of the Si NW is such that the 110 facets are parallel to the yz plane, setting the option npools to 5 and scaling up from 96 to 480 cores, there is a gain of 5.4 times of the calculation time and a good performance with an efficiency of ~ 82%. This improvement in the performance is mainly due to (1) the rotation of the system and (2) the npools option of the code. Since the code distributes the workload along the z dimension, making a rotation so that the side of the supercell along this direction is the largest, causes that the workload is better distributed among the cores. The npools option allows to dedicate for each k point a group of cores minimizing communication between them. This type of "parallelization" is almost linear with number of k points.

3 Results and discussion

In Figure 1 and Figure 2 the initial and optimized configurations of the four systems are reported. In all the initial configurations the octane moiety forms an angle, φ, of 60° with respect the (111) or (110) plan, depending on the surface chosen to adsorb. After relaxation, φ increases for both the chlorinated configurations with an increment (+Δφ), of about 37° and 40° for the octane adsorbed on the (111) and (110) surface, respectively (Figure 1). A +Δφ of about 46° was observed for the hydrogenated system with the octane adsorbed on the (111) surface. While a decrease, (-Δφ), of about 8° occurs for the hydrogenated system with the octane adsorption on the (110) surface (Figure 2).
For each system we calculated the bond dissociation energy (BDE) (Table 1). We found higher BDE value for both the chlorinated systems with respect to the hydrogenated systems. This means that the Cl atoms improve the structural stability of the wire better than H atoms. Moreover, the BDE of the C_8H_{17} molecule on Cl-SiNW is up to 1.00 eV larger than on H-SiNW, which can be attributed to the major electronic affinity of chlorine atoms relative to hydrogen atoms.

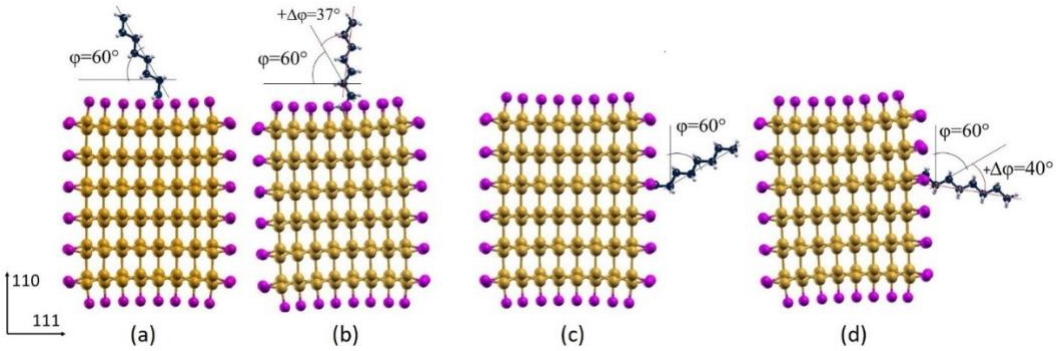

Figure 1. Initial (a, c) and optimized (b, d) geometry configurations of the octane moiety on the (111) (a,b) and (110) (c,d) surfaces of Cl-functionalized <112> oriented SiNWs (mustard-colour: Si atoms, magenta: Cl atoms, white: H atoms, blue: C atoms).

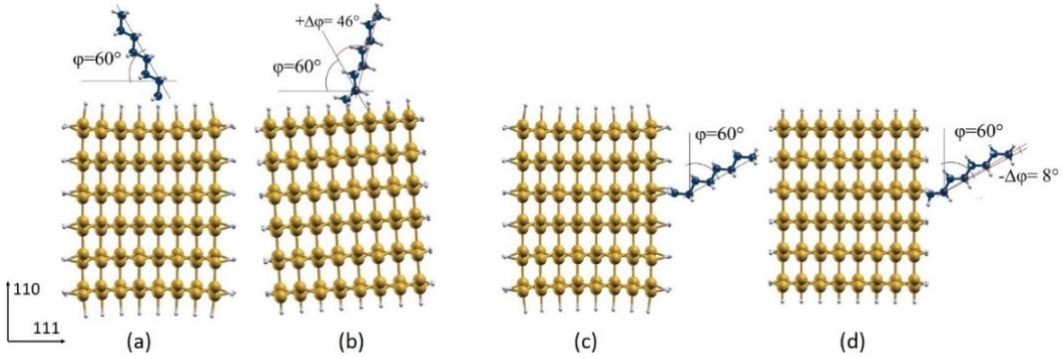

Figure 2. Initial (a, c) and optimized (b, d) geometry configurations of the octane moiety on the (111) (a,b) and (110) (c,d) surfaces of H-functionalized <112> oriented SiNWs (mustard-colour: Si atoms, white: H atoms, blue: C atoms).

Table 1. Bond dissociation energy values of the modelled systems.

NW Structure	BDE (eV)	BDE (kJ/Mol)
[(111)_C_8H_{17}]-Cl-SiNW	7.60	733.85
[(110)_C_8H_{17}]-Cl-SiNW	7.42	716.47
[(111)_C_8H_{17}]-H-SiNW	6.60	637.30
[(110)_C_8H_{17}]-H-SiNW	6.49	632.67

The calculated formation energy per atom, E_F, is quite independent on the molecule adsorption surface resulting:

- E_F([(111)/(110)_C_8H_{17}]-Cl-SiNWs) ~ -0.48 eV, and
- E_F([(111)/(110)_C_8H_{17}]-H-SiNWs) ~ -0.053 eV.

In agreement with the DBE calculations, the chlorinated systems present the more stable configurations.

The calculated band structure of the four systems (Figure 3) presents the maximum of the valence-band near the Γ point, and the minimum of the conduction-band near the Z point, exhibiting an indirect band gap in all cases. The band structures and the PDOS (Figure 4) show a weak dependence on the adsorption surface. The valence and conduction band edges of the H-SiNW is mainly composed of the silicon-p orbitals, Si(p), while a major contribution of chlorine p-orbitals, Cl(p), can be noted for the Cl-SiNW. The resulting valence-conduction band gap is 1.26 eV and 1.29 eV for the chlorinated and hydrogenated systems respectively.

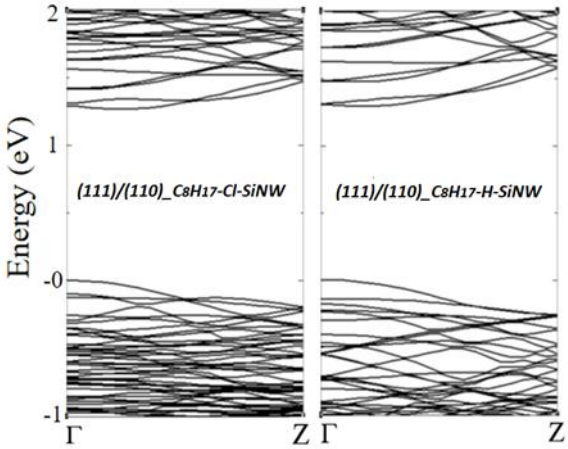

Figure 3. Band structure of Cl- (left) and H-SiNWS-C_8H_{17} (right) systems. The top of the valence band is set to zero.

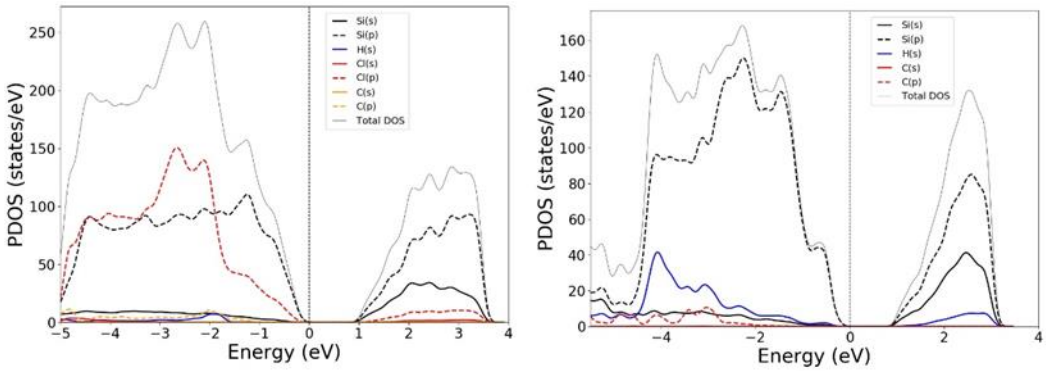

Figure 4. Projected electron density of states (PDOS) of Cl-SiNWS-C_8H_{17} (left) and H-SiNWS-C_8H_{17}(right) systems.

The differential charge density was calculated to further investigate the electronic properties of the four systems. Figure 5 shows the iso-surface plots of the differential charge density. There is a charge accumulation between the Si and C atoms along the Si-C bond, and over the C atom close to the Si-C bond. Moreover, a charge depletion around the Si atom and near the bond edge of the C atom can be observed, and a more minor charge depletion and accumulation on the C-C bond edges close to the Si-C bond.

For all the four adsorption configurations, the Löwdin charge analysis shows a partial charge of 48.5 *e* localized on the molecule, corresponding to an increase of 0.2 e with respect the partial charge of 48.3 *e* of the isolated C_8H_{17}. Therefore, a charge transfer from the SiNW to the molecule is observed for both surface orientations with no dependence on Cl- or H-functionalization which explaining the increase in the stability.

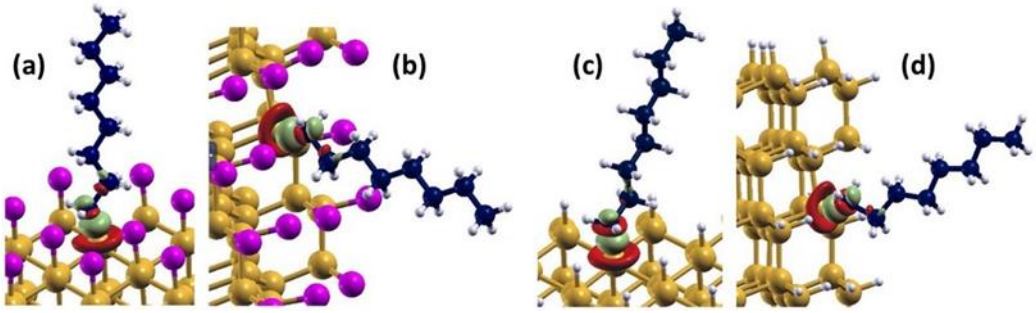

Figure 5. Iso-surface of differential charge density of [(111)_C_8H_{17}]-Cl-SiNW, (a);[(110)_C_8H_{17}]-Cl-SiNW, (b); [(111)_C_8H_{17}]-H-SiNW, (c); and [(110)_C_8H_{17}]-H-SiNW, (d). The isosurface value is set 0.005 (mustard-colour: Si atoms, white: H atoms, magenta: Cl atoms, blue: C atoms) regions of green and red indicate charge accumulation and depletion respectively.

4 Conclusions

The SiNWs functionalization of nanomaterials plays a critical role since it affects properties and improves performances of the nanobased devices. The alkyl functionalization can enhance protection of the hydrogenated and chlorinated nanowire quantum surfaces against oxidation without substantial modification of the electronic properties. This research will allow to design efficient procedures to increase the overall efficiency of the devices based on Si NWs.

References

[1] M. Bashouti et al. Covalent Attachment of Alkyl Functionality to 50 nm Silicon Nanowires through a Chlorination/Alkylation Process. *J. Phys. Chem. C* **113** pp. 14823–14828 (2009).

[2] J.P. Perdew, K. Burke and M. Ernzerhof. Generalized Gradient Approximation Made Simple. *Phys. Rev. Lett.* **77** pp. 3865−3868 (1996).

[3] F. Iannone et al. CRESCO ENEA HPC clusters: a working example of a multifabric GPFS Spectrum Scale layout. 2019 *International Conference on High Performance Computing & Simulation (HPCS)*, Dublin, Ireland, pp. 1051-1052 (2019).

[4] D. Vanderbilt. Soft Self-Consistent Pseudopotentials in a Generalized Eigenvalue Formalism. *Phys. Rev. B: Condens. Matter Mater. Phys.* **41**, p. 7892, (1990).

[5] B. Ferrucci, F. Buonocore, S. Giusepponi, M. Celino. Ab initio study of the electronic properties of H- and Cl-functionalized silicon nanowires. In “High Performance Computing on CRESCO Infrastructure: research activity and results 2020”, pp. 181−186. ISBN: 978-88-8286-429-3.

BENCHMARK OF PWSCF CODE ON CRESCO 6 FOR THE STUDY OF SILICON BASED MATERIALS HETEROINTERFACE

Simone Giusepponi[1*], Francesco Buonocore[1], Massimo Celino[1], Sebastian Achilles[2], Edoardo Di Napoli[2], Irene Aguilera[3] and Alessandro Pecchia[4]

[1]*ENEA-TERIN-ICT Division, CR Casaccia, Via Anguillarese 301, Roma, Italy.*

[2]*JSC, Forschungszentrum Jülich, Wilhelm-Johnen Straße, Jülich, Germany.*

[3]*IEK-5, Forschungszentrum Jülich, Wilhelm-Johnen Straße, Jülich, Germany.*

[4]*CNR-ISMN, Sede Montelibretti, Via Salaria Km 29, 300, Montelibretti, Italy.*

ABSTRACT. In this report we present benchmark results for PWscf code (Quantum Espresso suite) to perform ad-initio study of a crystalline Silicon/hydrogenated amorphous Silicon heterointerface system.

1 Introduction

In view of an intensive use of computational resources for an *ab initio* study of a crystalline Silicon (c-Si) and hydrogenated amorphous Silicon (a-Si:H) heterointerface (see Fig. 1), a measure of the performances of PWscf (Plane-Wave Self-Consistent Field) code of the Quantum ESPRESSO suite ver. 6.6 [1, 2] on ENEA-CRESCO6 HPC infrastructure is carried out.

The *ab initio* characterization of the c-Si/a-Si:H/c-Si heterointerface, giving the electronic properties, can provide useful indications in the understanding of the transport mechanisms underlying photovoltaic devices based on silicon heterojunction technology [3, 4].

This benchmark enables us to set up the optimal computational resources and to give us an estimation of the required computational times. The benchmark is based on the time required to execute a Self-Consistent Field (SCF) calculation and a Non-Self-Consistent Field (NSCF) calculation, for a single energy minimization in the computation of the ground-state energy of the c-Si/a-Si:H heterointerface system depicted in Fig. 1. The system is made up of 336 atoms (320 Si + 16 H atoms), the simulation cell dimensions are $L_X = L_Y = 15.48$ Å and $L_Z = 28.36$ Å and periodic boundary conditions (PBC) are imposed in all directions. We use Si and H ultrasoft pseudopotentials with Perdew-Burke-Ernzerhof (PBE) [5] approximant GGA exchange-correlation potential. The electronic wave functions are expanded in a plane-wave basis set with a kinetic energy cut-off equal to 30 Ry (the charge density cut-off was 300 Ry). For the SCF calculation the Brillouin zone integration is performed over 4 k-points, instead for NSCF calculation 9 k-points are selected. Methfessel-Paxton smearing of 0.08 Ry is needed to reach convergence due to defect states at the Fermi level. All the parameters are chosen by preliminary calculations.

Quantum ESPRESSO suite is compiled using Intel compilers, MKL (BLAS, LAPACK and ScaLAPACK) library, and MPI parallelization. CRESCO6 is a HPC system consisting of 434 dual 24 cores Skylake cpu nodes, with a peak performance of 1.4 PFlops. The nodes are interconnected by an Intel Omni-Path network with a bandwidth equal to 100 GB/s, latency equal to 100ns.

* Corresponding author. E-mail: simone.giusepponi@enea.it.

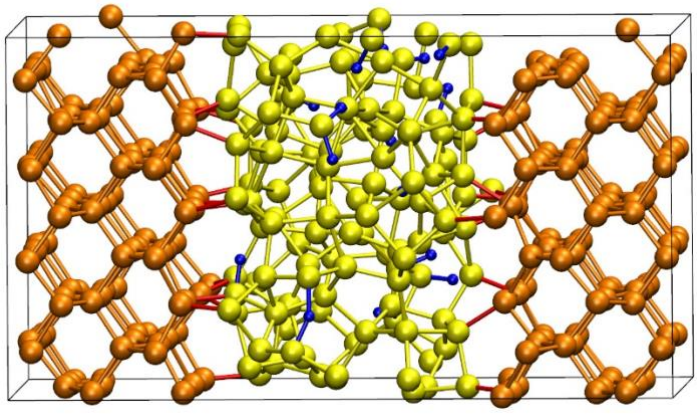

Fig.1: Snapshot of the c-Si/a-Si:H heterointerface in the simulation cell. Hydrogen atoms are in blue, Silicon atoms are in orange in the c-Si side and are in yellow in the a-Si:H side.

2 Results and discussion

To evaluate the performance and scalability of the PWScf code on CRESCO6, we collect the time necessary to perform SCF and NSCF calculation for the minimization of the ground-state energy of the c-Si/a-Si:H heterointerface system depicted in Fig. 1.

In Quantum ESPRESSO several parallelization levels, specified at run-time via command-line options to the executable, are implemented with MPI. This permits to distribute both calculations and data structures across processors. We test two of them, primarily **pools** (**nk**) and then **tasks** (**nt**).

By **pools**: each calculation can be sub partitioned into "pools", each taking care of a group of k-points. These are loosely coupled and then inter-processors communication between different pools is modest. Processors within each pool are instead tightly coupled and communications are significant. This means that fast communication hardware is needed if your pool extends over more than a few processors on different nodes. To have better performance, nk have to be a divisor of the number of the k points.

Tasks is used in order to allow good parallelization of the 3D FFT when the number of processors exceeds the number of FFT planes, FFTs on Kohn-Sham states are redistributed to "task" groups so that each group can process several wavefunctions at the same time. Alternatively, when this is not possible, a further subdivision of FFT planes is performed.

Fig.2 and Fig.3 show benchmark results for SCF and NSCF calculations, respectively. Graphs on the top of the figures depict the total time required for the calculations in function of the number of cores used. Those in the middle, report the speed-up calculated with respect to the time for 48 cores (1 node) calculation. The efficiency of the parallelization is shown in the bottom graphs of the figures. Red symbols refer to the cases in which no Quantum Espresso parallelization levels are used, i.e., **nk**=1 and **nt**=1 (default values). We can observe that efficiency in the parallelization degrades very quickly dropping at about 50 % for more than 192 cores (4 nodes). Taking advantage of the **pools** parallelization levels, it is possible to improve the speed-up reaching an efficiency higher than 75% for the SCF calculation with **nk**=2 (green symbols) and 192 cores and for the NSCF calculation with **nk**=3 (green symbols) and 288 cores. A number of **pools** equal to the maximum number of k points, **nk**=4 for SCF (blue symbols) and **nk**=9 for NSCF (blue symbols), produces a further improvement in the performance. For SCF calculation the efficiency is about 75% with 384 cores and it is higher than 50 % doubling the cores at 768. The NSCF calculation, having a greater number of k points, exhibits an almost linear speed-up up to 864 cores with an efficiency of 78%. In the latter case, nine **pools**, each of two nodes, perform the calculation in parallel. Each **pool** takes care of a single k point.

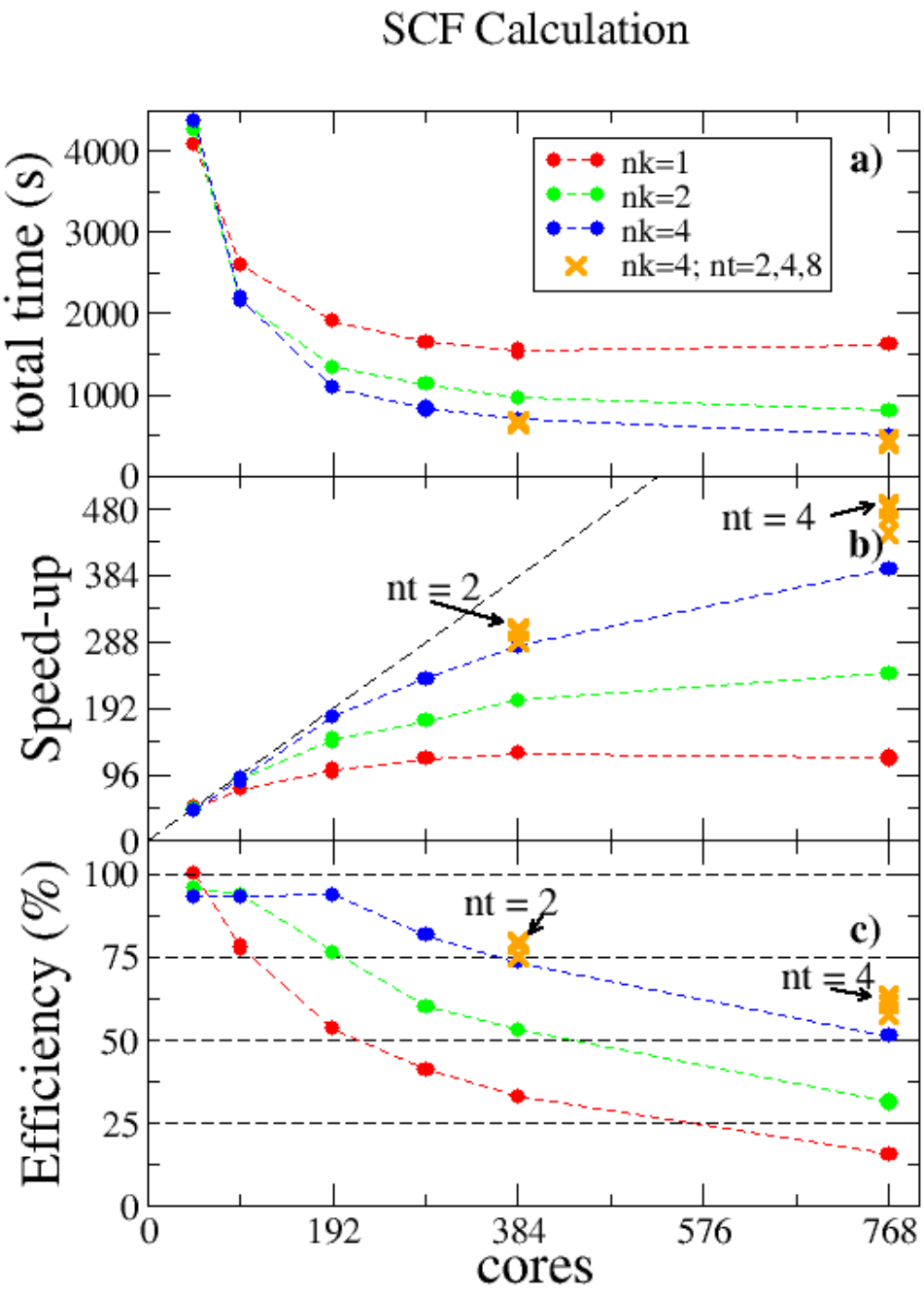

Fig.2: a) Total time (s) for a self-consistent field (SCF) calculation. b) Speed up calculated with respect to the time in the 48 cores calculation, and c) the corresponding efficiency (%). Red symbols(lines) are for **pools**(**nk**)=1, green symbols(lines) are for **pools**(**nk**)=2 and blue symbols(lines) are for **pools**(**nk**)=4. Orange symbols refer to different values of **tasks**(**nt**).

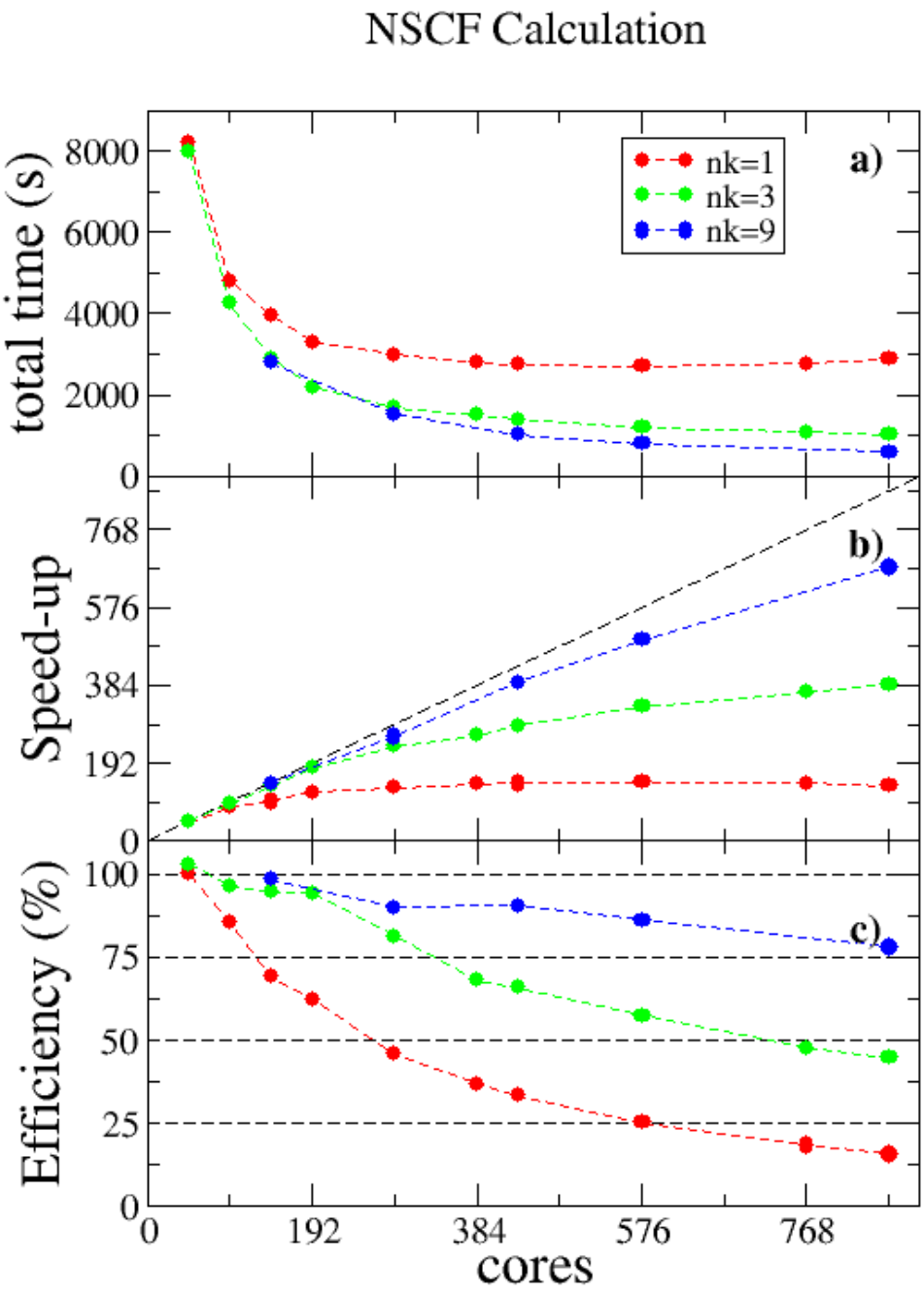

Fig.3: a) Total time (s) for a Non Self-Consistent Field (NSCF) calculation. b) Speed up calculated with respect to the time in the 48 cores calculation, and c) the corresponding efficiency (%). Red symbols(lines) are for **pools**(**nk**)=1, green symbols(lines) are for **pools**(**nk**)=3 and blue symbols (lines) are for **pools**(**nk**)=9.

As a final test we try the **tasks** level of parallelization, even if we limit our analysis only to the SCF calculation with **nk**=4. Differently to the **pools** option, we observe a lower impact in the parallelization

scalability, however, the efficiency rises from 73% up to 80% for 384 cores with **nt**=2, and from 51% up to 63% for 768 core with **nt**=4.

In conclusion, we explored some run time options (**pools** and **tasks**) of the code PWScf to increase its parallel scalability. Thanks to this possibility we reached a good parallel scalability up to several hundreds of cores. This is particularly useful for systems, like our that is made up of many atoms, that are very computationally demanding. The benchmark results schematically provide a sort of "recipe" to identify the computational parameters for a profitably use of the **pools** and **tasks** options.
Firstly, perform calculations with default values for **pools** and **tasks**, and identify the maximum number of cores "nc_1" for which the efficiency is greater than 70-80 %: in our case 96 cores for both SCF and NSCF calculations. Then, choose a number of cores equal to nc_1 × number of k points and set **nk**=number of k points: in our case 96 × 4 = 384 cores and **nk** = 4 for SCF, and 96 × 9 = 864 cores and **nk**=9 for NSCF calculation, respectively. Finally, setting nt equal to 2 or 4 can improve performance, but with less noticeable effects.

References

[1] P. Giannozzi, S. Baroni, N. Bonini, M. Calandra, R. Car, C. Cavazzoni, D. Ceresoli, G. L. Chiarotti, M. Cococcioni, I. Dabo, A. Dal Corso, S. Fabris, G. Fratesi, S. de Gironcoli, R. Gebauer, U. Gerstmann, C. Gougoussis, A. Kokalj, M. Lazzeri, L. Martin-Samos, N. Marzari, F. Mauri, R. Mazzarello, S. Paolini, A. Pasquarello, L. Paulatto, C. Sbraccia, S. Scandolo, G. Sclauzero, A. P. Seitsonen, A. Smogunov, P. Umari, R. M. Wentzcovitch. J.Phys.: Condens.Matter **21**, 395502 (2009).
[2] P. Giannozzi, O. Andreussi, T. Brumme, O. Bunau, M. Buongiorno Nardelli, M. Calandra, R. Car, C. Cavazzoni, D. Ceresoli, M. Cococcioni, N. Colonna, I. Carnimeo, A. Dal Corso, S. de Gironcoli, P. Delugas, R. A. DiStasio Jr, A. Ferretti, A. Floris, G. Fratesi, G. Fugallo, R. Gebauer, U. Gerstmann, F. Giustino, T. Gorni, J Jia, M. Kawamura, H.-Y. Ko, A. Kokalj, E. Kucukbenli, M .Lazzeri, M. Marsili, N. Marzari, F. Mauri, N. L. Nguyen, H.-V. Nguyen, A. Otero-de-la-Roza, L. Paulatto, S. Poncé, D. Rocca, R. Sabatini, B. Santra, M. Schlipf, A. P. Seitsonen, A. Smogunov, I. Timrov, T. Thonhauser, P. Umari, N. Vast, X. Wu, S. Baroni. J.Phys.: Condens.Matter **29**, 465901 (2017).
[3] F. Buonocore, S. Giusepponi, M. Celino, P. L. Garcia-Muller, R. Mayo-Garcia. 2020 Winter Simulation Conference p. 3117 (2020).
[4] A. Pecchia, F. Buonocore, M. Celino, S. Giusepponi, E. Di Napoli, S. Achilles, P. L. Garcia-Muller, R. Mayo-Gacia. 2021 Winter Simulation Conference p. 1 (2021).
[5] J. P. Perdew, K. Burke, M. Ernzerhof. Phys. Rev. Lett. **77**, p. 3865 (1996).

DEVELOPMENT OF MONTE CARLO RADIATION TRANSPORT ALGORITHMS AND APPLICATION TO PWR GEN-II AND GEN-III SAFETY PROBLEMS

K.W. Burn[1], P. Console Camprini[2]

[1]*ENEA, Bologna – IT (retired)*

[2]*ENEA, C.R. Brasimone 40032 Camugnano (Bologna) – IT*

ABSTRACT. The development and application of innovative Monte Carlo algorithms applied to radiation transport, continuing from previous years, is summarized. Parallel processing with MPI is employed with typically 192 or 384 CPU's. A feature of the algorithm is the passing between CPU's (between slaves and slaves-to-master) of large data arrays.

We have continued the collaboration with the French Nuclear Safety Authority IRSN (Institut de Radioprotection et de Sûreté Nucléaire) on lengthening the lifetime of currently-operating Pressurized Water Reactors (PWR's) and improving the safety of next-generation PWR's.

In 2021 the main activity was the production of four papers (two external and two ENEA internal support) [1-4]. Also work was started on an external paper which was submitted for publication in 2022 [5].

We apply innovative Monte Carlo variance reduction (VR) algorithms, developed at ENEA, to modelling critical radiation responses in current and future reactor models. The algorithms that we developed and employ may be found in [1-5] and references cited therein. Our approach is based on the DSA (Direct Statistical Approach) [6,7]. There are two aspects of the DSA codes that are worth noting in the context of their execution on the machines of the CRESCO system.

1 The handling of large arrays of variable format and their integration at rendez-vous points

This has been discussed in previous CRESCO reports and will therefore only be summarized here.

The current version of the DSA uses as vehicle MCNP6 ver. 1.0 [8]. On the CRESCO6 system it is compiled with the default intel compiler (**intel17**) and with the default parallel processing option: **openmpi_intel17-3.1.2**. We have seen a continued improvement in the data passing performance compared to 2020, presumably due to "tweaks" to the implemented MPI.

2 Minimizing the quality function using DUMING from IMSL

Again, this has been discussed in previous CRESCO reports and only the changes from 2020 will be reported here.

We employ a program we wrote in FORTRAN-90 that calls the routine DUMING of the commercial IMSL library in scalar mode (unconstrained minimization of a multi-variate function using a quasi-Newton method and a user-supplied gradient). After an update of the CRESCO machines in April 2021, IMSL ceased to work.

Subsequently a dedicated node (cresco4x169.portici.enea.it) was made available with the software that preceded the update to allow legacy software to continue to be used. Since that time we have been running the minimization program on that node. Unfortunately the node seems to us slightly slow, even compared to the previous CRESCO4sm01/02 although we have not made quantitative tests. Furthermore the node does not support LSF, which for runs of 10-20 h can create problems.

Therefore while continuing to use IMSL for the results reported in the references, we looked for other software that might substitute DUMING.

We looked at the GNU Scientific Library (called GSL) (written in C) in the multidimensional minimization section https://www.gnu.org/software/gsl/doc/html/multimin.html to try to find a routine as near as possible to DUMING.

Focusing on the category "Algorithms with Derivatives": https://www.gnu.org/software/gsl/doc/html/multimin.html#algorithms-with-derivatives, we saw the routine "**gsl_multimin_fdfminimizer_vector_bfgs2**". This routine employs the Broyden-Fletcher-Goldfarb-Shanno (BFGS) algorithm which is close to the algorithm that DUMING is using.

We downloaded the penultimate version of GSL is 2.6 (note the latest version is 2.7 but this version does not support FGSL (see below)) and (we believe) successfully installed it on CRESCO6. The documentation of GSL seems very poor, at least compared with IMSL.

We saw that there are "wrappers" or "binders" (which we interpret as interface programs) that can be employed when linking a program written in a language that is not C, to GSL. For FORTRAN, such interface program is "FGSL"
https://doku.lrz.de/display/PUBLIC/FGSL++A+Fortran+interface+to+the+GNU+Scientific+Library

The latest version of FGSL is 1.5.0. This works with the penultimate version of GSL, 2.6. We successfully installed FGSL1.5.0 on CRESCO6. Of the 59 test problems in the installation, 58 ran and 1 failed. As FGSL interfaces with GSL, this gave us some confidence that at least some parts of GSL were functioning correctly. Unfortunately the 59 problems do not include any multidimensional minimizations, so a substantial amount or work would still need to be done to construct the interface. Again the documentation of FGSL is not optimal.

Notwithstanding the obstacles outlined above to the implementation of this freesoftware, for the transportability of the VR algorithms we will continue to try to implement and test it on the CRESCO system.

3 Some illustrations

The implementation of the VR algorithms in eigenvalue problems such as a reactor core, or a storage array of fissile material, involves the introduction of a number of features in the Monte Carlo transport. One such is "fictitious source cells" [1,2]. These are illustrated in Fig. 1 for an idealized situation of 7 spatial cells and 4 energy groups.

In Fig. 2 are shown the results of various spatial decoupling approximations on the $^{54}Fe(n,\gamma)$ activation rate at two depths in the radial concrete surrounding the well in a PWR GEN III model.

References

[1] M. Brovchenko, K.W. Burn and P. Console Camprini, "On Integrating Monte Carlo Calculations in and around Near-Critical Configurations – I. Methodology," *Ann. Nucl. Energy* **172** (2022) 109063

[2] P. Console Camprini, K.W. Burn and M. Brovchenko "Monte Carlo with Variance Reduction in and around Near-Critical Configurations," ENEA NK-N-R-570 Rev.1 (2022)

[3] M. . Brovchenko, K.W. Burn and P. Console Camprini, "On Integrating Monte Carlo Calculations in and around Near-Critical Configurations – II. Pressurized Water Reactors," *Ann. Nucl. Energy* **180** (2023) 109417

[4] P. Console Camprini, K.W. Burn and M. Brovchenko, "Comparison of Integrated and Decoupled Monte Carlo Results outside Pressurized Water Reactor Cores," ENEA NK-N-R-579 Rev.1 (2022)

[5] K.W. Burn, "Comparing the 1st and 2nd Moment Approaches to Variance Reduction in Monte Carlo: an Example," submitted for publication in *Ann. Nucl. Energy* (2022)

[6] K.W. Burn, "Optimizing variance reduction in Monte Carlo eigenvalue calculations that employ the source iteration approach," *Ann. Nucl. Energy,* **73**, pp. 218–240 (2014)

[7] K.W. Burn, "A correction and a clarification to 'Optimizing variance reduction in Monte Carlo eigenvalue calculations that employ the source iteration approach'," *Ann. Nucl. Energy*, **85**, pp. 776–777 (2015)

[8] Denise B. Pelowitz (Ed.), "MCNP6™ User's Manual – Version 1.0", Los Alamos National Laboratory, LA-CP-13-00634, Rev. 0 (2013)

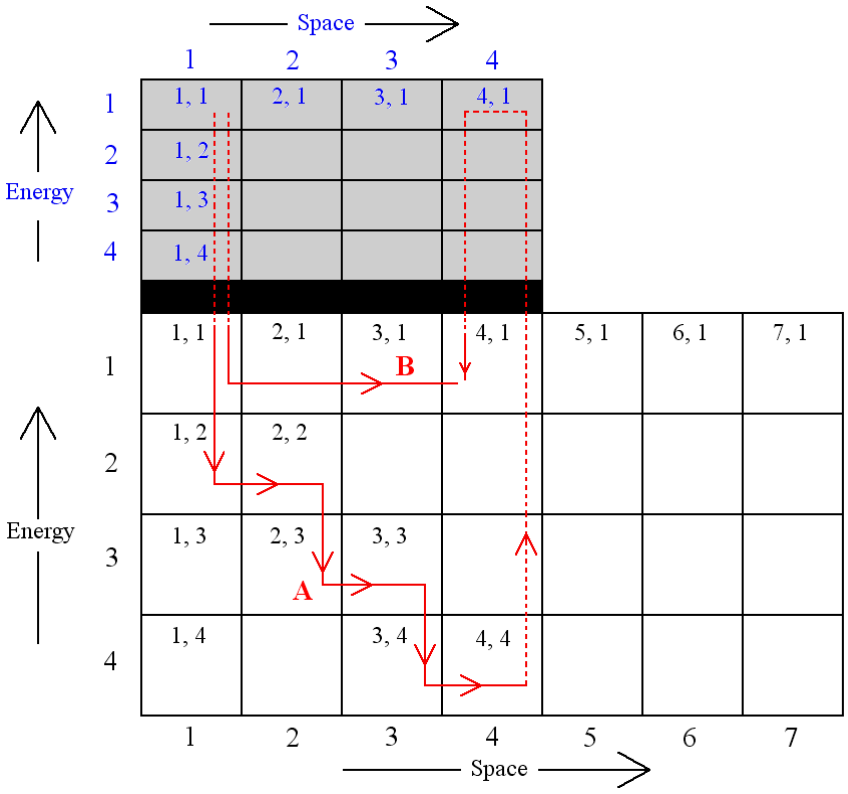

Fig. 1. Depiction of a configuration of phase space cells in a fissile zone with fictitious source cells (Fig. 3 in [2])

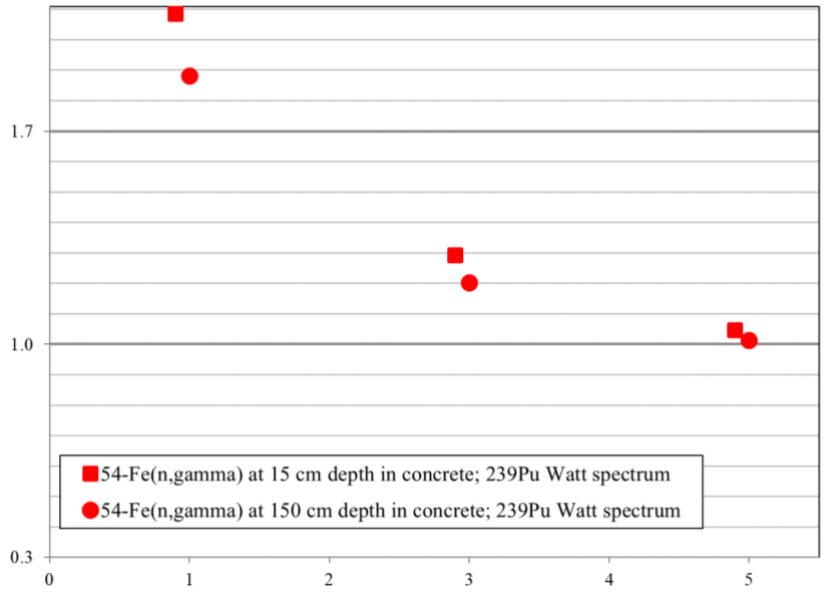

Fig. 2. PWR GEN III: Ratio of decoupled to eigenvalue result for the ^{54}Fe(n,γ) rate in the concrete for the Watt spectrum for thermal neutron-induced fission on ^{239}Pu and following spatial binning of the fission sites (x: 1: homogeneous; 3: assembly-wise; 5: dual pin-wise) (Fig. 53 in [4])

STATISTICAL PROCESS MONITORING AIDED BY NEURAL NETWORKS WITH AN APPLICATION TO HVAC SYSTEMS IN PASSENGER RAIL VEHICLES

Fiorenzo Ambrosino[1], Antonio Lepore[2*], Biagio Palumbo[2] and Gianluca Sposito[2]

[1]*ENEA, Italian National Agency for New Technologies Energy and Sustainable Economic Development, Portici, Italy*

[2]*Department of Industrial Engineering, University of Naples Federico II, Naples, Italy*

ABSTRACT. For the rail industry, efficient temperature regulation is becoming a crucial task to improve passenger thermal comfort. Its importance is due to government regulations that require rail industries to implement monitoring systems and methods for controlling Heating, Ventilation and Air Conditioning (HVAC) systems of modern trains. Modern automated systems create a new dimension in the diagnostics and maintenance of complex systems in a new cost-effective and efficient way. This framework calls for new methods to deal with high-dimensional, high-correlated and heterogeneous data. In this article, a novel method based on the application of Neural Networks to pattern recognition in statistical quality control is introduced by means of real industrial data to support the prognosis of faults.

1 Introduction

In recent years railways are going through a process of restructuring, characterized by an increase in competition between operators. In fact, travellers are increasingly choosing rail as a viable alternative to other means of transport. Over the past few years, new European standards were developed for thermal comfort, considering the different operating requirements of rail vehicles. European Standard UNI EN 14750 [1] prescribes requirements for controlling the air temperature, relative humidity, and air speed within passenger compartments. To meet this standard and to improve the performance of heating, ventilation, and air conditioning (HVAC) systems, railway companies have been collecting and storing data to improve their reliability, maintenance, and safety. During the working life of a system, different kinds of faults may occur, and the original design functions may be lost. It is very important to identify and monitor a fault in a complex system since fault detection can help to reduce maintenance costs and operations to improve the system reliability and schedule maintenance efficiently. To reach this goal, we have many sensors, collecting different parameters in different working conditions. Modern automated systems create a new dimension in the diagnostics, maintenance, and operation of these systems in a new cost-effective and efficient way. The challenge is to turn these high-dimensional, high-correlated, and heterogeneous data affected by noise and environmental fluctuations into value. In the modern big data framework, classical Statistical methods [2] and Machine Learning [3] methods interplay without sharp boundaries. In particular, Artificial Neural Networks (NNs) can automatically extract significant features from data, meaning that they will be representative of the actual health state of the system. We can generally refer to two types of training processes: supervised and non-supervised. Supervised NN methods can identify normal and out-of-normal behaviours but require a sufficiently large number of labelled training data, showing normal and non-normal behaviour observations. Ideally, the same number of training data should be available for each behaviour class. In this way, the method will work, but since we will not use most of the information, present in the dataset, the accuracy will be very coarse. In common practice, this is not feasible as systems usually work under normal conditions for most of their life and faults are generally very rare making real datasets usually unbalanced. Moreover, fault conditions may be not properly

*Corresponding author. e-mail: antonio.lepore@unina.it

recorded by fault logging systems. So stated, it is usually hard to correctly label anomalies. On the other hand, unsupervised NN approaches do not require labelled training data and any additional information on the input data, but generally show a lower performance accuracy. In this paper, we refer to a semi-supervised approach that exploits the characteristics of the two approaches described before. Non-normal data are filtered away from the training set in such a way that the reference sample shows only normal behaviour. In this way, we can obtain three main advantages: (i) the possibility of detecting anomalies in the training set even if they are not reported; (ii) we do not have necessarily to change the working condition of our system of interest to collect anomalous data; (iii) the model is directly trained on a row time series coming from heterogeneous data without hand-crafting any features.

2 Methods

In this paper, we introduce an approach based on a particular type of NN, an Autoencoder, that will be trained only on data in which the system shows normal behaviour in such a way that, after training, anomaly data, not included in the training set, will be considered as outlier. Then, two control charts based on statistics H^2 [4] and the squared prediction error (*SPE*) [5] will be designed in a non-parametric framework. In the following subsections, we describe the proposed model in more detail.

2.1 Artificial Neural Networks

A NN is a brain-inspired system, as the name *neural* suggests, whose goal is to replicate the human learning process. A NN is a collection of neurons organized in different layers and characterized by three types of layers: input, hidden and output. The input layer is used to bring the data to the network. It does not perform any computations and just passes the information to the hidden layers. The hidden layers are in between the input and the output layer and are responsible for the learning of the relationships in the model. In an NN, more than one hidden layer can exist, depending on the complexity of the training data. An NN with one or more hidden layers is referred to as a multi-layered network. The output layer takes inputs from the hidden layer and its results are the outputs of the NN.

2.2 Autoencoder

An Autoencoder is a symmetric NN used to learn from a set of data in an unsupervised way by minimizing the reconstruction errors [6]. Its goal is to copy the input to the output, getting the significant aspects of the data to be copied. Autoencoder has two main parts: an encoder, to map the input $x \in R^d$ into the so-called code or latent representation $h \in R^{d'}$, represented by the function $h = f(x)$ and a decoder, whose goal is to obtain a representation $x' \in R^d$ very similar to its original input. It is described by the function $x' = g(f(x))$. An Autoencoder may be thought as a traditional feed-forward, nonrecurrent NN and may be trained with all the same techniques [6]. In other words, it has an input layer, an output layer and an appropriate number of hidden layers with an optimal number of neurons. The decoder may be symmetric to the encoder in terms of layer structure and the output layer must have the same number of neurons as the input layer, since the purpose is to reconstruct the input itself. Only copying the input to the output may be useless. In fact, our goal is to capture into the code layer the main proprieties of the input for fault detection analysis. One way to obtain this from data is to consider a smaller dimension of *h* than that of the input. An Autoencoder, whose code dimension *d'* is less than the input dimension *d*, is called *undercomplete*. Learning an undercomplete representation forces the Autoencoder to get the most important features of the training data. Autoencoders are trained minimizing the reconstruction errors, often referred to as the *loss function* $L\left(x, g\left(f(x)\right)\right)$, where L is the loss function penalizing $g\left(f(x)\right)$ for being dissimilar from the input vector x. In this paper, L is assumed to be the mean squared error. For example, if we consider an Autoencoder with one hidden layer, we need to compute $h = \sigma(Wx + b)$, where σ is the activation function (sigmoid, rectified linear

unit, hyperbolic tangent), W is the weight matrix and b is the bias vector between the input layer and the hidden layer. Then, we have to evaluate the reconstructed output $x' = \sigma'(W'x + b')$, where σ' , W' and b' are now referred to the decoder and are the activation function, the weights and the bias between the hidden layer and the output layer. In the general case, if we have more hidden layers, we have to compute all these values for any layer of the NN. At the end, the function we want to minimize is $L\left(x, g\left(f(x)\right)\right) = L(x, x') = \|x - x'\|^2$. This can be realized using the back-propagation stochastic gradient descent algorithms [6].

2.3 Monitoring statistics

The output of the Autoencoder can be embedded in a control charting scheme. For each input x, the H^2 statistic is defined as $H^2 = h^T h$ and the *SPE* statistic as $SPE = (x' - x)^2$. These two monitoring statistics can be then plotted against a time index in two different control charts, named H^2 and *SPE* control charts, respectively. An alarm will be issued, if an observation of at least one monitoring statistic falls above the relative upper control limit (UCL). The UCLs of the H^2 and *SPE* control charts, denoted by H_l^2 and SPE_l, respectively, are estimated using the block bootstrap approach [7] and will be computed by averaging the $(1 - \alpha')$-quantiles of the H^2 and *SPE* statistics obtained on each of the 2000 bootstrap samples taken from the training set. It should be noted that $\alpha' = 1 - (1-\alpha)^{1/2}$ is determined by utilizing the Sidák correction [8] to guarantee a family wise error rate [8] smaller than or equal to the specified α.

In addition to what is reported in [9], the H^2 statistic is introduced to also monitor the square distance of the projection of the input x from the origin of the latent representation space [5], and the UCLs are calculated taking into account possible autocorrelation in the data.

3 A real-case study in the railway industry

3.1 HVAC and data description

In the following section, real operational data from railway HVAC systems are considered to illustrate the proposed approach. Operational data were collected during a period of two months and stored for analysis in the current railway industry scenario. A microprocessor temperature control monitors the HVAC systems' performances by using enough temperature sensors to properly regulate heating and cooling mode in response to temperature changes inside and outside the coach. These sensors monitor the temperature provided by the HVAC system (T_{supply}), the outside temperature (T_{Out}) and the interior temperature (T_{In}), adjusting the system's cooling and heating functions to maintain a comfortable internal temperature and humidity level throughout the range of environmental and climatic conditions identified in UNI EN 14750-1. The target temperature (T_{set}) represents the target value at which the HVAC systems attempt to maintain the desired interior temperature and avoid thermal shock. The air conditioning system is designed adequately to maintain the internal temperature as close as possible to the target temperature.

3.2 Results

The dimension of each input observation x is $d = 24$, corresponding to the 4 variables monitored for each of the 6 coaches of the train. The optimal Autoencoder hyperparameters (e.g., the number of neurons in the hidden layer, the activation function) are chosen by a numerical grid search as those achieving the smallest reconstruction error estimated by means of a 10-fold cross-validation applied to the training data. The proposed approach is numerically implemented through the open-source software environment Python. A simple Autoencoder with a single hidden layer having two neurons is trained and the UCLs of the monitoring statistics are estimated by means of the block bootstrap with $\alpha = 0.05$.

To demonstrate the applicability of the proposed approach, Figure 1 reports the H^2 and *SPE* control charts for faulty HVAC data, respectively. The fault is successfully identified by the *SPE* control chart.

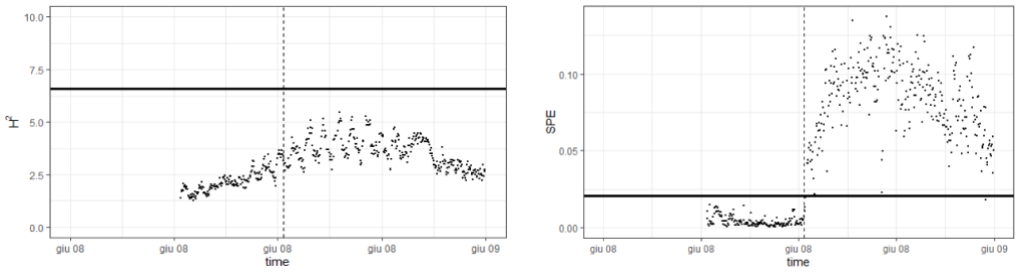

(a) (b)

Fig.1: (a) H^2 and (b) SPE control charts. The bold line indicates the UCL at $\alpha' = 0.025$, whereas the dashed line indicates the instant at which a fault is known to occur.

4 Conclusion

In this paper, we showed the benefits and practical applicability of a non-parametric statistical process control approach based on Autoencoder and the joint use of the H^2 and *SPE* control charts. In particular, the method is demonstrated to be capable of exploiting the operational HVAC data and quickly alerting practitioners if and when an anomaly in the performance of the HVAC system happens.

Acknowledgments

The computing resources and the related technical support used for this work have been provided by CRESCO/ENEAGRID High Performance Computing infrastructure and its staff [10]. CRESCO/ENEAGRID High Performance Computing infrastructure is funded by ENEA, the Italian National Agency for New Technologies, Energy and Sustainable Economic Development and by Italian and European research programmes, see http://www.cresco.enea.it/english for information.

References

[1] EN 14750-1. 2006. Railway applications - Air conditioning for urban and suburban rolling stock - Part 1: Comfort parameters.

[2] James, G., Witten, D., Hastie, T., & Tibshirani, R. *An introduction to statistical learning* (Vol. 112, p. 18). New York: springer (2013).

[3] Montgomery, D. C. *Statistical quality control* (Vol. 7). New York: Wiley (2009).

[4] Yan, W., Guo, P., & Li, Z. Nonlinear and robust statistical process monitoring based on variant autoencoders. *Chemometrics and Intelligent Laboratory Systems*, *158*, 31-40 (2016).

[5] MacGregor, J. F., & Kourti, T. Statistical process control of multivariate processes. *Control engineering practice*, *3*(3), 403-414 (1995).

[6] Goodfellow, I., Bengio, Y., & Courville, A. Deep learning book. *MIT Press*, *521*(7553), 800 (2016).

[7] Lahiri, S. N. (1999). Theoretical comparisons of block bootstrap methods. *Annals of Statistics*, 386-404.

[8] Lehmann, E. L., Romano, J. P., & Casella, G. *Testing statistical hypotheses* (Vol. 3). New York: springer (2005).

[9] A. Lepore, F. Ambrosino, G. Sposito, B. Palumbo, Neural Networks for Statistical Process Control of Multiple Stream Processes, in High Performance Computing on CRESCO infrastructure: research activities and results 2019, ENEA, pages 29-33 (2020).

[10] Iannone, F., Ambrosino, F., Bracco, G., De Rosa, M., Funel, A., Guarnieri, G., ... & Procacci, P. CRESCO ENEA HPC clusters: A working example of a multifabric GPFS Spectrum Scale layout. In 2019 International Conference on High Performance Computing & Simulation (HPCS) (pp. 1051-1052). IEEE (2019).

MONTE CARLO SIMULATION OF THE MICADO PROJECT INTEGRATED GAMMA STATION

Giada Gandolfo[1], Luigi Lepore[1*]

[1]*ENEA, FSN-FISS-CRGR, Nuclear Material Characterization Laboratory and Nuclear Waste Management ENEA Casaccia Research Center Via Anguillarese, 301, 00123 Roma, RM, Italy*[13]

ABSTRACT. Nuclear and radioactive materials characterization is a pivotal action in management of waste streams coming from nuclear power plants, medical, industrial and research applications, and for legacy wastes coming from the past. Performing a high-quality characterization, e.g., to determine the radiological content, is crucial when items that need to be analysed are already packed, and analyses need not to compromise the integrity of the radioactive waste itself.

The MICADO Project (Measurement and Instrumentation for Cleaning and Decommissioning Operations, Grant Agreement No. 847641, Horizon 2020 Framework Programme) is to propose a cost-effective solution for non-destructive characterization of nuclear waste, implementing a digitization process that could become a referenced standard facilitating and harmonizing the methodology used for the in-field Waste Management and Dismantling & Decommissioning operations.

Within MICADO, an entire work package is devoted the conception, realization and demonstration of a first 'integrated gamma station' for radioactive waste packages of different nature, obtained by combining different gamma detection technologies "helping" each other to the most effective and comprehensive non-destructive gamma characterization.

Monte Carlo simulation for radiation transport has been extensively used to quantify the station performances, and to get a database of "efficiencies" populated as to run some neural network analysis on data acquired, as to increase quality, accuracy, and reliability of results obtained.

1 Introduction

Currently, the Decommissioning and Dismantling (D&D) process of nuclear infrastructures demands methods for a full traceability of waste materials, to improve quality management and operational safety. Precise procedures provide twofold benefits: the optimization of costs, associated with D&D, and the minimization of the dose exposure to operators and personnel.

The absence of a consistent and straightforward solution to a full radiological characterization of all types of materials, along with the lack of an integrated solution for digitizing the huge amount of data produced, is a critical issue. Today, systems and procedures used in D&D applications rely most on the operator's ability to maintain high operational skills and quality assurance, as long as the utilization of several un-automatized procedures (manual inspection of waste with instruments, taking hand-notes, manual recording in databases), without the direct possibility to combine data, including previously available legacy data if present.

The MICADO Project is proposing the application of a Radiological Characterisation & Monitoring System Digi-Waste system (RCMS Digi-Waste in brief) as a modular solution offering an opportunity to proactively develop a unified and standardized Radioactive Waste Non-Destructive Analysis (NDA) Characterization Procedures and Methods, that could become an international reference allowing all Nuclear Operators, Research Laboratories & Safety Authorities to facilitate their exchanges. The digital platform is the common background where all radiological characterization techniques may live and rely on, exchanging information to setup the technique to be applied (e.g. withdrawing data about the

[13] Corresponding author. E-mail: luigi.lepore@enea.it

features of the package to be analysed, or to initiate the technique), and sending achieved results to the central database, for comparison with other similar data (e.g. some quantities already determined by other methodologies, if available), and for centralized recording and storage.
Within the MICADO Project, radiological characterization techniques foreseen and applied are:

- gamma detection analyses,
- passive and active neutron measurements,
- and photo-fission based methodologies.

The core issue is to determine the radiological content of a radioactive waste package in terms of radionuclides emitting gamma and neutron radiations, with a special regard to Uranium and Plutonium isotopes.
The whole Project has relied on Monte Carlo simulation significantly, as to design devices, to optimize parameters and experimental setup of techniques, for calibration purposes, and for neural network optimization applications.
This work is describing Monte Carlo works realized at the ENEA Nuclear Material Characterization and Nuclear Waste Management Laboratory. The Laboratory is involved in MICADO gamma detection applications mainly, realizing the first "integrated gamma station" by combining current state-of-the-art gamma technologies available on the market. The station is foreseeing 1) high resolution gamma spectrometry by High Purity Germanium detector, 2) a Sodium-Iodide scintillation detector for dosimetry, raw spectrometry and isotopes identification, and 3) a gamma camera device to a 2D visualization of geometrical distribution of the radioactive content inside the waste package.
The gamma station has requested extensive calculations to quantify the performances, and to get a database of "efficiencies" populated as to run some neural network and inference analyses on data acquired, as to increase quality, accuracy, and reliability of results obtained.

2 Methodology

2.1 Monte Carlo simulation for radiation transport

Currently, the most efficient method to simulate the radiation transport in media through complex (many volumes or "cells", several radioactive sources, and different materials) and large (few centimetres to hundreds of meters) geometries is the Monte Carlo simulation.
By this approach, a lot of 'histories' of the particle of interest are run, in order to reproduce, into a virtual world, all the possible paths travelled by the radiation, by means of random samplings from all the probability density functions ruling physical phenomena. Very complex geometries can be built, and very accurate results can be produced if all the elements important to the transport of the analysed radiation are described into the model; moreover, an adequate computational power should be available for running a statistically significant number of histories. For this work, the MCNPX (Monte Carlo N-Particle eXtended) code has been used, in its version MCNPX 2.5.0 [1].
Simulations have exploited the usage of multi-processing on CRESCO High Parallel Computing Resources extensively. The computing resources and the related technical support used for this work have been provided by CRESCO/ENEAGRID High Performance Computing infrastructure and its staff [2]. CRESCO/ENEAGRID High Performance Computing infrastructure is funded by ENEA, the Italian National Agency for New Technologies, Energy and Sustainable Economic Development and by Italian and European research programmes, see http://www.cresco.enea.it/english for information. In particular, the whole Monte Carlo work has requested 350000 hours per core, using 144 cores per about 2430 hours.

2.2 Database of detection efficiencies

A database of detection efficiencies for the ENEA Tomographic System has been built through Monte Carlo simulations. Part of the work has involved the modelling and an extensive study of two 120 litre

drum models, inspired to real radioactive waste packages. Such virtual models have been implemented to calibrate the high resolution gamma spectrometry technique, and to illustrate the main benefits of the RCMS DigiWaste toolbox in terms of waste package characterization. The first 'real' drum is filled with 5 bags of decontamination wipes only containing alpha emitters (plutonium isotopes), the second one is filled with 6 high density compacted waste drums containing alpha and beta/gamma emitters. Such virtual drums have been transformed in two other Monte Carlo surrogate models foreseeing the discretization of a 120L drum into five or six disc shape sub-volumes of equal dimensions. The source distribution is considered homogeneous within a single disc and the matrix density and chemical composition of each disc have been changed in a fixed range in order to build a database of detection efficiencies. For each of the two surrogate models, the efficiencies have been calculated for each density – chemical composition combination and each single sub-volume through MCNP simulations. In order to simulate the rotation of the drum and the detector movements during the scan, eight detectors have been placed at different angular positions and different heights relative to the drum.

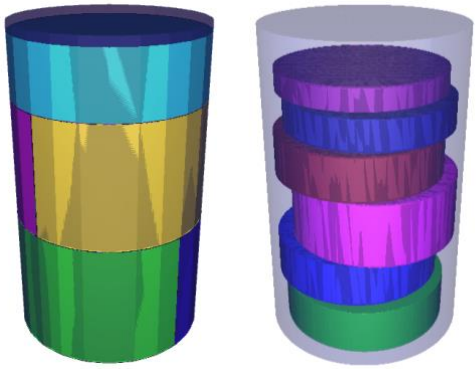

Fig. 1: 'Real' drums converted in Monte Carlo models, Virtual Case #1 (left) and #2 (right).

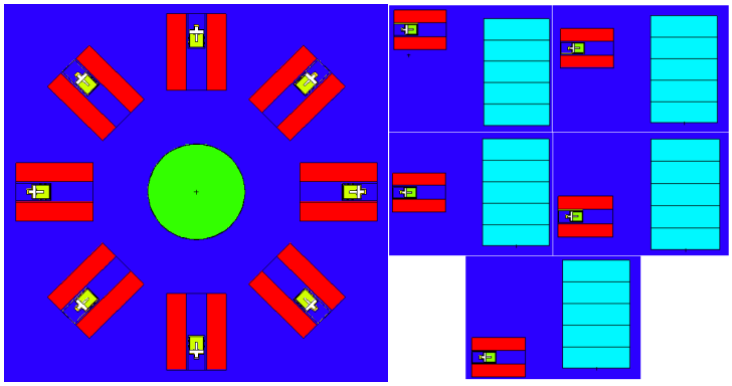

Fig. 2: MCNP plot for simulations of surrogate model.

The database of the efficiencies for the surrogate models has been used to calculate the efficiencies for the 'real' cases through Bayesian inference approach. In order to check the goodness of the results, the simulation of the 'real' drums have been performed and the obtained efficiencies compared with the extrapolated ones.

2.3 Bayesian inference to determine 1D gamma activity vertical profile in waste drums

The availability of the efficiencies database has allowed to run a special analysis on spectra acquired in the application of the Segmented gamma scanning (SGS) technique. SGS means that the radioactive

waste package is conceptually divided in disks along the vertical coordinate. Gamma spectra are acquired with the HPGe detector analysing disk by disk, with the drum on rotation. Consider the presence of a gamma source in a single "disk": the acquisition of a gamma spectrum for each disk would result in vertical distribution of counts in spectra according to geometry of the measurement (relative position of detector with respect to the radiological content), the actual geometrical distribution of radiological content inside the drum, the actual distribution of matrix materials inside the drum (that may provide self-shielding of the radiological content itself).
The basics of the Bayesian 1D inference reconstruction technique can be found in [3].

3 Results and Conclusions

The approach of Bayesian inference is well suited to assess the uncertainty of quantities that result from the application of a mathematical model. According to [3], Bayesian inference is particularly attractive for radiological characterization. Instead of simplifying probability distributions as is done for first-order Taylor expansion, any type of distribution can be applied both in a Monte Carlo error propagation and a Bayesian approach. Overall, while Monte Carlo (or first-order Taylor) error propagation just propagates uncertainties from pre-defined distributions with no concern for the correctness of the underlying mathematical equations or used prior assumptions (i.e. "forward model"), Bayesian inference seeks to derive a representative set of all possible solutions that are consistent with both the measurement data and available prior information.
When an NDA Characterization Procedures is applied, prior assumptions are made normally, e.g. a Monte Carlo model of the waste package is hypothesized with all information available to calibrate the instrumentation. Such assumptions play a very critical role in results obtained. Test the hypotheses with the Bayesian approach proposed could be a significant improvement to get the "true" value of the activity of the radionuclide searched for with a better accuracy, and to lower uncertainty of the final result achieved.
The discretization of waste packages in surrogate models, and the Monte Carlo calculation of the database of efficiencies for all combinations of the parameter values according to expected probability distributions between minima and maxima, leads in a large set of results that could be inferred to get a posterior probability distribution for the activity value, but also for all other inferred parameters. Ideally, the posterior distribution of each inferred parameter is narrower compared to its prior distribution, implying a reduction of the uncertainty and a best estimate closer to the "true" value.
With the Monte Carlo outcomes realized at ENEA, a Bayesian approach to probabilistically infer vertical activity distributions within a radioactive waste drum from segmented gamma scanning (SGS) measurements of the two Virtual Cases analysed within the MICADO Project is now ongoing at SCK·CEN. SCK·CEN is partner of the MICADO Project and leader in such applications. For virtual case #1 results are completely satisfactory; case #2 calculations are still on progress. All achieved output will be discussed extensively in Project Deliverables and scientific publications.

References

[1] J. F. Briesmeister, Ed., "MCNP: A General Monte Carlo N-Particle Transport Code," 2000.

[2] F. Iannone et al., "CRESCO ENEA HPC clusters: a working example of a multifabric GPFS Spectrum Scale layout," in 2019 International Conference on High Performance Computing Simulation (HPCS), 2019, pp. 1051–1052.

[3] Eric Laloy, Bart Rogiers, An Bielen, Sven Boden, Bayesian inference of 1D activity profiles from segmented gamma scanning of a heterogeneous radioactive waste drum, Applied Radiation and Isotopes, Volume 175, 2021, 109803, ISSN 0969-8043.

CLASSICAL MOLECULAR DYNAMICS SIMULATIONS AS TOOL TO PREDICT THE NON COVALENT INHIBITION OF SARS-COV-2 PL^{PRO} BY SELENO-DERIVATIVES

Carla Orlando, Isabella Romeo, Nino Russo*, Mario Prejanò, and Tiziana Marino*

[1]*Dipartimento di Chimica e Tecnologie Chimiche, Università della Calabria, I-87136 Rende, CS, Italy*
*Corresponding author: nino.russo@unical.it; tiziana.marino65@unical.it

ABSTRACT. Organoselenyl molecules has been indicated to act as either covalent or non-covalent SARS-CoV-2 PL^{pro} inhibitors and the present "in silico" investigation based on classical molecular dynamics simulations confirm these properties. From our classical molecular dynamics emerged a different conformational behavior of the tested seleno-quercetin derivatives non-covalent inhibitor. Atomistic insights from our comparative analysis can contribute rationally to design new efficient inhibitors of SARS-CoV-2 PL^{pro} with novel scaffolds

1 Introduction

Severe Acute Respiratory Syndrome Coronavirus 2 (SARS-CoV-2) is the causative agent of the COVID-19 pandemic in a different manner from SARS-CoV [1]. The high homology of SARS-CoV-2 with other coronaviruses revealed to be very useful to quickly understand its whole viral cycle. [2]
SARS-CoV-2 encodes two cysteine proteases essential for the virus proliferation cycle, the papain-like protease (PL^{pro}, encoded in nsp3) and the 'major' chymotrypsin-like protease ($3CL^{pro}$ or M^{pro}, encoded by nsp5). [1] The papain-like protease PL^{pro} is a cysteine peptidase and represents a crucial enzyme for the coronaviruses, since it is required to process viral polyproteins that allow the viral spread. [3] PL^{pro} cleaves at three sites and it is also essential because its activity goes beyond the cleavage of polyproteins. The enzyme found in nsp3 is highly conserved and is found in all coronaviruses. This cysteine protease cuts the peptide bonds between nsp1-nsp2 and nsp2-nsp3, thus releasing three proteins. nsp1 consists of 180 residues and interacts with the 80S ribosome, inhibiting host translation. Its centrality in the viral replication makes it an attractive candidate as a therapeutic agent. [3] Thereby, the inhibition of PLpro becomes a strategy to prevent disruption of the host immune response to the viral infection, in addition to the inhibition of viral replication. In fact, viral proteases can inhibit host innate immune response mounted initially as an inflammatory response, and subsequently as an interferon response. [4] A signature of COVID-19 are dysregulated inflammatory responses with a high degree of morbidity and mortality associated with cytokine storms.[4,5] From a structural point of view, the analysis of the crystal structures of SARS-CoV PL^{pro} by Ratia et al. demonstrated that a 6-amino-acid flexible loop named blocking loop 2 (BL2, 267–272 residues), in proximity of the catalytic site, is involved in the access control to the active site, [1] remotely from the active-site cysteine and that could be stabilized by small molecule, like SARS-CoV PL^{pro} inhibitors used in the present contribution. In this contribution, we will show as the classical Molecular Dynamics (MD) along with the Quantum Mechanic (QM) methods is able to contribute in a rational design of new inhibitors of PL^{pro}.

2 Computational strategy and methods

2.1 Molecular dynamics

The initial coordinates of the protein PL^{pro} were obtained from the X-ray structure (PDB ID: 6W9C). PL^{pro} was positioned in a 15×15×15 Å cubic box containing the buffer and with counterions to make the total charge zero. MD simulation was performed on protein in apo-form with His272 protonated in δ by using the Gromacs package [6] Combination of Amber99 force field and TIP3P water model was

used for the simulations. The parameters for the investigated non-covalent inhibitors (see Scheme 1) were calculated from HF/6-31G* optimizations using the Gaussian09 D.01 code. [7] To extrapolate non-bonded parameters and charges, the General Amber Force Field (GAFF) and the Restrained Electrostatic Potential methods were adopted, as described in ref. [8]. After a minimization phase, detailed in ref [8], on the solvated systems of apo- and inhibitor bounded- forms of PL^{pro} , a progressive heating up to 300 K for 50 ps, followed by 5 ns at 300 K using Langevin thermostat in NVT ensemble was performed, selecting the Berendsen barostat with a time constant $\tau p = 2.0$ ps. The production phase was performed in NPT ensemble for 150ns of MDs (step of 2 fs), with the SHAKE algorithm coupled with the Particle Mesh Ewald (PME) summation method. Electrostatic potential and long-range electrostatic interactions were calculated with cut-off distance 12 Å. The representative conformations were collected through RMSD-based geometric clustering, sampling similar structures during the MD simulations, selecting Gromos algorithm with a cut-off of 2.5Å.

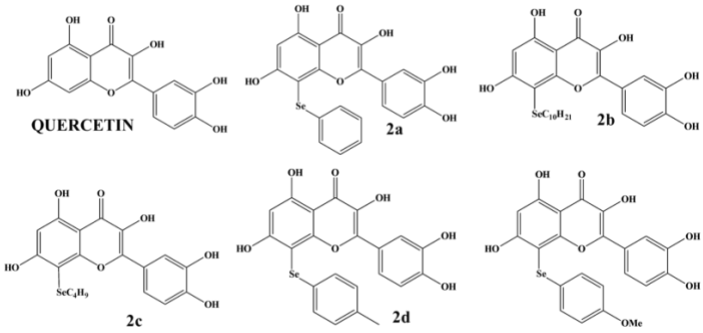

Scheme 1: Seleno-derivatives of quercetin investigated in the present work.

2.2 Molecular docking

To study the possible binding modes and interactions of different selenium-containing ligands in proximity of the catalytic triad of PL^{pro} protein (Cys111, His272, Asp286), molecular docking simulations were performed using AutoDock version 4.2.[9] Each representative structure was prepared by assigning atom types and adding Gasteiger charges. Docking area was established using AutoGrid. A size of 45x45x45 Å was chosen and the grid was centered on the sulfur atom of Cys111. Docking simulations of each inhibitor were performed on the most representative clustered geometry arising from the apo-form MD of PL^{pro} system, with a population size of 150, random initial position and conformation, local search rate of 0.6, and 2500000 energy ratings. Final docked poses were clustered using a root mean square deviation (RMSD) tolerance of 2Å. The best docked pose for the examined ligands in complex with PL^{pro} was chosen for an additional 150 ns of MDs.

3 Results and discussion

3.1 Non-covalent inhibition

Flavonoids, extracted from the many plants, were revealed as an ideal library for the screen and identification of new drug candidates targeting SARS-CoV-2 PL^{pro}, since they already showed in vitro PL^{pro} inhibitory effects and antiviral activities against SARS-CoV [10] Recent works evidences that seleno-derivatives of quercetin can represent good candidates [11] as non-covalent inhibitors against SARS-CoV-2 proteases. The examined systems are sketched in Scheme 1.

The analysis of the trajectory, derived from 150ns of MD simulation, for apo PL^{pro}, reveals a satisfactory protein stability (RMSD values of about 4 Å) and reveals a structural homogeneity of the protein during the simulation. The superposition of initial X-ray and the most representative clustered geometry further indicated that PL^{pro} conformation is quite similar to that observed in the crystal. The catalytic triad of

chain A (Cys111, His272 and Asp286) was selected as center of the grid where inhibitors were docked. The RMSD in the 150 ns of MD simulation reveals that, despite binding in the same pocket, the inhibitors can differently affect the protein surrounding but do not affect its secondary structures (see Fig. 1).

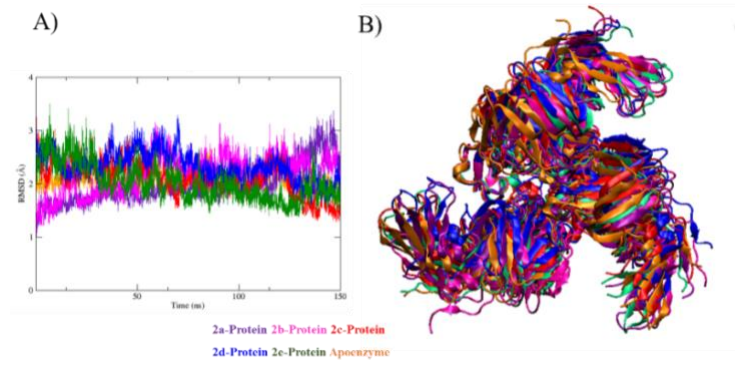

Fig. 1: A) RMSD plots of PL^{pro} chain A, B) superposition of the different PL^{pro}-inhibitor complexes.

The presence of the inhibitor, however, affected the conformation of catalytic triad atoms due to a different hydrogen bond network established by the amino acids and disrupts the alignment of catalytic triad, affecting in particular, the H-bond interaction occurring between the O atoms of Asp286A carboxylate group and the H-Nε of His272A imidazole ring, affecting as consequence the protease reaction promoted by the enzyme. Furthermore, the presence of the inhibitor prevents the entrance of solvent molecules in the catalytic pocket as revealed by the presence of a lower number of solvent molecules with respect to the unbounded form of PL^{pro}. Such behavior is most likely linked to lipophilic nature of seleno-derivative moiety, as can be evidenced by the analysis of the molecular electrostatic potential in Fig. 2. These results suggest that the non-covalent inhibition of the enzyme can occur preventing the entrance in the catalytic pocket of both the substrate and the water molecules, with the latter that are crucial for the protease's activity. In this report, we show as modern computational methods are able to predict and at the same time to elucidate at atomistic level, as a series of selenium containing system are able to act as promising inhibitors of the PL^{pro} SARS-CoV-2 protein with non-covalent reaction mechanisms. Detailed analysis of all the MD simulations is reported in the ref [8].

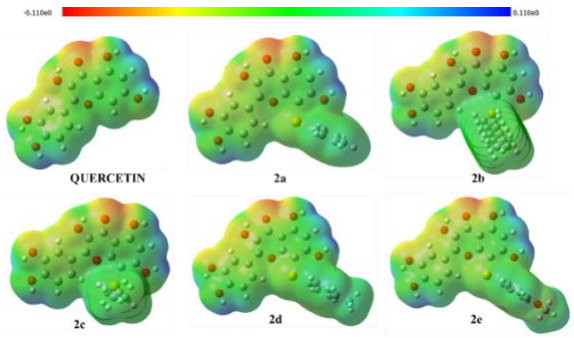

Fig. 2. Molecular electrostatic potential calculated for each considered inhibitor.

Acknowledgments

The authors thank the Dipartimento di Chimica e Tecnologie Chimiche of Università della Calabria for the financial support.
The computing resources and the related technical support used for this work have been provided by CRESCO/ENEAGRID High Performance Computing infrastructure and its staff [12]. CRESCO/ENEAGRID High Performance Computing infrastructure is funded by ENEA, the Italian

National Agency for New Technologies, Energy and Sustainable Economic Development and by Italian and European research programmes, see http://www.cresco.enea.it/english for information.

References

[1] Ratia, K.; Pegan, S.; Takayama, J.; Sleeman, K.; Coughlin, M.; Baliji, S.; Chaudhuri, R.; Fu, W.; Prabhakar, B.S.; Johnson, M.E.; Baker, S.C.; Ghosh, A.K.; Mesecar, A.D. A noncovalent class of papain-like protease/deubiquitinase inhibitors blocks sars virus replication. *Proc. Natl. Acad. Sci. U. S. A. 105*, 16119−16124 (2008).

[2] V'Kovski, P.; Kratzel, A.; Steiner, S.; Stalder, H.; Thiel, V. Coronavirus biology and replication: Implications for sars-cov-2. *Nat. Rev. Microbiol. 19*, 155−170 (2021).

[3] Shin, D.; Mukherjee, R.; Grewe, D.; Bojkova, D.; Baek, K.; Bhattacharya, A.; Schulz, L.; Widera, M.; Mehdipour, A.R.; Tascher, G.; Geurink, P.P.; Wilhelm, A.; van der Heden van Noort, G.J.; Ovaa, H.; Müller, S.; Knobeloch, K.-P.; Rajalingam, K.; Schulman, B.A.; Cinatl, J.; Hummer, G.; Ciesek, S.; Dikic, I. Papain-like protease regulates SARS-CoV-2 viral spread and innate immunity. *Nature 587*, 657-662 (2020).

[4] Del Valle, D.M.; Kim-Schulze, S.; Huang, H.-H.; Beckmann, N.D.; Nirenberg, S.; Wang, B.; Lavin, Y.; Swartz, T.H.; Madduri, D.; Stock, A.; Marron, T.U.; Xie, H.; Patel, M.; Tuballes, K.; Van Oekelen, O.; Rahman, A.; Kovatch, P.; Aberg, J.A.; Schadt, E.; Jagannath, S.; Mazumdar, M.; Charney, A.W.; Firpo-Betancourt, A.; Mendu, D.R.; Jhang, J.; Reich, D.; Sigel, K.; Cordon-Cardo, C.; Feldmann, M.; Parekh, S.; Merad, M.; Gnjatic, S. An inflammatory cytokine signature predicts covid-19 severity and survival. *Nat. Med. 26*, 1636−1643 (2020).

[5] Berlin, D.A.; Gulick, R.M.; Martinez F.J. Severe Covid-19. *N. Engl. J. Med.* **2020**, *383*, 2451-2460.

[6]Pronk, S.; Schulz, P.R.; Larsson, P.; Bjelkmar, P.; Apostolov, R.; Shirts, M.R.; Smith, J.C.; Kasson, P.M.; van der Spoel, D.; Hess, B.; Lindhl, E. GROMACS 4.5: A high-throughput and highly parallel open source molecular simulation toolkit. *Bioinformatics 29*, 845–854 (2013).

[7] Frisch, M.J.; Trucks, G.W.; Schlegel, H.B.; Scuseria, G.E.; Robb, M.A.; Cheeseman, J.R.; Fox, D.J. Gaussian 09. *Gaussian, Inc*.: Wallingford, CT, USA, (2009).

[8] Orlando C., Romeo, I., Russo, N., Prejanò, M., Marino, T. Seleno-derivatives of quercetin as possible non covalent inhibitors of SARS-Cov-2 PL^{pro}: Predictions from computational study, submitted to Int J. Mol. Sci., (2022) manuscript ID: ijms-2100909.

[9] Morris, G. M.; Huey, R.; Lindstrom, W.; Sanner, M. F.; Belew, R. K.; Goodsell, D. S.; Olson, A. J. Autodock4 and AutoDockTools4: automated docking with selective receptor flexiblity. *J. Comput. Chem. 30*, 2785– 2791 (2009).

[10] Solnier, J.; Fladerer, J.P. Flavonoids: A complementary approach to conventional therapy of COVID-19? *Phytochem. Rev. 20*, 773–795 (2021).

[11] Mangiavacchi, F.; Botwina, P.; Menichetti, E.; Bagnoli, L.; Rosati, O.; Marini , F.; Fonseca, S.F.; Abenante, L.; Alves, D.; Dabrowska, A.; Kula-Pacurar, A.; Ortega-Alarcon, D.; Jimenez-Alesanco, A.; Ceballos-Laita, L.; Vega, S.; Rizzuti, B.; Abian, O.; Lenardão, E.J.; Velazquez-Campoy, A.; Pyrc, K.; Sancineto, L.; Santi, C. Seleno-functionalization of quercetin improves the non-covalent inhibition of Mpro and its antiviral activity in cells against SARS-CoV-2. *Int. J. Mol. Sci. 22*, 7048 (2021).

[12] Iannone, F.; Ambrosino, F.; Bracco, G.; De Rosa, M.; Funel, A.; Guarnieri, G.; Migliori, S.; Palomb, F.; Ponti, G.; Santomauro, S.; Procacci, P. CRESCO ENEA HPC clusters: a working example of a multifabric GPFS Spectrum Scale layout. International Conference on High Performance Computing & Simulation (HPCS), Dublin, Ireland, 2019, pp. 1051-1052, doi: 10.1109/HPCS48598.2019.9188135

NUCLEAR ANALYSES FOR THE ASSESSMENT OF THE LOADS ON THE ITER RADIAL NEUTRON CAMERA IN-PORT SYSTEM

Fabio Moro[1*], Basilio Esposito[1], Daniele Marocco[1], Giorgio Brolatti[1], Andrea Colangeli[1], Fabio Crescenzi[1], Davide Flammini[1], Nicola Fonnesu[1], Giada Gandolfo[1], Giovanni Mariano[1], Rosaria Villari[1], Domenico Marzullo[2], Ryszard Kantor[3]

[1]*ENEA, Department of Fusion and Nuclear Safety Technology, I-00044, Frascati (Rome), Italy*

[2]*Trieste University, Department of Engineering and Architecture, 34127 Trieste Italy*

[3]*Institute of Nuclear Physics PAN, ul. Radzikowskiego 152, 31-342, Krakow, Poland*

ABSTRACT. The Radial Neutron Camera (RNC) is a key ITER diagnostic system designed to measure the uncollided 14 MeV and 2.5 MeV neutrons from deuterium-tritium (DT) and deuterium-deuterium (DD) fusion reactions, through an array of detectors covering a full poloidal plasma section along collimated Lines of Sight (LoS). Its main objective is the assessment of the neutron emissivity/α source profile and the total neutron source strength, providing spatial resolved measurements of several parameters needed for fusion power estimation, plasma control and plasma physics studies. The present RNC layout is composed by two fan-shaped collimating structures viewing the plasma radially through vertical slots in the Diagnostic Shielding Module (DSM) of ITER Equatorial Port 1 (EP01): the ex-port sub-system and the in-port one. The ex-port sub-system, devoted to the plasma core coverage, extends from the Port Interspace to the Bioshield Plug: it consists of a massive shielding unit hosting two sets of collimators lying on different toroidal planes, leading to a total of 16 interleaved LoS.

The in-port system consists of a cassette, integrated inside the port plug DSM, containing two detectors per each of the of six LoS looking at the plasma edges. The in-port system must guarantee the required measurement performances in critical operating condition in terms of high radiation levels, given its proximity to the plasma neutron source. The present document presents an updated neutronic analysis based on the latest design of the in-port system and port plug. It has been performed by means of the Monte Carlo MCNP code and making use of the ENEA CRESCO High Performance Computing infrastructure.

1 Introduction

The Radial Neutron Camera (RNC) is a diagnostic system located in the ITER Equatorial Port #1 (EP01) which main function is the measurement of uncollided 14 MeV and 2.5 MeV neutrons from deuterium-tritium (DT) and deuterium-deuterium (DD) fusion reactions through an array of flux monitors/spectrometers located in collimated lines of sight (LoS). The line-integrated neutron fluxes are used to assess the local radial profile of plasma neutrons emitted per unit time and volume (neutron emissivity, [1, 2]) and therefore the neutron yield and the alpha particles birth profile. The temperature profile of the bulk ions can be derived [3] from the Doppler broadened widths of the RNC line-integrated spectra, that also provide insight on the supra-thermal ions produced by the injection in the plasma of electromagnetic waves and neutral particles. Moreover, the RNC emissivity and temperature

measurements can be employed to estimate the composition of the ITER fuel, namely the ratio between the tritium and deuterium densities [1].
The RNC (fig. 1) is based on two fan-shaped collimating structures viewing the plasma radially through optical paths in the EP01 Diagnostic First Wall (DFW) and Diagnostic Shielding Module (DSM) [4,5]. The ex-port RNC, devoted to probe the plasma core coverage (r/a<0.54, a = minor radius), consists of a massive shielding unit extending from the Port Interspace to the Bioshield Plug that hosts two sets of collimators lying on different toroidal planes, leading to a total of 16 interleaved LoS equipped with scintillators and diamond detectors. The four central collimators of the right set (looking towards the plasma) are respectively dedicated to the Radial Gamma Ray Spectrometer (RGRS, 3 LoS), and to the High Resolution Neutron Spectrometer (HRNS, 1 LoS), both placed backwards, in the Port Cell.

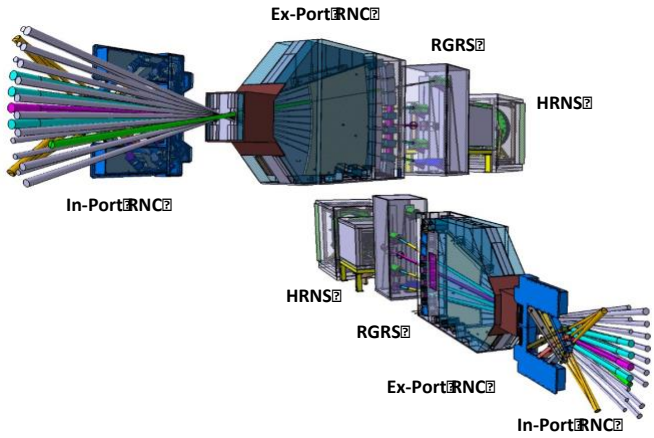

Fig. 1: Overall layout of Radial Neutron Camera.

The in-port RNC (fig. 2), integrated in the DSM Drawer #3 of the EP01 consists of a removable stainless steel cassette (SS316L(N)-IG), equipped with electrical and vacuum feedthrough, with two sets of three LoS each, looking at the plasma edges (r/a>0.67). The neutrons from the plasma are collected by means of conical optical paths hollowed out in the DFW and DSM and pass through the collimators up to the detector modules that contain two in-line devices: a single Crystal Diamond (sCD) matrix as main detector, also enabling spectrometric measurements [6] and a ^{238}U fission chamber (FC) as complementary detector.

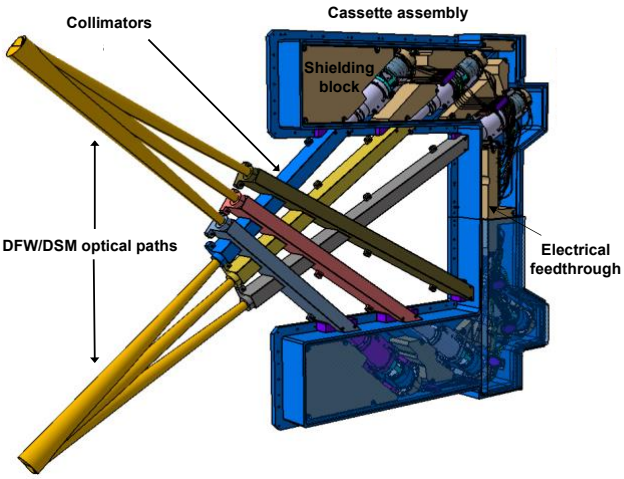

Fig. 2: In-port RNC subsystem.

The in-port RNC has to withstand severe environmental conditions during ITER operations in terms of thermal, magnetic and radiation fields. The present study aims at evaluating the nuclear loads on the in-

port sub-system components by means of the MCNP Monte Carlo code [7]. Such analysis enables the optimization of the RNC design, provides data for the thermo-mechanical studies and the assessment of the diagnostic measurement performances.

2 Nuclear loads on the In-port RNC subcomponents

A detailed MCNP model of the in-port RNC has been developed and successively integrated into an upgraded version of the ITER C-model provided by the Port Integrator, in which the EP01 features are incorporated in the central equatorial port (fig. 3) including all the diagnostic systems and related cut-outs (e.g. Bolometers penetrations, close to the in-port cassette and collimators), so that cross-talk effects are taken into account.

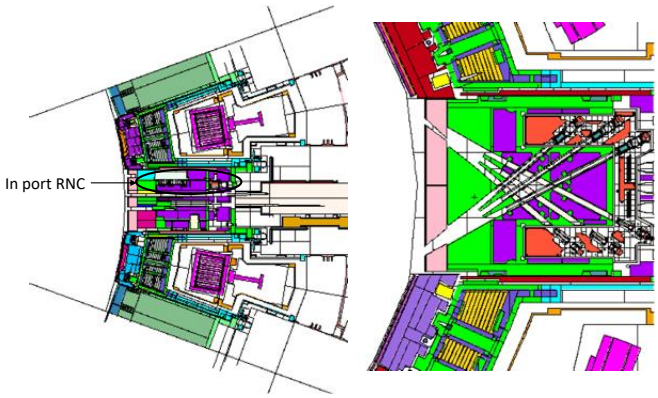

Fig. 3: ITER C-model integrating the EP01 features, with the in-port RNC structure in the full central equatorial port.

The above mentioned model has been used to assess the following nuclear responses, computed in 3D maps format (1 cm voxel size), using the MCNP FMESH tally capability with proper tally multipliers which take into account materials, involved nuclear reactions and normalization factors:

- Neutron and gamma flux;
- Nuclear heating density;
- Damage and He production on stainless steel.

In the frame of the accomplishment of such analyses, performed in a very complex 3D environment, the usage CRESCO HPC infrastructure played a critical role in order to achieve the needed statistical compliancy (statistical uncertainty on each voxel <10% in the area of interest). As a sample of the result of the performed studies, fig. 4 show the total neutron flux map across the in-port RNC LoS [8].

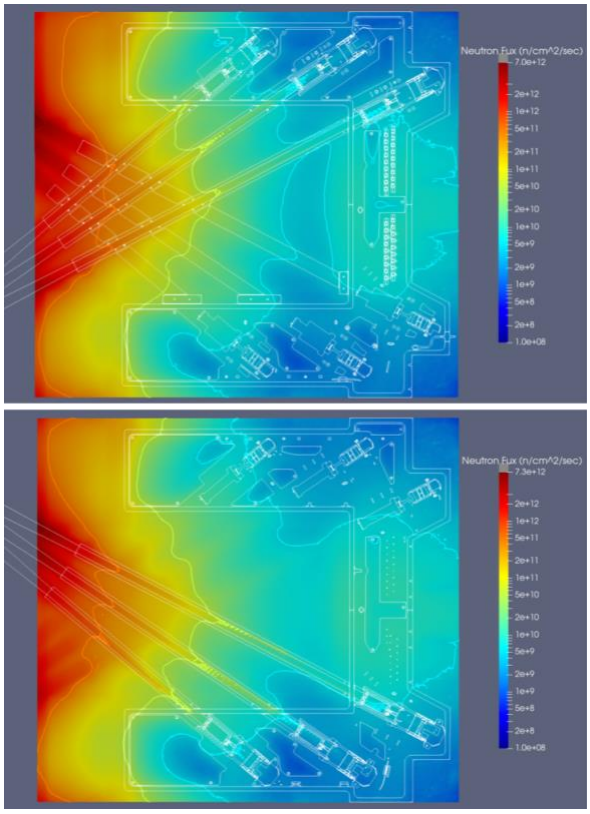

Fig. 4. Sections of the total neutron flux (n/cm^2/s) map across the upper LoS (top panel) and lower LoS (bottom panel).

The nuclear heating density data calculated on the in-port RNC subcomponents have been used as input for thermo-mechanical analyses (fig. 5): results show that the maximum temperature reached by the detectors is well below their operational limits.

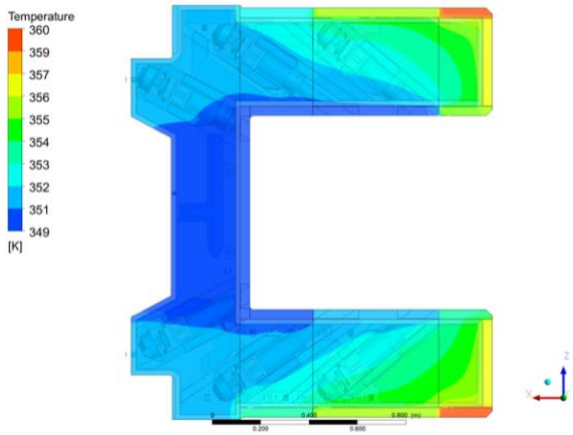

Fig. 5: Temperatures obtained through the thermal analysis performed using nuclear heat loads inputs.

Acknowledgments

F4E: This publication reflects only the views of the authors, Fusion for Energy cannot be held responsible for any use of the information contained therein. ITER: The views and opinions expressed herein do not necessarily reflect those of the ITER Organization.

References

[1] D. Marocco et al., “Neutron measurements in ITER using the Radial Neutron Camera”, Journal of Instrumentation, vol. 7, no. 3, Art. no. C03033, 2012.
[2] M. Cecconello et. al., ”Neural network implementation for ITER neutron emissivity profile recognition”, Fusion Engineering and Design, vol. 123, pp. 637-640, 2017.
[3] D. Marocco et al., “Combined unfolding and spatial inversion of neutron camera measurements for ion temperature profile determination in ITER”, Nuclear Fusion, vol 51, Art. no. 053011, 2011.
[4] B. Esposito et al., “Design of the ITER Neutron Camera”, Journal of Fusion Energy, vol 41, issue 2, Art. no. 22, 2022.
[5] D. Marocco et al., “System level design and performances of the ITER radial neutron camera”, Proceedings of the 26th IAEA Fusion Energy Conference, Kyoto, 2016.
[6] D. Rigamonti et al., “Neutron spectroscopy measurement of 14 MeV neutrons at unprecedented energy resolution and implications for deuterium-tritium fusion plasma diagnostics”, Measurement Science and Technology, vol. 29, no. 4, Art. no. 045502, 2018
[7] X-5 Monte Carlo Team: MCNP - A General Monte Carlo N-Particle Transport Code, Version 5, LANL Report: LACP-03-0245, 2005.
[8] F. Moro et al., “Nuclear Analyses for the Assessment of the Loads on the ITER Radial Neutron Camera In-Port System and Evaluation of Its Measurement Performances”, IEEE Transactions on Plasma Science, doi: 10.1109/TPS.2022.3185801, 2022.

AB INITIO STUDY OF OXYGEN REDOX ACTIVITY IN LAYERED TRANSITION METAL OXIDES AS HIGH-ENERGY CATHODES FOR NA-ION BATTERIES

Arianna Massaro[1], Aniello Langella[1], Ana B. Muñoz García[2], Michele Pavone[1*]

[1]*University of Naples "Federico II", Department of Chemical Sciences, Comp. Univ. Monte Sant'Angelo Via Cintia 21, 80126, Naples, Italy*

[2]*University of Naples "Federico II", Department of Physics "Ettore Pancini", Comp. Univ. Monte Sant'Angelo Via Cintia 21, 80126, Naples, Italy*

ABSTRACT. We provide the first-principles investigations of layered transition metal oxides, Na_xTMO_2 (TM = Ni, Mn, Fe/Ru), for the design of high-energy cathodes for Na-ion batteries (NIBs). The aim is to determine the role of each element sublattice in compensating the electronic charge along desodiation, focusing on the anionic contribution. The high TM-O covalency provided by Ru and Fe doping prevents oxygen loss and ensures full capacity recovery. These theoretical insights can help in the design of efficient, high-energy NIB cathodes with better reversible capacity.

1 Introduction

The research carried out at the University of Naples "Federico II" focused on the ab initio investigation of layered transition metal oxides (Na_xTMO_2) for their use as cathodes in sodium-ion batteries (NIBs). Enhancing the cathode energy density is one of the key goals of ongoing battery research. This requires simultaneously increased cell voltage and specific capacity. Selecting appropriate redox centers enables to control the potential but increasing capacity without structural alterations is more challenging [**1**]. Anionic redox activity represents the ideal benchmark for boosting energy density [**2**, **3**]. However, anionic activity is related to the uncontrolled $O^{2-}/O_2^{n-}/O_2$ evolution, which can lead to irreversible structural disorder, cationic migrations, and capacity fading [**4**-**6**]. Increasing the TM-O bond strength has emerged as an effective strategy for preventing oxygen loss and ensuring full capacity recovery [**7**]. Based on our prior work on $Na_xNi_{0.25}Mn_{0.68}O_2$ (NNMO) [**7**], where we proved the release of O_2 upon cleavage of the labile Ni-O bond, herein we suggest the rational design pursued by partial substitution of Ni with Fe and Ru to increase the TM-O covalency.

2.1 Methods and Computational details

Spin-polarized DFT calculations are performed with projector-augmented wave (PAW) potentials and plane-wave (PW) basis set, as implemented in the Vienna Ab-initio Simulation Package (VASP) code (ver. 5.4.4). We use the Perdew-Burke-Ernzerhof (PBE) exchange-correlation functional with the +U Hubbard-like correction scheme to overcome the large self-interaction error (SIE) that affects DFT when applied to mid-to-late first-row TM oxides with tightly localized d electrons. The on-site correction is applied to the d electrons of Fe, Ru, Ni, and Mn atoms with a unified average effective U-J parameter, U_{eff}, equal to 4 eV [**8, 9**]. The D3-BJ dispersion correction is also added to account for interlayer van der Waals (vdW) interactions [**10**-**12**]. A kinetic energy cutoff of 750 eV and a 4×4×4 Γ-centered k-points sampling mesh are required to converge the PW basis set.

2.2 Results and discussion

The investigated structures, $Na_{0.75}Fe_{0.125}Ni_{0.125}Mn_{0.75}O_2$ (NFNMO) and $Na_{0.75}Ru_{0.125}Ni_{0.125}Mn_{0.75}O_2$ (NRNMO) are P2 type systems [**13**]. To mimic the desodiation process, we model various Na contents (x = 0.75, 0.5, 0.25, 0.125). These structural models consist of 4x4x1 supercells within the $P6_3/mmc$ space group. The special quasi-random structure (SQS) approach was used to simulate the TM disorder in TMO_2-layers. The Na atoms are placed in edge (e) and face (f) sites to achieve an e/f ratio of 2 [**14**] (**Figure 1** left, top panels). We compared the stoichiometric bulk structure of each material to a Mn-deficient phase to see how TM-vacancy affects oxygen redox activity. As shown in the voltage-capacity profiles (**Figure 1** left, bottom panels), the presence of Mn vacancies raises the Na intercalation potential across the entire voltage range. All the curves follow the same general patterns as observed in experiments performed on similar materials [**15**,**16**]. Anionic activity is further supported by the observation that the capacity boost in Mn-deficient systems is more significant in the high voltage regions. Desodiation-induced changes in TM-O bond distances are examined by using pair distribution functions (PDFs). As a result, we are able to identify the redox centers. The Mn-O bond is unaffected by the Na content in NFNMO and NRNMO. In stoichiometric NFNMO (**Figure 1** middle panel), only Ni appears to be a redox active center while Fe is also involved in the redox process in the Mn-deficient structures. For NRNMO (**Figure 1** right panel), both Ru and Ni undergo a partial oxidation. All the analysis for NRNMO is conducted till x_{Na} = 0.25, as no experimental studies confirm the structure stability at higher voltages.

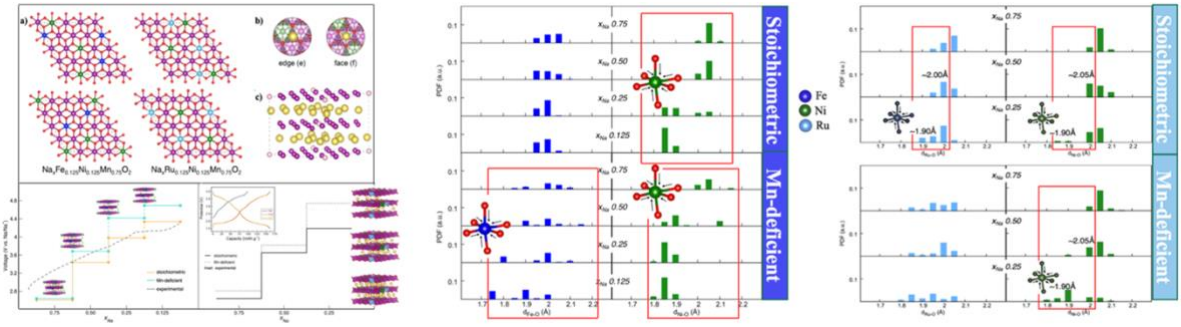

Figure 1 Structural models: LEFT (TOP): (a) SQS results for TM distribution (b) Na coordination details of edge and face sites; (c) configuration of Mn vacancies considered for Mn-deficient phase of each system. LEFT (BOTTOM): Voltage-capacity profiles for stoichiometric and Mn-deficient for NFNMO (left) and NRNMO (right). MIDDLE and RIGHT: Pair distribution functions of Fe-O (blue plot), Ni-O (green plot) and Ru-O (cyan plot) distances computed for stoichiometric and Mn-deficient NFNMO (middle) and NRNMO (right) as functions of Na content. Color code: Na atoms in yellow, Mn in purple, Ni in green, Fe in blue, Ru in cyan, O in red, Mn-vacancy site in pink.

The projected density of states (PDOSs) at increasing voltages reported in **Figure 2** show that Mn, Ni, Fe and Ru d states are strongly hybridized with O *p* ones, indicating that TM-O bonds have a high covalent nature. The stoichiometric NFNMO (Top panel **Figure 2a**) shows a bandgap that is persistent along desodiation. In contrast, in the bottom panel of **Figure 2a**, we can clearly see the O *p* band crossing the Fermi level in the Mn-deficient system at *x* Na = 0.25 and then at 0.125, suggesting an active participation of the oxide sublattice in the oxidation process. The PDOS of NRNMO at low Na content does not show O *p* states crossing the Fermi level (**Figure 2c**). Thus, we inquire if some anionic processes are enabled by the high state of charge of this material. During desodiation, the steady decrease of net magnetization on Mn, Ni, Fe and Ru species show that oxidation is happening. In both stoichiometric and Mn-deficient NFNMO and NRNMO, the Mn sublattice has mixed oxidation (*i.e.*, 3.5 μ_B), meaning that both Mn^{3+} and Mn^{4+} states are present. A clear indication of Ni redox activity in NFNMO is identified with $Ni^{2+} \rightarrow Ni^{3+}$ occurring at *x* Na = 0.25 for stoichiometric and at *x* Na = 0.50 for Mn-deficient NFNMO (*i.e.*, ~0.7 μ_B, d^7 low-spin configuration) and then up to Ni^{4+} at *x* Na = 0.125 (*i.e.*, ~0.1 μB, d^6 low-spin configuration) (see green lines in **Figure 2b**). The Fe sublattice shows different results, retaining its oxidation state in stoichiometric NFNMO, while undergoing oxidation to Fe^{4+} at *x* Na = 0.25 and 0.125 in the Mn-deficient case (*i.e.*, ~3.5

μ_B, d^4 high-spin configuration) (see blue lines in **Figure 2b**). The average Ni magnetization in NRNMO only slightly decreases upon desodiation in the stoichiometric form, while shifting down to ~0.8 μ_B at *x* Na = 0.25 in Mn-deficient NRNMO and indicating the $Ni^{2+} \rightarrow Ni^{3+}$ oxidation (see green lines in **Figure 2d**). Ru magnetization increases at *x* Na = 0.25 in stoichiometric NRNMO, indicating a partial variation from the mixed Ru^{3+}/Ru^{4+} oxidation state (~1.5 μB - d^5/d^4 low-spin configuration). In Mn-deficient structure, where the Ru is oxidized to Ru^{5+} (~2.4 μB - d^3 configuration) a more significant change is visible (see cyan lines in **Figure 2d**). This structural and electronic characterization of bulk suggests that anionic redox activity can be facilitated in Mn-deficient cathodes operating at high voltages. The goal is to understand the underlying mechanism of O-redox processes to determine the degree of oxidation within the oxide sublattice. At low Na loads (*i.e.*, *x* Na = 0.25**,** 0.125), the redox activity of the oxide sublattice is triggered and could lead to the formation of partially oxidized O-based species.

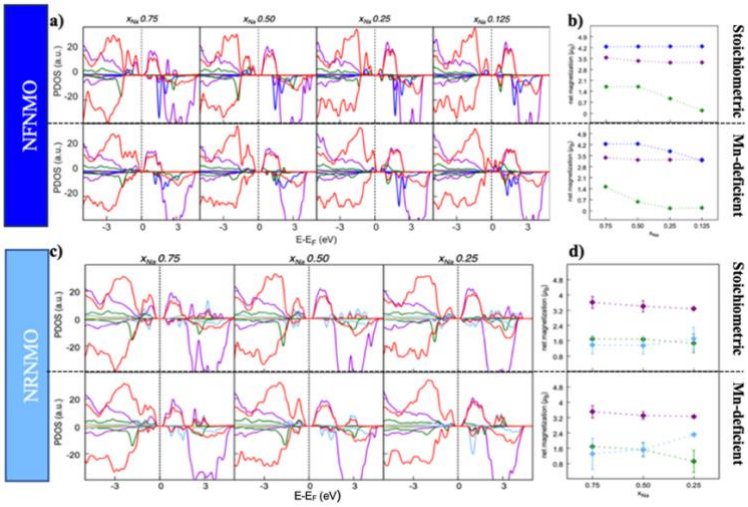

Figure 2. Electronic structure analysis of (top) NFNMO and (bottom) NRNMO as function of Na content. (a/c) atom- and angular momentum- PDOS; (b/d) Net magnetization of each TM sublattice as a function of Na content.

Here, we provide the results of the $O^{2-} \rightarrow O_2^{n-}$ process, that is the formation of dioxygen-metal complexes nearby the Mn deficiency, which can be thought as the binding of two oxygen atoms moving from two regular positions in the lattice and reaching certain intermediate structures. We investigated several configurations (**Figure 3**) differing for the chemical environment, and we discuss their stability in terms of formation energy (ΔE):

$$\Delta E = E_{dioxygen} - E_{NFNMO/NRNMO} \quad (1)$$

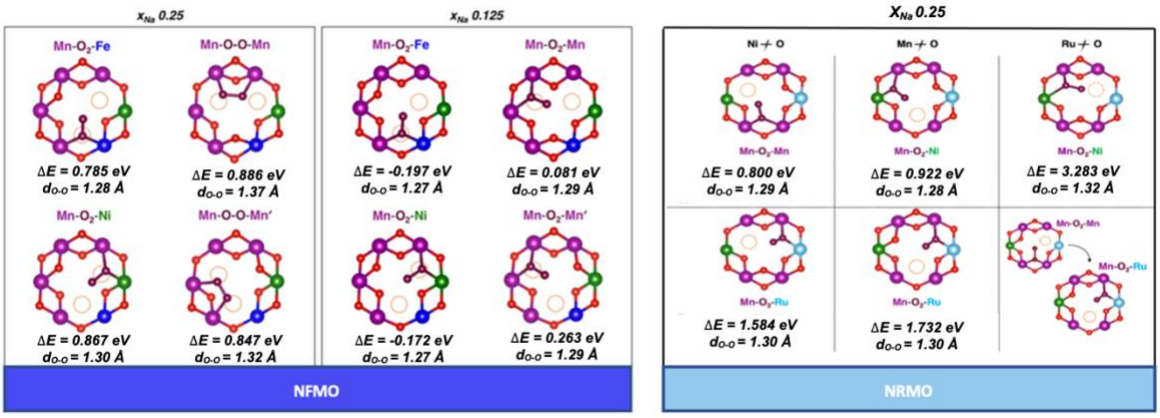

Figure 3. Dioxygen formation. O atoms involved in the dioxygen-metal complexes are depicted in brown. The orange circles highlight the initial positions before dioxygen formation. Only atoms around the dioxygen species are shown for clarity. The corresponding formation energy computed using Equation 1 at PBE+U(D3-BJ) is also reported.

According to these results, all the investigated cases can be attributed to O-superoxide species (d_{O-O} ~1.26 to 1.37 Å) binding the TM atoms in different coordination modes. Because of the higher degree of oxidation detected at higher voltage, the formation of dioxygen-metal complexes becomes more favorable overall when the Na content decreases. It is worth noting that, despite being positive, such energy variations are still accessible under NIB operating conditions (*i.e.*, when an external voltage upon battery charging is applied) and would represent a reliable mechanism for the anionic redox activity occurring at high voltage. In contrast to the undoped cathode [**7**], our calculations do not predict the release of molecular O_2 in the Mn-deficient NFNMO material. Fe/Ru atoms stabilize superoxide moieties at high voltages. Mild TM-O bond strengths prevent O_2 evolution, while the activation of anionic redox processes can still be enabled via the potentially reversible formation of superoxide species.

2.3 Conclusions

These results are subject of two scientific papers that have been recently published on Journal of American Ceramic Society and ACS Applied Energy Materials [**17**,**18**]. The computing resources and the related technical support used for this work have been provided by CRESCO/ENEAGRID High Performance Computing infrastructure and its staff; CRESCO/ ENEAGRID High Performance Computing infrastructure is funded by ENEA, the Italian National Agency for New Technologies, Energy and Sustainable Economic Development and by Italian and European research programmes. See: http://www.cresco.enea.it/english for information [**19**].

References

[1] Saubanère, M., et al. "An Intuitive and Efficient Method for Cell Voltage Prediction of Lithium and Sodium-Ion Batteries." *Nat. Commun.*, vol. 5, no. 1, 2014, p. 5559.

[2] Koga, H., et al. "Reversible Oxygen Participation to the Redox Processes Revealed for $Li_{1.20}Mn_{0.54}Co_{0.13}Ni_{0.13}O_2$." *J. Electrochem. S.*, vol. 160, no. 6, 2013, pp. A786–A792.

[3] Ben Yahia, M., et al. "Unified Picture of Anionic Redox in Li/Na-Ion Batteries." *Nat. Mater.*, vol. 18, no. 5, 2019, pp. 496–502.

[4] Ito, A., et al. "Cyclic Deterioration and Its Improvement for Li-Rich Layered Cathode Material $Li[Ni_{0.17}Li_{0.2}Co_{0.07}Mn_{0.56}]O_2$." *J. of Power Sources*, vol. 195, no. 2, 2010, pp. 567–573.

[5] Croy, Jason R., et al. "First-Charge Instabilities of Layered-Layered Lithium-Ion-Battery Materials." *Phys. Chem. Chem. Phys*, vol. 17, no. 37, 2015, pp. 24382–24391.

[6] Xie, Y., et al. "Requirements for reversible extra-capacity in Li-rich layered oxides for Li-ion batteries." *Energy Env. Sci.*, vol 10, no. 1, 2017, pp. 266–274.
[7] Massaro, A., et al. "Unveiling Oxygen Redox Activity in P2-Type $Na_xNi_{0.25}Mn_{0.68}O_2$ High-Energy Cathode for Na-Ion Batteries." *ACS Energy Lett*, vol. 6, no. 7, 2021, pp. 2470–2480.
[8] Mosey, N. J., at al. "Rotationally invariant ab initio evaluation of Coulomb and exchange parameters for DFT+U calculations." *J. Chem. Phys.*, vol. 129, no. 1, 2008.
[9] Ritzmann, A. M., et al. "Ab initio evaluation of oxygen diffusivity in $LaFeO_3$: the role of lanthanum vacancies." *MRS Commun.*, vol. 3, no. 3, 2013, pp.161–166.
[10] Grimme, S., et al. "A consistent and accurate ab initio parametrization of density functional dispersion correction (DFT-D) for the 94 elements H-Pu." *J. Chem. Phys*, vol. 132, no.15, 2010, pp. 154104.
[11] Barone, V., et al. "Role and effective treatment of dispersive forces in materials: Polyethylene and graphite crystals as test cases." *J. Comput. Chem.*, vol. 30, no. 6, 2009, pp. 934–939.
[12] Pecoraro, A., et al. "Structural and electronic properties of defective 2D transition metal dichalcogenide heterostructures." *J. Comput. Chem.*, vol. 41, no. 22, 2020, pp. 1946–1955.
[13] Delmas, C., et al. "Structural classification and properties of the layered oxides." *Physica*, vol. 99, no.1, 1980, pp. 81–85.
[14] Fielden, R., et al. "Investigation of the $NaNi_xMn_{1-x}O_2$ ($0 \leq x \leq 1$) system for Na-ion battery cathode materials." *J. Electrochem. Soc.*, vol. 162, no.3, 2015, pp. A453–A459.
[15] Zhang, Y., et al. "Revisiting the Na2/3Ni1/3Mn2/3O2 cathode: Oxygen redox chemistry and oxygen release suppression." *ACS cent. Sci.*, vol. 6, no. 2, 2020 pp. 232–240
[16] Kiziltas-Yavuz, et al. "Improving the rate capability of high voltage lithium-ion battery cathode material $LiNi_{0.5}Mn_{1.5}O_4$ by ruthenium doping." *J. Power Sources*, vol. 267, 2014, pp. 533–541.
[17] Massaro, A.; at al. "First-principles insights on anion redox activity in $Na_xFe_{1/8}Ni_{1/8}Mn_{3/4}O_2$: Toward efficient high- energy cathodes for Na-ion batteries", *J. Am. Ceram. Soc., vol.* 1, no.11 2022.
[18] Massaro, A.; at al. "Ru-Doping of P2-$Na_xMn_{0.75}Ni_{0.25}O_2$-Layered Oxides for High-Energy Na-Ion Battery Cathodes: First-Principles Insights on Activation and Control of Reversible Oxide Redox Chemistry", *ACS Appl. Energy Mater*., vol. 5, no. 9, 2022, pp. 10721-10730.
[19] Ponti, G; et al. "The Role of Medium Size Facilities in the HPC Ecosystem: The Case of the New CRESCO4 Cluster Integrated in the ENEAGRID Infrastructure". *2014 International Conference on High Performance Computing & Simulation (HPCS)*; IEEE, 2014; pp 1030−1033.

MAIN STAGES OF THE NEUTRONIC DESIGN OF THE LFR-TL-30 CORE

Roberto Pergreffi[1,14], Francesco Lodi[1], Giacomo Grasso[1],
Alessia Di Francesco[2], Giorgia Mantovani[2]

[1]*ENEA – Italian National Agency for New Technologies, Energy and Sustainable Economic Development*
Via Martiri di Monte Sole 4, 40129 Bologna - Italy
[2]*new*cleo srl
Via Galliano 27, 10129 Torino - Italy

ABSTRACT. As part of the collaboration with *new*cleo srl, ENEA was involved in the conceptual design of the core configuration of the LFR-TL-30, a long-lived, sealed and transportable small modular fast reactor cooled by lead with UO_2 fuel. Starting from a preliminary core configuration developed according to the key requirements of the company, the main stages of the neutronic design of the LFR-TL-30 core are described by analysing, for each of them, the most important neutronic results in terms of criticality, reactivity swing and power distributions among fuel assemblies. After several initial attempts to significantly reduce the reactivity swing by increasing fuel mass and/or reducing fuel enrichment in the inner zone, a promising neutronic configuration was found using on the one hand neptunium as a burnable poison homogeneously mixed in all fuel pins and on the other hand the barrel in place to the inner vessel so as to arrange the control elements closer to the fuel region improving their reactivity worth. All calculations were performed on CRESCO6 by means of the Monte Carlo transport code MCNP6.1.

1 Introduction

LFR-TL-30 (Lead Fast Reactor – Transportable Long-lived – 30 MW_{el}) is a sealed small modular reactor conceived by *new*cleo srl for low-power or remote (i.e., loosely or not connected to an electric grid) applications, the most remarkable being marine propulsion. This reactor was one of the systems included in the collaboration between *new*cleo srl and ENEA and for which ENEA was involved in the design of the core configuration.

The general core characteristics proposed by the company included the type of fuel (UO_2 only), the thermal power (90 MW), the core inlet/outlet temperatures (360/430 °C), the peak cladding outer temperature (480 °C), the peak irradiation damage on cladding (< 120 dpa), the maximum pressure drops in core (0.7 bar), the inner vessel diameter (2 m), the number of fuel assembly (37) and the control elements located outside the active region.

The ENEA activity started from the elaboration of a conceptual design for the core layout as presented in [1]. For this, the main geometrical parameters on which dimensions and performance of the core depend were investigated. At the end of this analysis, a preliminary core configuration including number of pins per assembly, lattice pitch and active height was proposed. This solution allowed for reasonable values of some key core parameters such as the peak linear power rating, peak rod power, peak burnup and pressure drops in bare bundle. Being however the output of a general design arrangement, its neutronic performance in terms of criticality, power distribution and absorbers worth

[14] Corresponding author. E-mail: roberto.pergreffi@enea.it.

needed to be investigated by actual calculations. The aim of the neutronic design of the LFR-TL-30 core was to achieve a configuration able to:

1. *criticality*: permit a potentially continuous operation for 15 years without refuelling;
2. *power distribution*: achieve sufficient flattening to i) better exploit all the fuel, ii) reduce peaks within the given limits;
3. *criticality*/*absorbers worth*: allow the compensation of the excess reactivity during operation without exceeding the importance of each single absorber device;
4. *absorbers worth*: provide further anti-reactivity for residual control and shutdown functions.

The main stages of the neutronic design developed to achieve a sustainable configuration of the LFR-TL-30 core are summarized below, emphasizing, in particular, the rationale behind each of them.

2 Main stages of the core neutronic design

The search for a sustainable neutronic configuration of the LFR-TL-30 core can be divided into six stages. For each of them, the main neutronic results in terms of criticality (k_{eff}) at Beginning of Life (BoL) and End of Life (EoL), reactivity swing (Δk_{eff}), loaded Heavy Metal (HM) mass, average burnup at discharge, maximum Fuel Assembly Distribution Factor (FADF) at BoL and EoL and absorbers reactivity worth are analysed. It should be noted that these results refer to the expanded configuration at the temperatures of the core operating at full power. Thermal power, availability factor and operational time were set at 90 MW, 95% and 15 years, respectively.

With reference to these neutronic results, and to the aimed performance introduced above, the objectives listed in Table ***2*** are established.

Table 2. Objectives of the neutronic design.

Target	Parameter	Objective
1	k_{eff} @ EoL	$[1-\varepsilon, 1+\varepsilon]$
2	FADF max	[1, ~1.25]
3a	absorbers worth (all devices)	$\geq \Delta k_{eff}$
3b	absorber worth (each device)	<< 650 pcm
4	absorbers worth (all devices)	$\geq \Delta k_{eff}$ + (≈2000 pcm) [tentative]

The neutronic results of each stage are reported in Table ***3***. All calculations were performed by means of the Monte Carlo transport code MCNP6.1 **Error! Reference source not found.**, considering 110 k-eigenvalue source iteration cycles, of which the first 10 skipped, with 1.0E+05 histories per cycle. Moreover, taking advantage of the parallel architecture implemented in MCNP6.1, all calculations were carried out on CRESCO6, with significantly increased computational performance. The use of the Linux cluster integrated in the ENEAGRID HPC infrastructure was in particular valuable for the depletion calculations distributed over 40 nodes for a total of 1920 cores with a CPU time per burnup step never exceeding 230,000 minutes.

Table 3. Main neutronic results of each design stage.

Parameter	Unit	Stage 1	Stage 2	Stage 3	Stage 4	Stage 5	Stage 6
k_{eff} @ BoL	-	1.11786	1.02172	1.07706	1.06339	1.04587	1.03146
k_{eff} @ EoL	-	1.01523	0.95394	1.01159	1.00931	1.00914	1.00314
Δk_{eff}	pcm	10263	6778	6547	5408	3673	2832
HM mass	t	7.3	7.3	8.5	9.7	12.8	9.5
Burnup	GWd/t_{HM}	64	64	55	48	37	49
FADF max @ BoL	-	1.521	1.208	1.189	1.260	1.160	1.230
FADF max @ EoL	-	1.337	1.230	1.147	1.210	1.190	1.140
Absorber worth	pcm	n.c.[1]	n.c.[1]	n.c.[1]	2759	2077	2910 5004[2]

[1] not calculated.

[2] with new absorber configuration.

In stage 1, the neutronic performance of the core configuration proposed in [1] was studied, assuming the whole fuel to be at the highest enrichment allowed by security limitations to first check the overall possibility to achieve a critical core. Criticality was not only achieved, but the reserve of reactivity was also found sufficient to operate the reactor for 15 years. However, the power distribution among the fuel assemblies at BoL was found to be very peaked, as expected, and the FADF of the central assembly was quantified to be 50% greater than that of the average assembly, with possible critical effects on the hot spots. Moreover, a reactivity swing greater than 10000 pcm was predicted, making the reactor control extremely difficult.

In stage 2, a more flattened power distribution and a reduced reactivity swing were pursued by considering, in the same reference configuration, two different enrichment zones, i.e., lowering the enrichment in a set of fuel assemblies at the centre (where the flux typically peaks). The beneficial effects on the maximum FADFs at both BoL and EoL are straightforward, being now about 20% higher than those of the average assembly. Furthermore, the reduction in the fissile inventory of the inner zone allowed a reduction of the reactivity swing by about 4000 pcm due to an increase of the breeding in the inner zone. Unfortunately, the lower reserve of reactivity was only sufficient for about 5 years, against the required 15.

In stage 3, the need to improve criticality was pursued by reducing the pitch among fuel pins i.e., the volume fraction of the coolant in the elementary fuel cell, and by increasing fissile inventory. To do this, both the number of pins per assembly and the number of outer assemblies with higher enrichment were increased. This last change was also designed to transfer importance from inner to outer zones in order to make the power distribution more flattened. The results in Table ***3*** confirm that the reactivity curve is shifted upward, with a reserve of reactivity at EoL of over 1000 pcm, and that the power distribution is further improved. Unfortunately, the reactivity swing, although slightly reduced compared to stage 2, continued to be too high to allow the control of the reactor.

In stage 4, the reactivity swing was further reduced by lowering the fuel enrichment in the inner zone, exploiting the margin on the excess in the reserve of reactivity. This choice, in fact, allowed on the one hand to enlarge the breeding contribution to the system reactivity as burnup increases and on the other hand to improve the absorber effectiveness, making the outer region even more important. At the same time, the active length was extended by 10% to compensate for the decrease in the fuel inventory at BoL. However, it should be noted that this extension has also a positive effect on reducing the reactivity swing as it produces a reduction in burnup. If compared to the previous step, a reduction in the reactivity swing of over 1000 pcm was obtained but this was not yet enough to make the reactor controllable by 6 circular control elements of B_4C with boron enriched to 90 wt.% in ^{10}B and located outside the inner

vessel. It is also worth noting that in this way the mass of uranium was increased by 17% going from 7.3 to 8.6 tons and the power distribution was slightly worse than before.

In stage 5, a further attempt to reduce the reactivity swing based on the increase in fuel mass was made. This was achieved by adding another 18 fuel assemblies in the inner zone with a consequent increment in the initial mass of uranium of 32% (9.7 to 12.8 t). At the same time, to avoid an excessive distortion in power distribution, the fuel enrichment in the inner zone was also slightly increased. Thanks to this increase in the fuel inventory, it was possible to shorten the active length by using the value of stage 3. The reduction of the pressure drops in core thus obtained was partially exploited to reduce the pitch among the fuel pins, which allowed to further decrease the parasitic absorption by the coolant with positive effects on reactivity. Unfortunately, this extreme effort to reduce the reactivity swing by levering the fuel inventory did not produce a fully viable solution. In fact, although the reactivity swing was found to be more than 30% lower, it needed to be further reduced being the reactivity worth of the control elements largely insufficient to allow for the reactor control.

Figure 2. Cross-sectional view of the final core configuration.

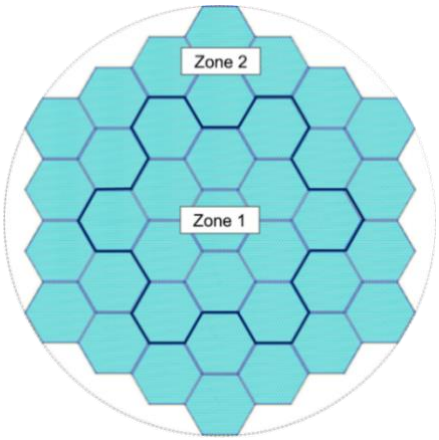

In stage 6, the idea of reducing the reactivity swing by increasing fuel mass and/or reducing fuel enrichment was therefore abandoned. Starting from the configuration of stage 4, a different approach was adopted. To reduce the reactivity swing, a neutronic solution was found using neptunium, as a burnable poison, homogeneously mixed in all fuel pins [3]. To this end, two different percentages of neptunium were used in the two enrichment zones shown in Figure 2. In addition, the blanket above and below the fuel column was replaced by magnesia (MgO) that, reducing the leakage of neutrons, increases the reactivity of the system. These solutions made it possible to halve the value of reactivity swing of stage 4, with even a small improvement in the power distribution, especially at EoL. Notwithstanding this significant reduction in reactivity swing, the worth of the control elements continued to be insufficient. However, this last configuration was the first exhibiting a reactivity swing low enough to imply the worth of a single absorber to respect the objective 3b, thus the first potentially viable. To improve the overall anti-reactivity worth of the entire system of absorbers, it was recognized the necessity for a new design, by modifying their configuration in terms of shape, with rectangular rather than circular sectors, and of position, by arranging them closer to the fuel region. To do this, the inner vessel was removed and the barrel was put in its place. Thanks to this new configuration, the reactivity of the control elements increased from 2910 to 5004 pcm, thereby satisfying objective 4 and making it possible to both control and protect the reactor.

3 Future activities

From a neutronic point of view, what was obtained appears to be a viable configuration for the LFR-TL-30 core. In fact, the neutronic results, although at preliminary level, prefigure a sustainable solution. Obviously, this is only a part of the neutronic analysis required by the conceptual design of a reactor core. In the future, this analysis should be completed calculating other crucial neutronic parameters such as the axial power distribution among fuel assemblies, power distribution among fuel pins and reactivity coefficients. Downstream of this, thermohydraulic and thermomechanical analyses should be carried out to confirm the overall viability of this configuration.

References

[1] G. Grasso, Considerations to conceptualize the core, Internal presentation, December 2021.

[2] J.T. Goorley et al. Initial MCNP6 release overview – MCNP6 version 1.0, internal report LA-UR-13-22934, LANL, Los Alamos, 2013.

[3] H. Guo, L. Buiron, P. Sciora, T. Kooyman, Optimization of reactivity control in a small modular sodium-cooled fast reactor, Nuclear Engineering and Technology, 2020.

LAMBDA-HOPPING IN ALCHEMICAL CALCULATIONS OF HYDRATION FREE ENERGIES IN CONFORMATIONALLY RESTRAINED MOLECULES

Piero Procacci[1*]

[1]*University of Florence, Chemistry Dept. U. Schiff, Via della Lastruccia 3, 50019 Sesto Fiorentino, Italy*

ABSTRACT. In the context of computational drug design, we examine the effectiveness of the enhanced sampling techniques in state-of-the-art free energy calculations based on alchemical molecular dynamics simulations. In a paradigmatic molecule with competition between conformationally restrained E and Z isomers, whose probability ratio is strongly affected by the coupling with the environment, we found that the pure λ-hopping, commonly used in solvation and binding free energy calculations via alchemical free energy perturbation techniques, is ineffective in enhancing the sampling of the isomeric states, exhibiting a pathological dependence on the initial conditions.

1 Background

The calculation of binding free energy (BFE) in ligand-receptor systems via molecular dynamics (MD) simulation is one of the major challenge in today's computational chemistry.[1] The consensus approach for computing BFEs is based on the alchemical protocol,[2] whereby the end-states of the A+B=AB reaction are connected via intermediate nonphysical states in which the ligand-environment interactions are progressively decoupled. The binding free energy is recovered via a thermodynamic cycle as the difference between two solvation free energies, namely that of the ligand in the bound state and in the pure solvent. The intermediate non-physical states (typically few tens) consist in the so-called λ-stratification,[3] with λ being the alchemical parameter controlling the level of interaction of the ligand with the environment. The free energy difference between two consecutive λ states is generally computed via free energy perturbation (FEP) or, equivalently, thermodynamic integration (TI).[3] Notably, these λ-simulations are completely independent and can be performed in parallel. On the other hand, convergence constitutes the major challenge in alchemical BFE calculations. Incomplete sampling, due to large free energy barriers between conformational states in ligand and proteins, may produce unreliable results that are strongly dependent on the initial conditions.[4] To overcome these serious drawbacks, the alchemical technology is combined with enhanced sampling techniques, typically based on the Hamiltonian Replica Exchange Method(HREM)[5] allowing Metropolis-regulated exchanges between λ-states, in the hope that the mixing of states with disparate alchemical coupling could facilitate the sampling.[6]

Despite its widespread use, however, the effectiveness of HREM techniques with λ-hopping in BFE or RBFE calculations has been recently questioned by several authors.[7,8] Here, to test the effectivenes of the HREM-FEP technology, we use as a paradigmatic example the E-Z equilibrium in 5-amino-3-enoic-acid (APA), a zwitterion molecule in solution characterized by torsional barrier around the central

sp_2 bond of tens of kcal/mol. We show that while ordinary HREM simulation with solute tempering (ST)[5] at full coupling is able to rapidly attain, in few ns, the E-Z conformational equilibrium of a solvated APA molecule at ordinary temperature, HREX-FEP with simple lambda hopping is pathologically dependent on the initial onfiguration and is ineffective in surmounting the the torsional barrier at any λ value.

2 Methods

In figure 1, we show the 2D and 3D structures of E-(trans) and Z-(cis) 5-Aminopent-3-enoic acid (APA) disastereoisomers. In water solution at pH=7, APA is in the zwitterionic state with pKa's of the carboxylic and amino groups of 4.49 and 9.65, respectively.[9] APA can be selectively obtained in the conformationally restricted Z or E forms. The Z isomer serves as the building block for the synthesis of macrocyclic pseudopeptides for the treatment of a variety of diseases.[10] The E-form is used to synthesize cyclic macrolactames aggregating in remarkable supramolecular structures with potential

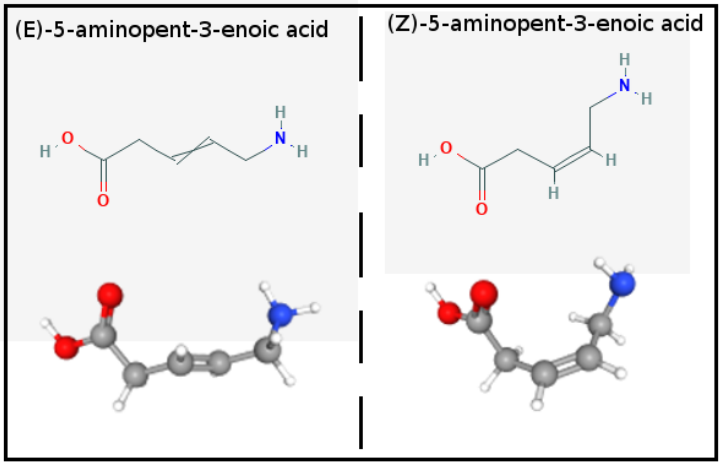

Fig.1: Structure of the E- and Z- 5-amino-3-enoic-acid diastereoisomers

application in drug delivery, photonics, material science and catalysis.,[11] While the E-Z thermodynamic equilibrium could be in principle easily achieved by photoisomerization of the double bond via excitation to the singlet π^* level, to our knowledge, no experimentally determined equilibrium cis-trans ratio is available in the literature.

The potential parameters for APA were obtained using the PrimaDORAC web interface[12] based on the well established GAFF2 force field for organic molecules. The barrier height for the torsional potential around the double bond is of the order of 40 kcal/mol, consistently with the experimental indications on non-conjugated olephins.

Simulations in the gas phase were done on a single molecule in a large box under constant temperature (300 K) via a Nosé-Hoover thermostat. Simulations in solution were performed dissolving a single APA molecule in 512 solvent molecules using the OPC3 three-site model for water in condition of constant pressure (0.1 Mpa) and temperature (300 K), imposed using an NPT extended Lagrangian with isotropic stress tensor. Electrostatic interactions were treated using the Particle Mesh Ewald technique.

All enhanced sampling simulations were performed with the public domain ORAC program[13] on the CRESCO6 cluster. For the HREM simulations, we used a minimum scaling factors for the potential energy of 0.1, corresponding to temperatures of 3000 K with a standard scaling protocol.[6] The total length of the HREM sampling on the target state was of 8 ns. HREM simulation with λ-hopping for solvated APA is emulated with ORAC by scaling only the solute-solvent interaction potential up to a

factor of λ = 0.05. All parallel HREM simulation were performed on the CRESCO6 cluster using 96 cores (8 MPI process for the HREM walkers, times 12 OpenMP threads for the force computation for each of the 8 walkers) .

3 Results and discussion

In Figure 2 (left panel), we show an HREM sampling of the C=C cis/trans state of the zwitterionic APA molecule in the gas phase (a,b) and in TIP3P water in standard conditions (c,d). The HREM protocol involves, in both cases, the scaling of the intrasolute potential with a solute temperature reaching 3000 K in the hottest GE state. Such intrasolute temperature reduces the cis/trans barrier by a factor of 10 hence affording on this hot state a quasi-unrestricted rotation around the C=C bond. Despite such high HREM temperature range, only the degrees of freedom of the solute are involved and 16 replicas are sufficient for a good exchange rate (40% on the average). Quite reasonably, the cis state is strongly favoured in the target state of the gas-phase (black circles in a) where the attractive interactions between the charged end groups are unscreened. The trans state, on the other hand, while easily and uniformly sampled in the hottest GE state (red circles in a), is very rarely transmitted to the target state. In b) the gas-phase distribution of the dihedral angle is shown for the target state (black) and the hottest GE state (red). The cis/trans exchange in TIP3P water is frequent and homogeneous on the target state

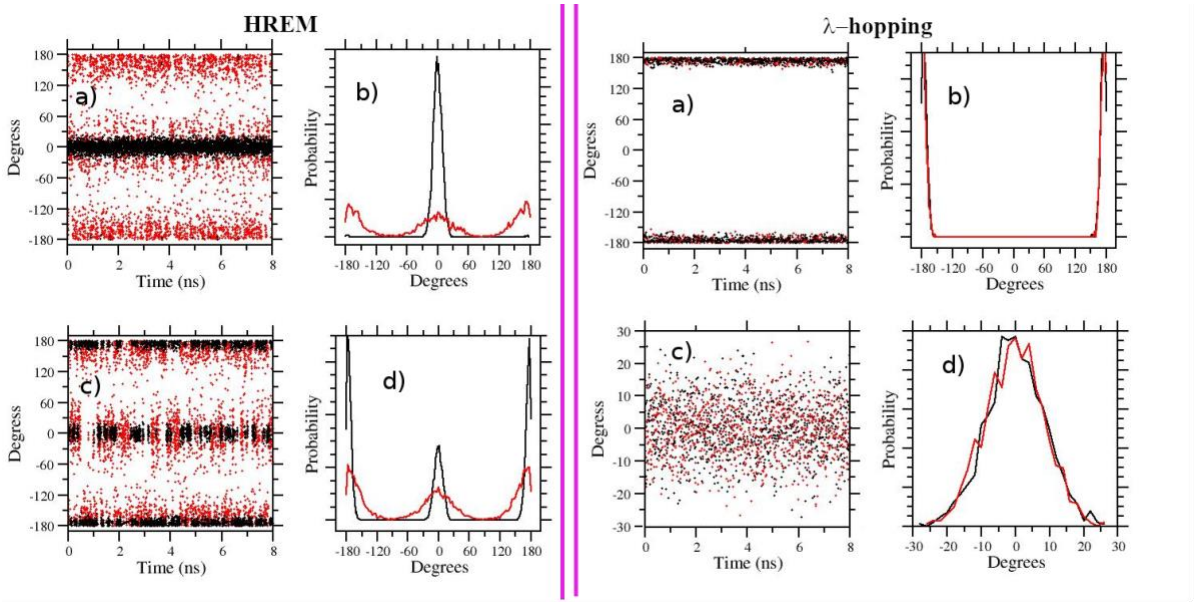

Fig. 2: *Left panel:* HREM sampling of the 5-Aminopent-3-enoic acid in the gas phase (a,b) and in OPC3 water (c,d). In a), c) the time records of the central dihedral angle around the double bond are reported for the target state (black circles) and for the hottest state (red circles). The corresponding distribution of the dihedrals are shown in b) and d). In all cases, the REM protocol is the same (S=0.1, N_{rep}=8). *Righ panel:* HREM sampling of the 5-Aminopent-3-enoic acid in TIP3P water with HREX/λ-hopping. In (a,b) and (c,d) the starting configuration were the trans and cis state, respectively. Time records are on (a,c) and dihedral distributions on (b,d). Black and red symbols/line in ab,cd refer to the λ=1 and λ=0 states. In all cases, the REM protocol is the same (S=0.1, N_{rep}=16)

(black circles) and on the hottest state (red circles) as well. The trans state in water is favoured in the target state (black curve in d), although the cis state population remains significant. The enhancement of the trans population in water is expected due to the solvent screening of the opposite charge end-group. The cis-trans population ratio increase in the hottest state (d). In the Figure 2 (right panel) the

HREX/λ-hopping in solution is emulated by scaling along the replica progression only the solute-water intermolecular interactions up to a quasi gas-phase state $\lambda = 0.1$. 16 replicas are needed in this case (hence engaging four CRESCO6 nodes and 192 cores) for an acceptable exchange rate. In (a,b) the HREX/lambda simulation was started from the trans state and in (c,d) from the cis state. Despite the fact that standard HREX diagnostics (round-trip times, exchange rates, uniform state distribution in the walkers) are fine, the HREX/lambda-hopping protocol is ostensibly unable to surmount the cis-trans barrier in any of the GE states. The same state (cis or trans) is found in all walkers depending on the starting configuration (cis or trans) of the simulation. Lambda-hopping is not enhancing in any way the sampling in 5-Aminopent-3-enoic acid.

Acknowledgments

The computing resources and the related technical support used for this work have been provided by CRESCO/ENEAGRID High Performance Computing infrastructure and its staff. CRESCO/ENEAGRID High Performance Computing infrastructure is funded by ENEA, the Italian National Agency for New Technologies, Energy and Sustainable Economic Development and by Italian and European research programmes (see www.cresco.enea.it for information).

References

Reference identification numbers as [1], [2],…have to be put inside the text, where they are mentioned; each reference has to be quoted in text queue according to the following order: author/s, title of the author's paper, further specific elements of the cited document. Use **Times New Roman 11** font. If possible, adhere to the following example:

[1] In-Silico Drug Discovery Market. 2022; https://www.psmarketresearch.com/market-analysis/in-silico-drug-discovery-market, accessed June 12 2022.

[2] Jorgensen, W. L.; Buckner, J. K.; Boudon, S.; TiradoRives, J. Efficient computation of absolute free energies of binding by computer simulations. Application to the methane dimer in water. *J. Chem Phys.* **89**, pp. 3742–3746 (1989).

[3] Pohorille, A.; Jarzynski, C.; Chipot, C. Good Practices in Free-Energy Calculations. *J. Phys. Chem.* B **114**, pp. 10235–10253 (2010).

[4] Bhati, A. P.; Wan, S.; Hu, Y.; Sherborne, B.; Coveney, P. V. Uncertainty Quantification in Alchemical Free Energy Methods. *J. Chem. Theory Comput.* **14**, pp. 2867–2880 (2018).

[5] Sugita, Y.; Okamoto, Y. Replica-exchange molecular dynamics method for protein folding. *Chem. Phys. Lett.* **314**, pp. 141–151 (1999).

[6] Hritz, J.; Oostenbrink, C. Hamiltonian replica exchange molecular dynamics using soft-core interactions. *J. Chem. Phys.* **128**, pp. 144121 (2008).

[7] Baumann, H. M.; Gapsys, V.; de Groot, B. L.; Mobley, D. L. Challenges Encountered Applying Equilibrium and Nonequilibrium Binding Free Energy Calculations. J. Phys. Chemi. B **125**, pp 4241–4261 (2021)

[8] Wan, S.; Tresadern, G.; Perez-Benito, L.; van Vlijmen, H.; Coveney, P. V. Accuracy and Precision of Alchemical Relative Free Energy Predictions with and without Replica-Exchange. *Adv. Theory Simul.* **3**, 1900195 (2020).

[9] Pka's for APA computed with *Chemicalize*, developed by ChemAxon (2021).

[10] Sun, D. Recent Advances in Macrocyclic Drugs and Microwave-Assisted and/or Solid-Supported Synthesis of Macrocycles. *Molecules* 27(3) (2022).

[11] Baillargeon, P.; Bernard, S.; Gauthier, D.; Skouta, R.; Dory, Y. Efficient Synthesis and Astonishing Supramolecular Architectures of Several Symmetric Macrolactams. *Chemistry A European Journal* **13**, 9223–9235 (007).
[12] Procacci, P. PrimaDORAC: A Free Web Interface for the Assignment of Partial Charges, Chemical Topology, and Bonded Parameters in Organic or Drug Molecules. *J. Chem. Inf. Model.* **57**, 1240–1245 (2017).
[13] Procacci, P. Hybrid MPI/OpenMP Implementation of the ORAC Molecular Dynamics Program for Generalized Ensemble and Fast Switching Alchemical Simulations. *J. Chem. Inf. Model.* **56**, 1117–1121 (2016).

AB-INITIO CALCULATIONS OF COMPLEX SYSTEMS: APPLICATION TO BATTERIES AND TO ELECTRONIC DYNAMICS

Domenico Corona[1], Margherita Marsili[2], Paola Gori[3], Francesco Buonocore[4] and Olivia Pulci[1]

[1]*Department of Physics, University of Rome Tor Vergata, I-00133 Rome, Italy*

[2]*Department of Physics and Astronomy, University of Bologna, I-40127 Bologna, Italy*

[3]*Department of Industrial, Electronic and Mechanical Engineering, University of Roma Tre, I-00146 Rome, Italy*

[4]*ENEA Casaccia Research Center, I-00123 Rome, Italy*

ABSTRACT. The strength of first principles calculations lies on the fact that they are predictive, the method is transferable from one system to the other, and the results are reliable. The drawback, for many atoms systems, is the high computational cost, which requires the use of supercomputers. As an example, we report here the results of ab-initio calculations on two different systems: Density Functional Theory investigation of new anodes based on Boron Nitride endofullerenes plus Magnesium; and Many-Body Green's function perturbation theory results for real time electronic dynamics of molecules close to a plasmonic nanoparticle.
All the calculations have been performed on CRESCO HPC.

1 Introduction

With the advent of supercomputers, it is by now possible to create and investigate *in silico* the geometry, the electronic and optical properties of new materials. This is of outmost technological importance for developing new devices for energy production, for energy storage, new sensors, novel optoelectronic devices, quantum computing and so on.
Here we report our results obtained within ab-initio computational studies using CRESCO. We present results for energy storage, batteries, and for surface plasmons, important for several chemical reactions.

Rechargeable batteries, among all energy storage technologies, have become indispensable since the 1990s, when lithium-ion batteries (LIBs) have been commercialized. However, the growing electrified world gives rise to market concerns about lithium resource depletion and its consequent increasing cost; therefore, it is widely accepted that the future of rechargeable batteries is in the search and development of alternative battery chemistries. Magnesium (Mg) is among the ten most abundant elements in Earth's crust, it is atoxic, light, perfectly recyclable, has high theoretical specific capacity and low redox potential. There is hence an increasing attention on magnesium as a complement and as an alternative to lithium for the next generation of power sources.
Another hot topic Surface plasmon resonances (SPRs) are the origins of the tunability and strength of the optical spectra of metallic nanoparticles (NPs) which are thus extremely effective and versatile in

harvesting light. One of the most intriguing and exploited properties of SPRs is their ability to concentrate the optical field and amplify it by several orders of magnitude, strongly enhancing light−matter interaction in the proximity of the NP. Such a combination of field enhancement and spatial localization has led to the development of spectroscopies with single-molecule sensitivity such as plasmonic enhanced fluorescence and Raman spectroscopies. Moreover, SPRs can strongly enhance yields and selectivity of several (environmentally and industrially important) chemical reactions, the NP either functioning as an effective photocatalyst or as an antenna that magnifies the activity of a standard catalyst.

2 Methods

For the BN endofullerenes the calculations have been obtained in the DFT framework, using the DMOl3 package from Materials Studio [1] with GGA-PBE XC functional taking into account van der Waals interaction. For the electron dynamics near plasmonic particles, DFT calculations have been performed using the Quantum Espresso suite [2], whereas the Many-Body results have been obtained with the GWMOL code [3].

3 Results

3.1 BN nanocages

We have studied of the effect of encapsulation of halogen (Cl^-, Br^-) and chalcogen anions (O^{2-}, S^{2-}, Se^{2-}) in the interaction of the $B_{12}N_{12}$ nanocages with the Mg^{2+} cation. Our aim is to predict whether these BN endofullerenes could be suitable anode materials for magnesium-ion batteries, which are considered a cheap, sustainable, and safe substitute to lithium batteries. Some of the BN endofullerenes studied are depicted in Fig.1.

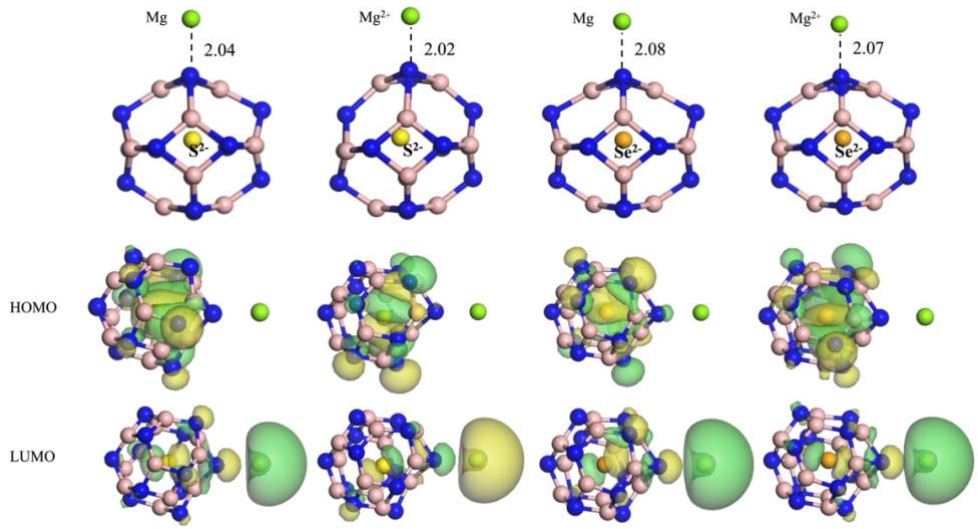

Fig.1: Geometrically optimized structures and molecular orbitals plots for $B_{12}N_{12}/S^{2-}$//Mg, $B_{12}N_{12}/S^{2-}$//Mg^{2+}, $B_{12}N_{12}/Se^{2-}$//Mg, $B_{12}N_{12}/Se^{2-}$//Mg^{2+}. Distances are in Angstroms.

To assess their potentiality as negative electrodes, the formation energy, the interaction energy, and the cell voltage have been calculated for each system. Remarkable cell voltages have been obtained with the encapsulation of divalent chalcogenide anions; the effect increases down the group, reaching a cell voltage of 3.37 V for Selenide based anodes. The resulting voltages are shown in Fig.2 [4].

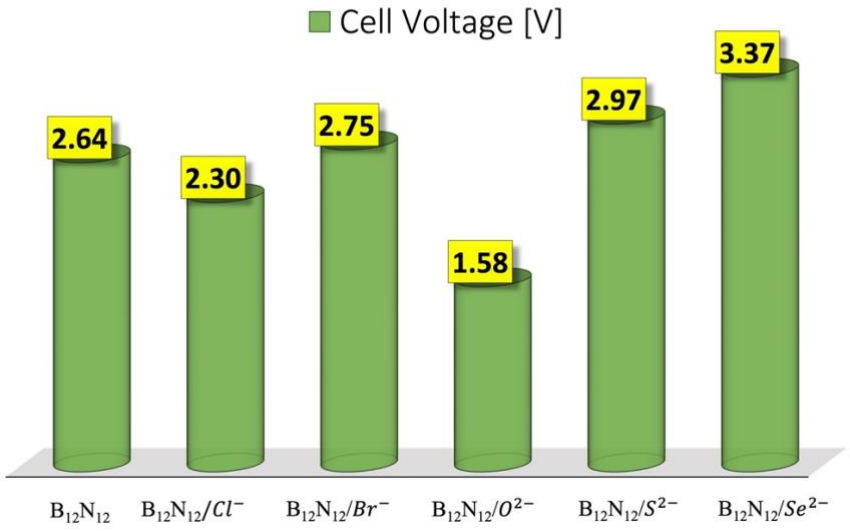

Fig.**2**: Resulting cell voltages for the various BN endofullerenes studied.

3.2 Real time electronic dynamics of molecules close to a plasmonic nanoparticle

We developed a novel multiscale approach (PCM-NP) for the description of the coupled dynamics of the electronic system of a molecule (or a generic quantum system treated atomistically) and a polarizable plasmonic nanoparticle (NP) in the presence of a (time-dependent) external field. Following Refs [5] and [6], within our approach the plasmonic (NP) is treated as a continuous body characterized by its frequency dependent dielectric function, its shape and size. There is no particular constraint on the NP shape.

The peculiarity of our novel approach is that the electronic dynamics of the quantum system develops within a GW-BSE derived polyelectronic active space, as shown in Ref. [7]. The GW-BSE derived active space allows us to overcome the limitations of current implementation (employing time-dependent configuration interaction singles and real-time density functional theory) in terms of achievable accuracy without compromising on the accessible molecular sizes.

Within the PCM-NP approach the coupling between the NP and quantum system is of electrostatic nature and is provided by defining an effective Hamiltonian for the molecule in which an interaction term is added to the one of the isolated case. The problem to be solved is nonlinear as the added term, induced by the presence of the classical subsystem, self-consistently depends on the charge distribution of the quantum one. We have applied this approach to two prototype systems: LiCN molecule close to a 5 nm diameter metallic nanosphere, and the p-nitroaniline molecule close to a silver nanotip. The dielectric constant of the metallic NP was chosen in order to match the NP resonance and the dipole switch transition energy of the LiCN. The external pulse frequency was also set at this energy. The LiCN molecule was placed at increasing distances from the NP, and we were able to probe the space dependent amplification of the electric field, due to the NP and felt by the molecule, through the Rabi frequency of oscillation of the population of the molecule excited states. A summary of the results is presented in Fig. 3.

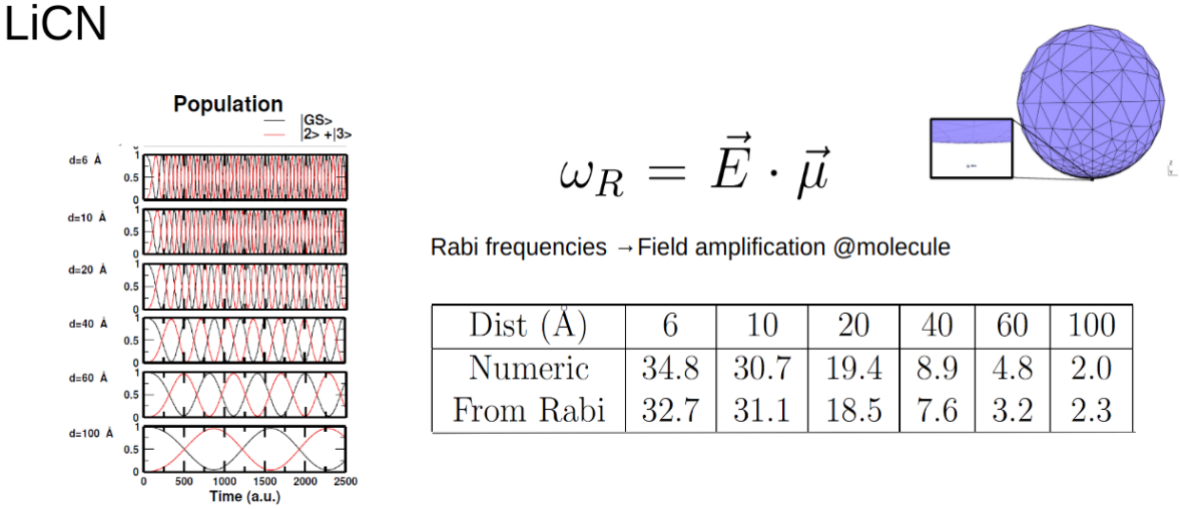

Dist (Å)	6	10	20	40	60	100
Numeric	34.8	30.7	19.4	8.9	4.8	2.0
From Rabi	32.7	31.1	18.5	7.6	3.2	2.3

Fig.3: Summary of the multiscale simulation of the electronic dynamics of the LiCN molecule set at increasing distances from a spherical nanoparticle. Left panel: population dynamics of the molecule at increasing distances. The Rabi oscillation frequencies decrease when the nanoparticle-molecule distance increases. Central panel: computed field enhancement compared to the one extracted from the Rabi frequency. The field enhancement is non monotonic with respect to nanoparticle-molecule distance. Left panel: pictorial representation of the nanoparticle molecule system.

Acknowledgments

All calculations have been performed on ENEA-CRESCO HPC, which we gratefully thank.

References

[1] BIOVIA, Dassault Systèmes, Material Studio 2020, San Diego: Dassault Systèmes, (2019).
[2] P. Giannozzi et al.,Advanced capabilities for materials modelling with Quantum ESPRESSO. *J. Phys. Condens. Matter* **29**, 465901, (2017)
[3] F. Bruneval, et al., MOLGW 1: Many-body perturbation theory software for atoms, molecules, and clusters. *Comput. Phys. Commun*. **208**, 149−161 (2016).
[4] D. Corona et al., in preparation
[5] S. Pipolo, S. Corni, Real-time description of the electronic dynamics for a molecule close to a plasmonic nanoparticle. *J. Phys. Chem. C*, **120**, 28774 (2016)
[6] D.G. all'Osto, G. Gil, S. Pipolo; S. Corni, Real-time dynamics of plasmonic resonances in nanoparticles described by a boundary element method with generic dielectric function. *J. Chem. Phys.* **153**, 184114 (2020).
[7] M. Marsili and S. Corni, Electronic Dynamics of a Molecular System Coupled to a Plasmonic Nanoparticle Combining the Polarizable Continuum Model and Many-Body Perturbation Theory, *Phys. Chem. C* **126,** 8768 (2022)

MCNP ANALYSES ABOUT THE POSSIBLE UTILISATION OF COMPACT NEUTRON GENERATORS FOR CANCER RADIOTHERAPY

Massimo Sarotto[1*], Maurizio Martellini[2]

[1*]*ENEA FSN-SICNUC-PSSN, C.R. Saluggia, Strada per Crescentino 41 – 13040 Saluggia (VC)*[15]

[2]*UNINSUBRIA, Via Ravasi 2 – 21100 Varese. Theranosti Centre S.r.l. scientific director*

ABSTRACT. In the framework of the LINCER regional project funded by Emilia Romagna and of the collaboration agreement between ENEA and Theranosti Centre S.r.l., several Monte Carlo simulations (with the MCNP code ported to CRESCO HPC) were performed to contribute to the development - from the conceptual design to the construction - of compact systems for the neutron irradiation of materials. A challenging application is represented by the Neutron Capture Therapy where the beam is adopted for cancer radiotherapy. The driving idea was the development of a 100 kV-10 mA DD neutron generator to be used for the neutron Intra-Operative Radiation Therapy (nIORT®) in which superficial solid neoplasms are irradiated after the removal of the primary tumour mass. The high dose rate levels (~1÷2 Gy (RBE)/min) in the tumour bed in "open wound" tissues allow to limited treatment times for the patients: ~5 ÷ 20 minutes depending on the clinical end-point chosen.

1 Introduction

This work has been carried out in the framework of the collaboration agreement between ENEA and the Theranosti Centre Srl company (TC, Milan) [1]. The main purpose was the development - from the conceptual design to the construction - of compact systems for the neutron irradiation of materials. A challenging application is represented by the Neutron Capture Therapy (NCT) where the beam is used for cancer radiotherapy. In comparison with other application fields (e.g., study of materials structure, activation analyses, fast neutron imaging, geological prospecting, etc.), the NCT requires a very high flux (~10^8 n cm^{-2} s^{-1}) to limit the treatment time for the patient at manageable values (~10÷60 min, depending on the NCT technique chosen). By exploiting the synergy between the objectives of:

- the ENEA-TC collaboration, in which TC supplied the detailed mechanical drawings of an innovative Compact Neutron Generator (CNG) to be used for a new promising field of NCT applications represented by the neutron Intra-Operative Radiation Therapy (nIORT®[16] [2]);
- the LINCER ("Laboratorio per la caratterizzazione di Irradiatori Neutronici Compatti in Emilia Romagna") project [3], in which a new infrastructure is under construction at the ENEA research centre in Brasimone (BO) for the CNG experimental characterisation;

several Monte Carlo simulations were performed for the design optimisation of a Beam Shaping Assembly (BSA). The BSA consists essentially of a shield (for people, environment) to be installed around the CNG and a collimator with an irradiation window from which to extract the neutron beam.

[15] Corresponding author. E-mail: massimo.sarotto@enea.it.

[16] The intraoperative radiotherapy (IORT) is a treatment technique which associates radiotherapy with surgery. It foresees the administration of a dose of radiation directly on the tumour by irradiating the tissue that cannot be attacked surgically, or on the tumour bed after having removed the primary neoplastic mass. Nowadays, this therapy is performed by high-energy electrons and photons (X-rays) and presents some limitations (e.g., most of X-rays pass through the body irradiating also healthy tissues, electrons deliver high doses even at ~5 cm depth with a potential damage of the nearest organs).

The apparatus for nIORT® applications is the subject of an international PCT patent [4] filed in July 2021 by TC, ENEA and Berkion Technology LLC (USA), that manufactured the whole CNG-BSA currently at ENEA Brasimone for the beginning of the experimental phase.

2 MCNP model for nIORT® treatments

The CNG is a cylindrical hermetic void tube made of High Density Polyethylene (HDPE) in which D+ ions (created in a plasma chamber) are accelerated against a titanium target where the Deuterium-Deuterium (DD) fusion reaction occurs by generating neutrons of 2.45 MeV energy (see left frame of Fig. 1). The basic idea in the nIORT® applications is to irradiate superficial tumour beds "directly" with the 2.45 MeV neutrons emitted by the DD source (e.g., without their moderation to epithermal / thermal energies as in the Boron NCT), which are very effective to cancer cells killing (by inducing double strand breaks) because of their high Relative Biological Effectiveness (RBE) [5].

The CNG and the surrounding BSA were modelled with the Monte Carlo Neutron Particle ver. 6.1 code (MCNP6.1) [6] - coupled with the ENDF/B-VIII.0 nuclear data library [7] - ported to CRESCO HPC, in which different instances of the code can run in parallel *e.g.*, for parametric investigations. As shown in the right frame of Fig. 1, the BSA includes the shield in borated Polyethylene (PE+B), an external layer in lead (Pb) and an HDPE neutron collimator delimiting the circular irradiation window. The whole CNG-BSA system results in a cylinder with limited size (30 cm diameter, ≅40 cm length) and weight (< 100 kg), making possible its remote handling by a robotic arm.

To evaluate the CNG-BSA performances for potential nIORT® treatments, the human tissues were also modelled. A zoom on the MCNP model of the BSA and breast tissues positioned at the irradiation window is also shown in the right frame of Fig. 1. The tumour bed and breast tissues (modelled with 0.5 cm thick cells) were surrounded by "healthy" skin and muscle tissues. For the IORT modality, the breast was not covered by skin in correspondence of the irradiation window. For the tissue compositions, the MCNP model of the EVA anthropomorphic phantom was adopted [8].

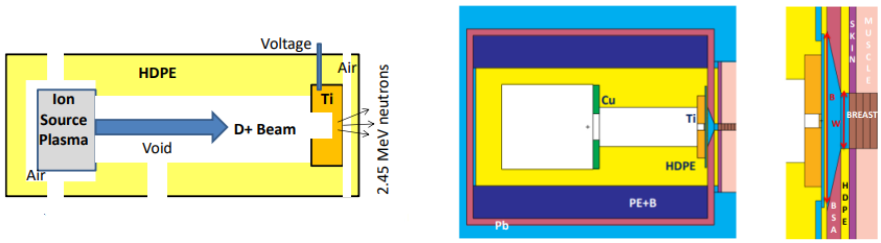

Fig.1: Conceptual design of D+ ion-based CNG (left), MCNP model of the CNG-BSA and breast tissues at the irradiation window (right).

3 Results and discussion

To irradiate tumour beds of different extensions (and conditions), the CNG-BSA was designed with a tuneable irradiation window diameter (see top part of Fig. 2) that can be varied in the 1 ÷ 6 cm range. The bottom part of Fig. 2 shows a 2D map of the neutron flux distribution into the biological tissues obtained by a BSA with 1 cm window diameter. The spatial distribution reveals a flux peak in the window centre and its decrease along the radial direction in surface tissues (i.e., muscle surrounding the tumour bed and skin) and going in depth into breast and muscle tissues. Consequently, in the view of potential nIORT® treatments, three advantages could be exploited:

(1) the flux and, hence, the dose peaks are released at tissues surface in the tumour bed centre;
(2) the neutrons diffusion into the tissues acts as a sort of ionizing radiation "foam" and allows them to kill cancer quiescent cells (i.e., metastases) around the tumour bed in the surgical cavity;

(3) going in depth in tissues, the flux levels reduce by a factor ≅2 in the first centimetre and by a factor ≅4 at 3 cm depth, that should preserve the nearest organs from harmful radiations. This feature can be clearly seen in Fig. 3 showing the MCNP model of the CNG-BSA for the brain irradiation (i.e., Glioblastoma cancer) with skull (left frame) and the equivalent dose rate profiles in brain depth obtained with and without skull (right frame). The irradiation without skull, as required by the IORT modality, would be preferable to avoid the peaks in skin/skull.

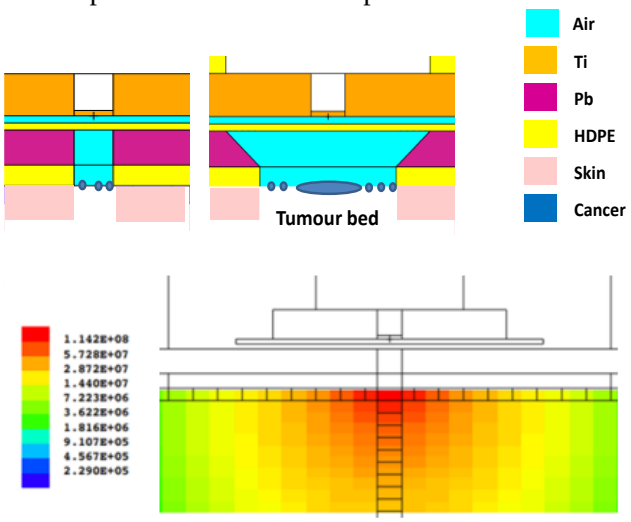

Fig.2: Illustrative sketch of two different tumour bed extensions to be irradiated by narrow and large CNG-BSA irradiation windows (top).
2D map of neutron flux spatial distribution in human tissues (1 cm BSA window diameter, bottom).

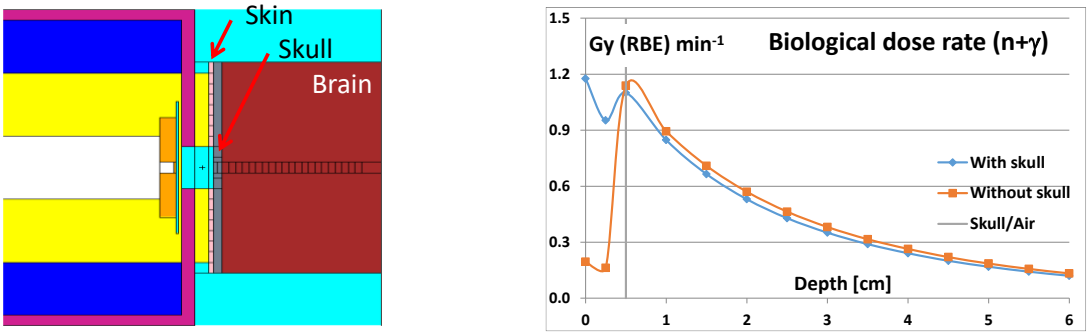

Fig.3: Some details of the MCNP model for brain irradiation (with skull, left), total equivalent dose profiles in brain depth with and without skull (right).

The flux and the equivalent dose rate distributions shown in Figs. 2 and 3, respectively, were obtained by foreseeing the CNG powered at 100 kV-10 mA supplying a neutron yield of 3.3 10^9 s^{-1}. Starting from the spatial distributions of the 2.45 MeV neutrons, provided by the CNG designer, the MCNP simulations were not restricted to neutrons (*i.e.*, the primary ones from the Ti target and the secondary ones coming from the scattering with the BSA walls and into the biological tissues), but they also considered photons (*i.e.*, gammas created by neutron radiative captures). The physical dose rates (Gy/min) into biological tissues due to neutrons ($D'_{f,n}$) and photons ($D'_{f,\gamma}$) were calculated by standard MCNP tallies, while the total equivalent dose rate ($D'_{eq,tot}$ in Gy (RBE)/min) was obtained by:

$$D'_{eq,tot} = D'_{f,\gamma} + \int w_n(E) D'_{f,n}(E) dE \qquad \text{[Gy (RBE)/min]} \qquad (1)$$

where "$w_n(E)$" is the radiation weighting factor [5] whose value, for 2.45 MeV neutrons, is about 16 (vs. 1 for electrons or X-rays). Thanks to the high flux at the irradiation window (≅0.5÷1 10^8 cm^{-2} s^{-1}

for 1÷6 cm window diameters) and the high RBE of neutrons, the maximum equivalent dose rates in surface tissues result to be ~1÷2 Gy (RBE)/min for all window diameters.
In the view of possible clinical applications, the CNG-BSA performances for potential nIORT® treatments were defined by adopting the clinical end-points used in the standard IORT techniques and evaluating the Treatment Time (TT) needed to reach such dose targets in a single session. Referring to the IORT technique with electrons (IOERT), two dose targets are usually adopted depending on the tumour bed (and patient) conditions. The so-called Boost IORT and Radical IORT regimes foreseeing end-points of about 10-12 and 20 Gy (RBE), respectively [9]. Once defined the equivalent dose target, the TT can be easily retrieved from the dose rate values of Eq. (1).
To highlight the CNG-BSA flexibility to deliver high dose levels in limited TTs for tumour beds having different extensions, Table 1 reports its performances for the Boost and Radical IORT clinical protocols assuming 12.6 and 20 Gy (RBE) as clinical end-points. The results refer to the MCNP analyses for the breast cancer (Fig. 1) and indicate that both dose targets can be reached in a one-shot irradiation of 5÷10 min only, depending on the end-point and the irradiation window diameter (1÷6 cm) chosen. Besides the peak delivered in the window centre, the average dose values (inside the irradiation window) and the peak values in the healthy skin (outside the irradiation window) were evaluated / monitored. Exploiting the high dose rates, the 100 kV-10 mA CNG-BSA could be also used in the so-called Ultra-Radical IORT regime - as required by the most severe Pancreatic Ductal Adenocarcinoma (PDAC) cases - by delivering e.g., up to 75 Gy (RBE) in TTs less than 1 hour [10].

Table 1: Boost and Radical clinical protocols for nIORT® treatments (CNG-BSA with 1÷6 cm window diameter).

Dose target	Ø [cm]	Peak dose in tumour bed [Gy (RBE)]	Average dose in tumour bed [Gy (RBE)]	Peak dose in healthy skin [Gy (RBE)]	TT [min]
12.6 Gy (RBE) as peak dose (Boost)	1	12.6	12.6	8.7	5.3
	2		11.9	7.1	5.7
	4		9.6	4.9	5.9
	6		7.5	3.2	6.0
20.0 Gy (RBE) as peak dose (Radical)	1	20	20.0	13.9	8.3
	2		18.9	11.3	9.0
	4		15.2	7.8	9.3
	6		11.8	5.2	9.6

References

[1] Collaboration agreement ENEA-Theranosti Centre Srl, ENEA/2019/25134/FSN-ING (2019).
[2] nIORT® deposit 302019000045726 of 3rd July 2019.
[3] LINCER project, funded by Emilia Romagna with "Legge Regionale 27/12/2018 N.25", DGR N. 545/2019 – *CUP I74I19000360003* (2019-2021).
[4] M. Martellini et al., Multi Purpose Compact Apparatus for the Generation of a high-flux of neutrons, particularly for Intraoperative Radiotherapy, *Int. Patent PCT/IT2021/000032* (2021).
[5] Annals of the ICRP, *ICRP n. 103, Vol. 37*, ISSN 0146-6453, ISBN 978-0-7020-3048-2 (2007).
[6] B. Pelowitz et al., "MCNP6 USER'S MANUAL", *Report LA-CP-13-00634 Rev. 0*, Los Alamos National Lab (2013).
[7] ENDF/B-VIII.0 evaluated nuclear data library, https://www.nndc.bnl.gov/endf/b8.0/
[8] R. Kramer et al., "The calculation of dose from external photons exposures using human phantoms and Monte Carlo methods: part I. The male (Adam) and female (Eva) adult mathematical phantom", *GSF-Report S885* (1986).

[9] S. Hashemi, “Comparison of IORT (Radical and Boost Dose) and EBRT in Terms of Disease-Free Survival and Overall Survival according to Demographic, Pathologic, and Biological Factors in Patients with Breast Cancer”, *Int. J. of Surgical Oncology, Article ID 2476527* (2021).
[10] M. Sarotto, “Parametric MCNP analyses to address the design of a neutron collimator for high-flux compact DD sources to be used in cancer radiotherapy”, *Technical Report ENEA SICNUC-P000-044* (2021).

PREDICTION OF ABRUPT COOPERATION TRANSITIONS IN EVOLUTIONARY GAMES ON NETWORKS

Irene Sendiña-Nadal[1,2], Inmaculada Leyva[1,2], and Stefano Boccaletti[1,3]

[1]*Universidad Rey Juan Carlos, Complex Systems Group, 28933 Móstoles, Madrid*

[2]*Universidad Politécnica de Madrid, Center for Biomedical Technology, 28223 Pozuelo de Alarcón, Madrid*

[3]*CNR-Institute for Complex Systems, 50019 Sesto Fiorentino, Firenze*

ABSTRACT. Networks determine our social circles and the way we cooperate with others. We know that topological features like hubs and degree assortativity affect cooperation, and we know that cooperation is favoured if the benefit of the altruistic act divided by the cost exceeds the average number of neighbours. However, a simple rule that would predict cooperation transitions on an arbitrary network has not yet been presented. Here we show that the unique sequence of degrees in a network can be used to predict at which game parameters major shifts in the level of cooperation can be expected, including phase transitions from absorbing to mixed strategy phases. We use the evolutionary prisoner's dilemma game on random and scale-free networks to demonstrate the prediction, as well as its limitations and possible pitfalls. We observe good agreements between the predictions and the results obtained with Monte Carlo methods for the update of the strategies, thus providing a simple and fast way to estimate the outcome of evolutionary social dilemmas on arbitrary networks without the need of actually playing the game.

1 Introduction

Cooperation is much more widespread in nature than the Darwinian premise of 'only the fittest survive' might suggest [1]. Evolutionary game theory is traditionally used to formalise the problem with social dilemmas [2], and networks are commonly used as the backbone for the simulation of these games. The fact that the structure of a network can positively affect the evolution of cooperation is today known as network reciprocity [3,4], and it constitutes one of five key mechanisms for cooperators to survive social dilemmas [5]. However, despite the wealth of research concerning the evolution of cooperation on networks, fundamental results have been relatively scarce.

In this work, we derive a simple conjecture for cooperation transitions in evolutionary social dilemmas based on the unique sequence of degrees in a network. As we will show, the conjecture predicts well at which game parameters important shifts in the level of cooperation can be expected, including phase transitions from absorbing to mixed strategy phases [6].

2 Model and conjecture formulation

We start by considering a network G made of N players connected according to a symmetric adjacency matrix $A = (a_{ij})$, where $a_{ij} = 1$ if players i and j interact, and $a_{ij} = 0$ otherwise. We introduce $k_i = \sum_{j=1}^{N} a_{ij}$ is the degree of player i. The strategy variable x_{ij} is defined as $x_{ij} = 1$ if player i cooperates with player j and $x_{ij} = 0$ if i defects j, and we introduce the strategy vector as $\overline{x}_{ij} = (x_{ij}, 1 - x_{ij})$.

Each player has an associated k_i-dimensional vector of independent strategies. The prisoner's dilemma interaction game [6] is governed by the payoff matrix:

$$P = \begin{pmatrix} 1 & 0 \\ b & 0 \end{pmatrix} \quad (1)$$

where $b$accounts for the gain of a defector (D) when meets a cooperator (C), and a gain of 1 if both players cooperate. The Nash equilibrium is mutual defection. In each round of the game, the payoff g_{ij} earned by each player i from its interaction with j is $g_{ij} = \overline{x}_{ij} P(b) \overline{x}_{ji}^{T}$. The average payoff of each player is therefore $g_i = \frac{1}{k_i} \sum_{j \in N_i} g_{ij}$ where N_i is the set of neighbors of i. The system's evolution is carried out by implementing Monte Carlo simulations such that whenever the payoffs of two engaged $i$and j randomly selected players verify $g_j > g_i$ then player i imitates j's strategy with a probability $p = D/2\Gamma$ for $D < 2\Gamma$ and $p = 1$ otherwise, being $D = \left(g_j - g_i\right) / \left(b \max\left(k_i, k_j\right)\right)$ the normalized payoff difference. One can define the node outcoming cooperation rate as $\rho_i = \frac{1}{k_i} \sum_{j \in N_i} x_{ij}$ and the macroscopic cooperation frequency of the whole network as $\rho = \frac{1}{N} \sum_{i=1}^{N} \rho_i$.

Let us focus now on the probability of changing strategy, which becomes 50% when the payoff difference $\Delta g_i = g_k - g_i = 0$. Whenever at some point during the iterated game a player i reaches such a null payoff difference with respect to its best performing neighbor k, the transition to keep the actual strategies x_{ij} or to change to x_{ki} is critical in the sense that it can occur only for a particular set of values of the parameter b, that we are going to name as b_c. Evaluating the payoffs of i and k, one can analytically obtain the following conjecture to locate the phase transitions for the dilemma P in Eq.(1):

$$b_c = \frac{n}{m}, \quad (2)$$

where m and n are integers such that $1 \leq m \leq n \leq \max(k)$, and $\max(k)$ is the maximum degree.

3 Results

3.1 Numerical methods and use of computational resources

We used the CRESCO resources for the computational study of the prisioner's social dilema in networks with two possible strategies, unfolding the dynamics with Monte Carlo simulations and considering different topologies, network size and different average degrees. Homemade MATLAB scripts were written and compiled with MATLAB Compiler and executed at CRESCO with MATLAB Runtime. Extensive distributed computations have been performed for large parameters sets, with statistical validation of the results. Calculations were performed in CRESCO4 and CRESCO5, using the h144 queues for full evolution simulations. Homemade MATLAB scripts were used for visualizing the results.

3.2 Conjecture validation

As the conjecture implies that the number of possible transitions depends on the set of degrees present in the network we tested our conjecture by running an extensive set of simulations of PD competition in a wide range of structural and dynamical conditions. In particular, we inspect the role of the degree distribution by carrying out simulations with random Erdös-Renyi and scale-free Barabási-Albert networks, with $N = 600$ and mean degree $\langle k \rangle = 4$ with initially equal densities of cooperation randomly distributed along with the nodes. Average cooperation frequency is monitored as a function of b, and each point is an ensemble average over 100 network realizations.

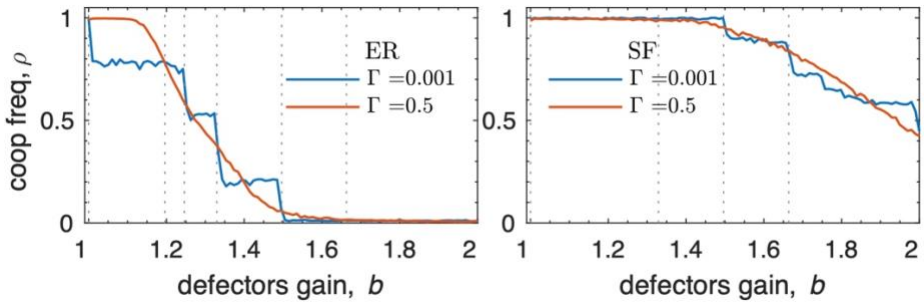

Fig.1: Validation of the conjecture for the prisoner's dilemma game. Average cooperation frequency ρ as a function of the defector's gain b for ER (left) and SF (right) graphs of size $N = 600$ and $\langle k \rangle = 4$. Each curve is the average of 100 network realizations implementing a Monte Carlo method following an updating rule given by $p = D$ for $0 \leq D \leq 2\Gamma$ and $p = D$ for $D > 2\Gamma$. Equilibrium frequencies are obtained by averaging the last 2,500 generations before the transient time of 10,000 generations. Vertical dotted lines in both panels correspond to b_c values fulfilling Eq. (2).

Figure 1 shows how the cooperation evolves as a function of the game parameter b of the dilemma for both ER and SF networks and two values of the parameter Γ which quantifies the uncertainty of strategy adoptions. We observe that cooperation evolves in a continuous way without abrupt changes for $\Gamma = 0.5$ (the probability p of changing strategy is directly the normalised payoff difference as used in Ref. [4]) while for very small Γ, phase transitions from pure cooperation to a mixed state (and from a mixed state to complete defection for ER topologies) are perfectly predicted by those values (marked as dotted vertical lines) fulfilling Eq. (2) whose probability density function is above a given threshold. One sees that reducing the value of Γ (i.e. increasing the likelihood of a player to change its strategy even for very low payoff differences) breaks the continuous evolution of the cooperation into a series of plateaux at different mixed levels of defection and cooperation [7].

3.3 Computer code

```
function [unos]=scalargame(T,A,b,gamma)
% INPUT: T=number of generations, A=adjacency matrix; b>1=defector's gain; gamma=
slope's probabilty to change strategy; % OUTPUT: unos = cooperation frequency
N=length(A);
G=graph(A);
degs=G.degree;
for n=1:N
    neigs{n}=G.neighbors(n);
end
fD=0.5; %Initial fraction of defectors
P=[1 0; b 0]; % Payoff matrix
D=P(2,1)-P(1,2);
unos=zeros(1,T);
ev=randsample(N,ceil(N*fD));
SC=ones(1,N); % Strategy vector: 1=C and 2=D
SC(ev)=2;
for t=1:T
    unos(t)=sum(SC==1)/N; %Cooperation frequency
    mc=randperm(N,N);
    for n=1:N
        x=mc(n);
        id=randi(length(neigs{x}),1);
        y=neigs{x}(id);
        z=[x y];
        for j=1:2
        Gij=10*SC(z(j))+SC(neigs{z{j}});
        Gij(Gij==11)=P(1,1);
        Gij(Gij==12)=P(1,2);
```

```
        Gij(Gij==21)=P(2,1);
        Gij(Gij==22)=P(2,2);
        Pxy(j)=sum(Gij);
        end
        Px=Pxy(1);
        Py=Pxy(2);
        Dp=(Py-Px)/(D*max(degs(x),degs(y)));
        p=Dp/(2*gamma);
        if(p>rand) SC(x)=SC(y);
        end
    end
end
```

4 Conclusion

Why and under which conditions cooperation thrives is an evergreen subject across the social and natural sciences [1,8]. Evolutionary game theory is traditionally used to formalise the problem mathematically with social dilemmas [2], and networks are commonly used as the backbone for the simulation of these games. We have shown that the structure of the former in terms of the unique sequence of degrees predict the outcome in the latter, particularly in terms of the game parameters at which significant shifts in the level of cooperation can be expected. In particular, we have proposed a conjecture for cooperation transitions in arbitrary networks, including phase transitions from absorbing to mixed strategy phases. Results based on the evolutionary prisoner's dilemma game on random and scale-free networks of various sizes demonstrate the effectiveness of the conjecture. Indeed, since the conjecture is based on the different degrees present in the network, the network size does not modify the set of game parameters critical to produce shifts in the cooperation frequency. Although we have explored the predictive power of the conjecture only for the prisioner's dilemma, it can be generalized to any social dilemma as the conjecture just operates on the payoff matrix and the critical game parameters are extracted only from the condition that the payoff difference between two agents is zero. The presence of high stochasticity levels in the probability of strategy update may compromise the emergence of sharp transitions, which can explain the fact that these have not been previously observed.

Acknowledgments

I.S.N. and I.L. acknowledge support from the Ministerio de Economía, Industria y Competitividad of Spain under project FIS2017-84151-P and the Ministerio de Ciencia e Innovación under project PID2020-113737GB-I00. They also acknowledge the computational resources and assistance provided by CRESCO, the supercomputing center of ENEA in Portici, Italy.

References

[1] R. Axelrod. The Evolution of Cooperation. Basic Books, New York (1984).
[2] M.A. Nowak. Evlutionary Dynamics. Harvard University Press, Cambridge, MA (2006).
[3] M.A. Nowak, R.M. May. Evolutionary games and spatial chaos. *Nature* **359,** pp. 826-829 (1992).
[4] F.C. Santos, and J.M. Pacheco. Scale-Free Networks Provide a Unifying Framework for the Emergence of Cooperation. *Phys. Rev. Lett*. **95**, 098104 (2005).
[5] M.A. Nowak. Five rules for the evolution of cooperation. *Science* **314**, pp. 1560-1563 (2006).
[6] L. M. Floría, C. Gracia-Lázaro, J. Gómez-Gardeñes, and Y. Moreno. Social network reciprocity as a phase transition in evolutionary cooperation. *Phys. Rev. E* **79**, 026106 (2009).
[7] A. Zhuk, I. Sendiña-Nadal, I. Leyva, D. Musatov, A.M. Raigorodskii, M. Perc, S. Boccaletti. Predicting transitions in cooperation levels from network connectivity. *New J. Phys.* **23**, 093040 (2021).
[8] D.G. Rand, M.A. Nowak. Human cooperation. *Trends Cogn. Sci* **17**, pp. 413-425 (2013).

A COMPUTATIONAL INVESTIGATION ON THE INTERFACIAL PROPERTIES BETWEEN TRIPHENYLAMINE AND PHENOTHIAZINE-BASED HOLE TRANSPORT MATERIALS AND MAPI PEROVSKITE

Adalgisa Sinicropi[1,2,3*], Carmen Coppola[1,2], Adriana Pecoraro[4], Ana B. Muñoz-Garcìa[4], Rossella Infantino[3,5], Alessio Dessì[3], Gianna Reginato[3], Riccardo Basosi[1,2,3], and Michele Pavone[6]

[1]*Università degli Studi di Siena, Dipartimento di Biotecnologie, Chimica e Farmacia, R[2]ES Lab, via Aldo Moro 2, 53100 Siena, Italia.* [17]

[2]*CSGI, Consorzio per lo Sviluppo dei Sistemi a Grande Interfase, via della Lastruccia 3, 50019, Sesto Fiorentino, Italia.*

[3]*Consiglio Nazionale delle Ricerche - Istituto di Chimica dei Composti OrganoMetallici (CNR-ICCOM), via Madonna del Piano 10, 50019 Sesto Fiorentino, Italia.*

[4]*Università degli Studi di Napoli Federico II, Dipartimento di Fisica "Ettore Pancini", Comp. Univ. Monte Sant'Angelo, Via Cintia 21, 80126 Napoli, Italia.*

[5]*Università degli Studi di Siena, Dipartimento di Biotecnologie, Chimica e Farmacia, via Aldo Moro 2, 53100 Siena, Italia.*

[6]*Università degli Studi di Napoli Federico II, Dipartimento di Scienze Chimiche, Comp. Univ. Monte Sant'Angelo, Via Cintia 21, 80126 Napoli Italia.*

ABSTRACT. In recent years, perovskite solar cells (PSCs) have caught a remarkable interest in the photovoltaic community, leading to sunlight-to-power conversion efficiencies (PCE) up to 25%. However, to drive this technology from the research lab to the industry, the optimization of the hole transport materials (HTMs) and their surface contact with the perovskite are critical issues for achieving higher devices' stability. In this report, we review the investigation of the structural and electronic properties of a recently designed phenothiazine (PTZ)- and triphenylamine (TPA)-based HTM (HTM1) when interacting with the (001) surface of the archetypal $CH_3NH_3PbI_3$ (MAPI) perovskite by means of Density Functional Theory (DFT) methods as implemented in the SIESTA software. To allow a direct comparison, we address the same investigation on well-known HTM molecular systems. Our results can help to shed further light on the charge transfer process involving TPA and PTZ-based molecules when MAPI is taken as the reference perovskite.

1 Introduction

Since 2009, lead halide perovskite compounds have been introduced as photoactive material in PSCs and great research efforts have pushed their PCE up to 25% [1]. Crucial components in PSCs are the HTM: they are responsible for the holes' extraction and transport, preventing direct contact and degradation at the metal-perovskite interface, thus contributing to enhancing the stability of the devices

[17] Corresponding author. E-mail: adalgisa.sinicropi@unisi.it

[2]. Currently, Spiro-OMeTAD is the most employed organic HTM in conventional PSCs. However, it can attain good hole mobility only by employing dopants, which are detrimental to PSCs' stability [2]. For these reasons, several alternative HTMs have been proposed and those based on the combination of TPA and PTZ moieties, e.g. PTZ2, have shown suitable properties and high PCE [3]. In this context, our group worked on the *in-silico* design of four novel TPA and PTZ-based HTMs (HTM1-4) in the last few years [4]. Among them, we fully investigated the electronic properties of HTM1 (Scheme 1 (a)) by means of DFT calculations, demonstrating that it possesses all the well-known requirements that make it a suitable candidate as HTM in PSCs: i) highest occupied molecular orbital (HOMO) and lowest unoccupied molecular orbital (LUMO) energies well aligned with the valence band (VB) and conduction band (CB) of MAPI perovskite; ii) suitable electron density and spin density distributions; iii) oxidation potential higher in energy than the VB of MAPI; iv) absorption maximum at 337 nm, outside the MAPI absorption range; v) chemical hardness higher than that of Spiro-OMeTAD, hence presumed higher stability; vi) reorganization energy lower than that of Spiro-OMeTAD and PTZ2, thus presumed higher hole mobility [4,5]. In perfect agreement with the computed results, the synthesis and spectroscopic characterization further confirmed HTM1 as a valid HTM in PSCs [6]. However, as the interface contact with the perovskite can largely affect the HTMs properties and perovskite/organic HTM interface electronic properties at the microscopic level are yet to be fully understood, we performed a DFT study on the HTM1 interaction with either the PbI_2- or MAI-terminated MAPI (001). The results have been compared to those obtained for Spiro-OMeTAD (Scheme 1 (b)), PTZ1 (Scheme 1 (c)), and PTZ2 (Scheme 1 (d)), to provide new insights into the hole transport behavior at the interface between MAPI and TPA and PTZ-based molecules [5].

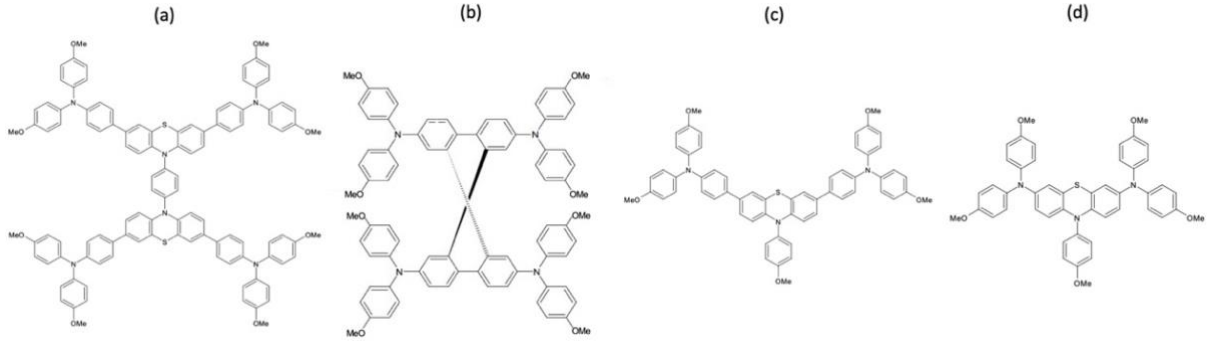

Scheme 1: Molecular structures of (a) HTM1 (b) Spiro-OMeTAD (c) PTZ1 and (d) PTZ2.

2 Computational Details

All the calculations have been performed by using SIESTA 4.1 program package [7] on HPC CRESCO resources. A typical run uses c.a. 816 processors on CRESCO4 cluster. All the optimizations have been performed with Periodic Boundary Conditions (PBC) via DFT at PBE-GGA [8], using DZP basis set (including $5d^{10}$ semicore electrons for Pb atoms) along with Troullier–Martins norm-conserving pseudopotentials and setting a mesh cutoff of 400 Ry. For sampling the Brillouin zone, 8 x 8 x 8 Γ-centered Monkhorst–Pack *k*-point grid has been selected for the optimization of the MAPI bulk and 1 x 1 x 1 Γ-centered Monkhorst–Pack *k*-point grid has been considered to optimize the four considered compounds and HTMs/MAPI energy minima. The binding energies have been determined through single-point calculations on the optimized systems at 8 x 8 x 1 Γ-centered Monkhorst–Pack *k*-point grid. The energies of all investigated systems have been corrected including the dispersion force calculated by the D3BJ damping scheme [9].

3 Results

The minimum energy interfaces have been calculated for each MAPI termination and HTM by considering two different HTMs adsorption modes (*up* and *down* orientations). After a preliminary rigid scan, they have been relaxed and the interface binding energies have been computed as (1):

$$E_{binding} = E_{interface} - E_{MAPI} - E_{molecule} \quad (1)$$

where $E_{interface}$ is the energy of the HTMs/MAPI system, E_{MAPI} is the energy of the isolated MAPI slabs and $E_{molecule}$ is the energy of the isolated HTMs. The electronic properties of the HTMs/MAPI systems have also been analyzed in terms of their projected density of states (pDOS). The HTMs/MAPI:PbI_2 and the HTMs/MAPI:MAI most stable interfaces and binding energies, together with their pDOS plots, are shown in Fig. 1 for HTM1 and PTZ2, and in Fig. 2 for Spiro-OMeTAD and PTZ1.

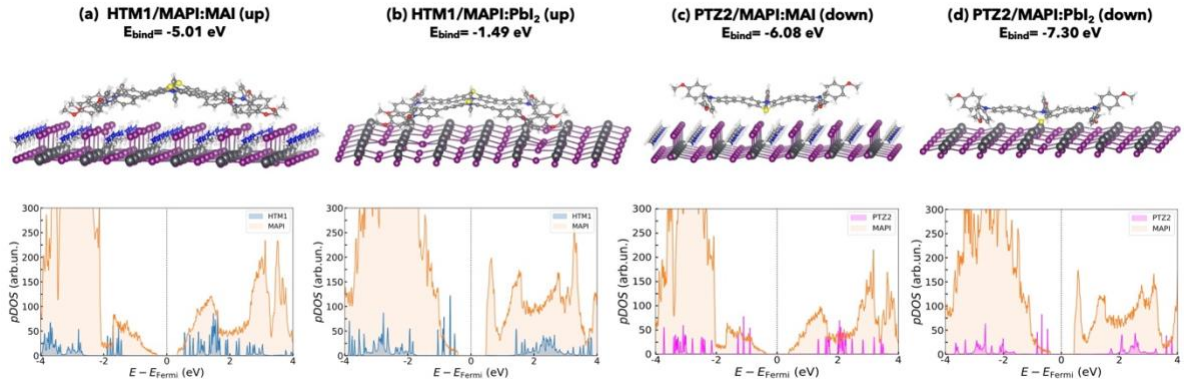

Fig.1: Most stable interfaces and pDOS plots of (a) HTM1/MAPI:MAI (up), (b) HTM1/MAPI:PbI_2 (up), (c) PTZ2/MAPI:MAI (down) and (d) PTZ2/MAPI:PbI_2 (down).

HTM1 has a favoured interaction with both MAPI:PbI_2 and MAPI:MAI when in the *up* orientation. In particular, HTM1/MAPI:MAI interaction is stronger than that of HTM1/MAPI:PbI_2, due to the formation of some hydrogen bonds between the molecule and the surface. Nevertheless, the pDOS plots show that the HOMO level of HTM1 has lower energy than the VB of MAPI, thus there is not the sufficient driving force for the hole injection process. Likewise, an inadequate driving force has been found for PTZ2/MAPI, even if the latter presents the most stabilized binding energies thanks to the presence of additional interactions that are not present in HTM1/MAPI systems.

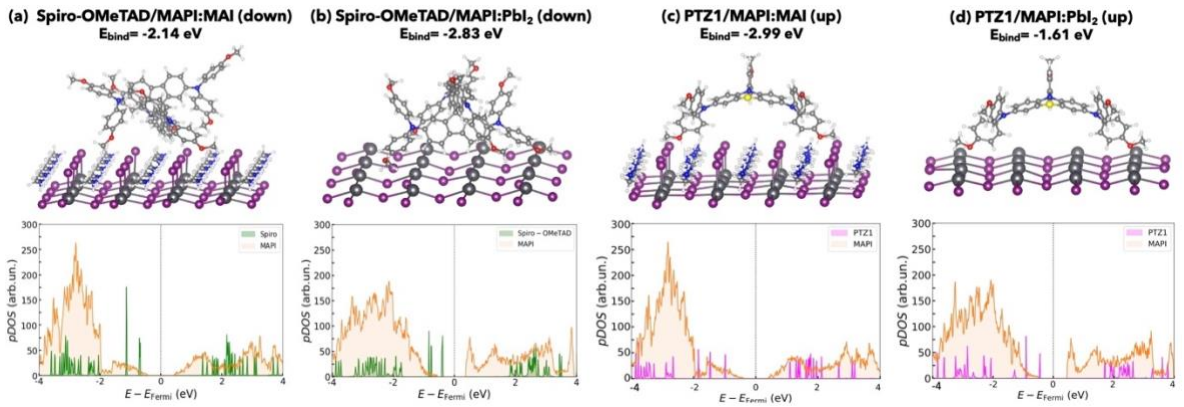

Fig.2: Most stable interfaces and pDOS plots of (a) Spiro-OMeTAD/MAPI:MAI (down), (b) Spiro-OMeTAD/MAPI:PbI_2 (down), (c) PTZ1/MAPI:MAI (up) and (d) PTZ1/MAPI:PbI_2 (up).

Spiro-OMeTAD preferably adopts the *down* orientation, while PTZ1/MAPI systems have similar behavior to HTM1/MAPI systems, exhibiting the *up* orientation as the preferred one. Furthermore, Spiro-OMeTAD and PTZ1 show a convenient but extremely low driving force for the hole extraction

only when the MAPI:PbI_2 termination is considered. All these results show that MAPI, which is often taken as the reference perovskite, provides an inefficient charge transport process when combined with TPA and PTZ-based HTMs, while other kinds of perovskite composition allow reaching very good PCE with the same molecules. Indeed, we recently demonstrated that the dopant-free HTM1 combined with $Cs_{0.17}FA_{0.83}Pb(I_{0.9}Br_{0.1})_3$ perovskite allows for achieving 17.26% PCE [6].

4 Conclusions

In this study, it emerged that the charge transport process can be largely affected not only by the isolated HTMs' properties and their interaction with the perovskite but also by the kind of perovskite employed. In particular, MAPI has resulted to be inadequate for TPA and PTZ-based molecules and this outcome also supports its limited employment for the real fabrication of devices.

Acknowledgments

The computing resources and the related technical support have been provided by the CRESCO/ENEAGRID High Performance Computing Infrastructure and its staff. CRESCO/ENEAGRID High Performance Computing Infrastructure is funded by ENEA, the Italian National Agency for New Technologies, Energy and Sustainable Economic Development and by Italian and European research programmes see https://www.cresco.enea.it for information. We also acknowledge the Department of Biotechnology, Chemistry and Pharmacy, Department of Excellence 2018– 2022 and the hpc@dbcf for providing computational resources.

References

[1] NREL. Best Research-Cell Efficiency Chart, https://www.nrel.gov/pv/cell-efficiency.html
[2] F. M. Rombach, S. A. Haque and T. J. Macdonald. Lessons learned from spiro-OMeTAD and PTAA in perovskite solar cells. *Energy Environ. Sci.* **14**, pp. 5161–5190, (2021).
[3] R. Grisorio, B. Roose, S. Colella, A. Listorti, G.P. Suranna and A. Abate. Molecular Tailoring of Phenothiazine-Based Hole-Transporting Materials for Highly Performing Perovskite Solar Cells. *ACS Energy Lett.* **2**, pp.1029–1034, (2017).
[4] C. Coppola, R. Infantino, A. Dessì, L. Zani, M.L. Parisi, A. Mordini, G. Reginato, R. Basosi and A Sinicropi. DFT and TDDFT investigation of four triphenylamine/phenothiazine-based molecules as potential novel organic hole transport materials for perovskite solar cells. *Materials Chemistry and Physics* **278**, pp. 125603, (2022).
[5] C. Coppola, A. Pecoraro, A.B. Muñoz-García, R. Infantino, A. Dessì, G. Reginato, R. Basosi, A. Sinicropi and M. Pavone. Electronic structure and interfacial features of triphenylamine- and phenothiazine-based hole transport materials for methylammonium lead iodide perovskite solar cells. *Phys. Chem. Chem. Phys*. **24**, pp. 14993-15002, (2022).
[6] L. Castriotta, R. Infantino, L. Vesce, M. Stefanelli, A. Dessì, C. Coppola, M. Calamante, G. Reginato, A. Mordini, A. Sinicropi, A. Di Carlo and L. Zani. Stable Methylammonium-Free p-i-n Perovskite Solar Cells and Mini-Modules with Phenothiazine Dimers as Hole Transporting Materials. *Energy & Environmental Materials* e12455 (2022).
[7] J. M. Soler, E. Artacho, J. D. Gale, A. García, J. Junquera, P. Ordejón and D. Sánchez-Portal. The SIESTA method for ab initio order-N materials simulation. *J. Phys.: Condens. Matter* **14**, pp. 2745–2779, (2002).
[8] J. P. Perdew, K. Burke and M. Ernzerhof. Generalized Gradient Approximation Made Simple. *Phys. Rev. Lett.* **77**, pp. 3865–3868, (1996).
[9] S. Grimme, J. Antony, S. Ehrlic and S. Krieg. A consistent and accurate ab initio parametrization of density functional dispersion correction (DFT-D) for the 94 elements H-Pu. *J. Chem. Phys*. **132**, pp. 154104, (2010).

3D MAGNETOHYDRODYNAMICS ANALYSES FOR NUCLEAR FUSION BREEDING BLANKETS

Simone Siriano* and Alessandro Tassone

[1]*Dep. of Astronautical, Electrical and Energy Engineering (DIAEE) - Nuclear Engineering Research Group, Sapienza University of Rome, Corso Vittorio Emanuele II, 244, Roma, 00186, Italy*
*simone.siriano@uniroma1.it

ABSTRACT. The Water-Cooled (WCLL) and Dual-Cooled (DCLL) Lead Lithium are two breeding blanket concepts that involve the use the liquid lead-lithium eutectic alloy (PbLi) as working fluid, due the possibility to double the coolant role as tritium breeder. Unfortunately, the liquid metal motion is influenced by the reactor confining magnetic field, leading to magnetohydrodynamics (MHD) effects. In this work, a prototypical manifold representative for both the WCLL and DCLL bottom collector, is investigated with a custom OpenFOAM solver. The aim is to investigate which configuration minimizes the flow imbalance, since the distribution of the flow is strongly influenced by the position of the feeding pipes and by the development of an MHD internal layer near the expansion. The channel aligned with the feeding pipe is the one carrying most of the flow, from 55% to 82%, while in the more distant one the flow is almost stagnant, carrying from 17% to 6% of the total flow rate. The total pressure loss is also estimated and its functional dependence on the collector configuration is discussed.

1 Introduction

The Breeding Blanket (BB) is a critical component of a fusion reactor which has the fundamental tasks of breed the tritium required for the reactor operations and of extract the thermal power generated by the fusion reactions. The most promising concepts involve the use of a Liquid Metal (LM) as working fluid, the lead-lithium eutectic alloy (PbLi), due to its excellent thermal properties and the possibility to double the coolant role as tritium breeder. In the framework of the development of the European fusion reactor industrial demonstrator DEMO [1], two LM blanket concepts are very promising: the Dual-Cooled (DCLL) [2] and Water-Cooled Lead Lithium (WCLL) blankets [3].

A challenging engineering issues in the BB design is the necessity to account for the interaction between the electrically conductive LM and the magnetic field employed to confine the plasma in the vacuum chamber, that leads to the magnetohydrodynamics (MHD) effects. Significant modifications in the flow features are observed even for moderate intensity of the magnetic field due to the Lorentz force generation, that can increase the pressure drop by several order of magnitude of the hydrodynamic losses and modify the velocity distribution in the effected component [4]. These effects are greatly emphasized by the presence of components with complex geometry (bend or sudden cross-section variations) which are widely used in BBs. For the study of this type of components, numerical analysis is often the only way.

In this framework, a prototypical manifold representing a generic BB collector is investigated through a custom solver considering different positions of the inlet channels with respect to the expansion, it is considered bot the case of an asymmetric expansion, such as that foreseen in the WCLL bottom collector, that a symmetric one considering one single inlet channel like in DCLL bottom collector. The complete exposition of this work is reported in [5].

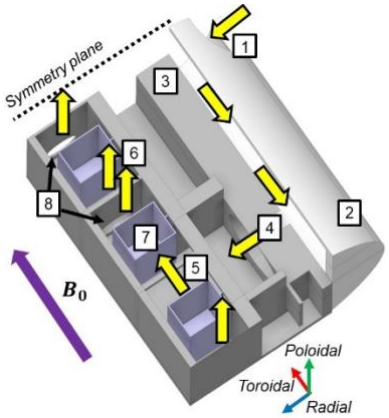

Fig. 2: Detail of the PbLi path (yellow arrow) in the WCLL2018 half bottom collector.

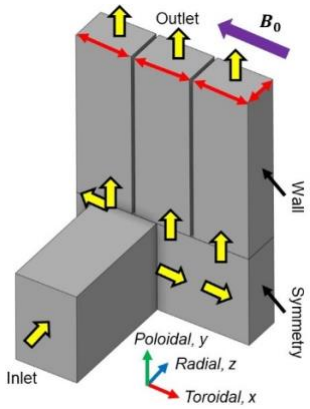

Fig. 3: Half geometry of the prototypical manifold configuration A

2 Numerical model

Fig. 2 shows one of the two identical parts of the WCLL2018 bottom collector where the PbLi, represented with yellow arrows, enters through two feeding pipes in radial direction (1 in the figure, only one channel represented), expand toroidally to an intermediate tank (2), curves and enters through a circular orifice (4), expands abruptly in toroidal direction (5) and, finally, it is distributed in six poloidal channels (6, three in the figure) constituting the PbLi manifold. The DCLL bottom collector is quite similar, where the collector is fed directly by a single central pipe connected to the center of the case and the poloidal channels stars after a small expansion length.

The model analyzed in this work considers perfectly electrical insulated walls and excludes the intermediate tank (number 2 in Fig. 2), the circular orifices (4), the obstacles inside the case, including the internal channels (7) and the internal orifices (8), as shown in Fig. 3 for the configuration A. The other two configurations considered in this work, configuration B and C, have the same parameters of configuration A except for the position of the inlet channels, that becomes single and central one for the configuration C.

It has been considered an adiabatic, isothermal and pressure-driven PbLi flow. The imposed magnetic field $\boldsymbol{B_0}$ (Fig. 2 and Fig. 3) is toroidal, stationary and uniform. The results are expressed according to its classic dimensionless representation for MHD flows, the Hartmann number Ha.

The governing equations have been discretized on a hexahedral, structured and non-uniform mesh, with greater refinement next to the walls and in proximity of the cross-section variation, in order to solve the thin MHD layers. The number of elements ranges from about 7 million to about 20 million as Ha increases. The simulation was performed on the CRESCO6 cluster until reaching steady state solution, determined by the non-significant change of some control quantities.

The numerical tool used is the `phiFoam` solver, based on the `icoFoam` solver of the OpenFOAM v8 distribution, an open-source C++ computational fluid dynamics toolbox that use openMPI domain and data decomposition for the parallelization. The solver was built by implementing the Lorentz force, the main MHD effect, as an explicit source term in the momentum equation and considering the electric potential as the fundamental electromagnetic variable. Related to the velocity by the electric potential Poisson equation [5]. The code was validated considering a 2D and a 3D forced convection benchmark and has been shown to be able to accurately predict the basic phenomena of a laminar, incompressible and isothermal MHD flow up to $Ha = 5000$ [5].

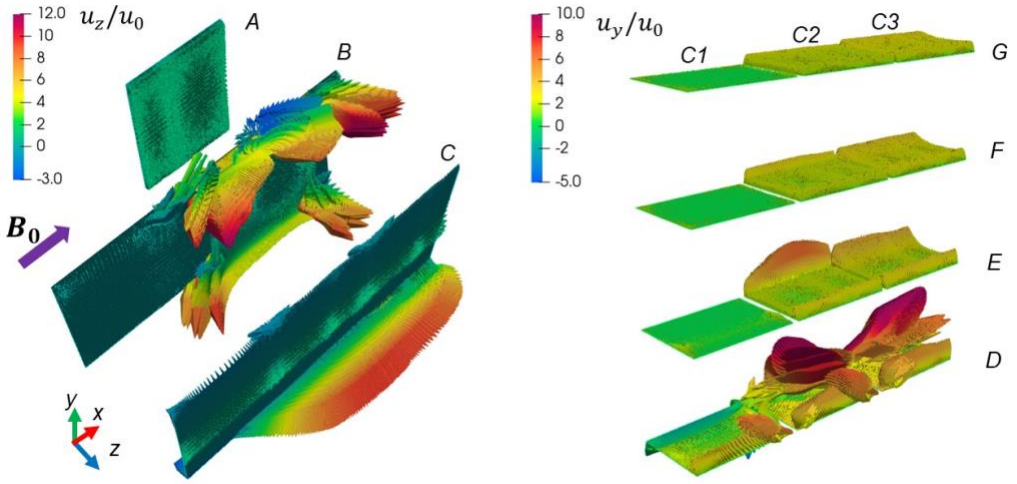

Fig. 4: Scaled stream-wise velocity vectors at six different cross-sections for the Ha = 2000 configuration A: section A, which is near the inlet, section B, which is located at beginning of the expansion but is shifted in the negative z-direction, section C, which is located in the middle of the expansion, section D, which is located at the beginning of the channels, and sections E, F and G, which are located along the outlet channels.

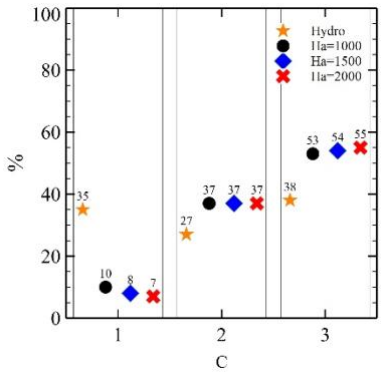

Fig. 5a: Configurations A

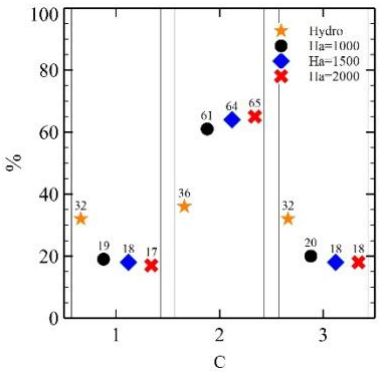

Fig. 4b: Configurations B

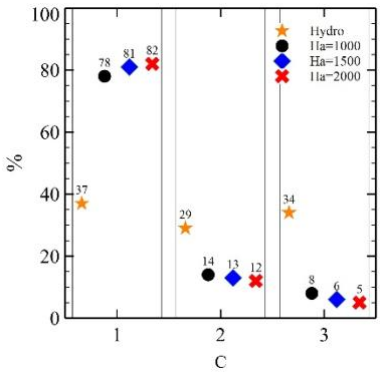

Fig. 4c: Configurations C

Fig. 6: Flow rate repartition between the outlet channels for the hydrodynamic (Ha = 0) and magnetohydrodynamic (Ha ≠ 0) flow regimes.

3 Results and discussion

Fig. 4 shows the velocity distribution for the configuration A at different locations and similar considerations can also be made for the other configurations [5]. At the beginning of the inlet channel (section A) the velocity distribution matched the imposed fully developed 2D distribution for a square channel with electrical insulated walls. By approaching the expansion, the flow is pushed by the Lorentz force toward the top and bottom walls, inside the very thin MHD layers. When it reaches the expansion it separates concentrating in two internal MHD layers that form on the expansion walls, leading to two jets (section B): one close to the backing plate of the case that has a typical M-shape profile (section B) and its able to expand undisturbedly (section C), one close to the top wall that impact on the channel connections leading a very complex velocity distribution (section B, D and E). This leads to an extremely unbalanced flow rate repartition in the channels. The velocity distribution derived from the upper jet is highly influenced by the position of the inlet channel, which changes the point of impact of the upper jet with the channels and therefore its morphology. This is the fundamental phenomenon that

differentiates the distribution of the flow rate in the outlet channels between the various configurations analysed.
Fig. 5a, Fig. 5b, Fig. 5c, show the flow rate repartition between the outlet channels for, respectively, configuration A, B and C. Configuration A (WCLL-like) shows an imbalance between channels C1, C2 and C3 equal to, respectively, 8%, 37% and 55% Configuration B is the one showing a more balanced distribution, respectively equal to 65% for the C2 channel and 17.5% for both C1 and C3 channels. Configuration C (DCLL-like), on the other hand, has the worst imbalance, equal to 82% for C1 channel, 12% for C2 and 6% for C3 channel. This flow repartition should also be significant in the conditions of the WCLL and DCLL ($Ha \approx 9000$), since passing from $Ha = 1000$ to 2000 the variation of the flow rate between the channels becomes smaller and smaller, due to the morphology of the upper jet that is already well defined for $Ha = 1000$ [5].
In any case, the channels distant from the inlet are reached by a flow rate that may be too low to guarantee the efficient recirculation of the breeder for the WCLL and is most likely unacceptable for heat transfer purposes in the DCLL. Countermeasures must be devised to ensure a better distribution. One of these may involve the use of an expansion length, sized on the thickness of the MHD internal layer, to allow the fluid to expand freely before being distributed in the channels, in order to avoid the asymmetry of the upper jet due to the impact with the channels. However, this could result in a reduction of the available blanket thickness for the breeding zone [3], which could negatively affect the amount of tritium bred, even if such geometry modification is confined to a location far away from the first wall and of limited extension. Integration and mechanical stability of the modified collector are other points that need to be evaluated.
Another strategy may rely on the positioning of calibrated orifices at the beginning of the channels, a solution which however increases the pressure drop of the component. Finally, the effect of the conductivity of the wall must be considered which is predicted to have a beneficial effect on the distribution of the flow rate at the expense of a pressure drop penalty [5].

Acknowledgments

This work has been carried out within the framework of the EUROfusion Consortium and has received funding from the Euratom research and training programme 2014-2018 and 2019-2020 under grant agreement No 633053. The views and opinions expressed herein do not necessarily reflect those of the European Commission.
The computational resources and the related technical support used for this work have been provided by CRESCO/ENEAGRID High Performance Computing infrastructure and its staff [6]. CRESCO/ENEAGRID High Performance Computing infrastructure is funded by ENEA, the Italian National Agency for New Technologies, Energy and Sustainable Economic Development and by Italian and European research programmes, see http://www.cresco.enea.it/english for information.

References

[1] L. V. Boccaccini *et al.*, “Status of maturation of critical technologies and systems design: Breeding blanket,” *Fusion Eng. Des.*, vol. 179, p. 113116, Jun. 2022, doi: 10.1016/j.fusengdes.2022.113116.
[2] D. Rapisarda *et al.*, “The European Dual Coolant Lithium Lead breeding blanket for DEMO: Status and perspectives,” *Nucl. Fusion*, vol. 61, no. 11, p. 115001, Nov. 2021, doi: 10.1088/1741-4326/ac26a1.
[3] P. Arena *et al.*, “The demo water-cooled lead–lithium breeding blanket: Design status at the end of the pre-conceptual design phase,” *Appl. Sci.*, vol. 11, no. 24, p. 11592, Dec. 2021, doi: 10.3390/app112411592.
[4] U. Müller and L. Bühler, *Magnetofluiddynamics in Channels and Containers*. Berlin, Heidelberg: Springer Berlin Heidelberg, 2001.
[5] S. Siriano, “Numerical simulation of MHD flows in breeding blanket and plasma-facing components,” Sapienza University of Rome, PhD thesis, 2022.

[6] F. Iannone *et al.*, “CRESCO ENEA HPC clusters: A working example of a multifabric GPFS Spectrum Scale layout,” in *2019 International Conference on High Performance Computing and Simulation, HPCS 2019*, Jul. 2019, pp. 1051–1052, doi: 10.1109/HPCS48598.2019.9188135.

TOWARD STABLE MAGNETIC GRAPHENE HYDROGENATED DERIVATIVES

Andrea Albino[1], Francesco Buonocore[2], Massimo Celino[2], Federico Totti[1*]

[1]*Università degli Studi di Firenze, Chemistry Department "U. Schiff", 50019, Sesto F.no, Italy*

[2]*ENEA, Casaccia Research Centre, 00123 Rome, Italy*

ABSTRACT. The implantation of magnetic moments in graphene would pave the way for the application of novel spintronics materials in quantum technology applications. The present work aims at a systematic and comprehensive understanding of the structural and magnetic properties of graphene across its conformational space when covalently functionalized with hydrogen or fluorine atoms in different stoichiometries. The hydrogenated systems are then adsorbed on Au(111) surface or on a graphene buffer layer. A new strategy, based on non homogeneous graphene hydrogenation, is rationalized to build stable magnetic structures and maximize the magnetic moment per unit area.

1 Introduction

Graphene (G-ene) is an ideal candidate material for spintronics due to its layer structure, and weak spin–orbit coupling that facilitates spin transport and modulation of electrical properties [1]. The use of G-ene for applications in electronics suffers from a major drawback: graphene is, in its pristine state, a zero-band gap semiconductor [2]. Furthermore, in the absence of d or f electrons, the production of magnetic moments is not trivial. To use G-ene in possible applications such as photodetectors, photovoltaics, sensors, organic light-emitting diodes, organic thin-film transistors, supercapacitors, and in catalytic applications, and in spintronics, it is essential to precisely modulate its electronic and magnetic properties. Several ways have been explored to tune the electronic structure of G-ene [3], among these, the chemical modification of pristine G-ene opens a challenging playground for chemists. Hydrogenation of G-ene is an attractive solution and it is foreseen to open a band gap and produce a magnetic behavior [4]. The question of inducing magnetic ordering, or just magnetic moments as a first step, is of vital importance. Notably, the above-mentioned properties are highly dependent on the hydrogenation degree, while hydrogenation is a reversible process. In this light, hydrogenated G-ene is undoubtedly a prominent two-dimensional nanomaterial with finely controlled properties.

2 Methods

The modelling of surfaces through slabs within PBC showed to be mandatory to have a reliable picture of the substrate@adsorbate scenarios. The packages of software CP2K were used for the periodic DFT calculations [5]. Calculation of energy and forces were performed by direct diagonalization using the Quickstep module. GTH pseudopotentials for the core electrons and valence pseudo-wavefunctions are expanded in Gaussian-type orbitals and the density is represented in a plane wave auxiliary basis set (GPW) to achieve the efficient calculations of very large condensed systems. In particular, for Au, C and H elements DZVP-MOLOPT-SR-GTH basis sets were used. The revised Perdew-Burke-Ernzerhof

(revPBE) functional was chosen for the calculation. The rVV10 non-local dispersion corrections were also included. The Conjugate Gradient minimizing procedure was employed to carry out the structure optimization. The convergence of the plane waves basis cut-off was reached for 500 Ry with a convergence threshold of $1 \cdot 10^{-7}$ a.u. for the SCF energy and $4.5 \cdot 10^{-4}$ a.u./Å for the forces. The uncommon high plane-waves cut-off was chosen for these systems to gain a level of precision mandatory for the study of magnetic properties. Exchange coupling parameters, *J*'s, have been calculated by broken-state calculations from the Eq. 1.

$$\Delta E(S_{max} - S_{BS}) = E(S_{max} = S_A + S_B) - E(S_{BS} = |S_A - S_B|) = \sum_{i<j} J_{ij} \left(2|s_i s_j| + s_j\right)\lambda_{ij}(s_i \geq s_j) \quad (1)$$

The calculations were performed on the CRESCO6 computing cluster of ENEA's ENEAGRID computing infrastructure [6]

3 Results

3.1 Tuning the approach

The reliability of a proposed computational protocol is based on the accurate reproduction of the available observables. In consideration of the fact that most of the systems considered in this work do not have or have a limited number of experimental data to be compared to, it is of basic importance to test our computational protocol on similar systems where there is an abundance of them. For such a reason, our reference calculations were performed on one layer of pristine G-ene through a Γ-point supercell approach. The hydrogenation and fluorination of G-ene have been also widely studied in the literature [7] and, therefore, its study in this work must be considered basically as another test for our computational protocol with a few new data added to those already present in literature. The hydrogenation process can lead to different isomers both in graphane (G-ane) and graphone (G-one) derivatives. The chair and boat are the ones that have been considered in this work (see **Fig**.**1** (b-c) and **Fig**.**1** (d-e), respectively), being the other possible conformers less stable.

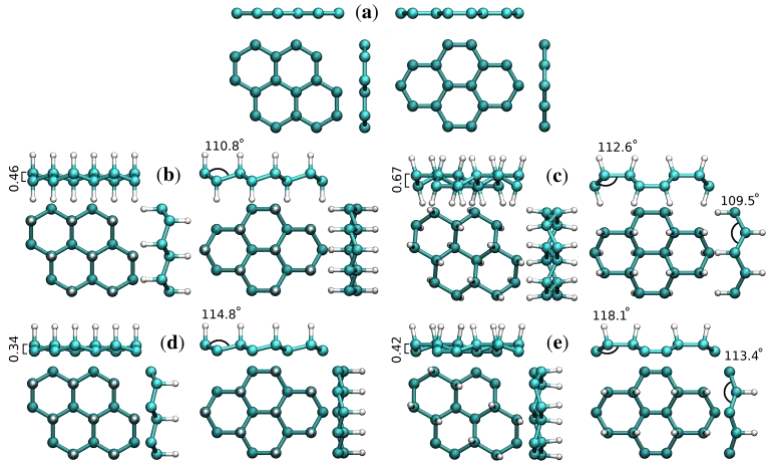

Fig.**1**: Side and top views of graphene, graphane and graphone structures in the isolated phase. (a) pristine graphene. (b) chair graphane. (c) boat graphane. (d) chair graphone. (e) boat graphone.

3.2 Stabilization of magnetic moments in hydrogenated/fluorinated G-ene

The chair-type G-one isomer is the only one showing a strong ferromagnetic interaction, its energy is far less stable than the boat-type isomer, though. Indeed, the needed selectivity for the 1,3,5 G-ene ring positions (50% coverage of G-ene sp^2 carbon sites) along with the necessity to have the kinetic process to collapse to vicinal substitutions inhibited, can be hardly achieved first of all for the inhomogeneity

in the addition process and the limited coverage limits that are usually yielded in hydrogenation processes.
Two main approaches aimed to achieve a stabilization of the magnetic moments for homogeneous and non-homogeneous hydrogenation were tested. The former consists of the adsorption of both types of G-one isomers on a substrate, Au(111), with the aim to see the effects of the new substrate@surface interactions in stabilizing the FM phase vs. the NM one. The latter consists of non-homogeneous hydrogenation, and selective patterning of hydrogenation positions to form localized islands characterized by a local G-ane structure. In this regard, a wide variety of different new hydrogenation patterns were studied and compared to some already presented in the literature.
Both the pristine G-ene and G-ane, as stand-alone systems, are not favouring the establishment of a magnetic moment. Some studies pointed out, regarding the ferromagnetically ordered localized states (H-vacancies) in G-ane, that increasing the vacancy concentrations the stability of the spin alignment is decreased and the total magnetization is suppressed, as also confirmed by our studies. Possible short-cut were tested allowing the derivation of some rules on the dependence of the instilled magnetic moment by several factors. In this regard, different structures were generated and compared **Fig**.**2** (a,b). In order to prove the applicability in potential devices (**Fig**.**2** (c)), a few systems were adsorbed on different substrates.

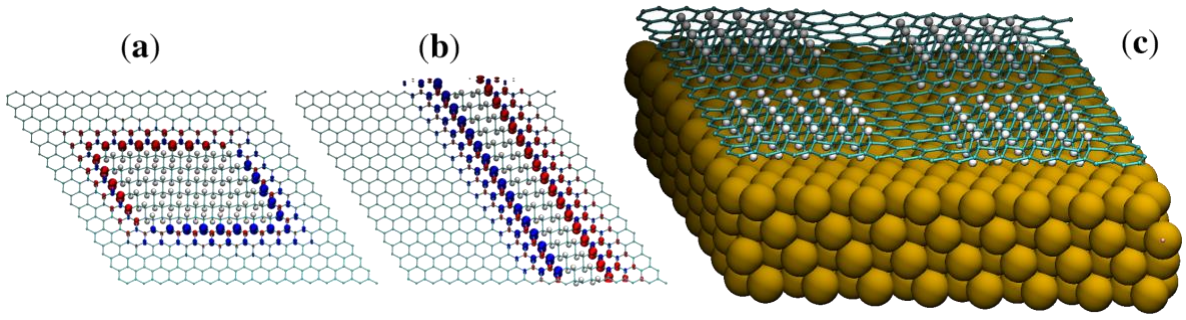

Fig.**2:** (a) structure of 200H single island system adsorbed on Au.
(b) G-ane/G-ene systems with ribbon pattern. (c) G-ane/G-ene system with island pattern.

4 Conclusions

The quest for magnetic materials for spintronics has been pushed forward, seeking at implantation of stable magnetic moments on covalently hydrogenated G-ene. Our results confirmed that it was possible to retain a certain amount of magnetic moment for heterogeneous hydrogenated G-ene derivatives on a metal surface. Our findings suggest that novel and magneto-active G-ene derivative nanostructure could become achievable more easily than extended G-one or G-ene nanoribbons.

Acknowledgments

The European COST Action CA15128 MOLSPIN, the Quantera ERA-NET cofund project SUMO, the FETOPEN project FATMOLS (GA 862893), the Italian MIUR for Progetto Dipartimenti di Eccellenza 2018-2022 (ref B96C1700020008)

References

[1] D. Pesin and A. H. MacDonald. Spintronics and pseudospintronics in graphene and topological insulators. *Nature Materials* **11.5**, pp. 409-416, (2012).
[2] K. S. Novoselov, A. K. Geim, S. V. Morozov, D. Jiang, M. I. Katsnelson, I. V. Grigorieva, S. V. Dubonos, and A. A. Firsov. Two-dimensional gas of massless Dirac fermions in graphene. *Nature* **438.7065**, pp. 197–200, (2005).

[3] S. Agnoli and G. Granozzi. Second generation graphene: Opportunities and challenges for surface science. *Surface Science* **609**, pp. 1-5, (2013).
[4] Wei Han, Roland K. Kawakami, Martin Gmitra, and Jaroslav Fabian. Graphene spintronics. *Nature Nanotechnology* **9.10**, pp. 794–807, (2014).
[5] J. Hutter, M. Iannuzzi, F. Schiffmann and J. Vandevondele. Cp2k: Atomistic simulations of condensed matter systems. *Wiley Interdisciplinary Reviews: Computational Molecular Science*, **4.1**, pp. 15–25, (2014).
[6] F. Iannone et al., CRESCO ENEA HPC clusters: a working example of a multifabric GPFS Spectrum Scale layout. 2019 International Conference on High Performance Computing & Simulation (HPCS), Dublin, Ireland, 1051-1052, 2019.
[7] F. Buonocore, A. Mosca Conte and N. Lisi. Effects of the substrate on graphone magnetism: A density functional theory study. *Physica E: Low-Dimensional Systems and Nanostructures* **78**, pp. 65–72, (2016).

NUCLEAR ANALYSES FOR THE DESIGN OF THE DEMO WATER COOLED LITHIUM LEAD BREEDING BLANKET CONCEPT

F. Moro[1], P. Arena[2], I. Catanzaro[3], A. Colangeli[1], A. Del Nevo[2], D. Flammini[1], N. Fonnesu[1], R. Forte[3], V. Imbriani[4], G. Mariano[1], R. Mozzillo[5], S. Noce[6] and R. Villari[1*]

[1]*ENEA, Department of Fusion and Nuclear Safety Technology, I-00044, Frascati (Rome), Italy*

[2]*ENEA, Department of Fusion and Nuclear Safety Technology, 40032, Camugnano (BO), Italy*

[3]*Department of Engineering, University of Palermo, 90128 Palermo, Italy*

[4]*CREATE, Department of Industrial Engineering, University of Naples Federico II, Naples, 80125, Italy*

[5]*CREATE, Engineering School of Basilicata University, 85100, Potenza, Italy*

[6] *University of Rome Tor Vergata, Industrial Engineering Department, Rome, 00133, Italy*

ABSTRACT. The development of a conceptual design for the Demonstration Fusion Power Reactor (DEMO) is a key issue within the EUROfusion roadmap. The DEMO reactor is designed to produce a fusion power of about 2 GW and generate a substantial amount of electricity, relying on a closed tritium fuel cycle: it implies that the breeding blanket (BB) shall guarantee a suitable tritium production to enable a continuous operation without any external supply.

The Water-Cooled Lithium Lead (WCLL) concept is a candidate for the DEMO BB: it uses liquid Lithium Lead as breeder and neutron multiplier and water in PWR condition as coolant.

A recently updated assessment of the tritium breeding ratio (TBR) requirement for DEMO, considering margins for calculation uncertainties and incomplete models of the whole machine, led to the definition of a tentative 1.15 value for the TBR. Moreover, the implementation of an accurate BB neutronics model, consistent with the engineering design, is recommended for the evaluation of the tritium self-sufficiency. In order to tackle these issues, an MCNP model of the DEMO tokamak, integrating a fully heterogeneous WCLL BB has been developed, including an accurate description of the First Wall (FW) water channels, as well as a comprehensive definition of the breeding zone inner structure. A complete assessment of the WCLL BB nuclear performances, through 3D neutron and gamma transport simulations, has been carried out by means the MCNP Monte Carlo code and JEFF nuclear libraries on the CRESCO High Performance Computing infrastructure.

1 Introduction

In the frame of the EUROfusion roadmap, the development of a breeding blanket (BB) system that guarantees the DEMO reactor [1] Tritium self-sufficiency is a fundamental issue. The Water-Cooled Lithium Lead (WCLL) concept, that encompass water in PWR (Pressurized Water Reactor) conditions as coolant and liquid Lithium Lead as breeder and neutron multiplier, is presently a reliable and promising candidate as DEMO BB; during the last years, its design development reached a significant

level of maturity and soundness, satisfying the nuclear design limits in terms of Tritium Breeding Ratio (TBR) and shielding performances.
An MCNP model of the DEMO tokamak, integrating a fully heterogeneous WCLL BB has been developed, including an accurate description of the FW water channels, as well as a detailed definition of the breeding zone inner structure. A comprehensive nuclear analysis has been carried out on the WCLL DEMO present design, aimed at verifying its compliancy with the design targets both in terms of tritium self-sufficiency and shielding performances [2,3], providing data for thermo-mechanical studies and guidelines for the optimization of the BB layout future development.
The nuclear responses have been assessed through three-dimensional coupled neutron and gamma transport simulations by means of the MCNP5v1.6 Monte Carlo code [4] and the Joint Evaluated Fusion File JEFF 3.3 nuclear data libraries [5].

2 The WCLL breeding blanket

The present WCLL BB design is based on a single-module-segment (SMS) concept where the basic inboard and outboard Breeding Units (BUs) are replicated along the poloidal direction (94 and 104 BUs for each poloidal sector in inboard and outboard respectively). With respect to the previous design [5], both the IB and OB BUs have been reviewed: as far as the IB is concerned, the breeding zone cooling pipe assembly has been completely redesigned on the basis of thermomechanical analyses results (fig. 1). The OB segment is no longer filled by a unique replicated BU, but it's characterised by 3 poloidal regions that host, respectively, 3 distinct BU layouts. The design of 3 OB BU concepts are shown in fig 2: each BU includes the FW and side walls, stiffening and internal baffle plates, BSS, cooling pipes, PbLi manifolds and water manifolds for the FW, side walls and breeding zone cooling circuit.

Fig. 1: WCLL inboard BU: perspective view of the Inboard breeding unit showing the inner cooling pipes layout.

Fig. 2: WCLL inboard BUs: perspective view of the Inboard breeding unit showing the inner cooling pipes layout (from left to right: 'alt. 22', 'v06b' and 'alt.24' concepts).

As far as the FW water channel is provided below:

- Inboard segment: 4 cooling channels for each BU, except for the upper area of the machine, where a more efficient heat removal system is needed (10 channels for each BU).
- Outboard segment: 4 cooling channels for each BU, except for the area close to the divertor cassette, where 6 water channels for each BU are needed.

Considering the above-mentioned updates in the WCLL BB layout, the total amount of water in the whole system has been augmented with respect to the previous layout [6]. Moreover, the LiPb and water manifolds system has been updated as well.

3 Nuclear analyses

The WCLL BB layout so far described has been converted into its equivalent MCNP geometrical representation and integrated into the EU DEMO1 2017 reference configuration model representing a 11.25° toroidal sector of the tokamak [7]: the obtained WCLL DEMO MCNP model shown in fig. 3 has been used to assess its nuclear performances in terms of shielding capability to protect the TFC and tritium self-sufficiency of the machine. The evaluation of those parameters, with a satisfactory statistic, relies on the transport of a consistent number of source particle (up to 10^{10}) in a very complex geometry, taking into account all the involved physical processes: consequently, the accomplishment of such demanding task is strongly dependent on the efficiency of the used computing system, ensured by the ENEA CRESCO6 HPC cluster.

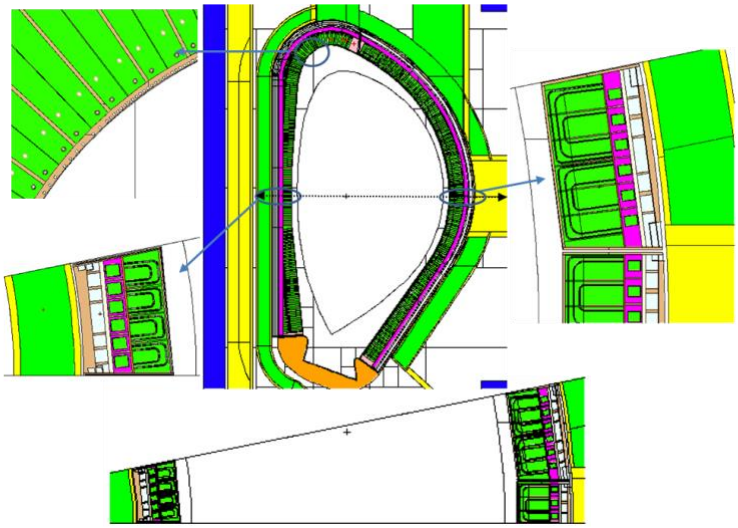

Fig. 3: WCLL DEMO MCNP model: poloidal section showing the inboard and outboard breeding blanket (top) and toroidal section along the equatorial plane (bottom). Details of the inboard/outboard BZ cooling pipes structure are shown, as well as an enlargement of the FW cooling channels (top left frame).

The total and fast (E>100 keV) neutron fluxes radial profiles are shown in fig. 4 for both the inboard and outboard equatorial BU. The total neutron fluxes at the inboard and outboard W armour are $6.4 \cdot 10^{14}$ n/cm²/s and $4.65 \cdot 10^{14}$ n/cm²/s, respectively.

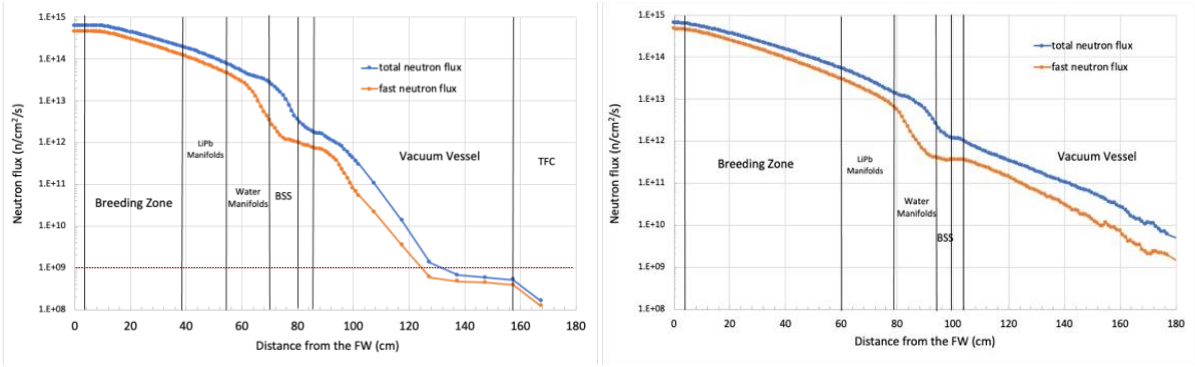

Fig. 4: Inboard (left) and Outboard (right) radial profiles at equatorial plane of the total (blue) and fast (red) neutron flux. The dotted red line indicates the design target for the fast neutron flux on the TFC (10^9n/cm²/s).

In inboard, the blanket/manifold system provides an attenuation of more than two orders of magnitudes to the VV inner shell and the neutron flux further decreases of three orders of magnitude across the VV, being $5.2 \cdot 10^8$ n/cm²/s (total), and $3.8 \cdot 10^8$ n/cm²/s (fast) on the TFC: thus, the WCLL BB shielding capability ensure that the 10^9 n/cm²/s design limit for the fast neutron flux on the TFC is fully satisfied. As far as the outboard is concerned, the larger BB radial extension provides an attenuation of the neutron flux across the blanket/manifold system of about 3 orders of magnitude. The radial profiles of the nuclear heating density evaluated in Eurofer and PbLi (blanket) and SS316L (Vacuum Vessel and TFC) are shown fig. 5 for both the inboard and outboard. As far as the inboard is concerned, the highest values are 23.12 W/cm³ on W armour and 7.5 W/cm³ on Eurofer in the FW and 0.026 W/cm^3 on the VV inner shell SS316L. On the coils, the maximum nuclear heating density is $4.7 \cdot 10^{-6}$ W/cm³, so the $5 \cdot 10^{-5}$ W/cm³ design limit is satisfied and the shielding capabilities of the BB system ensure sufficient protection of the TFC. As far as the outboard segment is concerned, the heat load on the W armour is 27 W/cm³, while the highest values assessed for the FW Eurofer and SS316L VV inner shell are 9.45 W/cm³ and $3.2 \cdot 10^{-2}$ W/cm³ respectively.

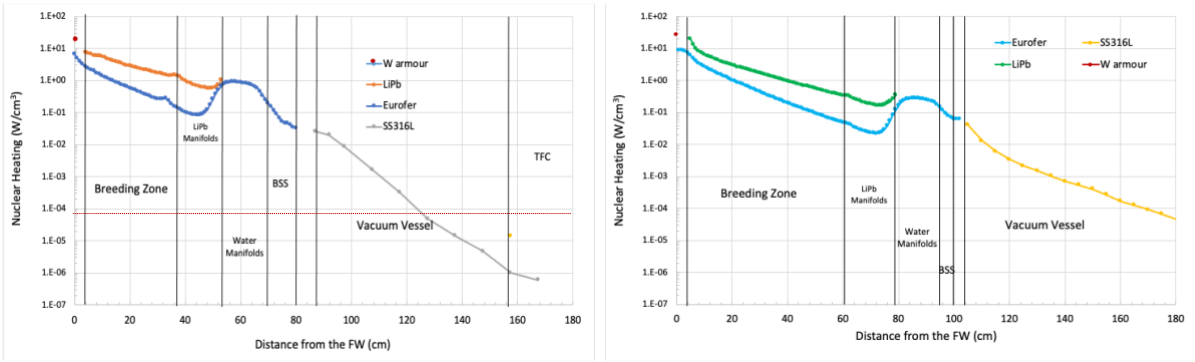

Fig. 5: Inboard (left) and Outboard (right) nuclear heating radial profiles in W armour, Eurofer, PbLi and SS316L. The dotted red line indicates the design target for the heat load on the TFC ($5 \cdot 10^{-5}$W/cm³).

The assessment of the total tritium breeding ratio (TBR) aimed at the verification of the tritium self-sufficiency for the WCLL DEMO reactor has been carried out for each subcomponent of the BB that contributes to the tritium generation (i.e. breeding zones enclosed in each BU and PbLi manifolds), taking into account both the neutron capture reactions on ^{6}Li and ^{7}Li isotopes. The resulting total TBR is 1.14, thus the obtained value is slightly below the design target for tritium self-sufficiency. With respect to the 2020 WCLL BB layout [6], the amount of water in both the inboard and outboard segments of the BB is increased, resulting in a reduced effective volume for the breeder. Moreover, the present concept presents a slight increase of the water content in the outboard FW with respect to the

previous WCLL BB design (6 channels for each BU in the two regions close to the divertor). The water has a double effect: it moderates the neutrons enhancing the probability that they could interact with the lithium nuclei (i.e. the neutron absorption cross section on lithium increases with the reduction of the incident neutron energy), but it also drastically inhibits the neutron streaming in the innermost breeding blanket segments. A further optimization of the BZ performance in terms of Tritium generation has to be taken into account, in order to achieve the required TBR design target.

Acknowledgments

This work has been carried out within the framework of the EUROfusion Consortium. The views and opinions expressed herein do not necessarily reflect those of the European Commission.

References

[1] G. Federici et al, 'Overview of the DEMO staged design approach in Europe', Nuclear Fusion, 59, (2019), 066013.
[2] U. Fischer et al., "Required, Achievable and Target TBR for the European DEMO", Fus. Eng. Des., 155, (2020), Article number 111553.
[3] U. Fischer et al., "Neutronic performance issues of the breeding blanket options for the European DEMO fusion power plant", Fus. Eng. Des., 109-111 (2016), 1458-1463.
[4] X-5 Monte Carlo Team: MCNP - A General Monte Carlo N-Particle Transport Code, Version 5, Los Alamos National Laboratory, Los Alamos, New Mexico, USA, April 2003.
[5] JEFF3.3 nuclear data library, http://www.oecd-nea.org/dbdata/jeff/jeff33/#neutron.
[6] F. Moro et al, "Nuclear performances of the Water-Cooled Lithium Lead DEMO reactor: neutronic analysis on a fully heterogeneous model", Fus. Eng. Des., vol. 168, Art. no. 112514, 2021.
[7] R. Wenninger, DEMO1 Reference Design - 2017_March ("EU_DEMO1_2017") - PROCESS Two Page Output, IDM Ref. EFDA_D_2NCX6E v1.0

PHASE TRANSITION OF DISSOCIATIVE (001) ANATASE SURFACE IN BULK WATER

Giuseppe Zollo[1*], Kersti Hermansson[2], Lorenzo Agosta[2]

[1]*Università di Roma "La Sapienza", Dipartimento di scienze di Base e Applicate per l'IngegneriaVia A. Scarpa 14–16, 00161 Rome, Italy*

[2]*Uppsala Universitet. Department of Chemistry, Ångström laboratoriet, , 751 21 Uppsala, Sweden*

ABSTRACT. Water on metal oxides interfaces generate a variety of ordered motifs that depend on the structural properties of the exposed solid surface and thermodynamics plays a crucial role in bulk water. Using ab-initio calculations and ab-initio molecular dynamics we have studied the thermodynamic behavior of the water induced reconstructed (WIR) anatase (001) surface both in vacuum and under full hydration.

In vacuum a preference seems to emerge for the (2x3) surface reconstruction but with indications that this configuration might not occur spontaneously in bulk water. Indeed ab-initio free energy calculations in bulk water show the existence of thermally activated surface phase transitions between (2x4) and (2x3) symmetries that are lead by the surface relaxation caused by the molecular adsorption and release phenomena at the interface.

1 Introduction

TiO_2 and TiO_2 surfaces of the various crystal phases (anatase, rutile and brookite) are being considered for a variety of applications with special mention to environment- and energy-related applications, such as the photodecomposition of organic pollutants, solar cells, and solar-hydrogen production [1,2]. All the mentioned systems involve the knowledge of the surface-water interaction processes because they imply the usage of either nano-sized TiO_2 or TiO_2 surfaces in water. For this reason, the atomistic scale characterization and modeling of the TiO_2-water interface is being studied intensively.

The anatase (001) facet has been theorized to be highly reactive in water and then a good candidate to obtain photo-reactive water splitting for energetic purposes and is currently debated in relation to the stability of the (001) surface itself. In-situ experimental findings have shown that stable (001) anatase surface undergoes a (1x4) reconstruction in vacuum that has been explained with an atomistic structural "ad-molecule" model (ADM) [3]. However, such model possesses a residual surface reactivity for water splitting that cannot be verified experimentally. There have been increasing difficulties to explain the experimentally observed surface inertness for water dissociation using the ADM model. The reactivity loss has been related to the decreasing of the surface stress with respect to the unreconstructed surface but, while the ADM model predicts a reduced surface stress due to the addition of TiO_2 molecules on the surface, this appears to be not sufficient because some residual surface reactivity, that is not confirmed by experiments, has been found. Moreover, it has been shown also that point defects like vacancies, oxygen ad-atoms or interstitials might even enhance the ADM reactivity and therefore the ADM model was modified proposing that the observed surface reactivity might be related to the oxidized or reduced state of the surface [4]. Regarding the behaviour of TiO_2 (001) surface in water,

some authors have suggested that water patterned TiO_2 (001) surface might compete with the ADM models from the stability point of view [5-7] with some peculiarities: first dissociative water adsorption forms a ridge-terrace geometry similar to the one of the ADM model. This surface modification is accompanied by the formation of a stabilizing network of hydrogen bonds so that the water induced reconstruction (WIR) geometry shows an apparent (2x4) periodicity (see Fig.1); secondly such a water induced surface reconstruction reduces the surface stress at a larger amount than the ADM model and the surface reactivity disappears.
Later it has been demonstrated that the anatase (001) WIR ground state in vacuum shows a (2x3) symmetry that is not compatible with the observed (1x4) one.
Because there are several examples showing that surfaces behave differently in bulk water, we want to study the WIR surface stability and its symmetry in bulk water at different thermodynamics conditions.

2 Computational models and theory

All the calculations have been performed in the context of state of the art density functional theory (DFT). The structural studies at 0K have been performed using the Quantum Espresso suite [8] while the CP2K software [9] has been employed of the ab-initio Molecular Dynamics at different temperatures.
0 K DFT has been employed to study the water molecular adsorption: in this case the usage of a dispersion energy term in the Hamiltonian is mandatory and the dispersion corrected PBE scheme [10] for the Exchange Correlation functional was employed. The anatase (001) surface has been modeled through a four layers slab geometry. The anatase bulk crystal was cleaved to expose the (001) surface and then relaxed. Moreover, the supercell size along the z-axis has been chosen to have a ∼40 Å-thick vacuum region to avoid artifacts due to the PBCs. An important choice is to keep fixed just the atoms belonging to bottom-most layer to reproduce the bulk atomic positions.
We have adopted different supercell sizes depending on the periodical ridge-terrace geometry investigated, namely (2x2), (2x3), (2x4) and (2x6) where the indexes refer respectively to the ridge direction [010] and to the orthogonal one [100].
Concerning the ab-initio Born-Oppenheimer Molecular Dynamics (BOMD) we have adopted periodic super cells of (7.5 × 11.3 × 42.9) and (7.5 × 15.1 × 42.9) ˚A for the (2x3) and (2x4) slabs respectively, the supercell size along z being the same for the two periodicities. We filled the vacuum space in the supercells with 100 and 134 water molecules for the (2x3) and (2x4) surfaces respectively to set the water density at 1g/cm^3. BOMD simulations were performed on the fully hydrated WIR anatase (001) surfaces with the mixed Gaussian and plane wave (GPW) method as implemented in the CP2K package. All the other technical aspects can be found elsewhere [11, 12].
The surface energy at 0 K is calculated according to

$$\gamma_{(2xN)} = \gamma + n_{H_2O}\frac{E^a_{(2xN)}}{A} \qquad (1)$$

Where $\gamma_{(2xN)}$, γ, $E^a_{(2xN)}$, n_{H2O} and A are the surface energy of the (2xN) WIR, of the unreconstructed surface, the average water adsorption energy, the number of adsorbed waters and the surface area.
At thermodynamics conditions the surface free energy difference between the (2x3) and the (2x4) surfaces is :

$$\Delta\eta = \Delta\left(\frac{F^a}{A}\right) = \left(\frac{F^a}{A}\right)_{(2x3)} - \left(\frac{F^a}{A}\right)_{(2x4)} = \Delta\left(\frac{F^a}{A}\right)^{(ave)} + \Delta\left(\frac{F^a}{A}\right)^{(fluct)} \qquad (2)$$

where

$$\left(\frac{F^a}{A}\right)_{(2xN)} = \left(\frac{F^a}{A}\right)^{(ave)}_{(2xN)} + \left(\frac{F^a}{A}\right)^{(fluct)}_{(2xN)} = \frac{k_B T}{A_{(2xN)}}\left[\frac{<U_{(2xN)}>}{k_B T} + ln\left(\sum_{n=0}^{\infty} < \left(\frac{1}{n!}\frac{\Delta U_{(2xN)}}{k_B T}\right)^n >\right)\right] \quad (3)$$

with $U_{(2xN)}$ is the ab-initio potential energy along the BOMD trajectory.

3 Results and discussion

At 0 K the calculated surface energy hierarchy is reported in Table 1.

Table 1: Surface energy values without ($\gamma_{(2xN)}$) and with ($\gamma'_{(2xN)}$) the dispersion energy contribution from bulk water

Surface reconstruction	$\gamma_{(2xN)}$ **(J/m2)**	$\gamma'_{(2xN)}$ **(J/m2)**
(2x2)	0.32	0.51
(2x3)	0.30	0.42
(2x4)	0.37	0.47

The possible molecular adsorption sites of water on the (2x3) and (2x4) surfaces and the corresponding water adsorption energy are shown in Fig. 1.

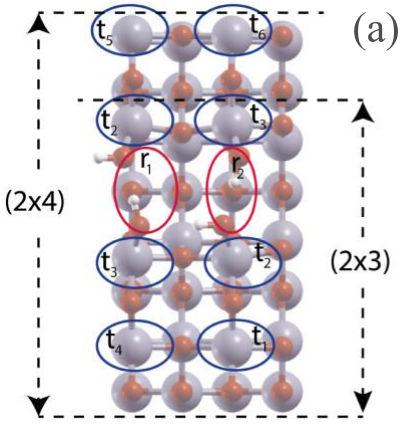

(b)

site	**(2x3) eV**	**(2x4) eV**
t1	-0.455	-0.542
t2	-0.329	-0.367
t3	-0.644	-0.672
t4	-0.486	-0.528
t5	-	-0.542
t6	-	-0.528
r1	-0.344	-0.411
r2	-0.689	-0.705

Fig.1: Molecular water adsorption sites onto the (2x4) and (2x3) water reconstructed surfaces. Terrace and ridge sites are indicated as t and r respectively (a). The corresponding adsorption surface energy values, without ($\gamma_{(2xN)}$) and with ($\gamma'_{(2xN)}$) the dispersion energy contribution from bulk water, are listed in (b).

It is evident that the adsorption energy values for the less stable (2x4) WIR surface are systematically higher that the ones for the ground state (2x3) WIR surface, thus indicating an higher stabilization in water for the (2x4). On this basis we have calculated the free energy difference in bulk water following Eqs. 2 and 3.

The results are summarized in Fig. 2. At 250 K the (2x3) surface is the most stable. As the temperature increases to 300 K, the fully hydrated (2x4) WIR surface becomes by far the most stable surface while the (2x3) WIR surface recovers the ground state between 300 K and 350 K.

This, apparently anomalous, behavior is understood if one considers the thermally activated desorption processes from the molecular adsorption basins on the two surfaces. The WIR surface stability in vacuum (Table 1) suggests that if one considers the dissociative water adsorption by taking the water molecules from a bulk water reservoir, the (2x4) WIR surface becomes more stable than the (2x2) one. Moreover, the difference in surface energy between the (2x4) and (2x3) WIR reconstructions is reduced. The observed free energy behavior in Fig. 2 can be related to the thermal
desorption from the TiO_2 surface molecular adsorption sites with adsorption energy reported in Figure 1(b). Indeed, in the intermediate region we observe that there are temperature values where some water molecules are released from their adsorption sites on the (2x3) WIR surface but not from the (2x4) ones. When the released energy is sufficient to compensate the difference of about 0.05 J/m2 obtained in vacuum the (2x4) WIR surface becomes more stable than the (2x3) one, thus giving rise to a sequence of surface phase transitions lead by the thermal release of physically adsorbed water molecules from the surface sites.

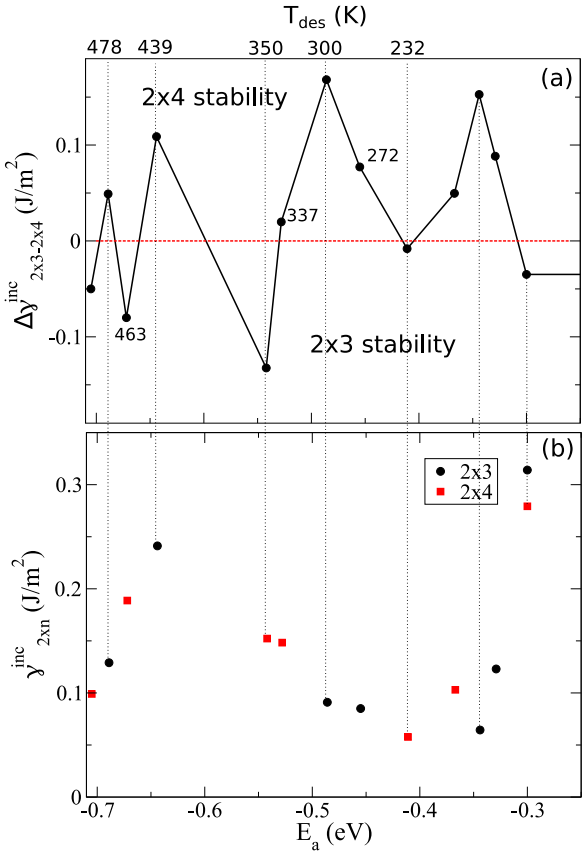

Fig. 2: Increase of the surface energy for the (2x3) and (2x4) WIR surfaces in correspondence of the thermally activated release of the molecular water adsorbed onto the surface according to the values of Figure 1(b). The activation proceeds from the weaker to the stronger adsorptions' sites. The cumulative curve (b) shows that the relative stability of the (2x3) and (2x4) WIR surfaces depends on the temperature in accordance with free energy calculations.

4 Conclusions

DFT based NVT Born-Oppenheimer molecular dynamics runs, in conjunction with ground state DFT total energy calculations, have been employed to study the stability of fully hydrated WIR (001) TiO_2 Due to the surface stress release induced by the water desorption, we observe surface phase transitions between 250 K and 300 K and between 300 K and 350 K with the (2x4) WIR surface stable at 300 K, thus demonstrating that the anatase (001) TiO_2 surface reconstruction depends on the thermodynamics

conditions of the bulk water above it. This finding could be extended to the large variety of water-oxides interfaces where ambient conditions can eventually determine a new equilibrium with respect to the monolayer adsorption at low temperature

Acknowledgments

Part of the computing resources and the related technical support have been provided also by CRESCO/ENEAGRID High Performance Computing infrastructure and its staff [13]. CRESCO/ENEAGRID High Performance Computing infrastructure is funded by ENEA, the Italian National Agency for New Technologies, Energy and Sustainable Economic Development and by Italian and European research programmes, see http://www.cresco.enea.it/english for information.

References

[1] X. Chen, S.S. Mao, Titanium Dioxide Nanomaterials: Synthesis, Properties, Modifications and Applications. *Chem. Rev.* **2007**, *107*, 2891–2959.
[2] A. Fujishima, X. Zhang, D.A. Trykc, TiO_2 Photocatalysis and Related Surface Phenomena. *Surf. Sci. Rep.* **2008**, *63*, 515–582.
[3] A. Vittadini, A. Selloni, F. P. Rotzinger, M. Gretzel, Structure and Energetics of Water Adsorbed at TiO_2 Anatase (101) and (001) Surfaces, *Phys. Rev. Lett.* **1998** 81 2954
[4] Y. Wang, H. Sun, S. Tan, H. Feng, Z. Cheng, J. Zhao, A. Zhao, B. Wang, Y. Luo, J. Yang, J. G. Hou, Role of Point Defects on the Reactivity of Reconstructed Anatase Titanium Dioxide (001) Surface, *Nature Communications* **2013** 4 2214 EP.
[5] S. Sel ̧cuk, A. Selloni, Surface Structure and Reactivity of Anatase TiO_2 Crystals with Dominant {001} Facets, *J. Phys. Chem. C* **2013** 117 (12) 6358–6362.
[6] E. Vitale, G. Zollo, L. Agosta, F. Gala, E. G. Brandt, A. Lyubartsev, Stress Relief and Reactivity Loss of Hydrated Anatase (001) Surface, J. Phys. Chem. C **2018** 122 (39) 22407–22417.
[7] I. Beinik, A. Bruix, Z. Li, K. C. Adamsen, S. Koust, B. Hammer, S. Wendt, J. V. Lauritsen, Water Dissociation and Hydroxyl Ordering on Anatase TiO_2(001)−(1×4), *Phys. Rev. Lett.* **2018** 121 206003.
[8] Giannozzi, P. et al. QUANTUM ESPRESSO: A Modular and Open-Source Software Project for Quantum Simulations of Materials. *J. Phys.: Condens. Matter* **2009**, *21*, 395502–1–19.
[9] J. Hutter, M. Iannuzzi, F. Schiffmann, J. VandeVondele, CP2K: Atomistic Simulations of Condensed Matter Systems, *Wiley Interdiscip. Rev.: Comput. Mol. Sci*. **2014** 4 15.
[10] Perdew, J.P.; Burke, K.; Ernzerhof, M. Generalized Gradient Approximation Made Simple. *Phys. Rev. Lett.* **1996**, *77*, 3865.
[11] G. Zollo, E. Vitale, A Deeper Insight on the Stability of Water-Induced Reconstruction of Anatase (001) surface, *Applied Sciences* **2018** 8 2522.
[12] G. Zollo, K. Hermansson, L. Agosta, Thermodynamics of Dissociated Water Motifs at Oxide-Bulk Water Interfaces: The TiO_2 Anatase (001) Case, *Appl. Surf. Sci.* **2021** 550 149354
[13] F. Iannone, F. Ambrosino, G. Bracco, M. De Rosa, A. Funel, G. Guarnieri, S. Migliori, F. Palombi, G. Ponti, G. Santomauro, P. Pro- cacci, Cresco enea hpc clusters: a working example of a multifabric gpfs spectrum scale layout, in: *2019 International Conference on High Performance Computing Simulation (HPCS)*, **2019**, pp. 1051–1052.

AUTHOR INDEX

ISBN: 978-88-8286-440-8